Theoretical and experimental investigation of magnetic layer coupling in spin-valves and magnetic tunnel junctions

Łukasz Gładczuk
Mansfield College
University of Oxford

A thesis submitted for the degree of
Doctor of Philosophy
Michaelmas 2020

This thesis is dedicated to
my father
for his love and continuous support.

Abstract

Heterostructures composed of ferromagnetic layers that are mutually interacting through a nonmagnetic spacer are at the core of magnetic sensor and memory devices. In the present study, layer-resolved ferromagnetic resonance was used to investigate the coupling between the magnetic layers of a Co/MgO/Permalloy magnetic tunnel junction (MTJ) and Co/Sn/Py spin valves.

Elemental tin in the α-phase is an intriguing member of the family of topological quantum materials. In thin films, with decreasing thickness, α-Sn transforms from a 3D topological Dirac semimetal to a 2D topological insulator (TI). Getting access to, and making use of its topological surface states is challenging and requires interfacing to a magnetically ordered material.

For both types of samples two magnetic resonance peaks were observed for both magnetic layers, as probed at the Co and Ni L_3 x-ray absorption edges, showing a strong interlayer interaction through the insulating MgO barrier. A theoretical model based on the Landau-Lifshitz-Gilbert-Slonczewski equation was developed, including exchange coupling and spin pumping between the magnetic layers. Fits to the experimental data were carried out, both with and without a spin pumping term, and the goodness of the fit was compared using a likelihood ratio test.

Evidence of two types of magnetic layer coupling were found for the studied MgO MTJ. A Likelihood ratio test performed between competing models showed that a model with only exchange coupling is insufficient, and the correct description of the experimental data requires

inclusion of spin pumping coupling between magnetic layers. The values characterising both the EC and the spin pumping were estimated. A recipe has been developed for spin-vale fabrication incorporating a α-Sn TI spacer layer. Up to 2 nm thick α-Sn layers were deposited onto a Co surface. The X-ray detected ferromagnetic resonance (XFMR) study of the α-Sn system has shown a strong exchange coupling interaction between the magnetic layers with no clear evidence for spin pumping.

The methods developed in this work can be used to interpret XFMR data, not only in the discussed cases, but potentially for all types of measurements in general. The explored idea of incorporating the TI α-Sn into a spin-valve has shown promising results, and will serves as a solid basis for further research.

Contents

1 Introduction **1**

2 Theoretical model for the magnetisation dynamics in thin films **4**

2.1 Micromagnetic energy 5

2.1.1 Zeeman energy 6

2.1.2 Demagnetisation energy 6

2.1.3 Anisotropy energy 8

2.1.4 Exchange energy 9

2.2 Static equilibrium 10

2.2.1 Static solution for Py 11

2.2.2 Static solution for Co 17

2.3 Magnetisation dynamics 27

2.4 Single layer dynamics 29

2.4.1 Derivations for FMR experiments 34

2.4.2 Derivations for XFMR 35

2.4.3 Uniaxial anisotropy (single term) 37

2.4.4 Uniaxial anisotrophy (two terms) 45

2.5 Cross-layer interaction 49

2.5.1 Exchange interaction 50

2.5.2 Spin current in conductors 54

2.5.3 Two-layer dynamics 59

3 Device Fabrication and Structural Characterisation **67**

3.1 Substrate preparation 68

3.2 Molecular Beam Epitaxy 69

3.3 Growth characterisation 70
3.3.1 Reflection high-energy electron diffraction 70
3.3.2 Low-energy electron diffraction 71
3.3.3 Atomic Force Microscopy 72
3.3.4 Scanning Tunnelling Microscopy 73
3.3.5 X-ray crystallography 73
3.3.6 Cross-Sectional Transmission Electron Microscopy 74
3.4 Growth conditions for selected materials 74
3.4.1 MgO/Co/Sn 74
3.4.2 MgO/Co/Sn/Py/Si 75
3.4.3 Al_2O_3/Mo/Au 75
3.4.4 Al_2O_3/Mo/Au/Co/MgO/Py/Au 75
3.4.5 Al_2O_3/Mo/Au/$(Co/Au)_N$/MgO/Py/Au 76
3.4.6 Al_2O_3/Mo/Au/Co/Sn/Py/Si 76

4 Characterisation of Magnetic Properties 77
4.1 SQUID Vibrating Sample Magnetometry 77
4.2 X-ray magnetic circular dichroism (XMCD) 78
4.3 Ferromagnetic Resonance (FMR) 79
4.3.1 Cavity Ferromagnetic Resonance (Cavity FMR) 79
4.3.2 Vector Network Analyser Ferromagnetic Resonance (VNA-FMR) 80
4.3.3 Time-resolved X-ray Ferromagnetic Resonance (XFMR) . . 81

5 Model Fitting and Hypothesis Testing 85
5.1 The Likelihood Ratio Test 86
5.1.1 Example 89
5.2 The Cavity FMR Model Fitting 92
5.3 XFMR Model Fitting 95

6 Classical Insulators 99
6.1 Initial studies 101
6.2 Cavity FMR measurements 103
6.3 VNA-FMR measurements 110

6.4 XFMR measurements . . . 113

7 Topological Insulators 122

7.1 α-Sn TI overview . . . 123
7.2 Device fabrication . . . 123
7.3 Characterisation of structural properties . . . 125
7.4 Characterisation of magnetic properties . . . 128
7.5 Summary of the results for the α-Sn spin-valves . . . 134

8 Summary and conclusions 135

8.1 Summary of the results for the MgO samples . . . 136
8.2 Summary of the results for the tin samples . . . 137
8.3 Perspective for further research . . . 138

A Extrema of the energy potential 139

A.0.1 $D > 0$, $\phi = \phi_H$ . . . 140
A.0.2 $D > 0$, $\phi = \phi_H + \pi$ . . . 140
A.0.3 $D < 0$, $\phi = \phi_H$ . . . 140
A.0.4 $D < 0$, $\phi = \phi_H + \pi$ . . . 141
A.1 Edge cases . . . 141

B Static solutions for an uni-axial anisotropy with two terms 143

C XFMR measurements for the S1655_II sample 148

D XFMR measurements for the LG002 sample 156

E XFMR measurements for the LG003 sample 161

Bibliography 166

List of Figures

2.1 Illustration of the magnetic hysteresis loop. B is used to denote the magnetic flux density and H is the magnetic field strength. Arrows on the loop indicate the direction of the transition path. 5
2.2 Coordinate system used to calculate the demagnetisation field . . . 7
2.3 Direction of the magnetisation vector in dependence on the magnitude of the dimensionless magnetic field and its orientation for negative values of the D parameter. The left panel presents how the value of θ changes with the dimensionless magnetic field b for four different orientations of the magnetic field (θ_H). The right panel summarises the same results for the orientations of the magnetic field in the range between 0° and 90°, with the resulting orientation of the magnetisation indicated by a color scale and grid-lines drawn every 10°. 14
2.4 Static orientation of the magnetisation vector for the sample with a positive D parameter. Two possible orientations in dependence on the magnetic field strength b and orientation θ_H are shown in panels a) and b). Panel c) shows the magnetisation orientation θ for three different orientations of the magnetic field. Panel d) presents the potential energy of the system as a function of the magnetisation orientation for the cases presented on panel c), where colors correspond to the legend on panel c) and the strength of the magnetic field is visualized by the opacity of the graph (highest opacity corresponds to $b = 1.5$, intermediate to $b = 1$, smallest to $b = 0.5$). 16

2.5 Projection of the magnetisation vector onto the direction of the magnetic field in dependence on the field strength for a sample with (left) $D > 0$, (right) $D < 0$. 17
2.6 Summary of the type of equilibrium position in dependence on the anisotropy of the thin film sample. In the "easy-axis" region, both $\theta_H = \pi$ and $\theta_H = 0$ orientations are stable. In the "easy-cone" region two solutions are possible that are neither oriented out-of-plane nor in-plane of the sample. In the "easy-plane" region, a single solution is possible, where the magnetisation is oriented in-plane of the sample. The "easy-axis" and "easy-plane" regions overlap, creating a region where three solutions are possible. In this region, either the "easy-axis" or the "easy-plane" is a global energy minimum. The critical value where both types of solution have the same energy is marked with a dotted line. 20
2.7 Graphical representation of the static orientation of the magnetisation vector when no external field is applied to the sample. 21
2.8 Energy as a function of the magnetisation orientation (θ) for the anisotropy angle (ψ) equal to: (A) 45°, (B) 157.5°, (C) 225°, (D) 325°, (E) 333.4°, and (F) 345°. 21
2.9 Plot showing the number and kind of solutions in dependence on the magnetic field and the sample anisotropies for the magnetic field oriented normal to the sample surface. The azimuthal angle ψ is defined by relation (2.43). The distance from the centre of the diagram is the dimensionless magnetic field b. The diagram on the right is a magnification of the centre region of the left diagram. . . 23
2.10 Energy as a function of the magnetisation orientation θ for the magnetic field oriented out-of-plane and the anisotropy angle (ψ) equal to: (A) 135°, (B) 45°, (C) 225°, (D) 130.4°, (E) 148°, (F) 328°, and (G) 310.4°. 24

2.11 Plot showing the number and kind of solutions in dependence on the magnetic field and the sample anisotropies for the magnetic field directed in-plane of the sample. The azimuthal angle ψ is defined by relation (2.43). The distance from the centre of the diagram is the dimensionless magnetic field b. Graphs on the right show the energy dependence on the magnetisation vector θ in the three qualitatively distinct regions. 25
2.12 Projection of the magnetisation vector onto the direction of magnetic field in dependence on field strength for the field oriented in-plane of the sample for different values of the anisotropy ψ. . . . 25
2.13 Projection of the magnetisation vector onto the field direction in dependence on field strength for the field oriented out-of-plane of the sample for different values of the anisotropy ψ. 26
2.14 Number of solutions (left column) and direction of the magnetisation vector θ at the global energy minimum (right column) in dependence of the anisotropy (ψ the azimuthal angle) and the dimensionless magnetic field (b the distance from the center), for a few chosen orientations of the external magnetic field (θ_H). 28
2.15 Coordinate system used to parametrise Equation (2.67); y is the the y component of the magnetic vector variation ($\delta\boldsymbol{M}$), p is perpendicular to both M and y components of the variation. 30
2.16 Amplitude of the oscillations of the magnetisation vector. On the left, (y, p) trajectories at four different driving frequencies (multiple of ω_R). On the right graph, the amplitude and phase of the oscillations are shown as a function of the driving frequency. Here, the calculation is shown for $\theta = \pi/2$, $\theta_H = \pi/2$, $K_1 = 200 \times 10^3\,\mathrm{J/m^3}$, $M_s = 0.6 \times 10^6\,\mathrm{A/m}$, $B = 20\,\mathrm{mT}$, $h_0 = 1\,\mu\mathrm{H}$, $\alpha = 0.1$. 33
2.17 Microwave absorption spectrum as a function of external magnetic field and driving frequency. For the calculations, the following parameters were used: $\theta = \pi/2$, $\theta_H = \pi/2$, $K_1 = 0\,\mathrm{J/m^3}$, $M_s = 0.6 \times 10^6\,\mathrm{A/m}$, $B = 100\,\mathrm{mT}$, $h_0 = 175\,\mu\mathrm{H}$, $\alpha = 0.02$. 36
2.18 Dependence of the absorption peak on the Gilbert damping parameter. 36

2.19 The projection of the magnetisation vector onto the photon beam direction (the XFMR signal) as a function of the external magnetic field. The graphs on the left show amplitude and phase. Graph on the right combines the information about both the phase and amplitude in a single graph where the horizontal value is given as $A\cos\phi$ and the vertical value as $A\sin\phi$. The value of the corresponding magnetic field is indicated by ticks along the curve. The example was calculated for: $\theta = \pi/2$, $\theta_H = \pi/2$, $K_1 = 0\,\mathrm{J/m^3}$, $M_s = 0.6 \times 10^6\,\mathrm{A/m}$, $B = 100\,\mathrm{mT}$, $h_0 = 175\,\mu\mathrm{H}$, $\alpha = 0.02$. 37
2.20 Dimensionless resonance frequency in dependence on the dimensionless magnetic field for different values of the external magnetic field orientation θ_H for $D < 0$ with $\alpha = 0$. 39
2.21 Dependence of the resonance magnetic field on the field orientation for different values of the driving frequency for the sample with an easy-plane of magnetisation $D < 0$. 39
2.22 Dimensionless resonance frequency in dependence on the dimensionless magnetic field for different values of the external magnetic field orientation θ_H for case of $D < 0$ with $\alpha = 0$. Two branches of the solutions are shown, one for the global energy minimum (left) and the other for the metastable state (right). 40
2.23 a) Set of points in the (θ, θ_H)-plane for which the frequency function $\nu(b)$ has an extremum: blue - frequency maxima, green - frequency minima. b) Resonance frequency in dependence on the magnetic field for various field orientations with an overlay curve connecting the maxima (solid, black) and minima (dashed, black) 43
2.24 Phase space presenting the number of distinct values of the resonance magnetic field in dependence on the magnetic field orientation and frequency of the driving magnetic field assuming the system is in its global minimum. The plot on the right is a magnification of the region marked on the left plot. 43
2.25 Dependence of the resonance frequency on the value of the external magnetic field for successive values θ_H. 44

2.26 Dependence of the resonance magnetic field on the field orientation for different values of the driving frequency for the sample with an easy-axis of magnetisation $D > 0$. The graph on the left shows the case of the magnetisation at a global minimum, and graph on the right a the case of a metastable state. 45
2.27 Resonance frequency dependence on the magnetic field strength for the magnetic field oriented out-of-plane for different anisotropies ψ. Blue line: magnetisation oriented in the direction of the magnetic field $\theta = 0$. Orange line: magnetisation oriented in the opposite direction $\theta = \pi$. 47
2.28 Resonance frequency dependence on magnetic field strength for the magnetic field oriented in-plane for different anisotropies ψ. 48
2.29 Resonance frequency dependence on the magnetic field strength for the field oriented at $\theta_H = 28.6°$ for the two different anisotropies ψ. Each line corresponds to different solution branches of the magnetisation orientation. 49
2.30 Resonance frequency dependence on the magnetic field strength for the field oriented at $\theta_H = 67.1°$ for the two different anisotropies ψ. Each line corresponds to different solution branches of the magnetisation orientation. 50
2.31 Orientation of the magnetisation vectors which correspond to the global potential energy minimum in dependence on the value of the external magnetic field in dimensionless coordinates. Layer '1' is marked by a solid lines, and layer '2' by dashed lines of the corresponding colour. The plot on the left shows the case of the magnetic field oriented in-plane ($\theta_H = \pi/2$), the plot on the right $\theta_H = \pi/4$. Both plots were made for the sample with the anisotropy $\psi = \pi/3$ and $\zeta = \pi/3$. In case of the magnetic field oriented in-plane with no exchange coupling ($j = 0$), the two orientations have the same energy value and the single global minimum cannot be distinguished. 54

2.32 Diagrams presenting the value of the potential energy in dependence on the orientation of the magnetisation of the two magnetic layers (θ_1, θ_2). Across the rows the value of the exchange coupling j is varied, and across the columns dimensionless magnetic field b is varied. The regions with low energy are marked in blue and regions with high energy in orange. Red dots were used to mark local energy minima. The diagrams were plotted for the magnetic field in-plane ($\theta_H = \pi/2$) and using the following parameters: $\psi = \pi/3$, $\zeta = \pi/3$, corresponding to the left graph in Figure 2.31. 55

2.33 Diagrams presenting the value of the potential energy in dependence on the orientation of the magnetisation of the two magnetic layers (θ_1, θ_2). Across the rows the value of the exchange coupling j is varied, and across the columns dimensionless magnetic field b is varied. The regions with low energy are marked in blue and regions with high energy in orange. Red dots were used to mark local energy minima. The diagrams were plotted for the magnetic field in-plane ($\theta_H = \pi/4$) and using the following parameters: $\psi = \pi/3$, $\zeta = \pi/3$, corresponding to the left graph in Figure 2.31. 56

2.34 Isolines of the constant magnetic field (left) and the constant EC parameter j (right) on a (θ_1, θ_2) plane. Solid lines are drawn in the region where the system is in a local minimum, dashed lines are used otherwise. The isolines are labelled with the numbers representing the value of the dimensionless magnetic field and the EC parameter, respectively. Black lines distinguish the regions where the system is at a minimum and the dimensionless magnetic field is positive ($b > 0$). The plots were drawn for the following system parameters: $\psi = -\pi/4$, $\zeta = \pi/3$, $\theta_H = \pi/2$. 57

2.35 Equilibrium positions of the magnetisation orientation (θ_1, θ_2) in dependence on the value of the dimensionless magnetic field (blue isolines), the EC parameter (thick red-green lines), and the orientation of the external magnetic field θ_H. The regions where the orientation of the magnetisation is stable are distinguished by black contours and solid magnetic field isolines. The plots were drawn for the following system parameters: $\psi = -\pi/4$, $\zeta = \pi/3$. 58
2.36 FMR absorption spectra obtained using Equation (2.137) for different values of the EC parameter j (left) and the SP parameter $a^{\uparrow\downarrow}$ (right). Sample parameters: $\psi = -2.614$, $\zeta = 0.405$, magnetic field oriented in-plane ($\theta_H = \pi/2$). 63
2.37 FMR absorption spectra obtained using Equation (2.137) for different values of the EC parameter j (left) and the SP parameter $a^{\uparrow\downarrow}$ (right). Sample parameters: $\psi = -2.614$, $\zeta = 0.405$, magnetic field oriented in-plane ($\theta_H = \pi/2$). 64
2.38 Effect of exchange coupling (left) and spin-pumping (right) on the XFMR signal. Blue and orange colors represent different magnetic layers. For comparison, the XFMR signal with no coupling between layers is plotted with dashed lines. System parameters: $\psi = -2.976$, $\zeta = 0.405$, $f = 8\,\mathrm{GHz}$. Coupling for the left graph: $j = 0.0068$ and $a^{\uparrow\downarrow} = 0$. Coupling parameters for the right graph: $j = 0$ and $a^{\uparrow\downarrow} = 0.34$. 65

3.1 RHEED images of the Co (111) surface along the two principal directions, with the sample being rotated by 30° between the images. 71
3.2 LEED images of the annealed Si(111) surface at few chosen values of the electron beam energy. By visual comparison with published data, it can be concluded that the LEED pattern corresponds to a 7×7 surface reconstruction [1]. 72

4.1 Illustration of the cavity FMR setup. A sample is placed into the microwave resonance cavity using a glass rod. Red and blue sine waves illustrate the generated microwaves and the ones reflected by the sample. 80

4.2 Illustration of the setup used in VNA-FMR experiments with the sample placed on the co-planar waveguide. Purple lines in the right image illustrate the magnetic field lines created by the current flowing through the signal line in the centre. 81
4.3 Schematic of the XFMR setup used for the layer-specific characterisation of the magnetisation dynamics of the magnetic heterostructure. Figure taken from Ref. [2]. 82

5.1 Null (red) and alternative (green) hypothesis models fitted to the observed data. The graph on the left shows the case where the error is given by the normal distribution with σ_L and on the right with σ_S. The true dependence given by $2x^2 + 0.25$ is marked with a dashed line. 90
5.2 The cumulative probability distribution of the LR under the assumption that the null hypothesis is true for the data obtained from the model (5.9). The case of σ_L is shown on the left and σ_S on the right. The respective values of the LR obtained in the test are indicated by the red vertical lines. In the second case, the LR value is outside of the horizontal axis range. The fitted χ^2 distribution is represented by the blue solid line. 90
5.3 Null (red) and alternative (green) hypothesis models fitted to the observed data. The graph on the left shows the case where the error is given by the normal distribution with σ_L and on the right with σ_S. The true dependence given by $0.5x + 0.25$ is marked with a dashed line. 91
5.4 The cumulative probability distribution of the LR under the assumption that the null hypothesis is true for the data obtained from the model (5.12). The case of σ_L is shown on the left and σ_S on the right. The respective values of LR obtained in the test are indicated with the red vertical lines. The fitted χ^2 distribution is shown by a blue line. 92

5.5 FMR absorption in dependence on the magnetic field acquired in the cavity FMR experiment at a driving frequency of 9.38 GHz and a magnetic field orientation of $\theta_H = 10°$ in blue, along with the fitted model (5.15) in red. The values of the fitted parameters: $B_0 = (635.21 \pm 0.02)\,\mathrm{mT}$, $\Delta B = (21.82 \pm 0.05)\,\mathrm{mT}$, $A_1 = 2.343 \pm 0.004$, $A_2 = -0.396 \pm 0.004$, $A_3 = -0.723 \pm 0.013$. 93

5.6 Experimental data (orange circles) for the Co sample at $T = 80\,\mathrm{K}$ together with model fits. The null hypothesis was marked by a semi-transparent black line, alternative hypothesis with black line. The cumulative probability distribution of LR under the assumption, that null hypothesis is true, is shown on the right plot. The obtained value LR (5.18) is far to the right of the plot range. 94

5.7 XFMR measurements for various values of delay (purple points) together with the fitted sinusoidal function (red). Green and orange graphs represent the sine and cosine components of the fitted model (5.19). The measurements were performed on a 10 nm thick Co sample at a driving frequency of 4 GHz, the magnetic field oriented in-plane ($\theta_H = \pi/2$), a magnetic field strength of $B = 13\,\mathrm{mT}$, and the sample held at a temperature of $T = 80\,\mathrm{K}$. The values of the fitted parameters are: $A = 1.391 \pm 0.007$, $B = -0.313 \pm 0.007$. . . . 96

5.8 Amplitude and phase (left), and the in- and out-of-plane components of the XFMR signal (right) for Co/MgO/Py (S1655_II introduced in chapter 6) measured at room temperature, with the magnetic field oriented in-plane of the sample. The XFMR measurement data are represented by points (orange for Co, and blue for Ni). The fitted models are shown by solid lines, whereby the alternative hypothesis is represented by an opaque line, and the null hypothesis by a semi-transparent line. 97

6.1 Illustration of spin dynamics in a MTJ when current flows through the junction. The electrons spins become polarised in the first magnetic layer (left), tunnel through the non-magnetic insulating barrier, and exert torque on the other magnetic layer (right). 100

6.2 Resonance curves depending on temperature for samples with 2 nm (left) and 10 nm (right) MgO barriers. The Py characteristics do not change with temperature. For a fixed value of the magnetic field, the Co resonance frequency decreases with decreasing temperature. Measurements done at temperatures (starting from the top curve): 332 K, 284 K, 247 K, 214 K, 184 K, 148 K, 112 K. 101
6.3 XRD (left) and XRR (right) measurements of the S1644_I and S1644_II samples. 102
6.4 Magnetic Hysteresis curves at 100 K, 200 K, and 300 K (room temperature) for the S1644_I (left) and S1644_II (right) samples, respectively 103
6.5 TEM images of the S1655_I (top) and S1655_II (bottom) samples. . 104
6.6 Strength of the FMR microwave absorption in dependence on the external magnetic field magnitude. Measurements are marked in blue, the fitted curve in red. Vertical dashed lines mark found resonance peaks position at: 135 mT, 175 mT. 105
6.7 Magnetic resonance field as a function of the magnetic field direction (θ_H) for: 5 nm Co sample at (a) 300 K and (b) 80 K, 10 nm Co sample at (c) 300 K and (d) 80 K, and 5 nm Py sample at (e) 300 K and (f) 80 K, 10 nm. The fitted theoretical dependence is represented by solid black lines. In case of the 5 nm Co sample, additionally, a fitted model with a single anisotropy term is shown by a dashed line. 107
6.8 Theoretical predictions for the magnetic resonance field for the sample with two magnetic layers. The Co and Py parameters were taken from Table 6.2 for the materials at 80 K. Three graphs show the results for different values of the EC parameter j. 108
6.9 Ferromagnetic resonance field in dependence on magnetic field direction (θ_H) for S1655_I at (a) 300 K and (b) 80 K, and S1655_II at (c) 300 K and (d) 80 K. Measurement points for Co are marked with orange dots, Py with blue. Fitted theoretical curves are shown in black. 109

6.10 Calculations of the resonance frequency dependence on the magnitude of the external magnetic field at $\theta_H = 90^\circ$ for the sample consisting of 10 nm Co layer and 5 nm Py layer held at room temperature. It is assumed that the magnetic layers interact only via EC. The anisotropy constants determined for the sample S1655_II (Table 6.3) are used. The value $\zeta = 0.13$ is assumed. The three graphs show plots for different values of the EC parameter j. 111
6.11 VNA-FMR measurements with superimposed theoretical curves (in red), calculated using parameters determined by cavity FMR measurements. From top to bottom: S1655_I at RT, S1655_I at 80 K, S1655_II at RT, S1655_II at 80 K. From left to right: field in-plane, 35°, and 10° away from the surface normal. 112
6.12 Amplitude and phase of the XFMR signal measured for the S1655_I sample at room temperature and at 80 K for the magnetic field orientation $\theta_H = 35^\circ$. 114
6.13 Amplitude and phase of the XFMR signal measured for the S1655_II sample at room temperature and at 80 K for the magnetic field orientation $\theta_H = 45^\circ$. 114
6.14 Amplitude and phase of the XFMR signal measured for the S1656_II sample at room temperature and at 80 K for the magnetic field orientation $\theta_H = 35^\circ$. 115
6.15 XFMR results for sample S1655_II at 80 K, and the external field direction $\theta_H = 20^\circ$. Orange and blue points represent the data for Co and Py, respectively. The solid lines represent the theoretical model with SP and EC, while the dashed lines represent the EC only model. The plot on the left shows the data in (A, B) coordinates, while the plots on the right show the results in on the amplitude and phase graphs as a function of external magnetic field. Green and red arrows, and a dashed vertical line were used to mark points for the same value of the external magnetic field (63.6 mT). 118

6.16 XFMR results for sample S1655_II at 300 K, and the external field direction $\theta_H = 35°$. Orange and blue points represent the data for Co and Py, respectively. The solid lines represent the theoretical model with SP and EC, while the dashed lines represent the EC only model. The plot on the left shows the data in (A, B) coordinates, while the plots on the right show the results in on the amplitude and phase graphs as a function of external magnetic field. 119
6.17 Values of the fitted anisotropy constants $D_{\theta_H}^{\mathrm{Co/Py}} = 2K_{\theta_H}^{\mathrm{Co/Py}}/M_{\mathrm{s}}^{\mathrm{Co/Py}}$ for S1655_II at (a) 300 K and (b) 80 K. Similar results were obtained for both cases, i.e., with and without SP. For clarity, the results for the fit of the model with SP is shown. 119

7.1 Crystallographic structure of (a) the HCP Co and b) the diamond cubic α-Sn. The Co(0001) direction corresponds to the hexagonal plane of the HCP crystal. (111) plane of the diamond cubic crystallographic structure of the α-Sn was marked with red triangle in panel (b). The value of $b = 4.572$ Å is the distance between atomic sites in this cross-section. Panel (c) illustrates a possible configuration of the α-Sn crystal atoms (white circles connected with red lines) on the Co surface (black disks connected with black lines) corresponding to the distance between the Sn atoms equal to 4.363 Å. This results in a $\sim 5\%$ mismatch with the α-Sn lattice. The values for the lattice constant of Co and Sn were taken from Refs. [3] and [4], respectively. 124
7.2 RHEED images of the Co(111) layer for the sample oriented along two distinct symmetry axes rotated by 30° with respect to each other [(a) and (b)]. The corresponding RHEED images of the Sn layer along the same two symmetry axes [(c) and (d)]. 125
7.3 X-ray diffraction (XRD) measurements of the (a) LG002, (b) LG003 samples performed in a temperature range between 80 K and 300 K (RT). 126

7.4 X-ray reflectivity (XRR) measurements of (a) LG002 and (b) LG003 samples performed in the temperature range between 80 K and 300 K (RT). Some of the measurements (at 274 K for LG002 and 80 K and 150 K for LG003) have a lower signal count, which is probably caused by misalignment of the sample. 126
7.5 Cross-sectional transmission electron microscopy (TEM) images of LG002 (left) and LG003 (right). The composition of individual layers was determined using EDX. A Pt capping layer was added for the purpose of TEM sample preparation. Images were taken by Prof. Piotr Dłużewski at the Institute of Physics, Polish Academy of Sciences. 127
7.6 The cavity FMR measurements for the LG003 sample performed at driving a frequency of $f = 9.38\,\mathrm{GHz}$. Two resonance peaks were identified and are marked with orange (Co) and blue circles (Py). The theoretical model for a system with two magnetic layers was fitted to the data resulting in the following values for the magnetic parameters: $\gamma_{\mathrm{Py}} = 224\,771\,\mathrm{m/(s \cdot A)}$, $\gamma_{\mathrm{Co}} = 245\,429\,\mathrm{m/(s \cdot A)}$, $D_{\mathrm{Py}} = -1.09\,\mathrm{T}$, $D^1_{\mathrm{Co}} = -1.01\,\mathrm{T}$, $D^2_{\mathrm{Co}} = -0.31\,\mathrm{T}$, and $j = 0.6{\times}10^{-3}$. The value of $\zeta = 0.068$ was estimated based on the layer thickness found in the TEM measurements, and assuming the layer magnetisation at saturation equal to $M_{\mathrm{s}}^{\mathrm{Co}} = 1.4 \times 10^6\,\mathrm{A/m}$ and $M_{\mathrm{s}}^{\mathrm{Py}} = 0.4 \times 10^6\,\mathrm{A/m}$. 129
7.7 VNA-FMR measurements on LG002 at 80 K, 300 K, and 347 K; with the magnetic field oriented in-plane. 129
7.8 VNA-FMR measurements on LG003 at: 80 K, 300 K, and 350 K; with the magnetic field oriented in-plane. 130
7.9 XFMR results for the LG002 sample at 152 K, and the external field direction $\theta_H = 90^\circ$. Orange and blue points represent the data for the Co and Py layers, respectively. 131
7.10 XFMR results for the LG002 sample at 328 K, and the external field direction $\theta_H = 90^\circ$. Orange and blue points represent the data for the Co and Py layers, respectively. 131

7.11 XFMR results for the LG003 sample at 201 K, and the external field direction $\theta_H = 90°$. Orange and blue points represent the data for the Co and Py layers, respectively. 132
7.12 XFMR results for the LG003 sample at 300 K, and the external field direction $\theta_H = 90°$. Orange and blue points represent the data for the Co and Py layers, respectively. 132

B.1 Number of solutions (left) and orientation of the magnetisation θ at the global energy minimum (right) in dependence on the anisotropy (the azimuthal angle ψ), and the field strength (b is distance from the centre), at different orientations of the external magnetic field (θ_H) as indicated. 147

C.1 XFMR results for S1655_II at 80 K, and the external field direction $\theta_H = 15°$. Orange and blue point represent the data for Co and Py, respectively. 148
C.2 XFMR results for S1655_II at 80 K, and the external field direction $\theta_H = 20°$. Orange and blue point represent the data for Co and Py, respectively. 149
C.3 XFMR results for S1655_II at 80 K, and the external field direction $\theta_H = 25°$. Orange and blue point represent the data for Co and Py, respectively. 149
C.4 XFMR results for S1655_II at 80 K, and the external field direction $\theta_H = 35°$. Orange and blue point represent the data for Co and Py, respectively. 150
C.5 XFMR results for S1655_II at 80 K, and the external field direction $\theta_H = 45°$. Orange and blue point represent the data for Co and Py, respectively. 150
C.6 XFMR results for S1655_II at 80 K, and the external field direction $\theta_H = 60°$. Orange and blue point represent the data for Co and Py, respectively. 151
C.7 XFMR results for S1655_II at 80 K, and the external field direction $\theta_H = 75°$. Orange and blue point represent the data for Co and Py, respectively. 151

C.8 XFMR results for S1655_II at 80 K, and the external field direction $\theta_H = 90°$. Orange and blue point represent the data for Co and Py, respectively. 152
C.9 XFMR results for S1655_II at 300 K, and the external field direction $\theta_H = 15°$. Orange and blue point represent the data for Co and Py, respectively. 152
C.10 XFMR results for S1655_II at 300 K, and the external field direction $\theta_H = 25°$. Orange and blue point represent the data for Co and Py, respectively. 153
C.11 XFMR results for S1655_II at 300 K, and the external field direction $\theta_H = 35°$. Orange and blue point represent the data for Co and Py, respectively. 153
C.12 XFMR results for S1655_II at 300 K, and the external field direction $\theta_H = 45°$. Orange and blue point represent the data for Co and Py, respectively. 154
C.13 XFMR results for S1655_II at 300 K, and the external field direction $\theta_H = 60°$. Orange and blue point represent the data for Co and Py, respectively. 154
C.14 XFMR results for S1655_II at 300 K, and the external field direction $\theta_H = 90°$. Orange and blue point represent the data for Co and Py, respectively. 155

D.1 XFMR results for the LG002 sample at 80 K, and the external field direction $\theta_H = 90°$. Orange and blue point represent the data for Co and Py respectively. 156
D.2 XFMR results for the LG002 sample at 152 K, and the external field direction $\theta_H = 90°$. Orange and blue point represent the data for Co and Py respectively. 157
D.3 XFMR results for the LG002 sample at 199 K, and the external field direction $\theta_H = 90°$. Orange and blue point represent the data for Co and Py respectively. 158

D.4 XFMR results for the LG002 sample at 218 K, and the external field direction $\theta_H = 90°$. Orange and blue point represent the data for Co and Py respectively. 158
D.5 XFMR results for the LG002 sample at 246 K, and the external field direction $\theta_H = 90°$. Orange and blue point represent the data for Co and Py respectively. 159
D.6 XFMR results for the LG002 sample at 274 K, and the external field direction $\theta_H = 90°$. Orange and blue point represent the data for Co and Py respectively. 159
D.7 XFMR results for the LG002 sample at 300 K, and the external field direction $\theta_H = 90°$. Orange and blue point represent the data for Co and Py respectively. 160
D.8 XFMR results for the LG002 sample at 328 K, and the external field direction $\theta_H = 90°$. Orange and blue point represent the data for Co and Py respectively. 160

E.1 XFMR results for the LG003 sample at 80 K, and the external field direction $\theta_H = 90°$. Orange and blue point represent the data for Co and Py respectively. 161
E.2 XFMR results for the LG003 sample at 163 K, and the external field direction $\theta_H = 90°$. Orange and blue point represent the data for Co and Py respectively. 162
E.3 XFMR results for the LG003 sample at 173 K, and the external field direction $\theta_H = 90°$. Orange and blue point represent the data for Co and Py respectively. 163
E.4 XFMR results for the LG003 sample at 201 K, and the external field direction $\theta_H = 90°$. Orange and blue point represent the data for Co and Py respectively. 163
E.5 XFMR results for the LG003 sample at 256 K, and the external field direction $\theta_H = 90°$. Orange and blue point represent the data for Co and Py respectively. 164

E.6 XFMR results for the LG003 sample at 275 K, and the external field direction $\theta_H = 90°$. Orange and blue point represent the data for Co and Py respectively. 164
E.7 XFMR results for the LG003 sample at 300 K, and the external field direction $\theta_H = 90°$. Orange and blue point represent the data for Co and Py respectively. 165

List of Acronyms

AFM Atomic Force Microscopy

CPW Co-planar waveguide

EC Exchange coupling

EDX Energy-Dispersive X-ray Spectroscopy

FCC Face-centred cubic

FM Ferromagnet

FMR Ferromagnetic Resonance

HCP Hexagonal close packed

iff if and only if

IFPAN Institute of Physics of the Polish Academy of Sciences

LEED Low-Energy Electron Diffraction

LR Likelihood ratio

MTJ Magnetic Tunnel Junction

NM Non-magnetic metal

POMS Portable Octopole Magnet System

Py Permalloy

RHEED Reflection High-Energy Electron Diffraction

RT Room temperature

SP Spin-pumping

STM Scanning Tunneling Microscopy

SQUID Sperconducting Quantum Interference Device

TEM Transmission Electron Microscopy

TI Topological Insulator

TMR Tunnel Magnetoresistance

VNA Vector Network Analyser

XAS X-ray Absorption Spectroscopy

XFMR X-ray Ferromagnetic Resonance

XMCD X-ray Magnetic Circular Dichroism

XPS X-ray Photoelectron Spectroscopy

XRD X-ray Diffraction analysis

XRR X-ray Reflectometry

Chapter 1

Introduction

Magnetic tunnel junctions (MTJs) are nanostructures composed of two magnetic layers separated by an ultrathin film of insulating material. Due to spin-dependent tunnelling, current flow in such systems is affected by the relative orientation of magnetization of the magnetic layers [5–7]. MTJs have attracted much attention in the past years [8–12] as promising candidates for spintronic devices, with a broad spectrum of practical applications, e.g., as sensor elements [13] or in memory devices [14, 15].

The interaction between magnetic layers in the MTJ can be realized in three different ways: exchange coupling – magnetic moments of neighbouring magnetic layers interacting directly with each other [16, 17], spin-pumping – a spin current emitted by precession of the magnetization vector of one layer is driving the dynamics of the other layer, and spin-transfer-torque – current passing through the junction becomes polarized by one of the layers and exerts torque on the other layer [18–20].

Extensive studies of spin-transfer-torque in MTJs have been undertaken [21–23]. Much less is, however, known about the effects of exchange coupling and spin-pumping. The study of these aspects requires detailed knowledge of the individual layer dynamics, which is difficult to measure due to nano scale thickness of the layers. In this work, we shed new light on those phenomena performing a detailed study of the magnetic layer dynamics in a Co/MgO/Permalloy (Py - $Ni_{81}Fe_{19}$) heterostructure. State-of-the-art X-ray Ferromagnetic Resonance (XFMR) was used, which has proven to provide unique, layer-resolved data [24, 25].

Topological insulators (TIs), a new class of materials which is insulating in its bulk and conducting on its surface, hold great promise for revolutionizing spintronics and other emerging fields of electronics. Introducing a prototypical TI, such as Bi_2Se_3 in place of a classical insulating barrier in a spin-valve has already been successfully demonstrated [26]. In this work, we explore the possibility of incorporating an elemental TI — tin in its α- phase — into a spin valve, whose topological properties were confirmed at room temperature by Angle-resolved photoemission spectroscopy (ARPES) [27].

The goal of my work was to investigate the dynamics of the magnetic layers embodied in a magnetic tunnel junction or a spin-valve hetrostructure, and to determine how the type of the spacer layer affects the type and strength of coupling between them. This was accomplished by performing detailed measurements of the ferromagnetic resonance, and by comparing the obtained results with mathematical models obtained within the micromagnetic framework.

The thesis is organised as follows. First, in Chapter 2, a theoretical model based on micro magnetic theory is introduced. A specific case of uniaxial anisotropy is discussed in detail, both in terms of static orientation of the magnetisation vector as well of its dynamics. Two types of coupling between magnetic layers are considered: Heisenberg-type exchange coupling and spin-current mediated exchange coupling. Conclusions from theory are focused on quantitative relations that can be related to data obtained in the experiments.

As part of my research, samples with MgO or Sn spacer layers of varying thickness were fabricated. The sample fabrication and structural characterisation procedures are discussed in Chapter 3. Section 3.4 contains details of the growth recipes used. The characterisation of the magnetic properties was performed using cavity FMR, Vector Network Analyser FMR (VNA-FMR), and XFMR, which are described in Chapter 4.

The comparison between the obtained experimental data and the theoretical model was done by fitting unknowns to maximise the likelihood of the model. The goodness of the fit was compared with alternative models, and objective criteria were established for the validation of the models. In particular, it was important to determine if spin-current (SP) coupling is present in the samples studied by

XMFR. This was accomplished by performing likelihood-ratio tests, and by comparing two models. The first only involves Heisenberg-type exchange coupling (null hypothesis), while the second also includes spin-current mediated coupling (alternative hypothesis). Details of the procedures employed are discusses in Chapter 5.

Two kinds of samples were investigated in this work, magnetic tunnel junctions with an insulating barrier between two magnetic layers (Chapter 6), and heterostructures with a topological insulator spacer (Chapter 7). In both cases, the magnetic materials were chosen to be Co and Py. MgO was used in the first case as an insulting barrier. In the second case, α-Sn was used, which is known to be a topological insulator at room temperature.

Finally, in Chapter 8, a conclusion is presented that summarises the results, and gives an outlook on future work in the field.

Chapter 2

Theoretical model for the magnetisation dynamics in thin films

Nonometer-sized magnetic systems have been intensely studied, and mathematical methods have been developed to capture their intriguing properties. Making use of those tools, one can predict, or at least approximate the behaviour of the system before its physical realisation. Mathematical modelling can be a useful tool for designing the system is such a way that interesting phenomena are pronounced and easy to measure.

This chapter presents an introduction to the theory of micromagnetism. The static and dynamic properties of single- and two-layer magnetic systems are discussed. The aim of the derivation is to provide formulas that are useful for interpreting the results obtained in cavity FMR, VNA-FMR, and XFMR experiments.

In principle, by knowing the system parameters, it is possible to predict the magnetic behaviour of the system. The problem I faced is my research was the inverse: by measuring the magnetic response of the system, the task was to extract he system parameters. For this purpose, a very thorough understanding of how the system parameters affect the measured results has to be obtained. Additionally, the systems discussed here exhibit bifurcations which are troublesome when performing an optimisation procedure as the minimisation algorithm may end up in the wrong branch of the solution. Due to those issues, a part of the discussion

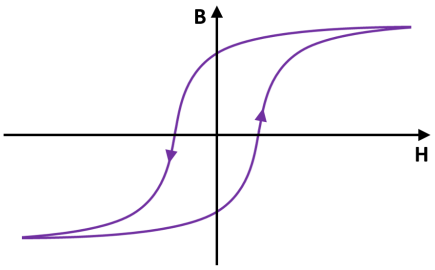

Figure 2.1: Illustration of the magnetic hysteresis loop. B is used to denote the magnetic flux density and H is the magnetic field strength. Arrows on the loop indicate the direction of the transition path.

is focused on purely theoretical conclusions that are helpful when designing such optimisation algorithms, and help to understand the results produced.

2.1 Micromagnetic energy

The properties of a magnetic specimen depend on the external magnetic field. The type and strength of this interaction classifies such a material as diamagnetic, paramagnetic, ferromagnetic, antiferromagnetic etc. [28]. Ferromagnetic materials are particular interesting as they display a strong response to the magnetic field, exhibit hysteretic behaviour, and the magnetisation persists even when the external magnetic field is zero.

A ferromagnetic specimen consists of multiple magnetic domains, where within each domain all of the atomic magnetic moment are oriented in roughly the same direction. The net orientation may vary between the domains, and does not necessarily align with the orientation of the external magnetic field. With increasing strength of the external magnetic field, more magnetic moments align with the field and the size of aligned domain grows. Once the value of the saturation field is reached, almost all magnetic moments face in the same direction, and the net magnetisation is strongest.

It is not feasible to define the state of the sample via the state of the individual atomic sites. Instead the magnetisation vector field is introduced that is defined as the quantity of the magnetic moments per unit volume [29]. This way, the

specimen properties are described by continuous functions which are easier to handle in the mathematical modelling. The study of static and dynamic behaviour of the magnetic materials is carried out under the assumption of the sample being a continuous medium.

Theoretical modelling in terms of the micromagnetic theory starts with expressing the sample energy in terms of its magnetisation and the external magnetic field. The energy consists of several distinct components [28][1]:

$$E = E_{\mathrm{Z}} + E_{\mathrm{D}} + E_{\mathrm{A}} + E_{\mathrm{EX}} + E_0 \quad , \tag{2.1}$$

where E_{Z} is the Zeeman energy, E_{D} is the demagnetisation energy, E_{A} is the crystalline anisotropy energy, E_{EX} is the exchange energy, and E_0 are other contributions. Each of the terms in Equation (2.1) is related to a different physical phenomenon. The nature and mathematical expression for each of them is discussed below.

2.1.1 Zeeman energy

The first term in Equation (2.1) is the potential energy of the interaction between the magnetised body and the external magnetic field. This energy is equal to the work required to move the magnetised specimen form a region with no magnetic field to a region with magnetic field (assuming the magnetisation of the body remains constant). The Zeeman energy (or the external field energy) in SI units is expressed as:

$$E_{\mathrm{Z}} = -\mu_0 \int_{\Omega} \boldsymbol{M} \cdot \boldsymbol{H}_{\mathrm{ext}} \, dV \quad , \tag{2.2}$$

where μ_0 is the magnetic permeability of vacuum, $\boldsymbol{M}$ is the sample magnetisation vector, $\boldsymbol{H}_{\mathrm{ext}}$ is the external magnetic field vector, and Ω is the sample volume.

2.1.2 Demagnetisation energy

The magnetised sample creates its own magnetic field called the demagnetisation field, whose distribution and magnitude depends on the sample shape and magnetisation. This field interacts with the sample itself, therefore work is required

[1]The magnetostrictive energy is omitted.

to magnetise an object even in the absence of the external magnetic field. The energy related to this interaction is given by:

$$E_D = -\frac{\mu_0}{2} \int_\Omega \boldsymbol{M} \cdot \boldsymbol{H}_D \, dV \quad , \tag{2.3}$$

where μ_0 is the magnetic permeability of vacuum, $\boldsymbol{M}$ is the sample magnetisation vector, $\boldsymbol{H}_\mathrm{D}$ is the magnetic field created by the sample (demagnetisation field), and Ω is the sample volume.

Thin magnetic layers with uniform thickness are particularly important (Figure 2.2). A thin film is a layer of a material whose typical thickness ranges from 1 to 100 nm, while the horizontal dimensions can be as large as 1 – 10 mm. Due to the large difference in horizontal and vertical dimensions, thin films are often approximated as uniformly magnetized, flat, and infinite plates. The effects of the edges of the sample have insignificant influence on the magnetic field at distances from the edge much greater than the sample thickness, which is true for almost the whole sample. The demagnetization field of a magnetised infinite plate can be calculated directly using Maxwell's equations:

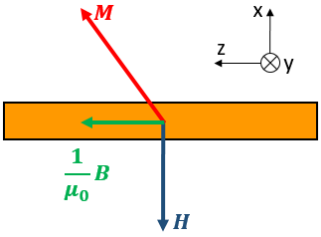

Figure 2.2: Coordinate system used to calculate the demagnetisation field

$$\nabla \cdot \boldsymbol{B} = 0 \tag{2.4}$$

$$\nabla \times \boldsymbol{H} = 0 \tag{2.5}$$

where $\boldsymbol{B}$-field and $\boldsymbol{H}$-field are related by:

$$\boldsymbol{H} = \frac{1}{\mu_0}\boldsymbol{B} - \boldsymbol{M} \tag{2.6}$$

with $\boldsymbol{M}$ being the magnetisation of the sample. The boundary conditions at the top and bottom edge of the thin film sample are given by:

$$H_2^\perp = H_1^\perp + M^\perp \tag{2.7}$$

$$H_2^\parallel = H_1^\parallel \tag{2.8}$$

where the subscript 2 denotes the region outside the thin film (empty space), and 1 the region inside the sample. Assuming fixed magnetisation $\boldsymbol{M}$, and no external magnetic field $\boldsymbol{H}_2$, the expression for the magnetic field inside the sample is given by:

$$\begin{aligned} \boldsymbol{H}_1 &= -(\boldsymbol{M} \cdot \hat{\boldsymbol{x}})\hat{\boldsymbol{x}} = -M \cos\theta \hat{\boldsymbol{x}} \\ \boldsymbol{B}_1 &= \mu_0(\boldsymbol{M} \cdot \hat{\boldsymbol{z}})\hat{\boldsymbol{z}} = \mu_0 M \sin\theta \hat{\boldsymbol{z}} \end{aligned} \quad . \tag{2.9}$$

There is no magnetic field outside the sample. In reality, a field can be observed outside the sample as a consequence of the irregularities in thickness or the magnetisation of the sample, as well as a consequence of the sample being finite in size (finite size sample equations for the magnetic field inside and outside of the sample can be found in Ref. [30]). The $\boldsymbol{H}$-field in Equation (2.9) is called the demagnetisation field, and the energy associated with it is given by:

$$E_D = \frac{\mu_0}{2} \int_\Omega (\boldsymbol{M} \cdot \hat{\boldsymbol{x}})^2 \, dV \quad , \tag{2.10}$$

where $\hat{\boldsymbol{x}}$ is the unit vector normal to the sample surface.

2.1.3 Anisotropy energy

Atoms in crystals are arranged in a periodic lattice which leads to the effect of crystalline anisotropy, i.e., it is easier to magnetise a crystal in certain crystallographic directions (it requires less energy) than in others. The directions that require the least energy are referred to as *easy axes*, and the directions that require the most energy are known as *hard axes*.

In the framework of micromagnetism, those effects are accounted for by introducing energy terms that depend only on the magnetisation direction:

$$E_\mathrm{A} = \int_\Omega e_\mathrm{a}(\boldsymbol{m}) \, dV \quad , \tag{2.11}$$

where e_a is the anisotropy energy density dependent on the magnetisation unit vector ($\boldsymbol{m}$). The exact expression for e_a is an unknown, and determined in experiments. Is is customary to parametrize e_a using a trigonometric basis. For

most cases, it is sufficient to use up to three terms of such a trigonometric expansion. This way the full anisotropy density function is described using only a few parameters. For uniaxial crystals, the formula takes form [31]:

$$e_{\mathrm{a}}(\theta,\phi) = K_0 + K_1 \sin^2\theta + K_2 \sin^4\theta + K_3 \sin^6\theta + ... \quad , \tag{2.12}$$

and for hexagonal anisotropy:

$$e_{\mathrm{a}}(\theta,\phi) = K_0 + K_1 \sin^2\theta + K_2 \sin^4\theta + K_3 \sin^6\theta \cos(6\phi) + ... \quad , \tag{2.13}$$

where K_i are the anisotropy constants whose values depend on the material used; and θ and ϕ are the spherical coordinates of the magnetisation unit vector.

Two materials are investigated closely in this work: cobalt (Co) and Permalloy (Py). Py can be sufficiently well described by uniaxial anisotropy using a single expansion term (K_1). In the case of HCP Co, two terms of the hexagonal anisotropy formula are needed (K_1, K_2), which is equivalent to the first two terms of the uniaxial anisotropy.

Thin film crystalline anisotropy constants differ from the ones found in bulk crystals. This is due to the interfacial effects, and the variation of the magnetisation direction near the sample surface. Additionally, in case of alloys such as Py, the anisotropy is dependent on the composition of the material and annealing conditions [32]. With many difficult to control factors affecting the value of the sample anisotropy, it is necessary to independently measure the value of the anisotropy constants for each of the studied thin film samples.

2.1.4 Exchange energy

The magnetic moments of the atomic sites interact with neighbouring sites by means of the exchange interaction. The exchange energy is given by the Heisenberg Hamiltonian:

$$\mathcal{H} = -2J \sum_{ij} \boldsymbol{S}_i \cdot \boldsymbol{S}_j \quad , \tag{2.14}$$

where J is the nearest neighbour exchange integral; $\boldsymbol{S}_i$, $\boldsymbol{S}_j$ are the spin angular momenta (usually the sum is carried out over the nearest neighbours). This type of

energy accounts for variations in site-to-site magnetisation, and can be translated into the micromagnetic framework (derivation by Landau and Lifshitz [33]):

$$E_{\mathrm{ex}} = \int_{\Omega} A \left(|\nabla m_x|^2 + |\nabla m_y|^2 + |\nabla m_z|^2 \right) \, dV \tag{2.15}$$

where A is the exchange constant, and $m_{\mathrm{x,y,z}}$ are the Cartesian components of the magnetisation unit vector.

In the thin film regime, it is customary to assume uniform magnetisation of the sample. In this case, the exchange energy is zero as for uniform magnetisation fields, all of magnetisation gradients vanish. The effects omitted by this simplification can be accounted for by introducing the surface anisotropy energy.

2.2 Static equilibrium

The theoretical analysis of a physical system starts by determining the points of stable equilibrium. A physical system is in a stable equilibrium when its potential energy is minimized. Using Equation (2.1), and the expressions for its components derived in the previous chapter, the total potential energy of a single layer magnetic system can be written as:

$$E(\boldsymbol{M}, \boldsymbol{H}_{\mathrm{ext}}) = \int_{\Omega} \left(-\mu_0 \boldsymbol{M} \cdot \boldsymbol{H}_{\mathrm{ext}} - \frac{\mu_0}{2} \boldsymbol{M} \cdot \boldsymbol{H}_D + e_a + A |\nabla \boldsymbol{m}|^2 \right) \, dV \, . \tag{2.16}$$

In the following discussion it is assumed that the external magnetic field $\boldsymbol{H}_{\mathrm{ext}}$ and the layer magnetisation $\boldsymbol{M}$, are uniform and the sample is fully saturated. In this case, the exchange energy is zero, and the integral in Equation (2.16) is equal to the integrand multiplied by the sample volume $|\Omega|$. The effective magnetic field is introduced:

$$\boldsymbol{H}_{\mathrm{eff}} = -\frac{1}{\mu_0 M_s} \frac{\partial \varepsilon}{\partial \boldsymbol{m}} \quad , \tag{2.17}$$

with $\varepsilon = E/|\Omega|$ being the energy density, $\boldsymbol{m} = \boldsymbol{M}/M_{\mathrm{s}}$ the unit vector in the direction of sample magnetisation, and M_{s} the value of saturation magnetisation. The derivative on the right is the total derivative of the energy density with respect to the magnetisation unit vector. Substituting Equation (2.15) into (2.17) gives the expression for the effective magnetic field in the magnetic layer:

$$\boldsymbol{H}_{\mathrm{eff}} = \boldsymbol{H}_{\mathrm{ext}} + \boldsymbol{H}_{\mathrm{D}} - \frac{1}{\mu_0 M_{\mathrm{s}}} \frac{\partial e_{\mathrm{a}}}{\partial \boldsymbol{m}} \quad . \tag{2.18}$$

The equilibrium position is found by minimising the energy (2.16) with respect to the orientation of the magnetisation vector. This is done by a variation procedure, which leads to Brown's equations [34]:

$$\begin{cases} \boldsymbol{m} \times \boldsymbol{H}_{\text{eff}} = 0 \\ \left.\frac{\partial \boldsymbol{m}}{\partial \boldsymbol{n}}\right|_{\partial\Omega} = 0 \end{cases} \tag{2.19}$$

where $\boldsymbol{n}$ is the unit vector perpendicular to the surface of the sample ($\partial\Omega$). Solving Brown's equations provides an orientation of the magnetization vector that is the potential energy extremum. The classification of the solution as the energy maximum, minimum or an inflection point is done by analysing the energy plot around the determined extrema, or by computing the second derivatives.

In many cases it is not easy to find the solutions to Equation (2.19) in a closed form. This is only possible when one can simplify the problem making use of the symmetries, or when the expression for the anisotropy function is simple enough. It is often more convenient to find the energy minima using numerical methods. As an example, a case of a thin film of Py and Co (materials that were used in the experimental study discussed in this work) is highlighted.

2.2.1 Static solution for Py

Permalloy is a ferromagnetic material composed of nickel (81%) and iron (19%). Although the exact composition can vary between the produced samples, the general properties remain the same: it has a very small or non-existent crystalline anisotropy, and its magnetic properties do no change with temperature. This makes it an ideal material for many research applications. Due to weak anisotropy, it is sufficient to approximate the crystalline anisotropy as being uniaxial with a single expansion term:

$$e_{\text{a}} \simeq K_0 + K_1 \sin^2\theta \quad . \tag{2.20}$$

For subsequent algebraic manipulations, it is convenient to express this energy in terms of the cosine of the angle θ:

$$\begin{aligned} e_{\text{a}} &= K_0 + K_1 - K_1 \cos^2\theta \\ e_{\text{a}} &= K_0 + K_1 - K_1(\boldsymbol{m} \cdot \boldsymbol{n})^2 \end{aligned} \tag{2.21}$$

with $\boldsymbol{n}$ being the unit vector normal to the sample. The associated anisotropy field is given as:

$$\boldsymbol{H}_{\mathrm{a}} = \frac{2K_1}{\mu_0 M_{\mathrm{s}}}(\boldsymbol{m}\cdot\boldsymbol{n})\boldsymbol{n} \quad , \tag{2.22}$$

where M_{s} is the saturation magnetisation of the Py layer, $\approx (0.3-0.7)\times 10^6\,\mathrm{A/m}$. The total effective magnetic field in the uniformly magnetised Py thin film is given as:

$$\boldsymbol{H}_{\mathrm{eff}} = \boldsymbol{H}_{\mathrm{ext}} + \frac{1}{\mu_0}\left(\frac{2K_1}{M_{\mathrm{s}}} - \mu_0 M_{\mathrm{s}}\right)(\boldsymbol{m}\cdot\boldsymbol{n})\boldsymbol{n} \tag{2.23}$$

The demagnetisation field and crystalline anisotropy can be grouped together, forming a quantity referred to as the effective anisotropy:

$$K_1^{\mathrm{eff}} = K_1 - \frac{1}{2}\mu_0 M_s^2 \quad . \tag{2.24}$$

For further calculations, the sample magnetisation and the magnetic field are parametrised using spherical coordinates:

$$\begin{aligned} \boldsymbol{H}_{\mathrm{ext}} &= \frac{1}{\mu_0} B\left(\cos\theta_H,\, \sin\theta_H \sin\phi_H,\, \sin\theta_H \cos\phi_H\right), \\ \boldsymbol{m} &= \left(\cos\theta,\, \sin\theta\sin\phi,\, \sin\theta\cos\phi\right), \\ \boldsymbol{e} &= (1,\, 0,\, 0) \quad . \end{aligned} \tag{2.25}$$

With this parametrisation, the sample energy can be expressed as:

$$E = -M_s B\left[\cos\theta\cos\theta_H + \cos\left(\phi-\phi_H\right)\sin\theta\sin\theta_H\right] - K_1^{\mathrm{eff}}\cos^2\theta\,, \tag{2.26}$$

where constant terms, not dependent on the system coordinates, were omitted. Both sides of the equation are divided by the value of the sample's magnetisation at saturation, and a new parameter is introduced:

$$D = \frac{2K_1^{\mathrm{eff}}}{M_{\mathrm{s}}} \quad . \tag{2.27}$$

Furthermore, by introducing a dimensionless constant $b = B/|D|$, the energy can be expressed in the dimensionless form:

$$E' = \frac{E}{|D|M_s} = \begin{cases} b\left[\cos\theta\cos\theta_H + \cos\left(\phi-\phi_H\right)\sin\theta\sin\theta_H\right] - \frac{1}{2}\cos^2\theta & D>0 \\ b\left[\cos\theta\cos\theta_H + \cos\left(\phi-\phi_H\right)\sin\theta\sin\theta_H\right] + \frac{1}{2}\cos^2\theta & D<0 \end{cases} \tag{2.28}$$

where the two branches are distinguished based on the sign of the anisotropy parameter D. As the energy is divided only by a positive constant, the position of the minima does not change.

The variables determining the orientation of the magnetisation (θ, ϕ) are the only parameters that are not fixed by the external conditions (θ_H, b). Their value is chosen by the physical system in such a way that the energy of the system is minimal. For a system parametrised with two variables, this is achieved when the first derivatives are zero:

$$\frac{\partial E}{\partial \theta} = 0 \quad \text{and} \quad \frac{\partial E}{\partial \phi} = 0 \quad , \tag{2.29}$$

and the second derivatives satisfy (as long as $0 < \theta < \pi$ and $0 < \theta_H < \pi$):

$$\frac{\partial^2 E}{\partial \theta^2} + \frac{\partial^2 E}{\partial \phi^2} > 0, \quad \text{and} \quad \frac{\partial^2 E}{\partial \phi^2}\frac{\partial^2 E}{\partial \theta^2} - \left(\frac{\partial^2 E}{\partial \phi \partial \theta}\right)^2 > 0 \quad . \tag{2.30}$$

For the given form of the energy (2.28), it can be shown that the equilibrium positions only exist if $\phi = \phi_H$, and the value of the inclination (θ) is a solution of (full derivation in Appendix B):

$$\begin{cases} 2b\sin(\theta - \theta_H) + \sin 2\theta = 0 & \text{for } D > 0 \\ 2b\sin(\theta - \theta_H) - \sin 2\theta = 0 & \text{for } D < 0 \end{cases} . \tag{2.31}$$

The solutions are stable equilibria iff:

$$\begin{cases} b\cos(\theta - \theta_H) + \cos 2\theta > 0 & \text{for } D > 0 \\ b\cos(\theta - \theta_H) - \cos 2\theta > 0 & \text{for } D < 0 \end{cases} . \tag{2.32}$$

Additionally, as θ is bound in the range $[0, \pi]$, a stable solutions could be situated at the limits of the interval. These cases are treated separately (see Appendix A).

Closed form expressions for the solutions to the Equations (2.31) can be found analytically by substituting trigonometric identities:

$$\sin\theta = \frac{2\tan\theta/2}{1+\tan^2\theta/2}, \quad \cos\theta = \frac{1-\tan^2\theta/2}{1+\tan^2\theta/2} \quad , \tag{2.33}$$

resulting in:

$$\begin{cases} T^4 b\sin\theta_H + 2T^3(b\cos\theta_H - 1) + 2T(b\cos\theta_H + 1) - b\sin\theta_H = 0 & \text{for } D > 0 \\ T^4 b\sin\theta_H + 2T^3(b\cos\theta_H + 1) + 2T(b\cos\theta_H - 1) - b\sin\theta_H = 0 & \text{for } D < 0 \end{cases} . \tag{2.34}$$

These are quartic equations with respect to T, and the exact solutions can be found using the general formula. The full expression for the roots is long and it is not shown here explicitly. Knowing T, the value of θ can be established.

The case of the positive and negative values of D are qualitatively different. When the anisotropy is negative ($D < 0$), and no external magnetic field is applied the system, the energy is lowest for the magnetisation oriented in-plane of the sample ($\theta = \pi/2$, this is a case of an easy-plane of magnetisation). When a magnetic field is introduced, the magnetisation orientation tilts its direction, with the tilt increasing with the increase in the field strength. For the magnetic fields much stronger than the sample anisotropy field, the magnetisation aligns with the magnetic field (Figure 2.3).

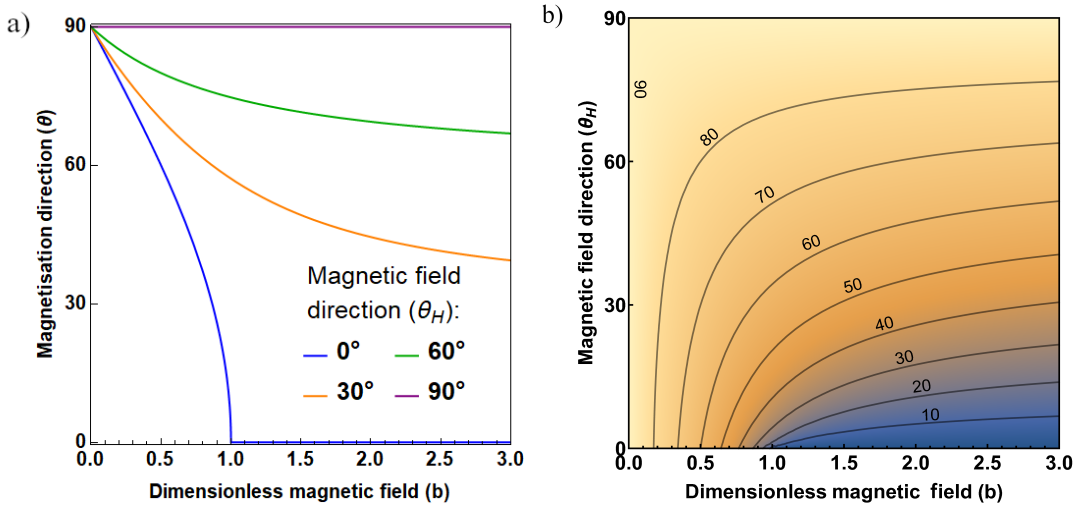

Figure 2.3: Direction of the magnetisation vector in dependence on the magnitude of the dimensionless magnetic field and its orientation for negative values of the D parameter. The left panel presents how the value of θ changes with the dimensionless magnetic field b for four different orientations of the magnetic field (θ_H). The right panel summarises the same results for the orientations of the magnetic field in the range between 0° and 90°, with the resulting orientation of the magnetisation indicated by a color scale and grid-lines drawn every 10°.

For positive anisotropy ($D > 0$), the out-of-plane orientation of magnetisation is energy favourable ($\theta = 0$ or $\theta = \pi$, an easy-axis of magnetisation). Close inspection shows that up to two solutions for θ are possible in this case. If the

magnetic field is low, the solutions include one with the magnetisation oriented in the same half-plane as the magnetic field $\theta \in [0, \pi/2]$, and one in the opposite half-plane $\theta \in [\pi/2, \pi]$. As shown in Figure 2.4d, the second solution is metastable, i.e., it is a local minimum but not a global minimum of the potential energy. When the magnetic field is strong enough, the second minimum disappears and the magnetisation orients itself in the direction of the global energy minimum $\theta \in [0, \pi/2]$. The critical value of the magnetic field needed to force the magnetisation into the global minimum is dependent on the magnetic field orientation (black line on Figures 2.4a and 2.4b). It was found that the lowest value of magnetic field ($b = 0.5$) is required when $\theta_H = \pi/4$, and the highest ($b = 1$) when $\theta_H = 0$ or $\theta_H = \pi/2$.

The presence of two solutions causes a hysteresis effect. One can consider a sample that is initially saturated using the magnetic field $b = 2$ and $\theta_H = 180°$. In this case, the magnetisation will orient itself in the direction of the magnetic field $\theta = 180°$. The magnetic field is then decreased to $b = 0$, and its orientation is flipped to being opposite $\theta_H = 0°$. At this point the magnetisation of the sample is still facing the previous direction ($\theta = 180°$). With increasing magnetic field, the direction of magnetisation will not change up to the point when it reaches $b = 1$, i.e., when $\theta = 180°$ is no longer a solution, and the magnetisation orientation flips to a new global energy minimum ($\theta = 0°$). This shows that the sample properties not only depend on the external parameters, but also on the history of the sample (Figure 2.5).

The magnetocrystaline anisotropy of a Py film is usually close to zero. Therefore, for the purpose of the following example, it is assumed that $K_1 \approx 0\,\mathrm{J/m^3}$. The magnetisation of Py at saturation can vary, and taken to be $M_s \approx 600 \times 10^3\,\mathrm{A/m}$, which gives:

$$K_1^{\mathrm{eff}} = -226.2 \times 10^3\,\mathrm{J/m^3}, \quad D = -0.754\,\mathrm{T} \quad . \tag{2.35}$$

The negative value of D parameter suggests that Py will prefer the in-plane magnetisation orientation, which agrees with the results observed in experiments. This implies that the change in external magnetic field will not lead to a hysteretic behaviour (Figure 2.5), which is contradicting the experimental observation of a hysteresis.

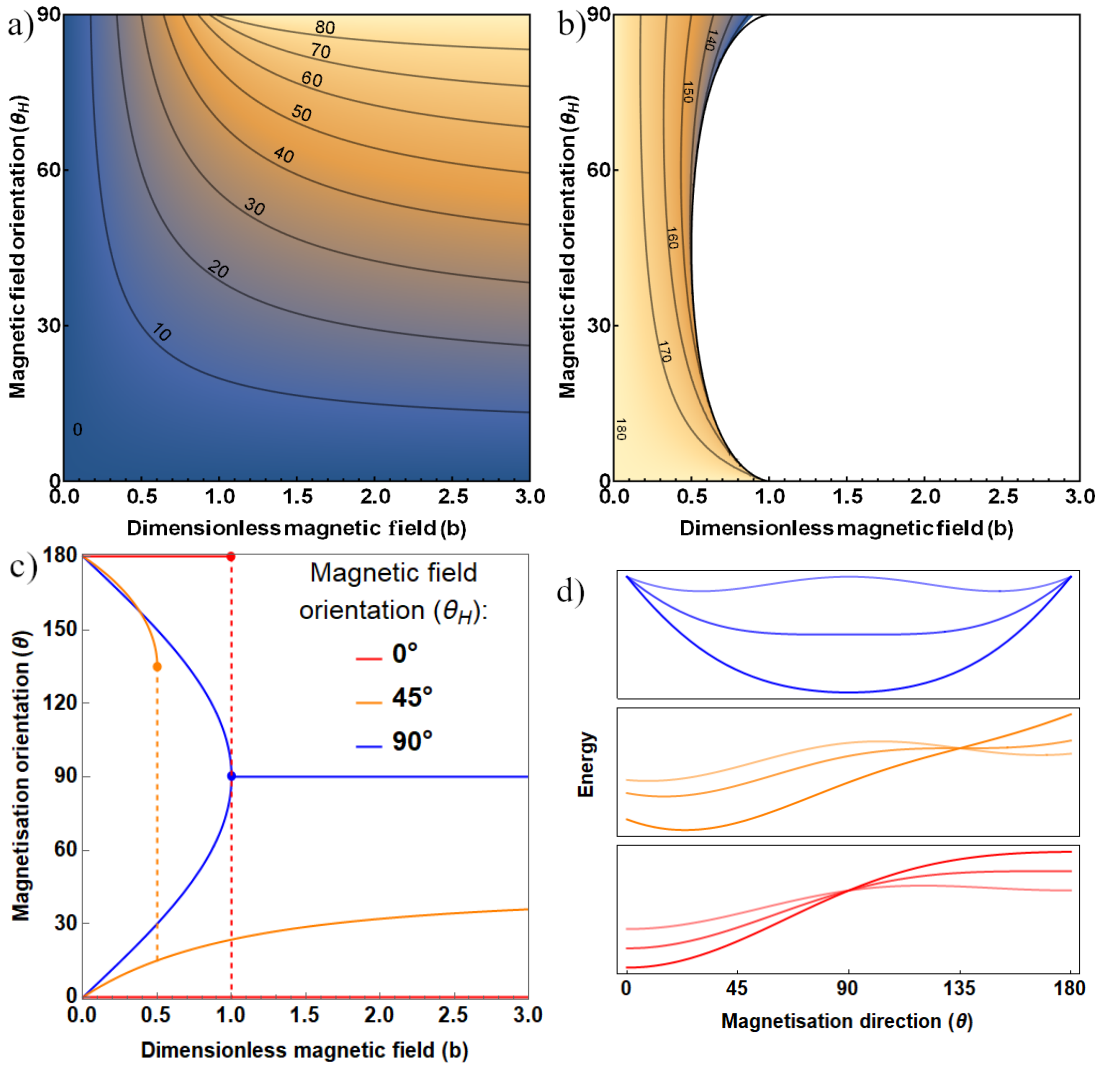

Figure 2.4: Static orientation of the magnetisation vector for the sample with a positive D parameter. Two possible orientations in dependence on the magnetic field strength b and orientation θ_H are shown in panels a) and b). Panel c) shows the magnetisation orientation θ for three different orientations of the magnetic field. Panel d) presents the potential energy of the system as a function of the magnetisation orientation for the cases presented on panel c), where colors correspond to the legend on panel c) and the strength of the magnetic field is visualized by the opacity of the graph (highest opacity corresponds to $b = 1.5$, intermediate to $b = 1$, smallest to $b = 0.5$).

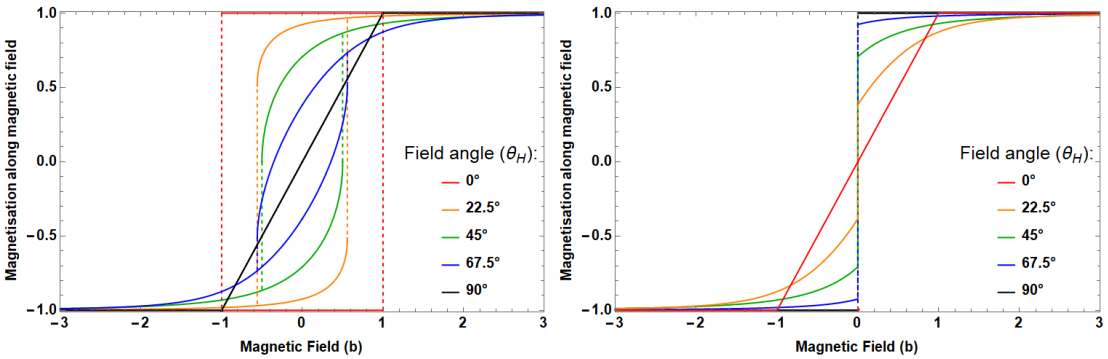

Figure 2.5: Projection of the magnetisation vector onto the direction of the magnetic field in dependence on the field strength for a sample with (left) $D > 0$, (right) $D < 0$.

The above observation highlights the limitations of the model presented. The model treats a sample as a single domain system with constant magnitude of the magnetisation. In reality, the samples consist of numerous magnetic domains that interact with each other. When the magnetic field is changed, the domain walls move and the internal magnetic structure of the sample is altered. Therefore, the collective behaviour of a multidomain system deviates from the single domain behaviour discussed in this chapter. Although having its limitations, the single domain theory remains sufficient for the studies of the fully saturated samples discussed in this work.

2.2.2 Static solution for Co

Thin layers of Co deposited on the a-plane of a sapphire substrate can form a HCP crystal structure with hexagonal crystalline anisotropy. The energy associated with this kind of anisotropy can be approximated by a trigonometric expansion up to the third term [31]:

$$e_a = K_0 + K_1 \sin^2\theta + K_2 \sin^4\theta + K_3 \sin^6\theta \sin 6\phi \quad , \tag{2.36}$$

out of which the third one is small and will be neglected in the further discussion. The first two terms are only dependent on the inclination from the normal to the crystalline orientation (which is assumed to coincide with the surface normal). This is a special case of the uniaxial anisotropy. For the purpose of the algebraic

manipulations, it is convenient to express the anisotropy energy in the following form:

$$\begin{aligned} e_{\mathrm{a}} &= K_0 + K_1 + K_2 - (K_1 + 2K_2)\cos^2\theta + K_2\cos^4\theta \\ e_{\mathrm{a}} &= K_0 + K_1 + K_2 - (K_1 + 2K_2)(\boldsymbol{m}\cdot\boldsymbol{n})^2 + K_2(\boldsymbol{m}\cdot\boldsymbol{n})^4 \quad , \end{aligned} \tag{2.37}$$

with $\boldsymbol{n}$ being the unit vector normal to the sample. The associated anisotropy field is given as:

$$\boldsymbol{H}_{\mathrm{a}} = \frac{2(K_1 + 2K_2)}{\mu_0 M_{\mathrm{s}}}(\boldsymbol{m}\cdot\boldsymbol{n})\boldsymbol{n} - \frac{4K_2}{\mu_0 M_{\mathrm{s}}}(\boldsymbol{m}\cdot\boldsymbol{n})^3\boldsymbol{n} \quad , \tag{2.38}$$

where M_s is the magnetisation of Co sample at saturation. The effective magnetic field in the sample can be expressed as:

$$\boldsymbol{H}_{\mathrm{eff}} = \boldsymbol{H}_{\mathrm{ext}} + \frac{1}{\mu_0}\left(\frac{2(K_1 + 2K_2)}{M_{\mathrm{s}}} - \mu_0 M_{\mathrm{s}}\right)(\boldsymbol{m}\cdot\boldsymbol{n})\boldsymbol{n} - \frac{4K_2}{\mu_0 M_{\mathrm{s}}}(\boldsymbol{m}\cdot\boldsymbol{n})^3\boldsymbol{n}\,. \tag{2.39}$$

In a similar fashion as for the case of Py, it can be shown that the azimuthal angle of the magnetisation follows the azimuthal angle of the magnetic field ($\phi = \phi_h$). With that, the total energy per unit volume of the system is given as:

$$E = -MB\cos(\theta - \theta_H) + \frac{\mu_0}{2}M_s^2\cos^2\theta + K_0 + K_1\sin^2\theta + K_2\sin^4\theta\,, \tag{2.40}$$

which can be rewritten in the form:

$$\frac{E}{M_s} = -B\cos(\theta - \theta_H) - \frac{1}{2}D_1\cos^2\theta - \frac{1}{4}D_2\cos^4\theta\,, \tag{2.41}$$

where the constant value $(K_0 + K_1 + K_2)$ is omitted, and

$$D_1 = \frac{2\left(K_1^{\mathrm{eff}} + 2K_2\right)}{M_{\mathrm{s}}}\,, \quad D_2 = -\frac{4K_2}{M_{\mathrm{s}}}\,, \quad K_1^{\mathrm{eff}} = K_1 - \frac{1}{2}\mu_0 M_{\mathrm{s}}^2\,. \tag{2.42}$$

This equation can be further simplified by introducing dimensionless constants:

$$\begin{aligned} b = \frac{B}{\sqrt{D_1^2 + D_2^2}}\,, \quad \sin\psi = \frac{D_1}{\sqrt{D_1^2 + D_2^2}}\,, \quad \cos\psi = \frac{D_2}{\sqrt{D_1^2 + D_2^2}}\,, \\ \sin\widetilde{\psi} = \frac{K_1^{\mathrm{eff}}}{\sqrt{K_1^{\mathrm{eff}\,2} + K_2^2}}\,, \quad \cos\widetilde{\psi} = \frac{K_2}{\sqrt{K_1^{\mathrm{eff}\,2} + K_2^2}} \end{aligned} \tag{2.43}$$

resulting in:

$$E' = -b\cos(\theta - \theta_H) - \frac{1}{2}\sin\psi\cos^2\theta - \frac{1}{4}\cos\psi\cos^4\theta \quad . \tag{2.44}$$

The energy is at its extremum when its first derivative is zero (equivalent to Brown's equations):

$$b\sin(\theta-\theta_H)+\sin\psi\cos\theta\sin\theta+\cos\psi\cos^3\theta\sin\theta=0 \quad , \tag{2.45}$$

where θ is in range $[0,\pi]$. In the general case, no closed form solutions to this equation exist. This can be seen directly when substituting into Equation (2.33), as the resulting polynomial is of 8^{th} degree and cannot be reduced:

$$\begin{aligned}\left(1+T^2\right)^2\left[2b\left(T+T^3\right)\cos\theta_H-2T\left(T^2-1\right)\sin\psi+b\left(T^4-1\right)\sin\theta_H\right]\\ -2T\left(T^2-1\right)^3\cos\psi=0\,,\end{aligned} \tag{2.46}$$

where $T=\tan(\theta/2)$. The general case requires a numerical study and is discussed later in the chapter. First, special cases are considered. If the magnetic field is small ($b\ll 1$), Equation (2.45) simplifies to:

$$\left(\sin\psi+\cos\psi\cos^2\theta\right)\sin 2\theta=0 \quad , \tag{2.47}$$

with solutions for θ:

$$\begin{aligned}\theta=0,\quad \theta=\pi,\quad \theta=\pi/2,\quad \theta=\arccos\left(\sqrt{-\tan\psi}\right),\text{ or}\\ \theta=\pi-\arccos\left(\sqrt{-\tan\psi}\right)\,.\end{aligned} \tag{2.48}$$

The first and second solution correspond to the easy-axis directed perpendicular to the sample plane. The third solution corresponds to the easy-plane of magnetisation, where the magnetisation vector tends to orient itself in-plane of the sample. The last two solutions correspond to the easy-cone of magnetisation, where the magnetisation vector is oriented at an angle with respect to the sample surface. Depending on the value of the ψ parameter, those solutions can represent a stable or unstable equilibrium. The flavour of the solution can be determined by computing the second derivative of the energy functional at the equilibrium points:

$$b\cos(\theta-\theta_H)+\sin\psi\cos 2\theta+\frac{\cos\psi}{2}(\cos 2\theta+\cos 4\theta)>0\,, \tag{2.49}$$

which in the limit of $b\to 0$, takes the form:

$$\sin\psi\cos 2\theta+\frac{\cos\psi}{2}(\cos 2\theta+\cos 4\theta)>0 \quad . \tag{2.50}$$

In case of $\theta = 0$ or $\theta = \pi$, the condition for stable equilibrium simplifies to:

$$D_1 + D_2 > 0 \quad \text{or} \quad K_1^{\text{eff}} > 0 \quad , \tag{2.51}$$

and for $\theta = \pi/2$:

$$D_1 < 0 \quad \text{or} \quad K_1^{\text{eff}} + 2K_2 < 0 \quad . \tag{2.52}$$

The last two solutions are viable only if $\tan(\psi) \in (-1, 0)$, which is equivalent to $D_1/D_2 \in (0, 1)$ or $(K_1 + 2K_2)/2K_2 \in (0, 1)$. Additionally, those solutions are an equilibrium solutions if:

$$\frac{D_1}{D_2}(D_1 + D_2) > 0 \quad \text{or} \quad \frac{K_1^{\text{eff}}}{K_2}\left(K_1^{\text{eff}} + 2K_2\right) < 0 \quad . \tag{2.53}$$

A summary of the possible solutions is shown in Figure 2.6. Depending on the value of parameters, 1, 2, or 3 solutions are possible. The regions of easy-plane, easy-axis, and easy-cone anisotropy can be distinguished.

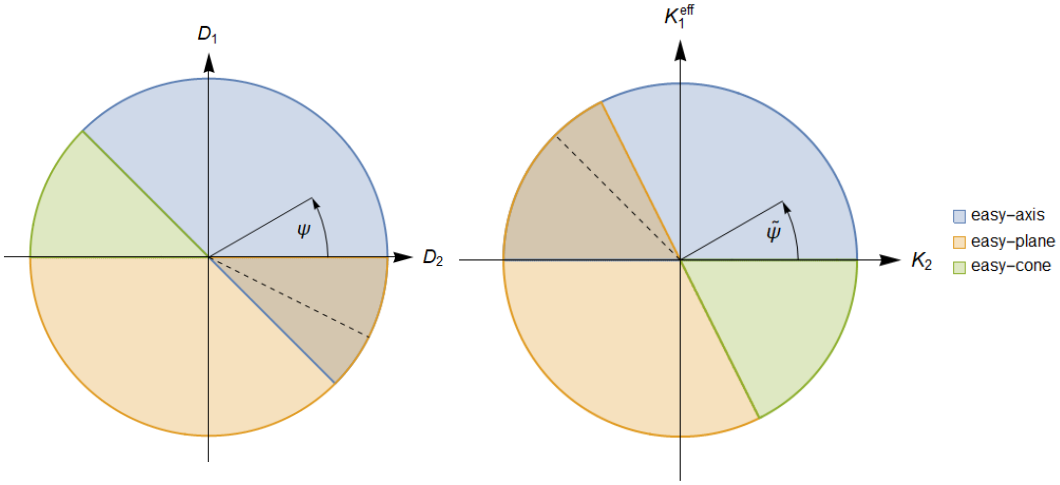

Figure 2.6: Summary of the type of equilibrium position in dependence on the anisotropy of the thin film sample. In the "easy-axis" region, both $\theta_H = \pi$ and $\theta_H = 0$ orientations are stable. In the "easy-cone" region two solutions are possible that are neither oriented out-of-plane nor in-plane of the sample. In the "easy-plane" region, a single solution is possible, where the magnetisation is oriented in-plane of the sample. The "easy-axis" and "easy-plane" regions overlap, creating a region where three solutions are possible. In this region, either the "easy-axis" or the "easy-plane" is a global energy minimum. The critical value where both types of solution have the same energy is marked with a dotted line.

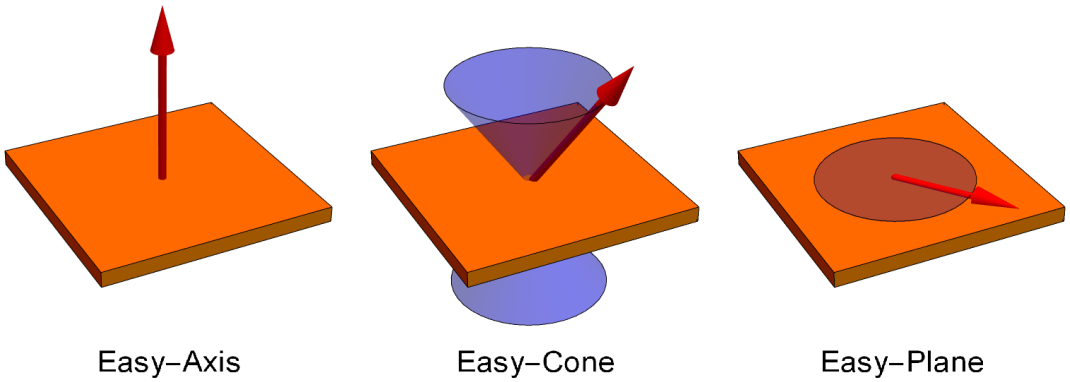

Figure 2.7: Graphical representation of the static orientation of the magnetisation vector when no external field is applied to the sample.

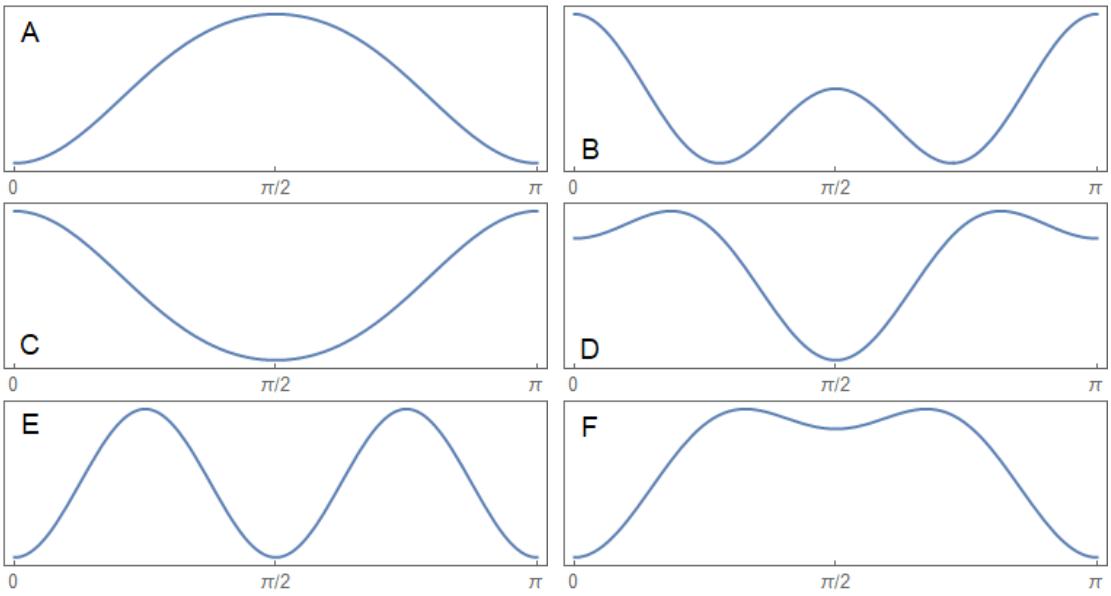

Figure 2.8: Energy as a function of the magnetisation orientation (θ) for the anisotropy angle (ψ) equal to: (A) 45°, (B) 157.5°, (C) 225°, (D) 325°, (E) 333.4°, and (F) 345°.

In the special case when

$$-\pi/4 < \psi < 0\,, \text{or} \quad \pi - \arctan(2) < \widetilde{\psi} < \pi \quad , \tag{2.54}$$

both the easy-plane and easy-axis of magnetisation exist, with the in-plane orientation being a global minimum if:

$$\psi < -\arctan\left(\frac{1}{2}\right), \text{or} \quad \frac{3}{4}\pi < \widetilde{\psi} \quad . \tag{2.55}$$

With the introduction of the external magnetic field the overall picture becomes more complex. The sample magnetisation diverges towards the direction of the magnetic field, and it is found that the number of solutions depends on the strength of the magnetic field. A full analysis requires a numerical study, yet closed form expressions can still be provided for specific cases when the magnetic field is oriented in the out-of-plane or in-plane direction.

For the out-of-plane magnetic field direction ($\theta_H = 0$), the equation for the equilibrium orientation of the magnetisation reduces to:

$$\left(b + \sin\psi\cos\theta + \cos\psi\cos^3\theta\right)\sin\theta = 0 \quad , \tag{2.56}$$

and it has the solutions of $\theta = 0$, $\theta = \pi$, or with $\cos\theta$ being the root of the cubic equation on the left (which can be expressed as a closed form expression). Substituting those solutions into the formula for the second derivative of energy allows for the determination of the conditions for this extremum to be a minimum. In case of $\theta = 0$, this gives:

$$b + \cos\psi + \sin\psi > 0 \quad . \tag{2.57}$$

And in case of $\theta = \pi$,

$$-b + \cos\psi + \sin\psi > 0 \quad . \tag{2.58}$$

Finding the solutions to the cubic equation is more involved. It has three distinct solutions that only for some values of the parameters give real values for θ. The full mathematical derivation is long and will be omitted; instead a summary of the possibilities is shown in Figure 2.9, where the azimuthal direction describes the ratio of anisotropy constants (ψ), and the distance from the center marks the

strength of the magnetic field (b). Depending on the value of the parameters, one, two or three stable solutions are possible. If the magnetic field is strong enough, the magnetisation will orient itself in the out-of-plane direction which coincides with the direction of the magnetic field.

Qualitatively distinct regions of the plot in Figure 2.9 were marked with letters A-F. In region "A", the magnetisation of the sample is oriented out-of-pane (orange). In region "B", apart from the out-of-plane solution, also the in-plane orientation is stable (green). In region "C", the magnetisation is at an angle (blue). For low values of the magnetic field (near the center of the graph), an additional four regions are recognised. In regions "D", "E", "G" two, and in region "F" three solutions are possible. The in-plane orientation is stable for regions "F" and "G", and the out-of-plane orientation is stable for regions "D" and "F". Representative energy plots are shown in Figure 2.8.

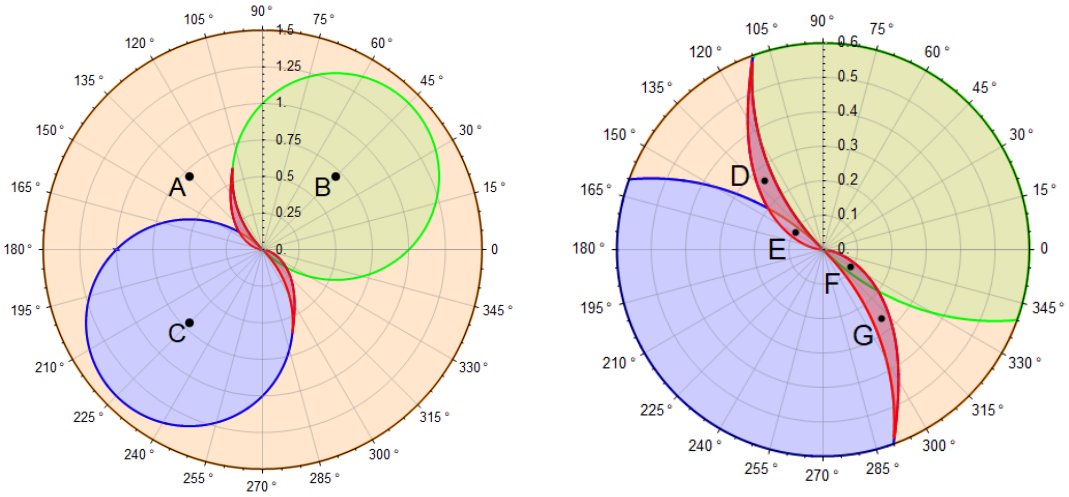

Figure 2.9: Plot showing the number and kind of solutions in dependence on the magnetic field and the sample anisotropies for the magnetic field oriented normal to the sample surface. The azimuthal angle ψ is defined by relation (2.43). The distance from the centre of the diagram is the dimensionless magnetic field b. The diagram on the right is a magnification of the centre region of the left diagram.

The same procedure can be repeated for the in-plane orientation of magnetic

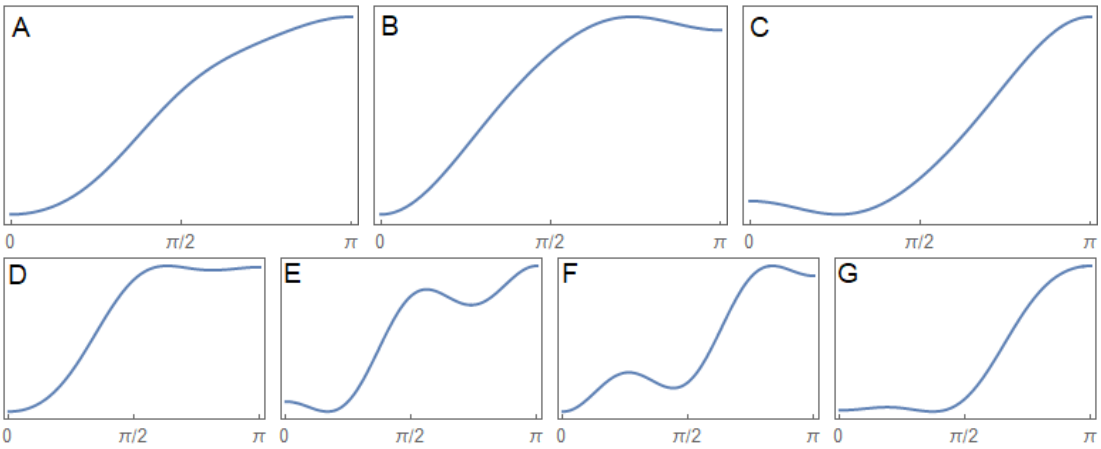

Figure 2.10: Energy as a function of the magnetisation orientation θ for the magnetic field oriented out-of-plane and the anisotropy angle (ψ) equal to: (A) 135°, (B) 45°, (C) 225°, (D) 130.4°, (E) 148°, (F) 328°, and (G) 310.4°.

field ($\theta_H = \pi/2$), where Equation (2.45) reduces to:

$$\left(b + (\cos\alpha + \sin\alpha)\sin\theta - \cos\alpha\sin^3\theta\right)\cos\theta = 0 \quad , \tag{2.59}$$

which is satisfied when $\theta = \pi/2$, or when $\sin\theta$ is a root of the cubic equation on the left. It can be shown that $\theta = \pi/2$ is a stable extremum only if:

$$b - \sin\alpha > 0 \quad . \tag{2.60}$$

If this condition is not fulfilled, the magnetisation vector can orient itself in one of the two directions that are symmetric with respect to the sample plane ($\theta_2 = \pi - \theta_1$). All distinct possibilities in dependence on the parameters b and ψ are shown in Figure 2.9. In regions "B" and "C", the in-plane orientation is stable. In regions "A" and "C", the magnetisation of the sample can orient itself at an angle. Again, if the magnetic field is strong enough, independent on the sample anisotropy ψ, the magnetisation will orient itself in-plane of the sample.

The presence of multiple stable orientations of the magnetisation vector affects the shapes of the hysteresis loops. The magnetisation will stay in the given position up to the point it is no longer a local minimum. Then, a transition to the global minimum occurs (as seen in case of permalloy). In Figures 2.12 and 2.13, a few examples of hysteresis loops are shown for different anisotropy of the sample for the in-plane and out-of-plane orientations of the magnetic field, respectively.

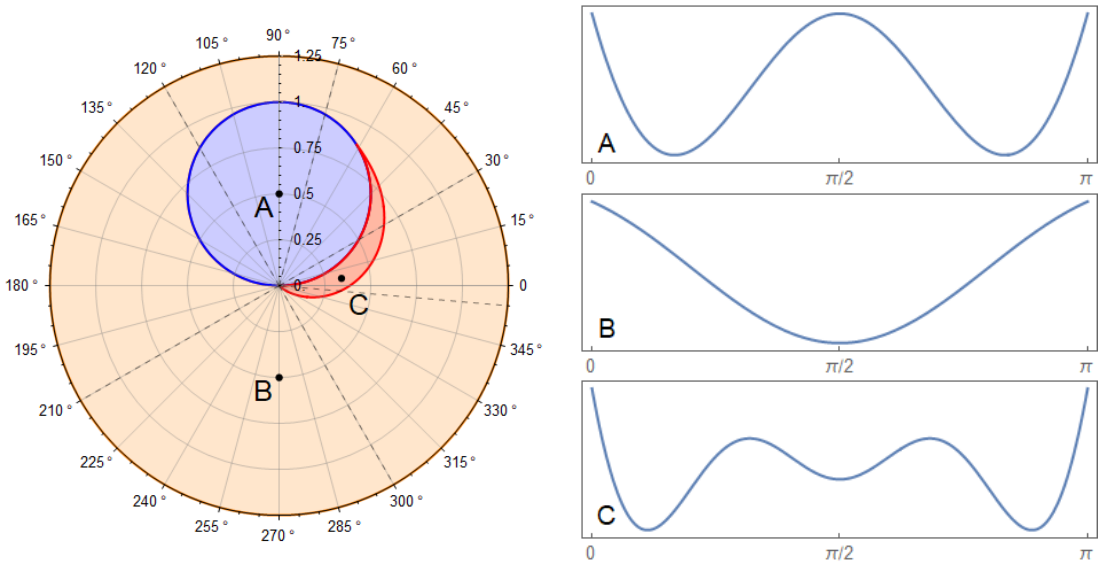

Figure 2.11: Plot showing the number and kind of solutions in dependence on the magnetic field and the sample anisotropies for the magnetic field directed in-plane of the sample. The azimuthal angle ψ is defined by relation (2.43). The distance from the centre of the diagram is the dimensionless magnetic field b. Graphs on the right show the energy dependence on the magnetisation vector θ in the three qualitatively distinct regions.

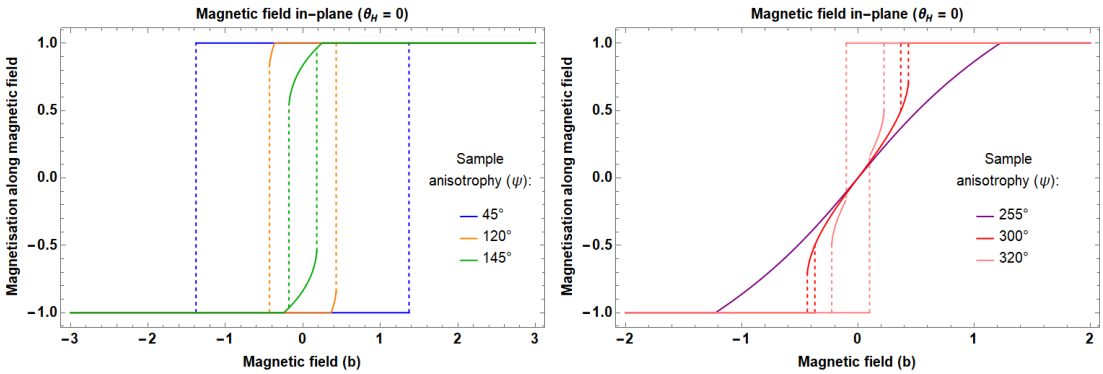

Figure 2.12: Projection of the magnetisation vector onto the direction of magnetic field in dependence on field strength for the field oriented in-plane of the sample for different values of the anisotropy ψ.

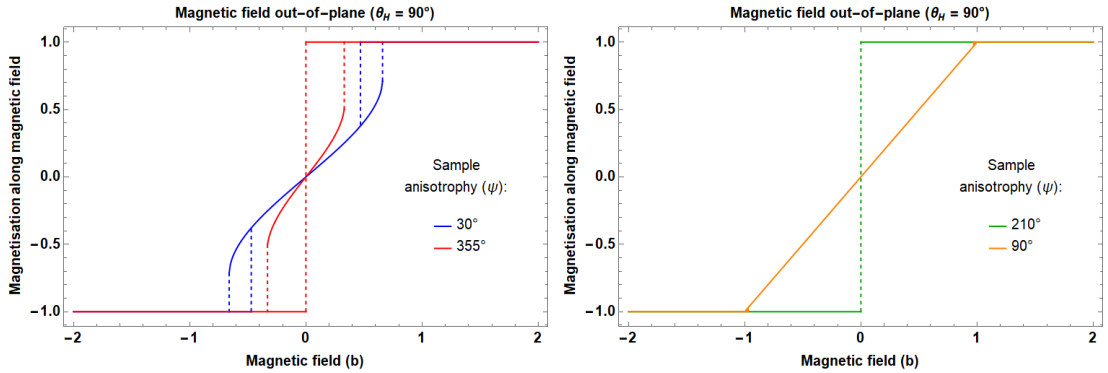

Figure 2.13: Projection of the magnetisation vector onto the field direction in dependence on field strength for the field oriented out-of-plane of the sample for different values of the anisotropy ψ.

At any other orientation of the magnetic field ($\theta \neq 0$, $\theta \neq \pi/2$, and $\theta \neq \pi$), the problem can only be studied using numerical methods. Yet, some conclusions made so far are still valid in the general case: regions with up to three stable solutions can be found for any orientation of the magnetic field, and only a single solution is possible for sufficiently high magnetic field, where the magnetisation orientation aligns with the direction of external magnetic field.

With three parameters affecting the system state (b, ψ, and θ), it is difficult to show the result on a single plot. Multiple cross-sections (each for a different orientation of the external magnetic field) are shown in Figure 2.10, where the number of solutions and orientation of the magnetisation at the global energy minimum are presented for different values of the anisotropy and the magnetic field strength (additional cross-sections can be found in the Appendix B).

The typical parameters for a Co thin film are: saturation magnetization $M_s = 1440 \times 10^3\,\mathrm{A/m}$, and anisotropy constants $K_1 = 450 \times 10^3\,\mathrm{J/m^3}$ and $K_2 = 150 \times 10^3\,\mathrm{J/m^3}$. For these parameters, the D constants are $D_1 = -0.7679\,\mathrm{J/(A \cdot m^2)}$ and $D_2 = -0.4167\,\mathrm{J/(A \cdot m^2)}$. Materials with such values of the anisotropy constants are placed in the region of the phase space, where independent on the field strength and its orientation, there exists a unique solution for the stable magnetisation orientation. When the magnetic field is low or there is no magnetic field, the magnetisation will orient in-plane of the sample (easy-plane of magnetisation). A hysteresis loop for Co with such an anisotropy will be caused purely by the

interaction between the magnetic domains, as a single domain approximation does not predict a hysteretic behaviour.

2.3 Magnetisation dynamics

When the external magnetic field is changed, the sample magnetisation will not react instantly. In particular, if the field variation is given as a sinusoidal perturbation the magnetisation vector will follow an elliptic trajectory resembling the precession of a spinning top. The equations governing the motion of the magnetisation vector in a non-equilibrium state were first proposed by Landau and Lifshitz in 1935 [35]. According to their study, the magnetisation vector follows similar dynamics to the magnetic dipole placed in an external magnetic field with the addition of the effects from demagnetisation and crystalline anisotropy:

$$\frac{\partial \boldsymbol{m}}{\partial t} = -\gamma\, \boldsymbol{m} \times \boldsymbol{H}^0_{\text{eff}}(\boldsymbol{m}) \tag{2.61}$$

with:

$$\boldsymbol{H}^0_{\text{eff}} = \boldsymbol{H}_{\text{ext}} + \boldsymbol{H}_{\text{D}}(\boldsymbol{m}) + \boldsymbol{H}_{\text{A}}(\boldsymbol{m}) \quad , \tag{2.62}$$

where $\boldsymbol{H}_{\text{ext}}$ is the static component of the external magnetic field, $\boldsymbol{H}_{\text{D}}$ is the demagnetisation field, $\boldsymbol{H}_{\text{A}}$ is the anisotropy field, and $\boldsymbol{m}$ is the unit vector pointing in the direction of magnetisation. The sample with oscillating magnetisation will experience energy loss caused by the non-local spin relaxation processes [36]. This is often accounted for by introducing a phenomenological Gilbert damping term α:

$$\frac{\partial \boldsymbol{m}}{\partial t} = -\gamma\, \boldsymbol{m} \times \boldsymbol{H}^0_{\text{eff}}(\boldsymbol{m}) + \alpha\, \boldsymbol{m} \times \frac{\partial \boldsymbol{m}}{\partial t} \quad . \tag{2.63}$$

If there is no external source of energy, the damping will cause dissipation of any excess energy and motion will stop at the equilibrium position. To counter this, and maintain precession, an additional weak, oscillating, external magnetic field $\boldsymbol{h}(t)$ can be introduced, giving the effective magnetic:

$$\boldsymbol{H}_{\text{eff}}(\boldsymbol{m}, t) = \boldsymbol{H}^0_{\text{eff}} + \boldsymbol{h}(t) \quad . \tag{2.64}$$

The nonlinear dependence of the effective magnetic field on the magnetisation of the sample, as well as the nonlinear damping term, pose considerable difficulty

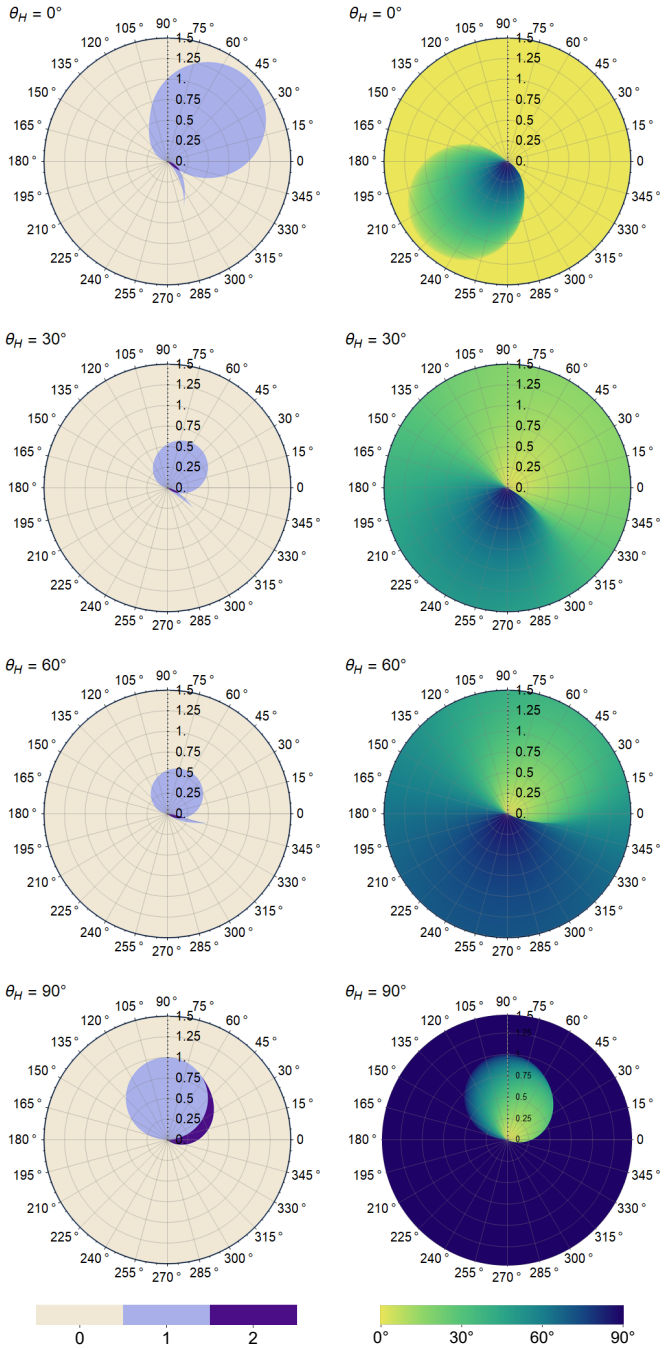

Figure 2.14: Number of solutions (left column) and direction of the magnetisation vector θ at the global energy minimum (right column) in dependence of the anisotropy (ψ the azimuthal angle) and the dimensionless magnetic field (b the distance from the center), for a few chosen orientations of the external magnetic field (θ_H).

when attempting to solve for the motion of the magnetisation vector. One way to solve Equation (2.63) is to study small perturbations around the equilibrium position. The variation of the magnetisation vector is given as a sum of a static solution and a component varying with time:

$$\boldsymbol{m}(t) = \boldsymbol{m}_0 + \delta\boldsymbol{m}(t) \tag{2.65}$$

It is assumed that the additional component $\delta\boldsymbol{m}(t)$ is perpendicular to the original magnetization vector $\boldsymbol{m}_0$, and is much smaller so that the magnitude of magnetisation is preserved: $\boldsymbol{m}(t) \approx \boldsymbol{m}_0$. This perturbation also affects the effective magnetic field $\boldsymbol{H}_{\text{eff}}$, which up to linear terms can be approximated as:

$$\boldsymbol{H}_{\text{eff}}(\boldsymbol{m}, t) = \boldsymbol{H}^0_{\text{eff}}(\boldsymbol{m}_0) + \frac{\partial \boldsymbol{H}^0_{\text{eff}}}{\partial \boldsymbol{m}}\Big|_{\boldsymbol{m}=\boldsymbol{m}_0} \delta\boldsymbol{m} + \boldsymbol{h}(t) \quad . \tag{2.66}$$

Substituting Equations (2.66) and (2.65) into (2.63) results in the linearised equation of motion:

$$\frac{\partial}{\partial t}\delta\boldsymbol{m}(t) = -\gamma \left[\delta\boldsymbol{m}(t) \times \boldsymbol{H}^0_{\text{eff}}(\boldsymbol{m}_0) + \boldsymbol{m}_0 \times \left(\frac{\partial \boldsymbol{H}^0_{\text{eff}}}{\partial \boldsymbol{m}}\Big|_{\boldsymbol{m}=\boldsymbol{m}_0} \delta\boldsymbol{m}(t) + \boldsymbol{h}(t)\right)\right] + \alpha\, \boldsymbol{m}_0 \times \frac{\partial}{\partial t}\delta\boldsymbol{m}(t) \tag{2.67}$$

where the second order terms have been omitted.

2.4 Single layer dynamics

Equation (2.67) is a starting point for the study of the dynamics of the single layer system. In the following derivation it is assumed that the sample is flat, infinite, and has uniaxial crystalline anisotropy. To simplify the calculations, a convenient coordinate system is chosen. The magnetic field and magnetisation are expressed in a Cartesian coordinate system with $\hat{\boldsymbol{e}}_x$ pointing out of the sample, and $\hat{\boldsymbol{e}}_y$, $\hat{\boldsymbol{e}}_z$ lying in plane of the sample. As it was shown in the previous chapters, under the discussed assumptions, both the static magnetisation vector and the effective field vector share the same azimuthal orientation ($\phi_H = \phi$). This allows to chose $\hat{\boldsymbol{e}}_y$ in such a way that the $\hat{\boldsymbol{e}}_y$ components of the magnetisation vector and the

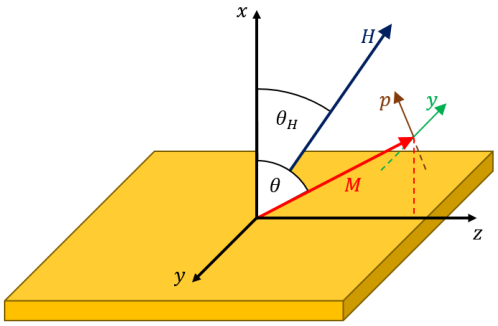

Figure 2.15: Coordinate system used to parametrise Equation (2.67); y is the the y component of the magnetic vector variation ($\delta \boldsymbol{M}$), p is perpendicular to both M and y components of the variation.

effective field are zero. The magnetisation vector and the external magnetic field are parametrised using a spherical coordinate system:

$$\boldsymbol{H}_{\text{ext}} = H\left(\cos\theta_H\,\hat{\boldsymbol{e}}_x + \sin\theta_H\,\hat{\boldsymbol{e}}_z\right) \qquad \boldsymbol{m}_0 = \cos\theta\,\hat{\boldsymbol{e}}_x + \sin\theta\,\hat{\boldsymbol{e}}_z\,. \tag{2.68}$$

The variation of the magnetisation vector $\delta\boldsymbol{m}(t)$ is parametrised using the Cartesian basis ($\hat{\boldsymbol{p}}$, $\hat{\boldsymbol{y}}$) such that the $\hat{\boldsymbol{y}}$ unit vector is directed parallel to the sample plane and perpendicular to the static magnetisation unit vector $\boldsymbol{m}_0$ (for convenience $\hat{\boldsymbol{y}} = -\hat{\boldsymbol{e}}_y$). The $\hat{\boldsymbol{p}}$ unit vector is chosen to be perpendicular to both $\hat{\boldsymbol{y}}$ and $\boldsymbol{m}_0$ (for convenience: $\boldsymbol{m_0} \times \hat{\boldsymbol{y}} = \hat{\boldsymbol{p}}$):

$$\delta\boldsymbol{m}(t) = y(t)\,\hat{\boldsymbol{y}} + p(t)\,\hat{\boldsymbol{p}} = p(t)\sin\theta\,\hat{\boldsymbol{e}}_x - y(t)\,\hat{\boldsymbol{e}}_y - p(t)\cos\theta\,\hat{\boldsymbol{e}}_z\,. \tag{2.69}$$

The driving magnetic field is assumed to be directed in the plane of the sample in the direction perpendicular to the static component of the external magnetic field (minus sign for convenience):

$$\boldsymbol{h}(t) = -\hat{\boldsymbol{y}}\,h(t) \quad . \tag{2.70}$$

Using the expression for the anisotropy field found in Chapter 2.2.2, the effective magnetic field can be expressed as:

$$\begin{aligned}\boldsymbol{H}_{\text{eff}} = \boldsymbol{H}_{\text{ext}} + \frac{1}{\mu_0}\left(\frac{2(K_1+2K_2)}{M_{\text{s}}} - \mu_0 M_{\text{s}}\right)(\boldsymbol{m}\cdot\hat{\boldsymbol{e}}_x)\hat{\boldsymbol{e}}_x \\ -\frac{1}{\mu_0}\left(\frac{4K_2}{M_{\text{s}}}\right)(\boldsymbol{m}\cdot\hat{\boldsymbol{e}}_x)^3\hat{\boldsymbol{e}}_x\end{aligned} \tag{2.71}$$

with the total derivative given as:

$$\begin{aligned}\frac{\partial \boldsymbol{H}_{\text{eff}}}{\partial \boldsymbol{m}}\Big|_{\boldsymbol{m}=\boldsymbol{m}_0} = \frac{1}{\mu_0}\left(\frac{2(K_1+2K_2)}{M_\text{s}} - \mu_0 M_\text{s}\right)\hat{\boldsymbol{e}}_x \otimes \hat{\boldsymbol{e}}_x \\ -\frac{3}{\mu_0}\left(\frac{4K_2}{M_\text{s}}\right)(\boldsymbol{m}_0 \cdot \hat{\boldsymbol{e}}_x)^2 \hat{\boldsymbol{e}}_x \otimes \hat{\boldsymbol{e}}_x\end{aligned} \tag{2.72}$$

Using this parametrisation, Equation (2.67) results in two linearly independent equations that can be expressed in matrix form:

$$\mathrm{A}\frac{\partial}{\partial t}\delta\boldsymbol{m} = \mathrm{B}\,\delta\boldsymbol{m} + \mathrm{C} \quad , \tag{2.73}$$

with

$$\mathrm{A} = \begin{bmatrix} 1 & \alpha \\ -\alpha & 1 \end{bmatrix}, \quad \mathrm{B} = \gamma \begin{bmatrix} 0 & -\Lambda(\theta) - H\cos(\theta - \theta_\text{H}) \\ H\csc\theta\sin\theta_\text{H} & 0 \end{bmatrix}$$

$$\mathrm{C} = \gamma \begin{bmatrix} 0 \\ -h(t) \end{bmatrix}, \quad D_1 = \frac{2(K_1+2K_2)}{M_\text{s}} - \mu_0 M_\text{s}, \quad D_2 = -\frac{4K_2}{M_\text{s}}$$

$$\Lambda(\theta) = \frac{1}{\mu_0}\left(D_1 + \frac{1}{2}D_2\right)\cos 2\theta + \frac{1}{2\mu_0}D_2\cos 4\theta, \quad \delta\boldsymbol{m} = \begin{bmatrix} y(t) \\ p(t) \end{bmatrix}.$$

This set of linear differential equations can be rewritten in a more familiar form as a set of two uncoupled second-order differential equations for $y(t)$ and $p(t)$:

$$\begin{aligned} y''(t) + 2\eta y'(t) + \omega_0^2 y(t) &= f(t) \\ p''(t) + 2\eta p'(t) + \omega_0^2 p(t) &= g(t) \end{aligned} \tag{2.74}$$

with:

$$\begin{aligned} 2\eta &= \frac{\alpha\gamma}{1+\alpha^2}\left(\Lambda + H\cos(\theta - \theta_\text{H}) + H\csc\theta\sin\theta_\text{H}\right) \\ \omega_0^2 &= \frac{\gamma^2}{1+\alpha^2}\left(\Lambda + H\cos(\theta - \theta_\text{H})\right)H\csc\theta\sin\theta_\text{H} \\ f(t) &= \frac{\alpha\gamma}{1+\alpha^2}h'(t) + \frac{\gamma^2}{1+\alpha^2}\left(\Lambda + H\cos(\theta - \theta_\text{H})\right)h(t) \\ g(t) &= -\frac{\gamma}{1+\alpha^2}h'(t) \end{aligned} \tag{2.75}$$

where it is assumed that $\Lambda + H\cos(\theta - \theta_H) > 0$, which is true when the magnetisation vector $\boldsymbol{m}_0$ is at the energy minimum (see Equation (2.49)). Since the

equations are linear, it is convenient to solve them assuming complex amplitudes $\tilde{y}$ and $\tilde{p}$, and recovering the adequate values from the obtained solution by taking their real part. For this purpose, it is assumed that the driving magnetic field is a sinusoidal function with the angular frequency ω:

$$\tilde{h}(t) = h_0 \exp(i\omega t) \quad , \tag{2.76}$$

which gives the expression for $\tilde{f}$ and $\tilde{g}$:

$$\begin{aligned} \tilde{f}(t) = \tilde{f}_0(\omega)\exp(i\omega t) &= h\left[\frac{i\alpha\gamma\omega}{1+\alpha^2} + \frac{\gamma^2}{1+\alpha^2}\left(\Lambda + H\cos(\theta-\theta_{\mathrm{H}})\right)\right]\exp(i\omega t) \\ \tilde{g}(t) = \tilde{g}_0(\omega)\exp(i\omega t) &= h\left[-\frac{i\gamma\omega}{1+\alpha^2}\right]\exp(i\omega t) \quad . \end{aligned} \tag{2.77}$$

With those assumptions, the solutions for $\tilde{y}$ and $\tilde{p}$ amplitudes in Equation (2.74) are given as:

$$\begin{aligned} \tilde{y}(t) &= \frac{\gamma}{1+\alpha^2}\frac{i\,\alpha\,\omega + \gamma\left(\Lambda + H\cos\left(\theta-\theta_H\right)\right)}{\omega_0^2 - \omega^2 + i\,2\,\eta\,\omega}h_0\exp(i\,\omega\,t) \\ \tilde{p}(t) &= -\frac{\gamma}{1+\alpha^2}\frac{i\,\omega}{\omega_0^2 - \omega^2 + i\,2\,\eta\,\omega}\,h_0\exp(i\,\omega\,t) \quad . \end{aligned} \tag{2.78}$$

Finally, small oscillations of the magnetisation vector about the equilibrium orientation are given by:

$$y(t) = y_0\cos(\omega t + \phi_y), \quad p(t) = p_0\cos(\omega t + \phi_p) \tag{2.79}$$

with the real valued amplitudes:

$$\begin{aligned} y_0 &= -\frac{\gamma}{1+\alpha^2}\frac{\sqrt{\alpha^2\omega^2 + \gamma^2\left(\Lambda + H\cos\left(\theta-\theta_H\right)\right)^2}}{\sqrt{\left(\omega_0^2-\omega^2\right)^2 + 4\eta^2\omega^2}}h_0 \\ p_0 &= -\frac{\gamma}{1+\alpha^2}\frac{\omega}{\sqrt{\left(\omega_0^2-\omega^2\right)^2 + 4\eta^2\omega^2}}h_0 \quad , \end{aligned} \tag{2.80}$$

and the phase of the oscillations:

$$\begin{aligned} \phi_y &= \arctan\left(\frac{-\frac{2\eta\omega}{\omega_0^2-\omega^2} + \frac{\alpha\omega}{\gamma(\Lambda+H\cos(\theta-\theta_H))}}{\frac{2\eta\omega}{\omega_0^2-\omega^2}\frac{\alpha\omega}{\gamma(\Lambda+H\cos(\theta-\theta_H))}+1}\right) \\ \phi_p &= \arctan\left(-\frac{2\eta\omega}{\omega_0^2-\omega^2}\right) - \frac{\pi}{2} \quad . \end{aligned} \tag{2.81}$$

Looking at the structure of Equation (2.80), it is observed that when the damping constant α is non-zero, the resonance frequency differs for the oscillations along the y and p axes. The phase between oscillations along both axes also varies with frequency. The trajectory (y, p) is an ellipse whose eccentricity and orientation depends on the driving frequency. For low values of the damping, the above relations can be simplified resulting in the phase between y and p equal to 90° (or $\pi/2$), and the resonance frequency:

$$\omega_R = \gamma\sqrt{(\Lambda + H\cos(\theta - \theta_{\mathrm{H}}))\, H \csc\theta \sin\theta_{\mathrm{H}}} \quad . \tag{2.82}$$

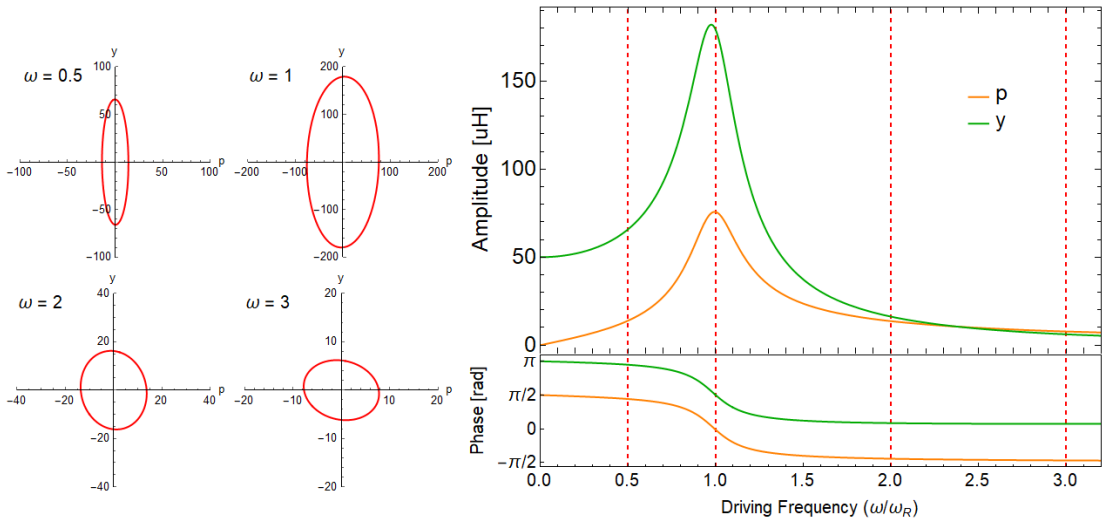

Figure 2.16: Amplitude of the oscillations of the magnetisation vector. On the left, (y, p) trajectories at four different driving frequencies (multiple of ω_R). On the right graph, the amplitude and phase of the oscillations are shown as a function of the driving frequency. Here, the calculation is shown for $\theta = \pi/2$, $\theta_H = \pi/2$, $K_1 = 200 \times 10^3\,\mathrm{J/m^3}$, $M_s = 0.6 \times 10^6\,\mathrm{A/m}$, $B = 20\,\mathrm{mT}$, $h_0 = 1\,\mu\mathrm{H}$, $\alpha = 0.1$.

An example showing the (y, p)-trajectory, the amplitude of the two coordinates, and the phase of oscillations associated with them are shown in Figure 2.16 as a function of the applied magnetic field.

There are two experimental techniques that are discussed in this work which can be used to measure the oscillations of the magnetisation vector, FMR and XFMR. For both techniques, different values derived from this theory will be important.

2.4.1 Derivations for FMR experiments

In an FMR experiment, microwaves are used to induce oscillations in the magnetised sample. Depending on the amplitude of the oscillations of the magnetisation vector, the sample will have a different impedance which can be measured a function of the current frequency or the external magnetic field. The rate of energy change of the system can be written as (using the chain rule):

$$\frac{d}{dt}\varepsilon(\boldsymbol{m},t) = \frac{\partial\varepsilon}{\partial\boldsymbol{m}}\frac{d\boldsymbol{m}}{dt} + \frac{\partial\varepsilon}{\partial t} \quad . \tag{2.83}$$

The derivative of the magnetisation direction $\boldsymbol{m}$ with respect to time can be substituted using an alternative form of Equation (2.63)

$$\frac{d\boldsymbol{m}}{dt} = -\frac{\gamma}{1+\alpha^2}\boldsymbol{m}\times\boldsymbol{H}_{\text{eff}} - \frac{\alpha\,\gamma}{1+\alpha^2}\boldsymbol{m}\times(\boldsymbol{m}\times\boldsymbol{H}_{\text{eff}}) \quad . \tag{2.84}$$

Here, $\boldsymbol{m}\cdot(\partial\boldsymbol{m}/\partial t) = 0$ was used. The derivative of the energy with respect to $\boldsymbol{m}$ is found from Equation (2.17). After algebraic manipulations, the rate of energy change can be expressed as:

$$\frac{d\varepsilon}{dt} = \frac{\alpha\gamma\mu_0 M}{1+\alpha^2}\left|\boldsymbol{m}\times\boldsymbol{H}_{\text{eff}}\right|^2 - \mu_0 M\left(\boldsymbol{m}\cdot\frac{d}{dt}\boldsymbol{H}_{\text{eff}}\right) \quad . \tag{2.85}$$

The first term on the right hand side is a term describing the energy loss due to Gilbert damping, while the second term is the energy absorption (or release) rate from the interaction with the external magnetic field. When system achieves a stable motion, its average energy gain should be zero: $\langle d\varepsilon/dt\rangle = 0$. In other words, the amount of energy absorbed should on average balance the energy gain from the external source. The energy dissipation rate is defined as:

$$I = -\mu_0 M\left\langle\boldsymbol{m}\cdot\frac{d}{dt}\boldsymbol{H}_{\text{eff}}\right\rangle \quad . \tag{2.86}$$

Using the expression for the effective magnetic field (2.71), and the solutions (2.78), the dissipation is found to be equal to:

$$I = -\frac{\mu_0 M}{2}\frac{\gamma}{1+\alpha^2}\frac{\alpha\left(\omega^2-\omega_0^2\right)+2\eta\gamma\left(\Lambda+H\cos\left(\theta-\theta_H\right)\right)}{\left(\omega^2-\omega_0^2\right)^2+4\eta^2\omega^2}\omega^2 h_0^2 \quad . \tag{2.87}$$

This equation gives the microwave absorption in an FMR experiment in dependence on the sample properties, magnitude and orientation of the magnetic field,

and the driving frequency. Contrary to popular believe [37], this function cannot be expressed as a Lorentzian. The maximum value is reached at:

$$\omega^2_{\mathrm{FMR}} = \frac{\alpha\omega_0^2 + 2|\eta|\sqrt{\gamma c\,(\gamma c - 2\alpha\eta) + \alpha^2\omega_0^2}}{2c\eta\gamma + \alpha\,(\omega_0^2 - 4\eta^2)}\omega_0^2 \quad , \tag{2.88}$$

where $c = \Lambda + H\cos(\theta - \theta_H)$. For small values of damping ($\alpha \to 0$), the maximum of the absorption is reached at the resonance frequency:

$$\omega_{\mathrm{FMR}} = \omega_R \quad . \tag{2.89}$$

An example of an absorption spectrum that can be observed in an FMR experiment is shown in Figure 2.17. With increasing Gilbert damping (α), the height of the absorption peak decreases and becomes broader (Figure 2.18). The position of the maximum deviates significantly only for very high Gilbert damping values. Typical experiential values of α of 0.02 should not affect the position of the maximum, therefore the position of the maximal absorption can be approximated by the position of the resonance. It is also found that for the presented example, the half-width of the absorption peak increases linearly with the Gilbert damping parameter.

2.4.2 Derivations for XFMR

In an X-ray resolved FMR experiment, a projection of the magnetisation onto the photon beam direction is measured. The value of the XFMR signal can be determined using the solutions found above. A special case is discussed here where the photon beam direction is directed such that its unit vector has only y and x components:

$$\hat{\boldsymbol{\sigma}} = \cos\beta\hat{\boldsymbol{e}}_y - \sin\beta\hat{\boldsymbol{e}}_x \quad . \tag{2.90}$$

The projection of the magnetisation vector onto this direction is given as:

$$P_{\mathrm{XFMR}} = A + B\,\delta\boldsymbol{m}(t)\cdot\hat{\boldsymbol{\sigma}} \quad , \tag{2.91}$$

where A and B are constants. Only the oscillating part of the magnetisation is measured in an XFMR experiment, thus the constant A can be omitted. The above expression can be evaluated to be:

$$P_{\mathrm{XFMR}} = y(t)\cos\beta + p(t)\sin\beta\sin\theta \quad . \tag{2.92}$$

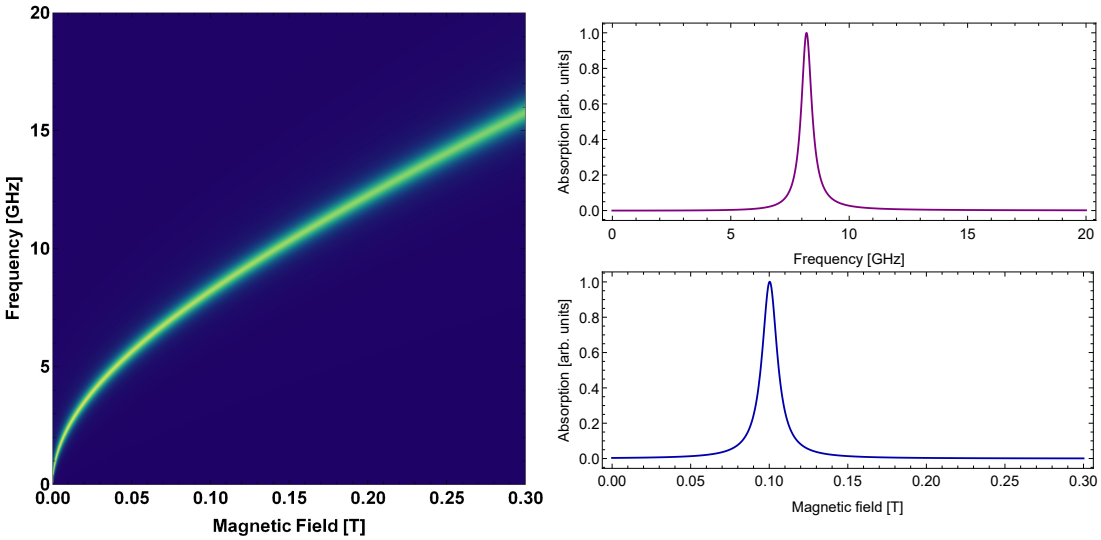

Figure 2.17: Microwave absorption spectrum as a function of external magnetic field and driving frequency. For the calculations, the following parameters were used: $\theta = \pi/2$, $\theta_H = \pi/2$, $K_1 = 0\,\mathrm{J/m^3}$, $M_s = 0.6 \times 10^6\,\mathrm{A/m}$, $B = 100\,\mathrm{mT}$, $h_0 = 175\,\mu\mathrm{H}$, $\alpha = 0.02$.

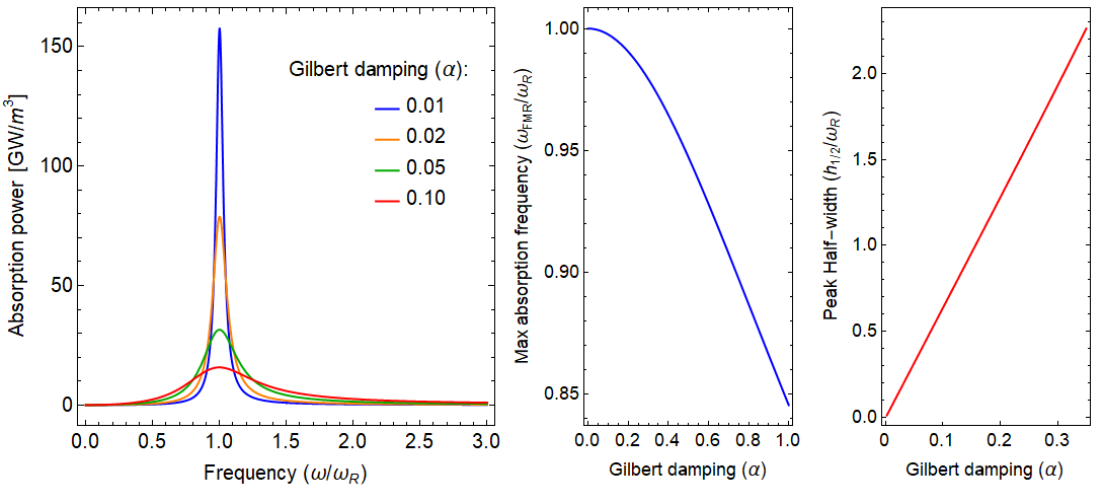

Figure 2.18: Dependence of the absorption peak on the Gilbert damping parameter.

Knowing that y and p are sinusoidal functions, the amplitude of the XFMR signal can be expressed as:

$$\sqrt{(y\cos\phi_y\cos\beta + p\cos\phi_p\sin\beta\sin\theta)^2 + (y\sin\phi_y\cos\beta + p\sin\phi_p\sin\beta\sin\theta)^2} \tag{2.93}$$

and the phase with respect to the driving magnetic field can be expressed as:

$$\tan\phi_{\mathrm{XFMR}} = \frac{y\sin\phi_y\cos\beta + p\sin\phi_p\sin\beta\sin\theta}{y\cos\phi_y\cos\beta + p\cos\phi_p\sin\beta\sin\theta} \quad , \tag{2.94}$$

where the phase and amplitude of the y and p oscillations is given by Equations(2.80) and (2.81).

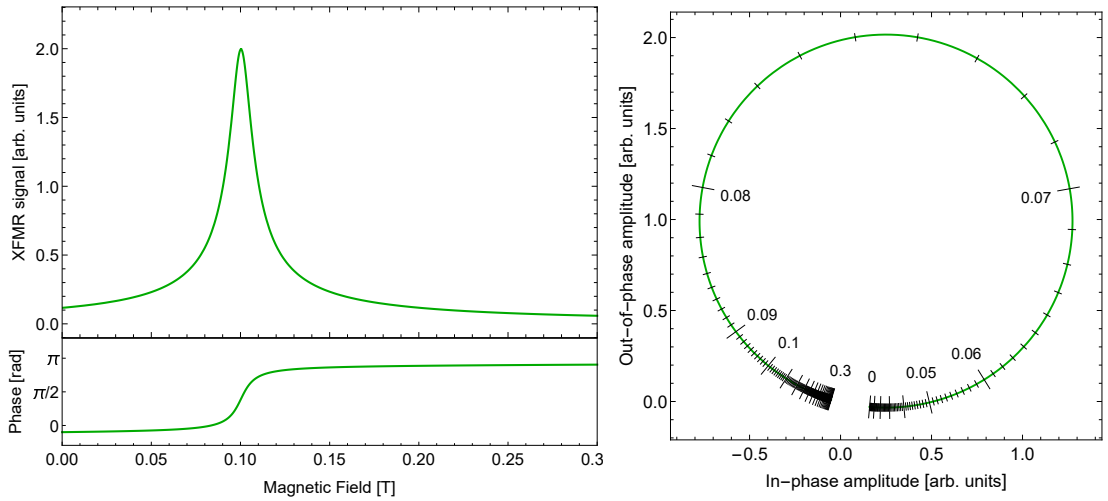

Figure 2.19: The projection of the magnetisation vector onto the photon beam direction (the XFMR signal) as a function of the external magnetic field. The graphs on the left show amplitude and phase. Graph on the right combines the information about both the phase and amplitude in a single graph where the horizontal value is given as $A\cos\phi$ and the vertical value as $A\sin\phi$. The value of the corresponding magnetic field is indicated by ticks along the curve. The example was calculated for: $\theta = \pi/2$, $\theta_H = \pi/2$, $K_1 = 0\,\mathrm{J/m^3}$, $M_s = 0.6\times10^6\,\mathrm{A/m}$, $B = 100\,\mathrm{mT}$, $h_0 = 175\,\mu\mathrm{H}$, $\alpha = 0.02$.

2.4.3 Uniaxial anisotropy (single term)

The crystalline anisotropy of materials like Py can be sufficiently described using a single trigonometric expansion term K_1. In this case, Λ in Equation (2.73) takes

the form:

$$\Lambda = \frac{1}{\mu_0} D_1 \cos 2\theta \quad . \tag{2.95}$$

As it has been already discussed in the analysis of the system stability (chapter 2.2.1), two branches of solutions can be distinguished, depending on the sign of the parameter D_1. Here, a study of the resonance frequency of the oscillations of the magnetisation vector (Equation (2.82)) is presented.

First, the case of negative anisotropy ($D_1 < 0$) is discussed, for which an easy-plane of magnetisation exists. As for the realistic values of the Gilbert damping, the dissipation has little effect on the resonance frequency, and it will be assumed that $\alpha = 0$. For simplifying the analysis, a dimensionless frequency is introduced as:

$$\nu = \frac{\mu_0}{\gamma} \frac{1}{|D_1|} \omega_R \quad . \tag{2.96}$$

Example plots of the resonance frequency as a function of the field strength (b) and its orientation (θ) are shown in Figure 2.20. For small magnetic fields ($b \ll 1$), that is when the magnetic anisotropy field is dominating over the external magnetic field, the resonance frequency is an increasing function, whose rate of increase is lower for higher values of the magnetic field. When the magnetic field is large ($b \gg 1$), that is when the external magnetic field is dominating over the magnetic anisotropy field, the resonance frequency becomes a linear function of the magnetic field with an intercept depending on the external field direction.

Figure 2.21 shows the resonance magnetic field as a function of the magnetic field orientation at a fixed frequency of the driving magnetic field (a quantity that is easier to measure in an experimental setup such as the cavity FMR). It can be observed that, independent of the driving frequency, the resonance frequency is highest when the magnetic field is oriented out-of-plane ($\theta_H = 0$), which is the least energetically favourable orientation for the sample magnetisation, which prefers an in-plane orientation (easy-plane of magnetisation).

In case of positive anisotropy ($D_1 > 0$), if the value of the magnetic field is low, the sample magnetisation will orient itself in the out-of-plane direction (easy-axis of magnetisation). It was shown in chapter 2.2.1 that depending on the external parameters (b, and θ_H), one or two solutions for θ are possible. In particular, if the external magnetic field is close to zero, the magnetisation direction can be either

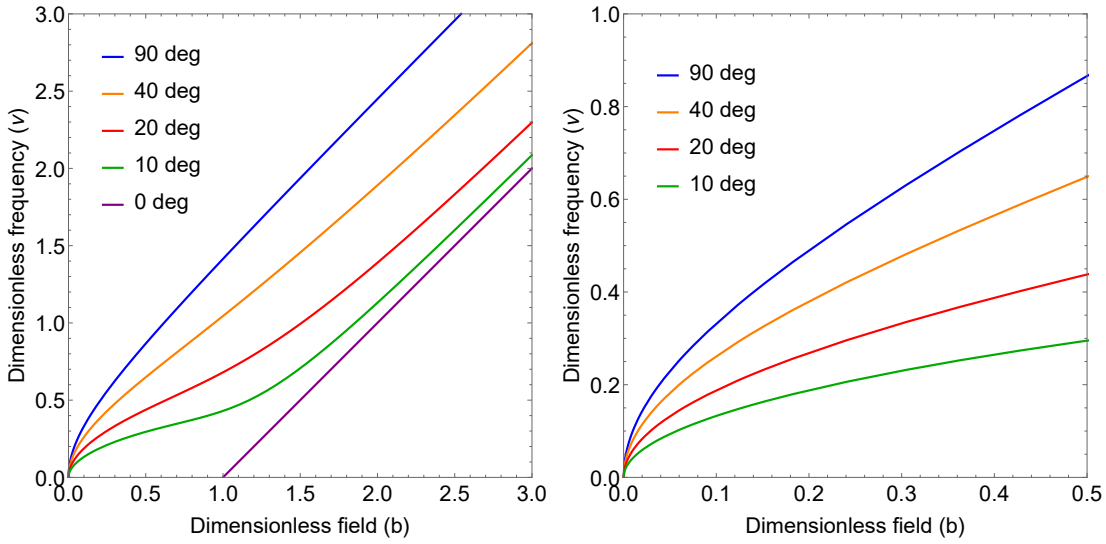

Figure 2.20: Dimensionless resonance frequency in dependence on the dimensionless magnetic field for different values of the external magnetic field orientation θ_H for $D < 0$ with $\alpha = 0$.

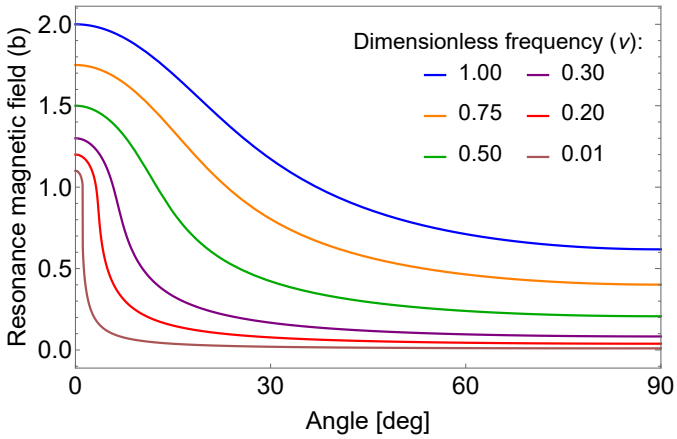

Figure 2.21: Dependence of the resonance magnetic field on the field orientation for different values of the driving frequency for the sample with an easy-plane of magnetisation $D < 0$.

$\theta = 0$ or $\theta = \pi$. As a resonance mode is associated with each of those solutions, as many as two resonance frequencies can be expected for a given magnetic field.

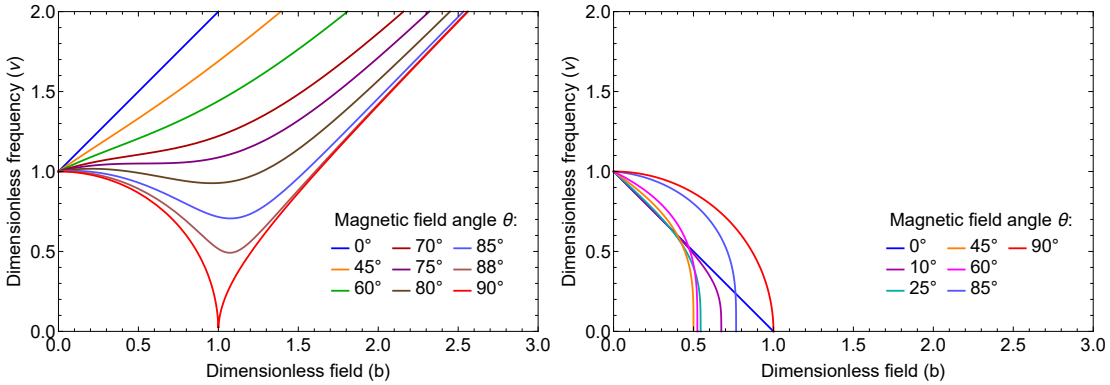

Figure 2.22: Dimensionless resonance frequency in dependence on the dimensionless magnetic field for different values of the external magnetic field orientation θ_H for case of $D < 0$ with $\alpha = 0$. Two branches of the solutions are shown, one for the global energy minimum (left) and the other for the metastable state (right).

Figure 2.22 shows the resonance frequency as a function of the external magnetic field for two different orientations of the sample magnetisation ($\theta \in [0, \pi/2]$ and $\theta \in [\pi/2, \pi]$). The second branch of the solution is only possible if the dimensionless magnetic field magnitude is lower than 1, i.e., for magnetic fields low enough to allow for a second magnetisation orientation to be possible. In case of this metastable solution, the increasing value of the magnetic field decreases the resonance frequency up to the point where it becomes zero. The first branch of the solutions is always possible. For the magnetic field orientation θ_H in the range from 0° to about 75°, the resonance frequency is a strictly increasing function. For θ_H closer to the out-of-plane orientation, up to some value of the magnetic field, a decrease in the resonance frequencies is observed with increasing magnetic field. However, independent of the magnetic field orientation, for large values of the magnetic field, the resonance frequency follows an increasing trend.

Because the resonance frequency isn't a monotonic function, multiple (up to four) resonance magnetic fields are possible for a fixed driving frequency. The exact number of possible solutions in dependence of the field orientation θ_H can be determined by studying the existence of minima and maxima of the resonance frequency function. This is done using Lagrange multipliers. The extrema of the

resonance frequency are found under the constraint of the magnetisation orientation pointing in the direction of the potential energy minimum. For simplicity, it is noted that the extremum of the function (2.82) is obtained when the formula under the square root achieves an extremum, the damping is omitted, and the dimensionless parameters are used. The Lagrange function takes the form:

$$\mathcal{L}(b,\theta,\lambda) = b\left(\cos 2\theta + b\cos\left(\theta-\theta_H\right)\right)\frac{\sin\theta_H}{\sin\theta} - \lambda\left(\sin 2\theta + 2b\sin\left(\theta-\theta_H\right)\right)\ . \quad (2.97)$$

By taking the appropriate derivatives, it evaluates to:

$$\sin 2\theta + 2b\sin\left(\theta-\theta_H\right) = 0 \quad (2.98a)$$

$$\left(\cos 2\theta + 2b\cos\left(\theta-\theta_H\right)\right)\frac{\sin\theta_H}{\sin\theta} - 2\lambda\sin\left(\theta-\theta_H\right) = 0 \quad (2.98b)$$

$$b\sin\theta_H\left(\cos\theta\left(3+\cot^2\theta\right)^2 + b\frac{\cos\theta_H}{\sin^2\theta}\right) - 2\lambda\cos\left(\theta-\theta_H\right) = 0\,. \quad (2.98c)$$

Further manipulations are done assuming $\theta_H \neq 0$, $\theta_H \neq \theta$, and that both angles are in the range between $(0, \pi/2)$.

The first equation above is the same condition as the one used to find the positions of the energy equilibrium. Here, this equation is used to determine the dimensionless magnetic field (b) for which the given magnetisation angle (θ) is minimizing the potential energy at the magnetic field orientation (θ_H):

$$b = -\frac{\sin 2\theta}{2\sin\left(\theta-\theta_H\right)} \quad . \quad (2.99)$$

The second equation is used to determine the Lagrange multiplier:

$$\lambda = \frac{\cos 2\theta + 2b\cos\left(\theta-\theta_H\right)}{2\sin\left(\theta-\theta_H\right)}\frac{\sin\theta_H}{\sin\theta} \quad . \quad (2.100)$$

The two results above are substituted into the third equation, resulting in the condition:

$$\sin\theta - 3\sin 3\theta - 3\sin\left(\theta-2\theta_H\right) + \sin\left(5\theta-2\theta_H\right) + 6\sin\left(\theta+2\theta_H\right) = 0\,. \quad (2.101)$$

The Lagrange function (2.97) has an extremum for a given θ_H if and only if there exists a corresponding θ solving Equation (2.101). This equation cannot be solved

analytically for θ (one would need to find the roots of the 5^{th} order polynomial), however, it is a quadric equation in terms of θ_H. Using the trigonometric identities:

$$\sin 2\theta_H = \frac{2\tan\theta_H}{1+\tan^2\theta_H} \quad and \quad \cos 2\theta_H = \frac{1-\tan^2\theta_H}{1+\tan^2\theta_H} \quad , \tag{2.102}$$

and substituting them into Equation (2.101) results in:

$$8t^2\cos^4\theta\sin\theta + t\left(\cos 5\theta - 9\cos\theta\right) + 4\cos 2\theta\sin^3\theta = 0\,, \tag{2.103}$$

with $t = \tan\theta_H$. This equations has two solutions:

$$\tan\theta_1 = \frac{1}{16\cos^4\theta\sin\theta}\left(9\cos\theta - \cos 5\theta + \sqrt{\Delta}\right) \tag{2.104a}$$

$$\tan\theta_2 = \frac{1}{16\cos^4\theta\sin\theta}\left(9\cos\theta - \cos 5\theta - \sqrt{\Delta}\right) \tag{2.104b}$$

with:

$$\Delta = \left(\cos 5\theta - 9\cos\theta\right)^2 - 128\cos^4\theta\sin^4\theta\cos 2\theta \quad . \tag{2.105}$$

The first solution corresponds to the static equilibrium of Equation (2.28) (the potential energy minimum), and the second one to the unstable equilibrium (this solution is discarded). The function (2.104a) is shown in Figure 2.23a. Only for some values of θ_H, there exist a corresponding θ satisfying Equation (2.101). In order for a solution to exist, the value of θ_H must be greater than the function minimum ($\theta_{H,i}$), which is found by setting the differential of the formula (2.104a) to zero, and calculating the corresponding values of θ and θ_H:

$$\theta_i = 27.0737...^\circ \quad , \quad \theta_{H,i} = 75.2069...^\circ \quad . \tag{2.106}$$

The solutions for θ are found by numerical inversion of Equation (2.104a). For almost all values of θ_H, there exist two corresponding values of θ. One of them ($\theta < \theta_i$) is related to the maximum of Equation (2.82), the other one ($\theta > \theta_i$) to the minimum. The corresponding frequencies are marked with black lines in Figure 2.23b.

The close examination of Figure 2.23b reveals that, depending on the value of the driving frequency, up to three solutions for the resonance magnetic field exist (assuming $\theta \in [0, \pi/2]$). The number of possible solutions in dependence on the parameters ν and θ_H is summarised in a phase plot (Figure 2.24). It is not marked

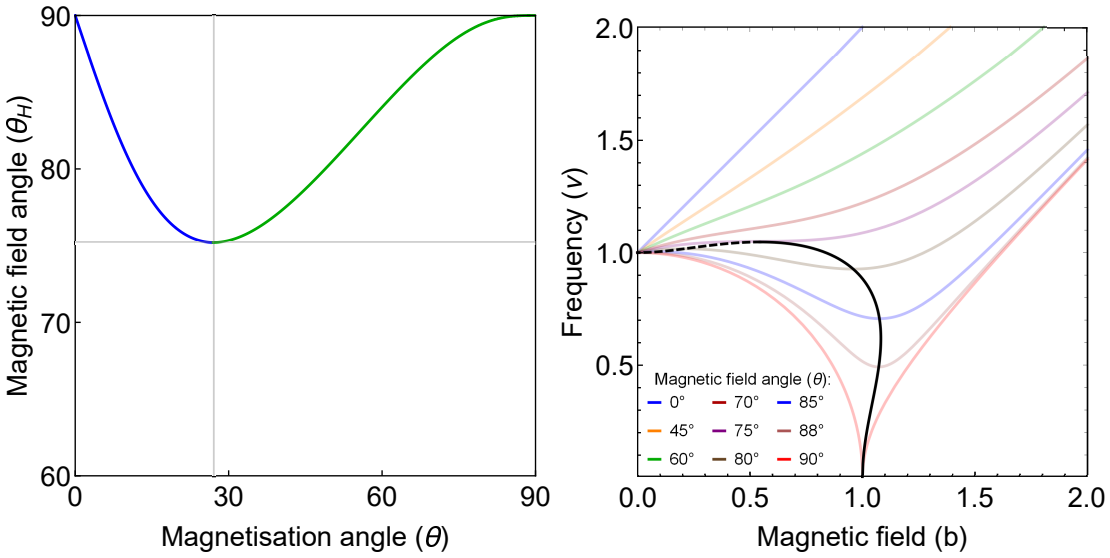

Figure 2.23: a) Set of points in the (θ, θ_H)-plane for which the frequency function $\nu(b)$ has an extremum: blue - frequency maxima, green - frequency minima. b) Resonance frequency in dependence on the magnetic field for various field orientations with an overlay curve connecting the maxima (solid, black) and minima (dashed, black)

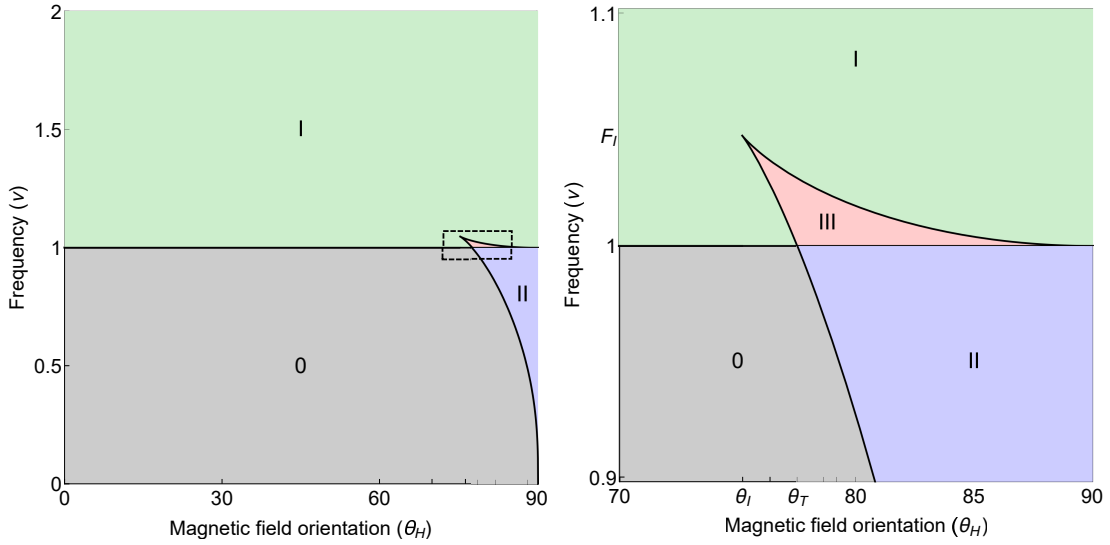

Figure 2.24: Phase space presenting the number of distinct values of the resonance magnetic field in dependence on the magnetic field orientation and frequency of the driving magnetic field assuming the system is in its global minimum. The plot on the right is a magnification of the region marked on the left plot.

here, but for $\nu < 0$, independent of θ_H, there always exists an additional resonance frequency corresponding to the solution where $\theta \in [\pi/2, \pi]$.

The effect of the magnetic field orientation (θ_H) on the resonance frequency function is illustrated in Figure 2.26. If the angle is smaller than $\theta_{H,i}$, the resonance frequency is an increasing function of the magnetic field. At $\theta_H = \theta_{H,i}$, the function has an inflection point, and for larger values of θ_H, a single minimum and maximum is observed. While the frequency at the minimum is greater than $\nu = 1$, no solutions exist for $\nu < 1$. However, when θ_H is greater than $\theta_T \approx 77.52°$, the resonance is possible also at frequencies for which $\nu < 1$. With a further increase in θ_H, the value at the minimum of the resonance frequency is decreasing until it reaches 0 at $\theta_H = 90°$.

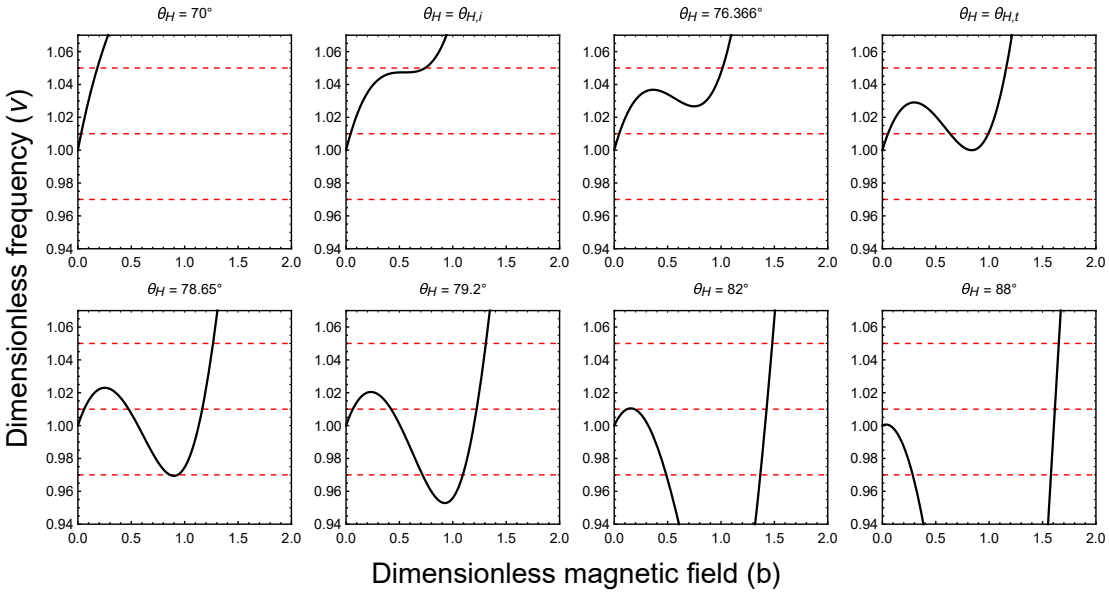

Figure 2.25: Dependence of the resonance frequency on the value of the external magnetic field for successive values θ_H.

The analysis done so far is helpful when plotting the dependence of the resonance magnetic field on the external field orientation at a fixed driving frequency (Figure 2.26). As for $D > 0$, the sample anisotropy tends to rotate the magnetisation toward the out-of-plane direction, the resonance magnetic field is lowest in the direction perpendicular to the sample plane, and highest when magnetic

filed is oriented in-plane. As discussed above, the additional solutions for the resonance magnetic field appear for driving frequencies $\nu < 1$, and the magnetic field orientations $\theta_H > \theta_{H,i}$.

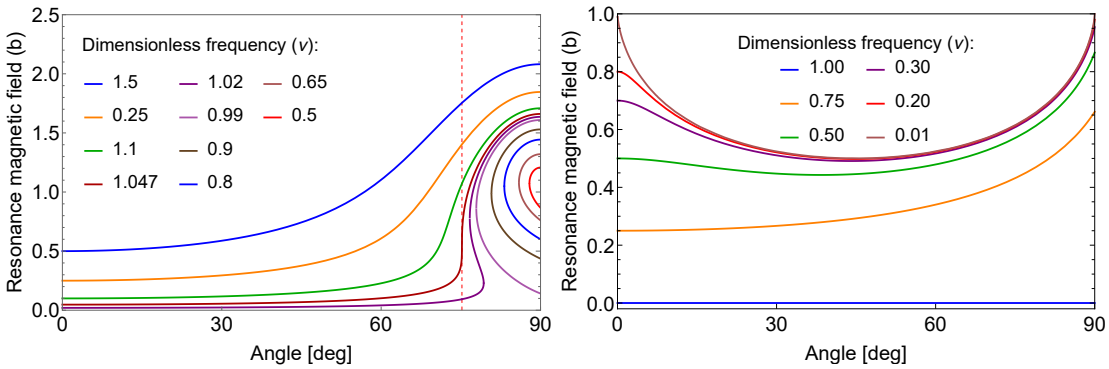

Figure 2.26: Dependence of the resonance magnetic field on the field orientation for different values of the driving frequency for the sample with an easy-axis of magnetisation $D > 0$. The graph on the left shows the case of the magnetisation at a global minimum, and graph on the right a the case of a metastable state.

For the other branch of the solutions with $\theta \in [\pi/2, \pi]$, only a single resonance magnetic field exists, and only if $\nu < 1$ (Figure 2.26). The resonance magnetic field increases with decreasing driving frequency, reaching the maximum value at $\theta = 90°$. For some values of the magnetic field orientation, a second maximum at $\theta = 0°$ is possible.

2.4.4 Uniaxial anisotrophy (two terms)

For materials that exhibit strong uniaxial anisotropy, such as Co, a single expansion term may be not sufficient to approximate the anisotropy energy function. In this case, two expansion terms can be used to provide a better description of the anisotropy of the system, with the Λ parameter taking the form: (2.4):

$$\Lambda = \frac{1}{\mu_0}\left(D_1 + \frac{1}{2}D_2\right)\cos 2\theta + \frac{1}{2\mu_0}D_2 \cos 4\theta \quad , \tag{2.107}$$

and the dimensionless frequency being defined as:

$$\nu = \frac{\mu_0}{\gamma}\frac{1}{\sqrt{D_1^2 + D_2^2}}\,\omega \quad . \tag{2.108}$$

The discussion is simplified by taking into account only low values of the damping constant ($\alpha = 0$). With this assumption, the dimensionless frequency takes the form:

$$\nu = \sqrt{b\frac{\sin\theta_H}{\sin\theta}\left[b\cos(\theta-\theta_H)+\frac{1}{2}\cos\psi\cos 4\theta+\cos 2\theta\left(\sin\psi+\frac{1}{2}\cos\psi\right)\right]}, \tag{2.109}$$

where the anisotropy ψ is defined as in Equations (2.43). Depending on the value of the anisotropy, one or more stable orientations of the magnetisation vector are possible, with a resonance associated with each of them. This creates a multiplicity of cases that need be discussed to obtain the full picture. Here, the discussion is limited to the case of the out-of-plane, in-plane, and only two other orientations of the external magnetic field.

For the magnetic field oriented out-of-plane ($\theta_H = 0$), there can exist up to three resonance frequencies related to the magnetisation orientations: $\theta_1 = 0$, $\theta_2 = \pi$, and $0 < \theta_3 < \pi$. In the third case, the frequency is zero as $\sin\theta_H = 0$. For the two other cases, both the numerator and the denominator become zero, therefore the calculations cannot be performed straightforwardly. Instead, the frequency is calculated by taking a limit:

$$\nu(\theta_H = 0, \theta) = \lim_{\theta_H \to 0^+} \nu(\theta_H, \theta) \quad , \tag{2.110}$$

which can be calculated by first linearising the trigonometric functions around the stable points, resulting in:

$$\begin{aligned}
&\nu = b + \cos\psi + \sin\psi && \text{for} \quad \theta = 0 \quad \text{and} \quad b + \cos\psi + \sin\psi > 0 \\
&\nu = -b + \cos\psi + \sin\psi && \text{for} \quad \theta = \pi \quad \text{and} \quad -b + \cos\psi + \sin\psi > 0 \\
&\nu = 0 && \text{for} \quad 0 < \theta < \pi \quad .
\end{aligned}$$

In this degenerate case of $\theta_H = 0$, the resonance frequencies are given by straight lines, with an intercept defined by the sample anisotropy (Figure 2.27).

For the magnetic field oriented in-plane ($\theta_H = \pi/2$), it was earlier found that the three solutions can exist with one being oriented in the direction of the magnetic field ($\theta = \pi/2$), and two others being symmetric with respect to the sample

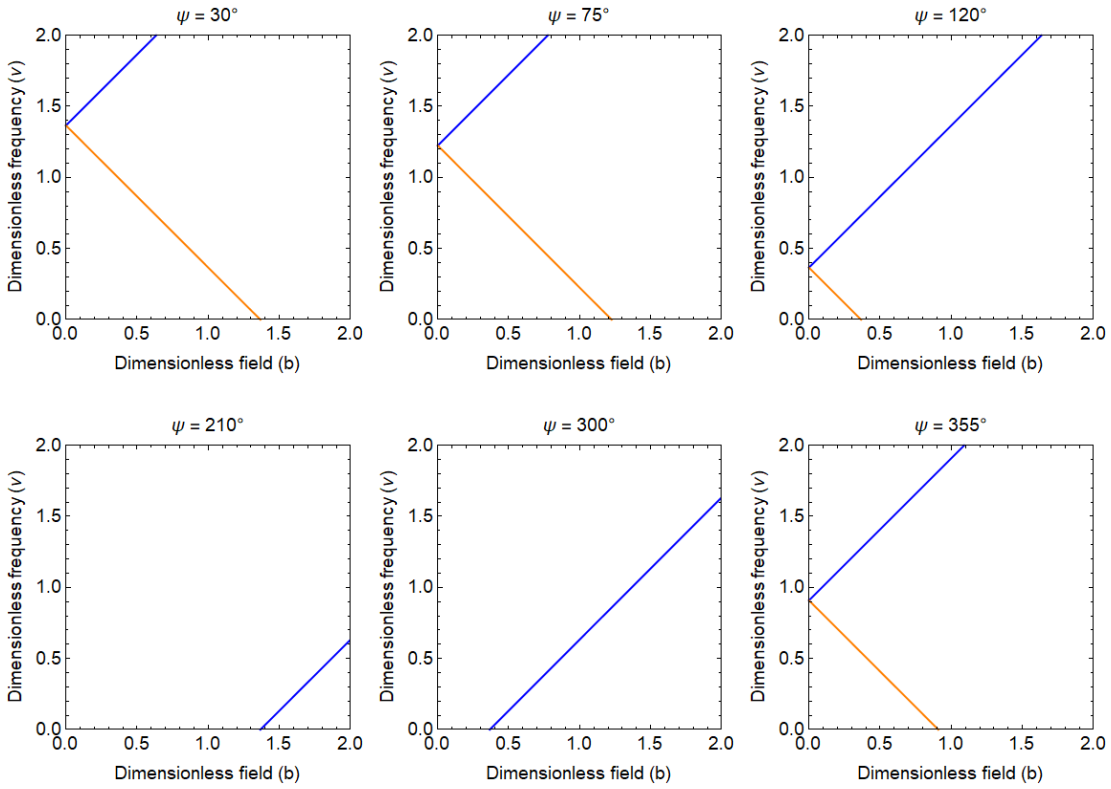

Figure 2.27: Resonance frequency dependence on the magnetic field strength for the magnetic field oriented out-of-plane for different anisotropies ψ. Blue line: magnetisation oriented in the direction of the magnetic field $\theta = 0$. Orange line: magnetisation oriented in the opposite direction $\theta = \pi$.

plane. For $\theta = \pi/2$, the resonance frequency can be calculated by directly substituting the variables into the expression (2.109). For the other cases, the value θ has to be determined first using numerical methods:

$$\nu = \sqrt{b\,(b - \sin\alpha)} \qquad \text{for} \quad \theta = \pi/2$$

$$\nu = \sqrt{b\frac{1}{\sin\theta}\left[\frac{1}{2}\cos\psi\cos 4\theta + \cos 2\theta\left(\sin\psi + \frac{1}{2}\cos\psi\right) + b\sin\theta\right]} \qquad \text{for} \quad \theta \neq \pi/2\,.$$

The solutions are plotted in Figure 2.28 for different anisotropies ψ that give qualitatively distinct results. Here, the resonance frequency is not a monotonous function at low magnetic fields, with multiple solutions possible for the magnetic orientations close to the out-of-plane direction ($\psi = 20°$).

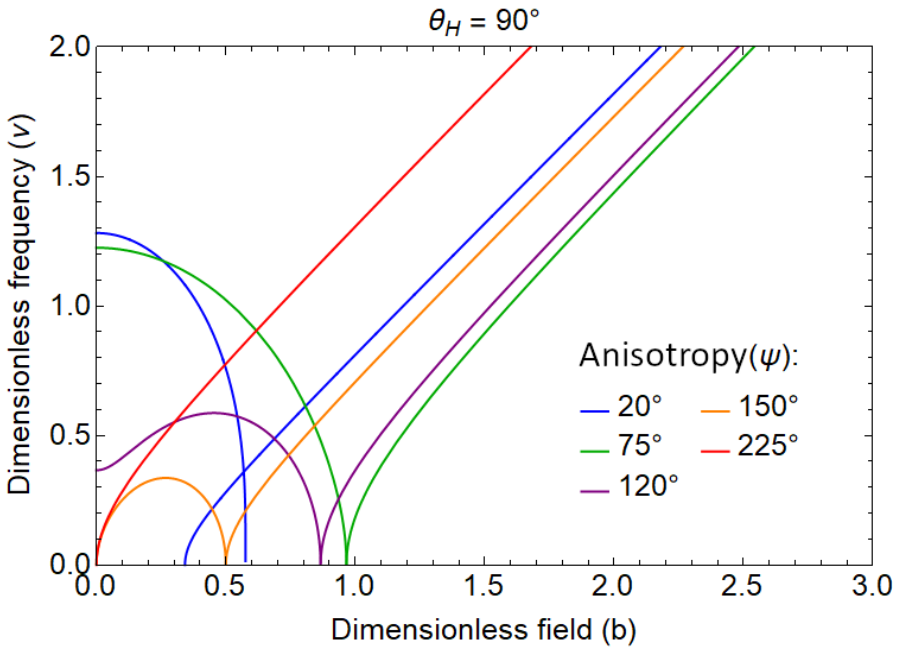

Figure 2.28: Resonance frequency dependence on magnetic field strength for the magnetic field oriented in-plane for different anisotropies ψ.

Both examples present degenerate solutions, where in case of $\theta_H = 0°$ one solution gives the resonance frequency that is zero, and two of the three solutions for $\theta_H = 90°$ produce the same frequency. This is not the case when the magnetic field is oriented in other directions. Figures 2.29 and 2.30 present the resonance frequencies when the magnetic field is oriented at $\theta_H = 28.6°$ and $\theta_H = 67.1°$,

respectively. For both orientations, three resonance frequencies can be observed. Further discussion of the qualitative changes that occur in the graph of the resonance frequency vs. strength of the magnetic field with the change of the magnetic field orientation are beyond the scope of this work.

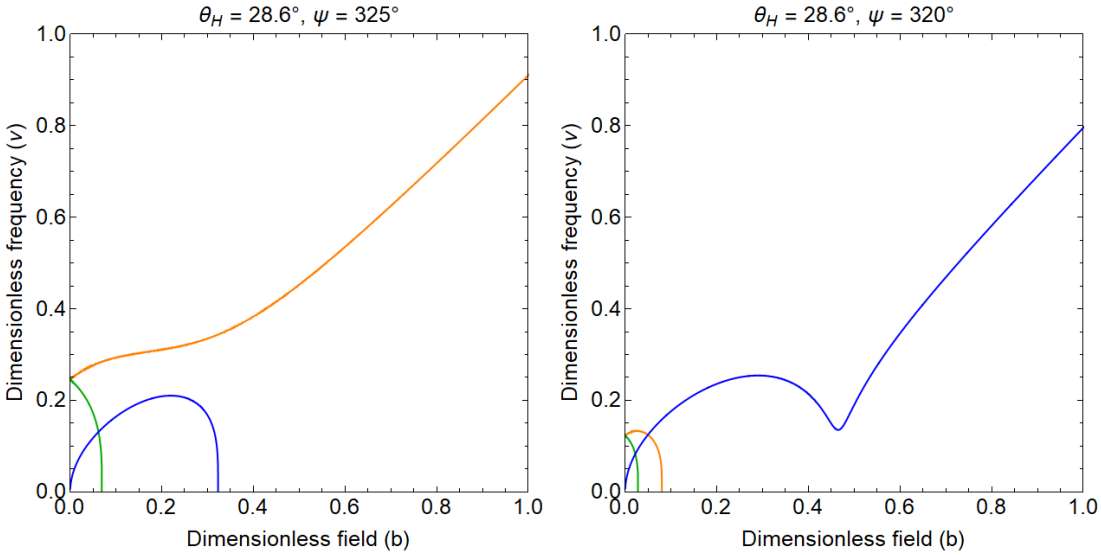

Figure 2.29: Resonance frequency dependence on the magnetic field strength for the field oriented at $\theta_H = 28.6°$ for the two different anisotropies ψ. Each line corresponds to different solution branches of the magnetisation orientation.

2.5 Cross-layer interaction

So far, the static and dynamic properties of single magnetic layers were discussed. It is, however, common to investigate heterostructures built out of multiple magnetic layers. If two or more magnetic layers are placed in close proximity to each other, they can interact, resulting in a qualitatively new behaviour. Two types of interlayer coupling are distinguished here: exchange coupling (EC) where the magnetic field produced by one of the magnetic layers interacts with the magnetic moment of the other layer, and spin-current coupling (SP) where the precession of the magnetisation of one of the magnetic layers produces a spin-polarised current that, once transferred to the other layer, induces spin-current torque, therefore affecting its dynamics.

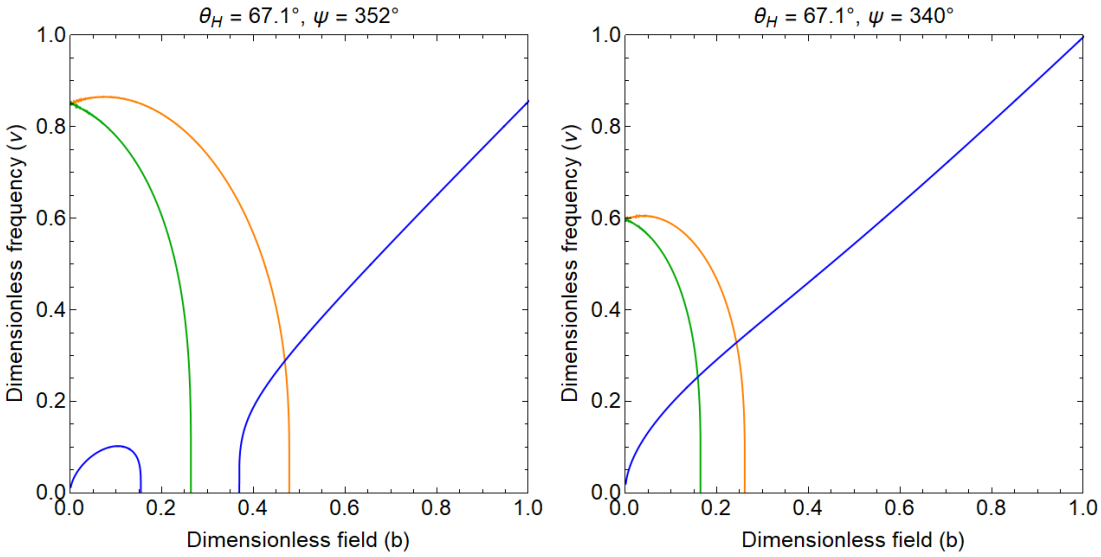

Figure 2.30: Resonance frequency dependence on the magnetic field strength for the field oriented at $\theta_H = 67.1°$ for the two different anisotropies ψ. Each line corresponds to different solution branches of the magnetisation orientation.

2.5.1 Exchange interaction

Two magnetic layers in close proximity can interact via the magnetic field they produce. Such an interaction is often modelled as a Heisenberg type interaction where the exchange energy per unit surface is give as:

$$e_{\mathrm{x}} = -J\boldsymbol{m}_1 \cdot \boldsymbol{m}_2 \quad , \tag{2.113}$$

with J being the EC constant and $\boldsymbol{m}_i$ being the unit vector in the direction of the respective layer magnetisation. The energy of the two layer system is given in a similar form as Equation (2.1) with the addition of the exchange energy (EC):

$$\begin{aligned} E(\boldsymbol{M}_1, \boldsymbol{M}_2; \boldsymbol{H}_{\mathrm{ext}}) = &\int_{\Omega_1} (-\mu_0 \boldsymbol{M}_1 \cdot \boldsymbol{H}_{\mathrm{ext}} - \frac{\mu_0}{2} \boldsymbol{M}_1 \cdot \boldsymbol{H}_{D_1} + e_{a_1}(\boldsymbol{m_1}) + A_1 |\nabla \boldsymbol{m}_1|^2)\, dV + \\ &\int_{\Omega_2} (-\mu_0 \boldsymbol{M}_2 \cdot \boldsymbol{H}_{\mathrm{ext}} - \frac{\mu_0}{2} \boldsymbol{M}_2 \cdot \boldsymbol{H}_{D_2} + e_{a_2}(\boldsymbol{m}_2) + A_2 |\nabla \boldsymbol{m}_2|^2)\, dV + \\ &\int_S (-J\boldsymbol{m}_1 \cdot \boldsymbol{m}_2) dS \quad . \end{aligned} \tag{2.114}$$

Assuming a uniform magnetization of each layer, a uniform external magnetic field and volume of the layers to be given by $V_1 = Sd_1$ and $V_2 = Sd_2$, the effective

magnetic field (2.18) for each of the layers can be evaluated:

$$\begin{aligned}\boldsymbol{H}_{\mathrm{eff},1} &= \boldsymbol{H}_{\mathrm{ext}} + \boldsymbol{H}_{\mathrm{D},} - \frac{1}{\mu_0 M_{\mathrm{s},1}}\frac{\partial e_{\mathrm{a},1}}{\partial \boldsymbol{m}_1} + \frac{1}{\mu_0 M_{\mathrm{s},1}}\frac{J}{d_1}\boldsymbol{m}_2 \\ \boldsymbol{H}_{\mathrm{eff},2} &= \boldsymbol{H}_{\mathrm{ext}} + \boldsymbol{H}_{\mathrm{D},2} - \frac{1}{\mu_0 M_{\mathrm{s},2}}\frac{\partial e_{\mathrm{a},2}}{\partial \boldsymbol{m}_2} + \frac{1}{\mu_0 M_{\mathrm{s},2}}\frac{J}{d_2}\boldsymbol{m}_1 \quad .\end{aligned} \tag{2.115}$$

The first three terms in the above equations are the same as for the single layer model; the last term results from the introduced exchange coupling. The corresponding Brown's equations are given by:

$$0 = \boldsymbol{m}_i \times \left(\boldsymbol{H}_{\mathrm{eff},i} + \frac{1}{\mu_0 M_i}\frac{J}{d_i}\boldsymbol{m}_j\right) \quad , \tag{2.116}$$

where i denotes layers 1 and 2.

In the further discussion, for simplicity, it is assumed that both layers have a uniaxial crystalline anisotropy, and a single trigonometric expansion term is sufficient to parametrise each of them:

$$\begin{aligned}e_1(\boldsymbol{m}) &= K_0 - K_1(\boldsymbol{m}\cdot\boldsymbol{e})^2 \\ e_2(\boldsymbol{m}) &= K_0' - K_2(\boldsymbol{m}\cdot\boldsymbol{e})^2 \quad .\end{aligned} \tag{2.117}$$

Also, as there is no in-plane anisotropy, it is assumed that the azimuthal component of the magnetisation of both layers matches the azimuthal orientation of the magnetic field $\phi_1 = \phi_2 = \phi_H$. With those assumptions, the potential energy of the system, per unit surface area, is given by:

$$\begin{aligned}E = d_1\left[-M_{\mathrm{s},1}B\cos\left(\theta_1-\theta_H\right) - K_1^{\mathrm{eff}}\cos^2\theta_1\right] + \\ d_2\left[-M_{\mathrm{s},2}B\cos\left(\theta_2-\theta_H\right) - K_2^{\mathrm{eff}}\cos^2\theta_2\right] - \\ J\cos\left(\theta_1-\theta_2\right) \quad ,\end{aligned} \tag{2.118}$$

where the effective anisotropy constants are defined as:

$$K_1^{\mathrm{eff}} = K_1 - \frac{1}{2}\mu_0 M_{\mathrm{s},1}^2 \quad \text{and} \quad K_2^{\mathrm{eff}} = K_2 - \frac{1}{2}\mu_0 M_{\mathrm{s},2}^2 \quad . \tag{2.119}$$

The energy of the system can be rewritten in a dimensionless form:

$$\begin{aligned}e = \frac{E}{\sqrt{D_1^2+D_2^2}\sqrt{\left(d_1M_1\right)^2+\left(d_2M_2\right)^2}} = \\ = -\csc\zeta\left[b\cos\left(\theta_1-\theta_H\right)+\sin\psi\cos^2\theta_1\right] + \\ -\sec\zeta\left[b\cos\left(\theta_2-\theta_H\right)+\cos\psi\cos^2\theta_2\right] + \\ -j\cos\left(\theta_1-\theta_2\right)\end{aligned} \tag{2.120}$$

where the

$$
\begin{aligned}
b &= \frac{B}{\sqrt{D_1^2 + D_2^2}}, \quad \sin\psi = \frac{D_1}{\sqrt{D_1^2 + D_2^2}}, \quad \cos\psi = \frac{D_2}{\sqrt{D_1^2 + D_2^2}}, \\
j &= \frac{J}{\sqrt{D_1^2 + D_2^2}\sqrt{\left(d_1 M_{\mathrm{s},1}\right)^2 + \left(d_2 M_{\mathrm{s},2}\right)^2}}, \quad \tan\zeta = \frac{d_1 M_{\mathrm{s},1}}{d_2 M_{\mathrm{s},2}}
\end{aligned}
\tag{2.121}
$$

parameters were introduced, with $D_1 = K_1^{\mathrm{eff}}/M_{\mathrm{s},1}$ and $D_2 = K_2^{\mathrm{eff}}/M_{\mathrm{s},2}$. This shows that the system is parametrised by the five independent parameters (b, θ_H, ψ, j, ζ), out of which the first two can be easily changed in the experiment, and the others are defined by the properties of the sample investigated. The effect of coupling on both layers is different and dependent on their magnetisation and thickness. The parameters j and ζ were defined in such a way that the change in the value of j gives a proportional effect on both layers, where the proportionality is defined by ζ. Since the thickness and magnetisation is always positive, the value of ζ is in the range between $[0, \pi/2]$.

As in case of single layers, the possible orientations of the magnetisation vectors for each layer are found by minimising the energy functional. The extremal points are found by taking the first derivatives with respect to θ_1 and θ_2:

$$
\begin{aligned}
\frac{\partial e}{\partial \theta_1} &= -b\sin\left(\theta_1 - \theta_H\right) - \sin\psi\sin 2\theta_1 - j\sin\zeta\sin\left(\theta_1 - \theta_2\right) = 0 \\
\frac{\partial e}{\partial \theta_2} &= -b\sin\left(\theta_2 - \theta_H\right) - \cos\psi\sin 2\theta_2 - j\cos\zeta\sin\left(\theta_2 - \theta_1\right) = 0\,.
\end{aligned}
\tag{2.122}
$$

An extremal point is a minimum if and only if[2]:

$$
\frac{\partial^2 e}{\partial \theta_1^2} + \frac{\partial^2 e}{\partial \theta_2^2} > 0 \quad \text{and} \quad \frac{\partial^2 e}{\partial \theta_1^2}\frac{\partial^2 f}{\partial \theta_2^2} - \left(\frac{\partial^2 e}{\partial \theta_1 \partial \theta_2}\right)^2 > 0\,. \tag{2.123}
$$

The conditions (2.122) are similar to the expression found for the single layer system with the addition of the third term representing the exchange interaction between the layers. As in case of the single layer, no closed form expression exists for θ_1 and θ_2, Additionally, due to the high dimensionality of the system (Dim = 5), it is difficult to provide a general discussion similar to one done for single layer systems.

[2]Edges of the interval for θ_1 and θ_2 need to be treated separately, see Appendix A

In order to understand such systems better, some qualitative conclusions can be made based on the form of the energy functional (2.114). One can notice that when the magnetic moments of the two layers are facing in roughly the same direction, the addition of a positive EC coupling term (J) results in a decrease of the value of the potential energy, therefore favouring a collinear orientation of the magnetisation vectors of both layers (the contrary is true for negative values of J) - Figure 2.31.

As it was shown in the previous chapter for some systems, more than one stable orientation of the magnetisation vector are possible. The addition of EC can favour one of those solutions. In case of $\theta = \pi/2$ (Figure 2.31) with no EC, the two orientations of the magnetic vectors are equivalent. Once EC is introduced the system favours a parallel orientation of magnetisation for a positive value of j, and an antiparallel orientation for negative j. The multiplicity of the solutions, and the effect of EC is visualised by plotting the potential energy (2.114) in dependence of the orientation of the magnetisation vectors (Figures 2.32 and 2.33).

Determining the position of the energy minima can be a time consuming process, especially when analysing its dependence on the magnetic field or the system parameters. This process can be improved by performing few algebraic manipulations. Equations (2.122) are used to eradicate the values of j and b:

$$\begin{aligned} b &= \frac{\cos\psi \sin\zeta \sin 2\theta_2 + \cos\zeta \sin\psi \sin 2\theta_1}{\cos\zeta \sin(\theta_H - \theta_1) + \sin\zeta \sin(\theta_H - \theta_2)} \\ j &= \frac{\cos\psi \sin 2\theta_2 \sin(\theta_H - \theta_1) - \sin\psi \sin 2\theta_1 \sin(\theta_H - \theta_2)}{\sin(\theta_1 - \theta_2)\left(\cos\zeta \sin(\theta_H - \theta_1) + \sin\zeta \sin(\theta_H - \theta_2)\right)} . \end{aligned} \tag{2.124}$$

With these relations, one can graph the isolines of constant b or j on a (θ_1, θ_2)-plane for given values of θ_H, ψ, and ζ. An example is shown in Figure 2.34. The values (2.124) correspond to the energy extremum and not necessarily to the energy minimum. In order to determine which points on the isolines are an energy minimum, the relations (2.123) are used. Additionally, only the positive values of the magnetic field ($b > 0$) are considered.

This picture allows for a closer study of the effect of the system parameters on the qualitative and quantitative behaviour of the sample magnetisation. The effect of magnetisation orientation is shown in Figure 2.35. It can be seen that

at high magnetic fields, all of the solutions converge to orient themselves with the orientation of magnetic field. Additionally, with an increase of the magnetic field, the metastable solutions disappear and the solutions collapse into the global energy minimum. The value of the magnetic field of this transition is dependent on the magnetic field orientation and the EC parameter.

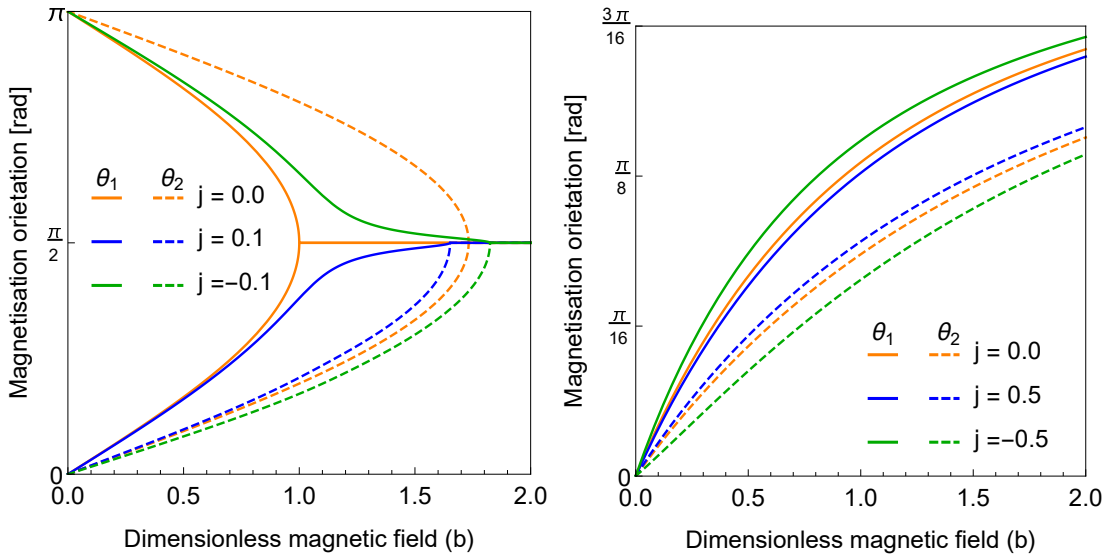

Figure 2.31: Orientation of the magnetisation vectors which correspond to the global potential energy minimum in dependence on the value of the external magnetic field in dimensionless coordinates. Layer '1' is marked by a solid lines, and layer '2' by dashed lines of the corresponding colour. The plot on the left shows the case of the magnetic field oriented in-plane ($\theta_H = \pi/2$), the plot on the right $\theta_H = \pi/4$. Both plots were made for the sample with the anisotropy $\psi = \pi/3$ and $\zeta = \pi/3$. In case of the magnetic field oriented in-plane with no exchange coupling ($j = 0$), the two orientations have the same energy value and the single global minimum cannot be distinguished.

2.5.2 Spin current in conductors

The exchange of spin polarised current is an another way magnetic layers can interact. The ferromagnetic material with precessing magnetic moment can produce an oscillating current that is spin-polarised. Such a current can enter the other layer inducing a torque on the magnetic moments in that layer. The full mechanism of this interaction is explained in Ref. [38], where it is shown that such an

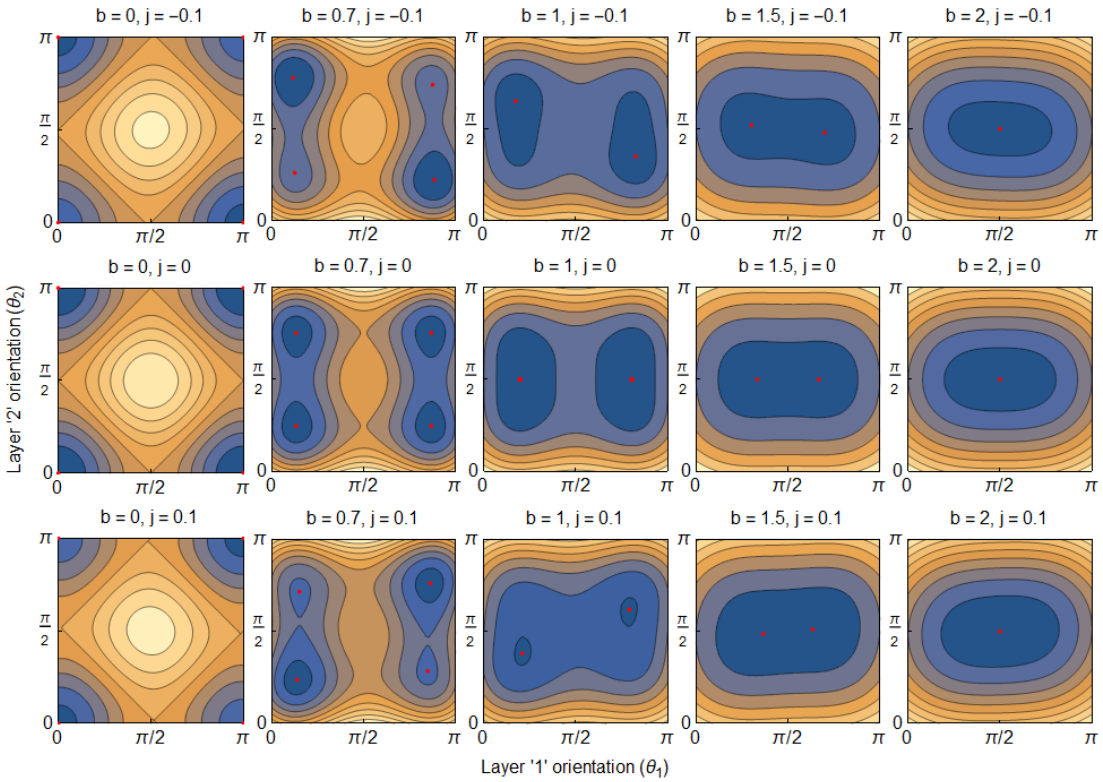

Figure 2.32: Diagrams presenting the value of the potential energy in dependence on the orientation of the magnetisation of the two magnetic layers (θ_1, θ_2). Across the rows the value of the exchange coupling j is varied, and across the columns dimensionless magnetic field b is varied. The regions with low energy are marked in blue and regions with high energy in orange. Red dots were used to mark local energy minima. The diagrams were plotted for the magnetic field in-plane ($\theta_H = \pi/2$) and using the following parameters: $\psi = \pi/3$, $\zeta = \pi/3$, corresponding to the left graph in Figure 2.31.

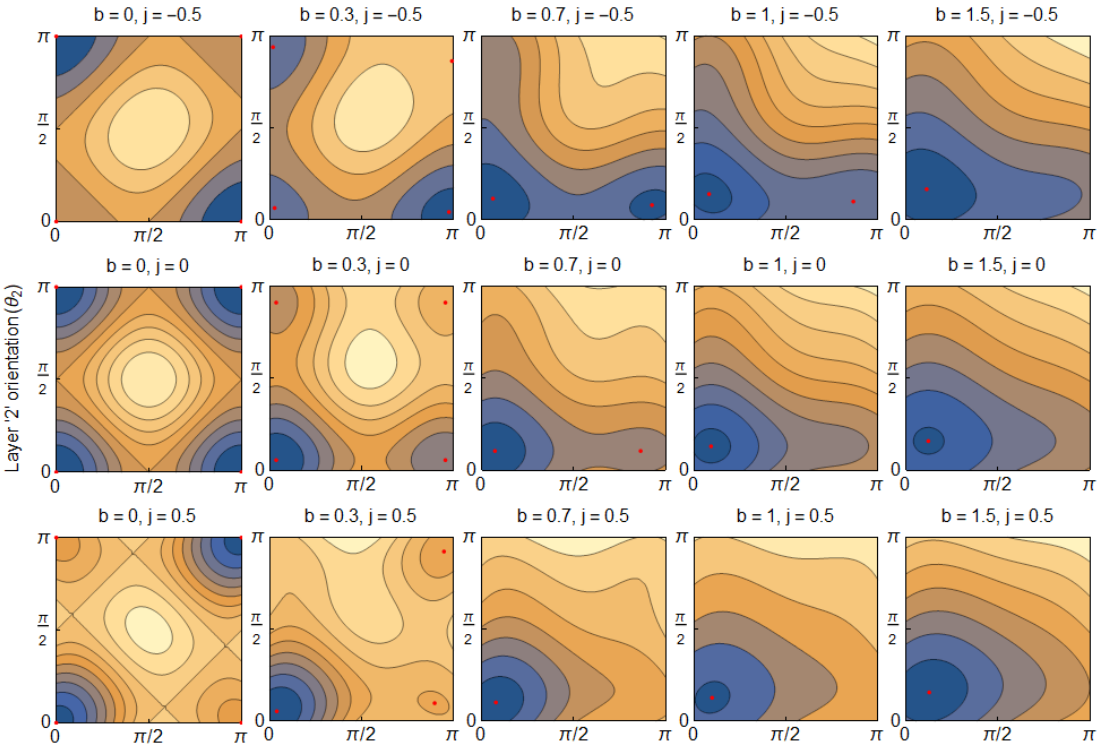

Figure 2.33: Diagrams presenting the value of the potential energy in dependence on the orientation of the magnetisation of the two magnetic layers (θ_1, θ_2). Across the rows the value of the exchange coupling j is varied, and across the columns dimensionless magnetic field b is varied. The regions with low energy are marked in blue and regions with high energy in orange. Red dots were used to mark local energy minima. The diagrams were plotted for the magnetic field in-plane ($\theta_H = \pi/4$) and using the following parameters: $\psi = \pi/3$, $\zeta = \pi/3$, corresponding to the left graph in Figure 2.31.

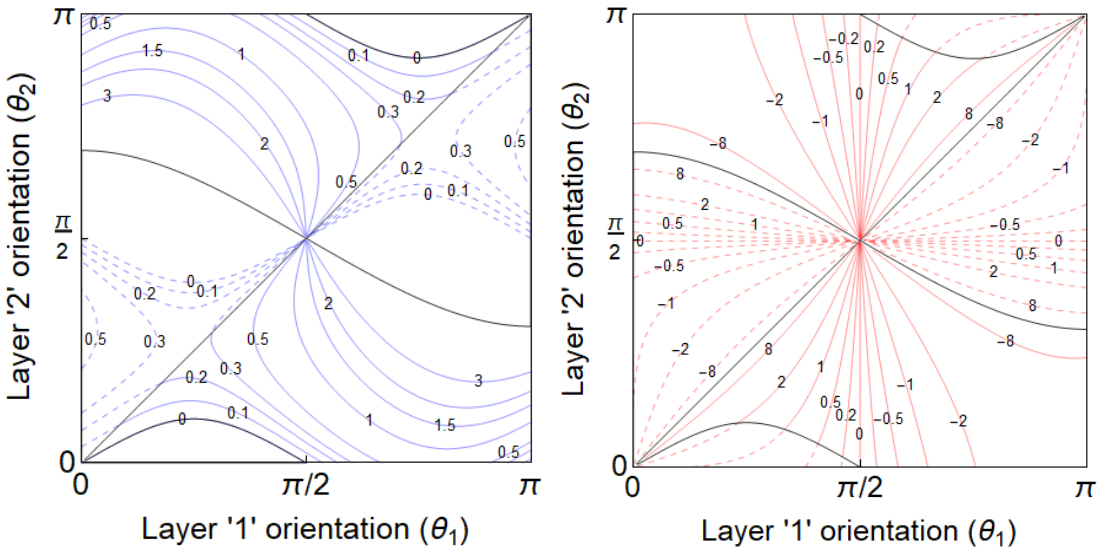

Figure 2.34: Isolines of the constant magnetic field (left) and the constant EC parameter j (right) on a (θ_1, θ_2) plane. Solid lines are drawn in the region where the system is in a local minimum, dashed lines are used otherwise. The isolines are labelled with the numbers representing the value of the dimensionless magnetic field and the EC parameter, respectively. Black lines distinguish the regions where the system is at a minimum and the dimensionless magnetic field is positive ($b > 0$). The plots were drawn for the following system parameters: $\psi = -\pi/4$, $\zeta = \pi/3$, $\theta_H = \pi/2$.

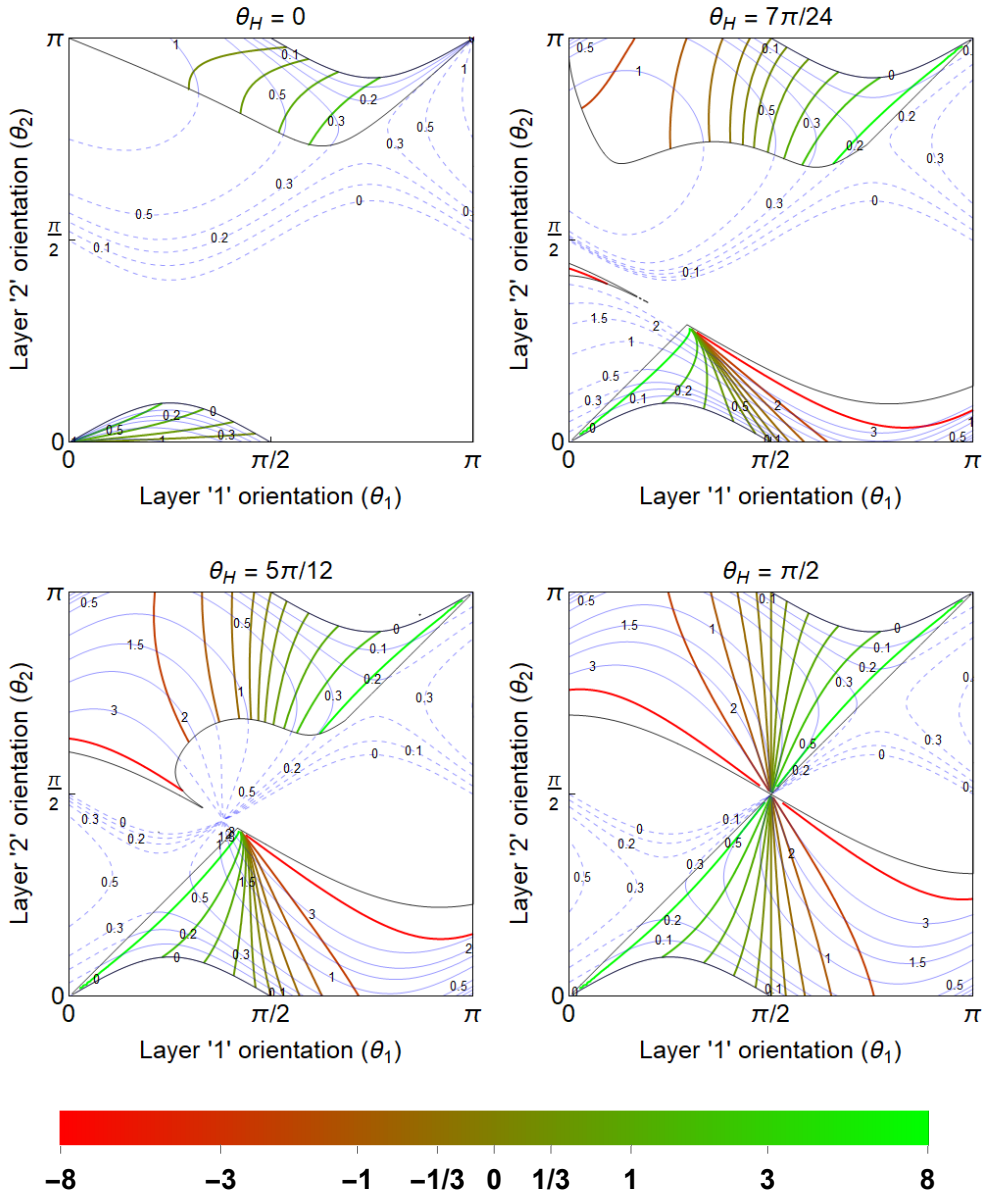

Figure 2.35: Equilibrium positions of the magnetisation orientation (θ_1, θ_2) in dependence on the value of the dimensionless magnetic field (blue isolines), the EC parameter (thick red-green lines), and the orientation of the external magnetic field θ_H. The regions where the orientation of the magnetisation is stable are distinguished by black contours and solid magnetic field isolines. The plots were drawn for the following system parameters: $\psi = -\pi/4$, $\zeta = \pi/3$.

effect can be modelled by introducing a new term into the LLG equations:

$$\frac{\partial \boldsymbol{m}_i}{\partial t} = -\gamma \boldsymbol{m}_i \times (\boldsymbol{H}_{\text{eff},i} + J_i \boldsymbol{m}_j) + (\alpha_i + \alpha_i^s)\boldsymbol{m}_i \times \frac{\partial \boldsymbol{m}_i}{\partial t} - \alpha_i^s \boldsymbol{m}_j \times \frac{\partial \boldsymbol{m}_j}{\partial t}\,, \quad (2.125)$$

where:

$$J_i = \frac{1}{\mu_0 M_i d_i} J\,, \quad \alpha_i^s = \frac{1}{M_i d_i} \alpha_{F|N|F}^{\uparrow\downarrow} \quad , \quad (2.126)$$

with $\alpha_{F|N|F}^{\uparrow\downarrow}$ being the SP parameter, characteristic for the Ferromagnetic/Nonmagnetic/Ferromagnet $(F|N|F)$ heterostructure, and J being the EC between the magnetic layers.

Since SP occurs only for excited systems, i.e., where the magnetisation is changing with time, it will not affect the static orientation of the magnetisation vectors.

2.5.3 Two-layer dynamics

Solutions to Equation (2.125) are found in a similar fashion as it was done for the single layer system. First, the LLG equations are linearised:

$$\begin{aligned}\frac{\partial}{\partial t}\delta \boldsymbol{m}_i(t) = &- \gamma \boldsymbol{m}_i^0 \times \left[\frac{\partial \boldsymbol{H}_{\text{eff,i}}^0}{\partial \boldsymbol{m}_i}\Big|_{\boldsymbol{m}_i = \boldsymbol{m}_{0,i}} \delta \boldsymbol{m}_i(t) + J_i \delta \boldsymbol{m_j}(t) + \boldsymbol{h}_i(t) \right] \\ &- \gamma \delta \boldsymbol{m}_i(t) \times \left[\boldsymbol{H}_{\text{eff,i}}^0(\boldsymbol{m}_{0,i}) + J_i \boldsymbol{m_j}(t) \right] \\ &+ (\alpha_i + \alpha_i^s) \left[\boldsymbol{m}_{0,i} \times \frac{\partial \delta \boldsymbol{m}_i}{\partial t} \right] - \alpha_i^s \left[\boldsymbol{m}_{0,j} \times \frac{\partial \delta \boldsymbol{m}_j}{\partial t} \right]\,,\end{aligned} \quad (2.127)$$

an in-plane external driving magnetic field is assumed (Figure 2.15):

$$\boldsymbol{h}_i(t) = -\hat{\boldsymbol{y}}\, h_i(t) \quad (2.128)$$

and the perturbation of the magnetic vectors from the static orientation is decomposed into the components along the p and y axes:

$$\delta \boldsymbol{m}_i(t) = y_i(t)\, \hat{\boldsymbol{y}} + p_i(t)\, \hat{\boldsymbol{p}} \quad . \quad (2.129)$$

It is convenient to express the resulting equation in the matrix form:

$$(\mathrm{A} + \mathrm{A}^s) \frac{\partial}{\partial t} \delta \boldsymbol{m} = \mathrm{B} \delta \boldsymbol{m} + \mathrm{C} \quad , \quad (2.130)$$

where:

$$\mathrm{A} = \begin{bmatrix} 1 & \alpha_1 & 0 & 0 \\ -\alpha_1 & 1 & 0 & 0 \\ 0 & 0 & 1 & \alpha_2 \\ 0 & 0 & -\alpha_2 & 1 \end{bmatrix}, \quad \mathrm{C} = \gamma \begin{bmatrix} 0 \\ -h_1(t) \\ 0 \\ -h_2(t) \end{bmatrix}, \quad \partial \boldsymbol{m} = \begin{bmatrix} y_1(t) \\ p_1(t) \\ y_2(t) \\ p_2(t) \end{bmatrix}$$

$$\mathrm{A}^s = \begin{bmatrix} 0 & \alpha_1^s & 0 & -\alpha_1^s \\ -\alpha_1^s & 0 & \alpha_1^s \frac{\sin\theta_2}{\sin\theta_1} & 0 \\ 0 & -\alpha_2^s & 0 & \alpha_2^s \\ \alpha_2^s \frac{\sin\theta_1}{\sin\theta_2} & 0 & -\alpha_2^s & 0 \end{bmatrix}, \quad \mathrm{B} = \gamma \begin{bmatrix} 0 & B_{12} & 0 & B_{14} \\ B_{21} & 0 & B_{23} & 0 \\ 0 & B_{32} & 0 & B_{34} \\ B_{41} & 0 & B_{43} & 0 \end{bmatrix}$$

$$B_{12} = -\frac{1}{\mu_0} D_1 \cos 2\theta_1 - H \cos\left(\theta_1 - \theta_H\right) - J_1 \cos\left(\theta_1 - \theta_2\right),$$

$$B_{34} = -\frac{1}{\mu_0} D_2 \cos 2\theta_2 - H \cos\left(\theta_2 - \theta_H\right) - J_2 \cos\left(\theta_1 - \theta_2\right),$$

$$B_{14} = J_1 \cos\left(\theta_1 - \theta_2\right), \quad B_{32} = J_2 \cos\left(\theta_1 - \theta_2\right),$$

$$B_{21} = J_1 \frac{\sin\theta_2}{\sin\theta_1} + H \frac{\sin\theta_{\mathrm{H}}}{\sin\theta_1}, \quad B_{43} = J_2 \frac{\sin\theta_1}{\sin\theta_2} + H \frac{\sin\theta_{\mathrm{H}}}{\sin\theta_2},$$

$$B_{41} = -J_2, \quad B_{23} = -J_1, \quad D_i = \frac{2K_i - M_i^2 \mu_0}{M_i}$$

These equations can be further simplified by expressing them in a dimensionless form, introducing:

$$b = \frac{\mu_0 H}{\sqrt{D_1^2 + D_2^2}}, \; b_i = \frac{\mu_0 h_i}{\sqrt{D_1^2 + D_2^2}}, \; \sin\psi = \frac{D_1}{\sqrt{D_1^2 + D_2^2}}, \; \cos\psi = \frac{D_2}{\sqrt{D_1^2 + D_2^2}},$$
$$j = \frac{J}{\sqrt{D_1^2 + D_2^2}\sqrt{\left(d_1 M_{\mathrm{s},1}\right)^2 + \left(d_2 M_{\mathrm{s},2}\right)^2}}, \quad \tan\zeta = \frac{d_1 M_{\mathrm{s},1}}{d_2 M_{\mathrm{s},2}}$$
$$a^{\uparrow\downarrow} = \frac{\alpha_{F|N|F}^{\uparrow\downarrow}}{\sqrt{D_1^2 + D_2^2}\sqrt{\left(d_1 M_{\mathrm{s},1}\right)^2 + \left(d_2 M_{\mathrm{s},2}\right)^2}}, \quad \tau = t \frac{\gamma}{\mu_0} \sqrt{D_1^2 + D_2^2} \tag{2.131}$$

resulting in:

$$\left(\mathrm{A} + \widetilde{\mathrm{A}}^s\right) \frac{\partial}{\partial \tau} \delta \boldsymbol{m} = \left(\widetilde{\mathrm{B}} + \widetilde{\mathrm{J}}\right) \delta \boldsymbol{m} + \widetilde{\mathrm{C}} \tag{2.132}$$

with:

$$\mathrm{A} = \begin{bmatrix} 1 & \alpha_1 & 0 & 0 \\ -\alpha_1 & 1 & 0 & 0 \\ 0 & 0 & 1 & \alpha_2 \\ 0 & 0 & -\alpha_2 & 1 \end{bmatrix}, \quad \widetilde{\mathrm{A}}^s = a^{\uparrow\downarrow} \begin{bmatrix} 0 & \csc\zeta & 0 & -\csc\zeta \\ -\csc\zeta & 0 & \csc\zeta\frac{\sin\theta_2}{\sin\theta_1} & 0 \\ 0 & -\sec\zeta & 0 & \sec\zeta \\ \sec\zeta\frac{\sin\theta_1}{\sin\theta_2} & 0 & -\sec\zeta & 0 \end{bmatrix}$$

$$\widetilde{\mathrm{J}} = j \begin{bmatrix} 0 & -\csc\zeta\cos(\theta_1-\theta_2) & 0 & \csc\zeta\cos(\theta_1-\theta_2) \\ \csc\zeta\frac{\sin\theta_2}{\sin\theta_1} & 0 & -\csc\zeta & 0 \\ 0 & \sec\zeta\cos(\theta_1-\theta_2) & 0 & -\sec\zeta\cos(\theta_1-\theta_2) \\ -\sec\zeta & 0 & \sec\zeta\frac{\sin\theta_1}{\sin\theta_2} & 0 \end{bmatrix}$$

$$\widetilde{\mathrm{B}} = \begin{bmatrix} 0 & \widetilde{B}_{12} & 0 & 0 \\ \widetilde{B}_{21} & 0 & 0 & 0 \\ 0 & 0 & 0 & \widetilde{B}_{34} \\ 0 & 0 & \widetilde{B}_{43} & 0 \end{bmatrix}, \quad \widetilde{\mathrm{C}} = \begin{bmatrix} 0 \\ -b_1(t) \\ 0 \\ -b_2(t) \end{bmatrix}, \quad \delta\boldsymbol{m} = \begin{bmatrix} y_1(t) \\ p_1(t) \\ y_2(t) \\ p_2(t) \end{bmatrix}$$

$$\widetilde{B}_{12} = -\sin\psi\cos 2\theta_1 - b\cos(\theta_1-\theta_H),$$

$$\widetilde{B}_{34} = -\cos\psi\cos 2\theta_2 - b\cos(\theta_2-\theta_H),$$

$$\widetilde{B}_{21} = b\frac{\sin\theta_{\mathrm{H}}}{\sin\theta_1}, \quad \widetilde{B}_{43} = b\frac{\sin\theta_{\mathrm{H}}}{\sin\theta_2},$$

Similarly, as in case of the single layer, the solutions to these equations are found by using complex valued variables (y_1, p_1, y_2, p_2):

$$\tilde{y_i}(t) = |\tilde{y_i}|\exp(i\Omega\tau), \quad \tilde{p_i}(t) = |\tilde{p_i}|\exp(i\Omega\tau) \quad , \tag{2.133}$$

and assuming that the driving magnetic field is the same for both magnetic layers:

$$\tilde{b_1}(t) = b_0\exp(i\Omega\tau), \quad b_2(t) = b_0\exp(i\Omega\tau) \quad , \tag{2.134}$$

with b_0 being a real number. In this case:

$$\frac{\partial}{\partial\tau}\delta\boldsymbol{m} = i\,\Omega\delta\boldsymbol{m} \quad , \tag{2.135}$$

and Equation (2.132) can be written as:

$$\left(\widetilde{\mathrm{B}} - i\,\Omega\mathrm{A} + \widetilde{\mathrm{J}} - i\,\Omega\widetilde{\mathrm{A}}^s\right)\delta\boldsymbol{m} + \widetilde{\mathrm{C}} = 0 \quad , \tag{2.136}$$

which is a compact expression for the set of four linear algebraic equations describing the dynamics of the system. This equation can be solved analytical, yet the resulting expressions are long and will be omitted. Instead, a discussion of the solutions with a focus on the values measured in the experiments is presented.

In an FMR experiment, the absorption for the two-layer system is given as a sum of the absorption of the individual layers (2.86):

$$I = -\mu_0 M_1 \frac{d_1}{d_1 + d_2} \left\langle \boldsymbol{m_1} \cdot \frac{d}{dt} \boldsymbol{H}_{\text{eff},1} \right\rangle - \mu_0 M_2 \frac{d_2}{d_1 + d_2} \left\langle \boldsymbol{m_2} \cdot \frac{d}{dt} \boldsymbol{H}_{\text{eff},2} \right\rangle , \quad (2.137)$$

where the formula was divided by $d_1 + d_2$ to sustain the convention of power per unit volume. Alternatively, the $d_1 + d_2$ factor can be omitted, and the power absorption per unit surface of the sample can be discussed.

The possible effect of different types of coupling are presented in Figure 2.37. Here, the sample with parameters: $\psi = -2.614$, $\zeta = 0.405$, and with the magnetic field oriented in-plane $\theta_H = \pi/2$ is studied. It can be observed that for low values of the coupling, two peaks of the absorption are observed, independent of the value of the magnetic field, with each of them corresponding to the resonance of the respective magnetic layer. The increase of the EC parameter j mostly affects the top absorption curve with the effect being most pronounced for low values of the magnetic field. The peak absorption frequency at zero magnetic field increases, starting with zero, with increasing EC parameter.

The introduction of SP has a very different effect on the absorption spectrum. The increase of the SP parameter $a^{\uparrow\downarrow}$ does not affect visibly the position of the absorption maxima, however, it causes a broadening of the FMR abortion lines. For high values of the SP parameter, only a single abortion line is visible.

These qualitative observations are useful when one performs a qualitative analysis of the obtained results. In order to extract numerical values of the coupling parameters, a quantitative study, using for example layer-sensitive techniques such as the XFMR, need to be performed.

By performing XFMR measurements, one can recover the dynamics of the individual layers. A theoretical prediction of the XFMR signal for a sample consisting of two magnetic layers is obtained in the the same way as it was done for a single

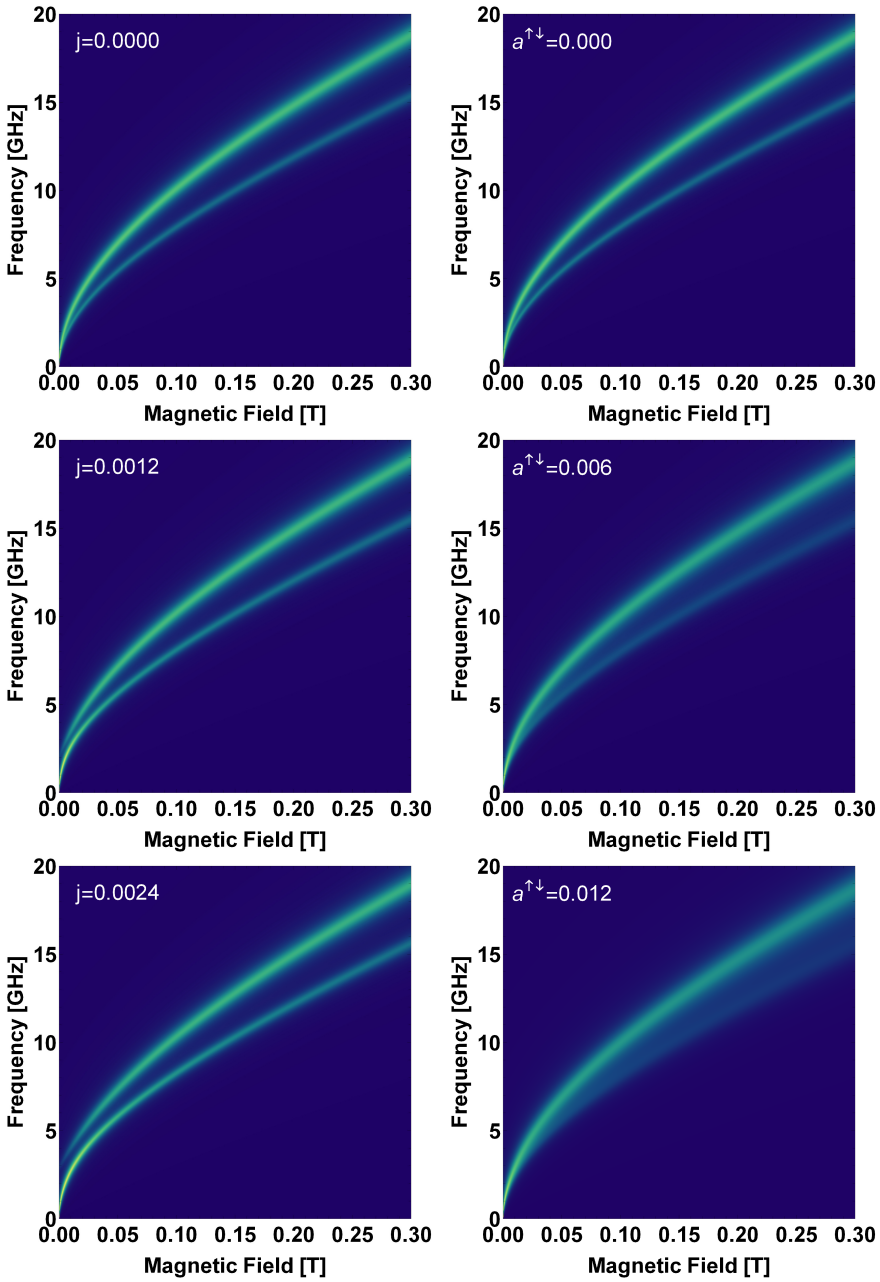

Figure 2.36: FMR absorption spectra obtained using Equation (2.137) for different values of the EC parameter j (left) and the SP parameter $a^{\uparrow\downarrow}$ (right). Sample parameters: $\psi = -2.614$, $\zeta = 0.405$, magnetic field oriented in-plane ($\theta_H = \pi/2$).

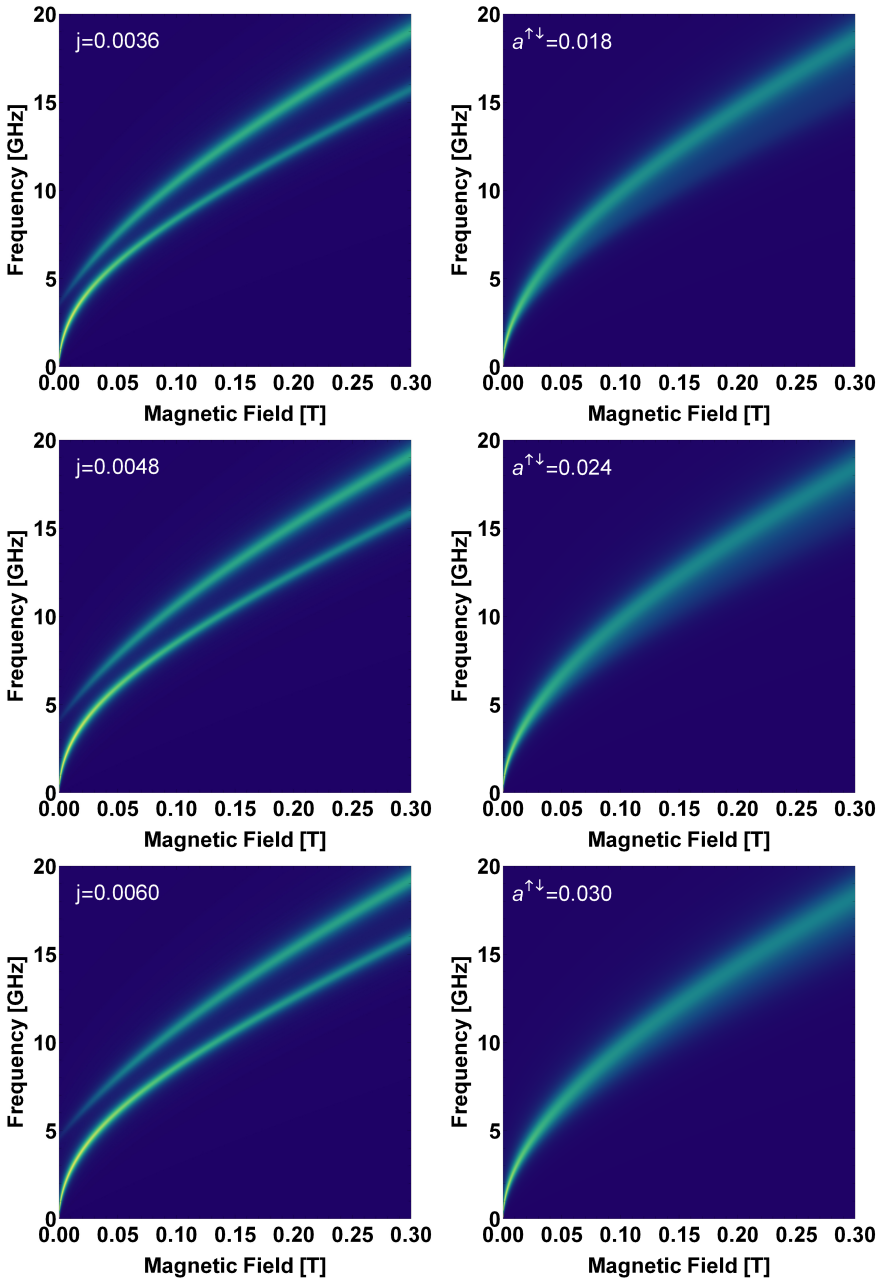

Figure 2.37: FMR absorption spectra obtained using Equation (2.137) for different values of the EC parameter j (left) and the SP parameter $a^{\uparrow\downarrow}$ (right). Sample parameters: $\psi = -2.614$, $\zeta = 0.405$, magnetic field oriented in-plane ($\theta_H = \pi/2$).

layer system:

$$\begin{aligned} P_{\mathrm{XFMR},1} &= y_1(t)\cos\beta + p_1(t)\sin\beta\sin\theta_1 \\ P_{\mathrm{XFMR},2} &= y_2(t)\cos\beta + p_2(t)\sin\beta\sin\theta_2 \end{aligned} \tag{2.138}$$

where β is the incidence angle of the X-ray photon beam.

The XFMR signal reveals subtle differences between EC and SP that were inaccessible in the FMR absorption spectrum. Most importantly, the XFMR signal shows that for each of the layers there exist two resonance peaks. This concludes that the system oscillates in two vibration modes with each of them being localized on both of the magnetic layers.

Under weak coupling, it is observed that one of the resonance peaks is positioned at a similar frequency and magnetic field as the resonance peak for the respective layer when it is independent (we will call this the "main resonance peak"). The second resonance peak corresponds to the resonance conditions for the neighbouring layer (we will call this the "secondary resonance peak").

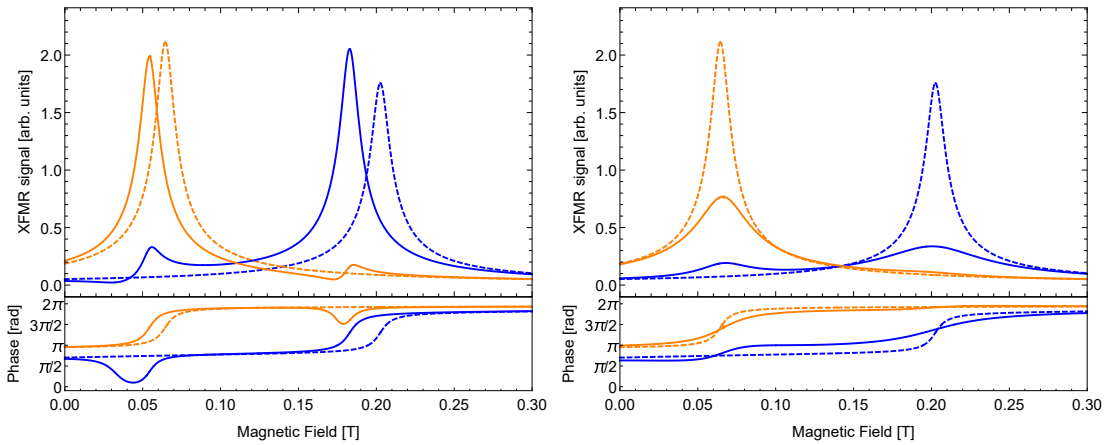

Figure 2.38: Effect of exchange coupling (left) and spin-pumping (right) on the XFMR signal. Blue and orange colors represent different magnetic layers. For comparison, the XFMR signal with no coupling between layers is plotted with dashed lines. System parameters: $\psi = -2.976$, $\zeta = 0.405$, $f = 8\,\mathrm{GHz}$. Coupling for the left graph: $j = 0.0068$ and $a^{\uparrow\downarrow} = 0$. Coupling parameters for the right graph: $j = 0$ and $a^{\uparrow\downarrow} = 0.34$.

Several qualitative differences are observed depending on the type of coupling between layers. EC shifts the values of the resonance magnetic field toward lower

values, and also the difference in resonance field for both layers is lower for higher values of the EC parameter j. Under EC, the width of the resonance peak remains roughly the same, independent of the strength of the coupling. The contrary is true for SP. With the introduction of SP, the position of the resonance peaks stay roughly the same, however, the resonance peaks become wider with increasing SP parameter $a^{\uparrow\downarrow}$.

The most striking difference between the types of coupling is observed in the phase of the oscillations. While the phase change around the main resonance peak resembles a sigmoid-like function, similar to one known for harmonic oscillators, the phase shift around the secondary peak has a bell-like shape in case of pure EC, and "s"-like shape in case of pure SP.

This observation can be used to qualitatively estimate the type of coupling in the system. However, if both types of coupling are present, it is not easy to determine which of them is dominating. In real systems, one can expect either pure EC or both, EC and SP ,to be present. Methods for evaluating the contribution of each type of coupling using experimental data are discussed in the following chapters.

Chapter 3

Device Fabrication and Structural Characterisation

Samples discussed in this work consist of multiple layers stacked on top of each other forming a heterostructure (sometimes referred to as a "sandwich"). The typical thickness of the grown films ranged between $2-20\,\mathrm{nm}$. The heterostructures were deposited on square or rectangle crystal substrates, measuring measuring $5\,\mathrm{mm} \times 5\,\mathrm{mm}$ or $10\,\mathrm{mm} \times 5\,\mathrm{mm}$, respectively.

Manufacturing samples with uniform layer thickness, composition (for a layer consisting of different elements) and the desired crystallographic structure is a challenging task. Due to the microscopic layer thickness, any roughness or contamination can a have significant impact on the properties of the resulting samples. In order to overcome such complications, highly sophisticated experimental procedures were employed.

The first step in growing successful sample is the preparation of the substrate which was acquired from a vendor, and which has been exposed to atmosphere. The preparations involve chemical cleaning, vacuum thermal processing (annealing) and treating the material with high energy ions to remove any left-over impurities (pre-sputtering). Details of the procedures are discussed in section 3.1.

The deposition of thin films was done using Molecular Beam Epitaxy (MBE). The procedure and the optimal conditions used for the film growth are discussed in chapter 3.2. Some of the studied heterostructures were grown using two MBE systems. The transport between the two different MBEs exposed the samples to air, resulting in contamination with organic residue, water, and atmospheric

gases. Recovering the surface quality required additional cleaning steps, which are discussed below.

3.1 Substrate preparation

The substrates used for the sample growth were thin plates ($\sim$0.5 mm thick) of high quality crystals that had been cut along a specific crystallographic plane. The type of substrate, and its quality, has a mayor impact on the material deposition. In order to reduce strain, the substrate was chosen to minimise the lattice mismatch with the deposited material. In this work, MgO, Si and sapphire (Al_2O_3) substrates were used.

Exposing substrates to air causes contamination. Depending on the substrate material, it is susceptible to different types of contamination and needs to be treated accordingly. For example, the surface of MgO is damaged by contact with water, and the Si crystal binds with organic molecules (carbon).

Microscopic contaminations are removed from a substrate by chemical cleaning. The usual process involves placing the substrate in a bath of boiling acetone for 5 min. Next, a substrate was moved to a bath of fresh acetone and the process was repeated. The substrates were then moved to a beaker with isopropanol (ISO), which was brought to a boil for 5 min (this was also repeated for a second time). In the final step, the samples were rinsed with distilled water (this step is omitted in case of MgO), and dried with nitrogen.

The chemically cleaned substrates were mounted onto a holder. The attachment was made mechanically, or by using a temperature-resistant glue. The load holders were placed into a vacuum loading chamber where initial outgassing was performed. To remove any residual gasses from the surface, the samples were heated to 200$-$700 °C.

As the removed contamination may have caused damage to the surface structure by creating microscopic cracks or by affecting the arrangement of atoms on the surface, the samples are annealed. To reconstruct the surface, the sample temperature is brought close to the material melting point. The high energy of the atoms allows them to move along the surface to find the energetically stable location. The exact conditions used for the annealing process depend on the material.

The temperature range, as well the heating and cooling rate, may produce distinct surface reconstructions [39, 40] that would be suitable for different applications.

In some cases, the steps presented above are not sufficient to remove the contamination that has strongly eroded the substrate. In the sputtering process, high energy ions are directed onto the sample, removing material from the surface. This process removes both substrate material and any contamination that lies within. If the contamination bond to the surface is weaker than the interatomic forces holding the crystal together, the energy of the ion beam can be tuned to limit the damage done to the surface. Any roughness resulting from this process is removed by annealing the substrate.

When working with materials like MgO, it is difficult to perform the annealing process as the melting point of the MgO crystal is as high as 2852 °C [41]. Reaching this temperature is beyond the capabilities of our experimental systems. Instead, to obtain high quality surfaces, a thick layer of MgO has to be grown under high vacuum conditions on top of the MgO substrate.

3.2 Molecular Beam Epitaxy

Molecular beam epitaxy is used to grow materials on a substrate with a precision that allows for control of the number of the deposited atomic layers ($\sim$0.3 nm). The deposition is done in ultrahigh vacuum ($\sim 1 \times 10^{-10}$ Torr) by evaporating the material and directing the beam of molecules onto the sample surface. Slow material growth in precisely controlled conditions provides a remarkable layer quality, especially when used to deposit metals.

The material deposition rate and temperature of the substrate have a major impact on the crystal growth and the quality of the thin film layer. The rate of material evaporation is determined by its temperature [42]. The deposition rate is monitored using build-in sensors such as a flux-monitor or a quartz microbalance. The sample is mounted on a holder that is in a close proximity to a heater, allowing for precise temperature control. During the growth process, the holder is constantly rotated to ensure a uniform material deposition.

In the presented research, two MBE systems were used. One of them was a micro-MBE system located at the I04-beamline at Diamond Light Source. This

system is equipped with eight crucibles heated using ohmic resistance, out of which five were used (filled with: Co, Ni, Fe, Sn, Si). The deposition rate was monitored using a beam-flux monitor, and the quality of the crystal growth was monitored using RHEED (reflection high-energy electron diffraction). Additionally, this system was connected to the sputtering and annealing chamber, equipped with LEED (low-energy electron diffraction). This allowed for surface quality studies without the need to expose the sample to air.

The second MBE was located at the Institute of Physics, Polish Academy of Sciences, in Warsaw (IFPAN). In this system, materials were heated using an electron beam directed onto the evaporant. This allowed for the growth of molybdenum (Mo) and MgO, which require very high temperatures to evaporate. For materials like Au and Co, an effusion cell was used. This system was also equipped with RHEED for growth quality control and a quartz micro-balance to monitor the deposition rate.

3.3 Growth characterisation

The grown samples were characterised to determine the quality of the obtained layers. Some details can be spotted by the naked eye: for example, metal covering a transparent substrate can reduce its transparency and create a mirror effect on the surface. However, most of the important features have dimensions that are comparable with the interatomic distances ($1-20\,\mathrm{nm}$).

Several in-situ techniques can be used, i.e., without exposure to air, which allows for the characterisation of the sample during the growth process. Other measurements require moving the sample ex-situ (exposing to air). These methods are used to characterise the sample after the layer deposition is complete. Here, a discussion of several methods used to study the quality of thin film heterostructures is presented.

3.3.1 Reflection high-energy electron diffraction

Reflection high-energy electron diffraction (RHEED) is an in-situ method that enables real time characterisation of the sample surface during the deposition process. A high energy electron beam ($8-20\,\mathrm{keV}$) is focused on the surface at a large

incidence angle (almost parallel to the sample surface). Diffraction occurs on the sample surface, and a RHEED pattern is observed on the phosphorus screen.

If the sample surface is amorphous, or no periodic structure is present, no pattern is observed. For a flat surface with periodic atom arrangements the RHEED pattern shows straight lines. Island growth is identified by a dotty RHEED pattern.

The surface of a crystalline layer has a periodic structure. Therefore, the diffraction, and hence the RHEED pattern, is dependent on the sample orientation. By analysing the dependence of the RHEED pattern on the rotation of the sample, one can study the symmetry of the surface and determine the basic crystallographic properties of the deposited layer.

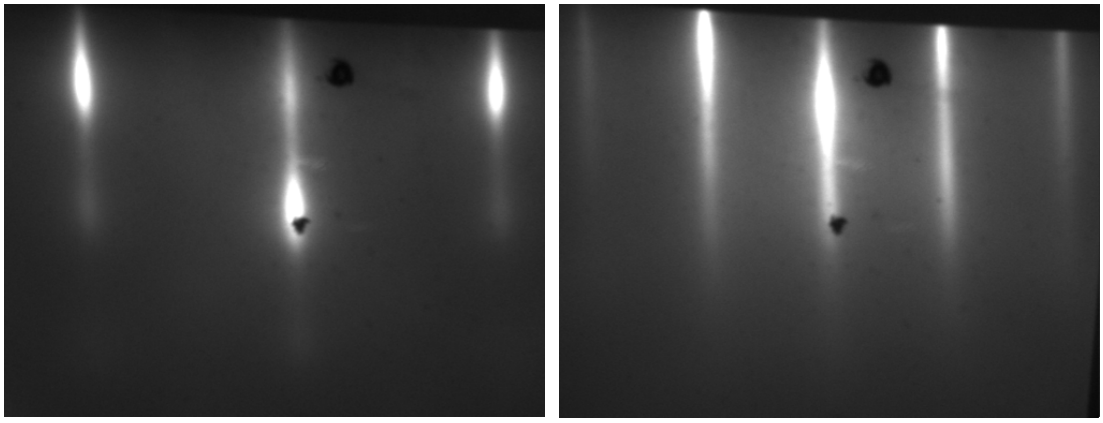

Figure 3.1: RHEED images of the Co (111) surface along the two principal directions, with the sample being rotated by 30° between the images.

3.3.2 Low-energy electron diffraction

Low-energy electron diffraction (LEED) is another in-situ method used for the sample surface characterisation. In contrast to RHEED this method cannot be performed during sample growth, as for the LEED measurement, the sample has to be moved to a separate chamber. An electron beam is directed perpendicular to the sample surface at an energy of $5-400\,\mathrm{eV}$. LEED allows for investigation of the surface quality and the atom arrangement. It can be used for a qualitative

investigation of the surface reconstruction or to measure intensity-energy curves which can be compared with theoretical predictions.

In the present study, LEED was used for the analysis of the effect of the annealing process on the sample surface reconstruction. The LEED is located in the sputtering and annealing chamber, allowing for the quick verification and tuning of the sputtering and annealing process. LEED was particularly useful for the optimisation of the annealing parameters of the Si(111) substrate, the recovery of the contaminated Au(111) layer, and the study of the Sn deposition process.

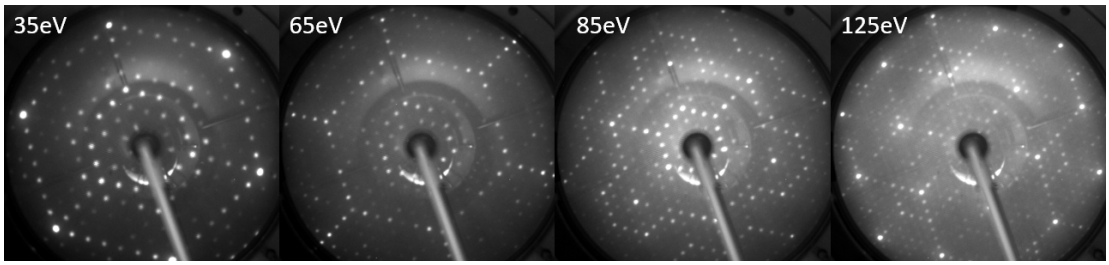

Figure 3.2: LEED images of the annealed Si(111) surface at few chosen values of the electron beam energy. By visual comparison with published data, it can be concluded that the LEED pattern corresponds to a 7×7 surface reconstruction [1].

3.3.3 Atomic Force Microscopy

The methods described above are based on diffraction phenomena that are a collective result of the surface periodicity over a large sample area. They are, however, not able to capture features that are local. A more detailed measurement of the film surface is possible using, for example, Atomic Force Microscopy (AFM). The AFM is capable of capturing features as small as several nanometres, i.e., its resolution is 1000 times better than of an optical microscope. The AFM principle of operation is based on "touching" the surface with a tip, and measuring the force acting on it. By scanning over the surface, the morphology of the sample's nano-landscape is obtained.

The AFM was used as a tool to study the quality of a substrate and the deposited layers. The type of growth was determined (flat, island, or pillar growth) and the surface roughness was studied. When optimising the conditions for the

permalloy deposition, it was noticed that too high amounts of Fe resulted in phase segregation that was visible on the AFM images.

3.3.4 Scanning Tunnelling Microscopy

A Scanning Tunnelling Microscope (STM) is related to the AFM technique. It is based on quantum tunnelling, which allows to scan the surface topology with atomic resolution. When a tip is brought close to the sample surface, and a voltage is applied between the sample and the tip, a tunnelling current may be measured. Its magnitude depends on the gap size, applied voltage, and local density of states of the sample surface [43].

Thanks to the very high resolution of the STM, detailed studies of the surface can be made. In particular, one can study surface reconstructions (periodic arrangement of atoms on the surface). Here, STM was used as an in-situ method to verify the sample surface quality, and to optimise the conditions for the Au surface reconstruction.

3.3.5 X-ray crystallography

Contrary to visible light, X-ray radiation can penetrate a sample and provide information about its internal structure. In particular, X-rays are scattered by atomic sites, which in case of a periodic crystalline lattice can lead to constructive interference. X-ray diffraction (XRD) is a useful tool used to determine the quality of the grown films, crystallographic phase, and crystallographic orientation of the obtained layers.

When an X-ray beam is directed at a high incidence angle (almost parallel to sample surface) the light becomes fully reflected. The physics of reflections considering scales comparable with the interatomic distance is different from classical considerations. When total internal reflection occurs, the electromagnetic waves entering the medium create so-called evanescent waves, whose intensity decreases exponentially with penetration depth. If a sample consists of multiple layers, the phase shift of the evanescent wave will depend on the layer thickness and their optical densities. Through the interference of reflected light, its intensity can vary with the value of the incidence angle resulting in fringes similar to the ones found

in the Fabry-Pérot effect. This method of measurement is known as X-ray reflectivity (XRR), and it is used to determine the layer thickness and surface roughness of the grown films.

Here, XRD and XRR were used to measure the layer thickness in a sample, determine the layer's crystallographic phase, and crystallographic orientation.

3.3.6 Cross-Sectional Transmission Electron Microscopy

The most detailed information about the sample structure can be obtained using Transmission Electron Microscopy (TEM). In this experiment, a 100 nm thick specimen covering the cross-section of the sample is cut using a beam of high energy ions. A beam of electrons is passed through the thin specimen forming an image that is magnified and focused onto a screen or a photo-sensing matrix.

The image resolution in TEM allows for the detection of individual atomic layers. By analysing the resulting image one can confirm the quality of the grown layers, the quality of the interfaces, measure the interatomic distances (lattice constant), and even determine the type of elements and the crystallographic phase of the material.

Performing TEM is a very time consuming process and it is used as a last step in the characterisation, after all of the other measurements have given satisfactory results, and a more detailed understanding of the sample structures is needed.

3.4 Growth conditions for selected materials

All samples presented in this work were grown in MBE systems and characterised using the methods describe above. Below, a brief summary of the used recipes is presented.

3.4.1 MgO/Co/Sn

The MgO(111) substrates were cleaned chemically and loaded into a vacuum chamber where they were outgassed and annealed at 700 °C for 30 min. Co was evaporated from a crucible at a temperature of 1400 °C, and a 15 nm layer was deposited onto the substrate held at 400 °C with a deposition rate of 0.016 nm/s.

The sample was cooled down to room temperature (RT) and a Sn layer was deposited from an effusion cell heated to 1050 °C. The thickness of the Sn layer was varied between $0 - 5$ nm. The growth process was monitored using RHEED and the finished samples were characterised using ex-situ methods.

3.4.2 MgO/Co/Sn/Py/Si

The MgO/Co/Sn/Py/Si samples were grown in a similar fashion as the MgO/Co/Sn samples, however, with an additional Py layer. It was found that the optimal Py growth conditions are achieved with the Ni effusion cell held at 1220 °C and the Fe effusion cell held at 1135 °C. The sample was held at room temperature, achieving the deposition rate of 0.0025 nm/s. The sample was capped with a Si layer to prevent oxidation.

3.4.3 Al_2O_3/Mo/Au

The Al_2O_3/Mo/Au heterostructure is proven to be a good base for the growth of HCP Co [44]. The a-plane $(11\bar{2}0)$ sapphire substrate was chemically cleaned and placed in the vacuum chamber, where it was outgassed at 400 °C. A buffer layer of Mo was deposited at a rate of 0.03 nm/s on the substrate heated to 900 °C. This created a 20 nm thick Mo(110) layer. The Mo buffer layer is deposited to smooth out any irregularities in the sapphire substrate and to provide good conditions for the Au (111) growth. Next, a 20 nm layer of Au was deposited with the sample held at room temperature after which the sample was annealed at 200 °C for 30 min.

Such heterostructures were grown at IFPAN and used for the growth of HCP Co and other materials in the same system, or transported to Diamond Light Source to be used with the on-site MBE systems.

3.4.4 Al_2O_3/Mo/Au/Co/MgO/Py/Au

Using samples prepared according to the Al_2O_3/Mo/Au recipe, a Co layer was deposited at rate of 0.02 nm/s with the sample held at room temperature. The thickness of the Co layer ranged between $2 - 10$ nm. The electron beam was used to evaporate MgO and deposit a $1 - 10$ nm film on top of the Co layer. A 5 nm

thick Py layer was grown by a co-deposition of Fe and Ni, both evaporated from the effusion cells. The sample was capped with a Au layer to prevent oxidation.

3.4.5 Al_2O_3/Mo/Au/$(Co/Au)_N$/MgO/Py/Au

A Co layer was deposited on top of the Al_2O_3/Mo/Au heterostructure at a rate of 0.02 nm/s with the sample held at room temperature, followed by the deposition of a Au monolayer (0.3 nm). This process was repeated 1, 2, or 3 times resulting in $(Co/Au)_N$ structure. On top, MgO/Py/Au layers were deposited following a similar recipe as described above.

3.4.6 Al_2O_3/Mo/Au/Co/Sn/Py/Si

A Al_2O_3/Mo/Au sample was shipped to the mini-MBE at Diamond Light Source, outgassed and annealed. The Co layer was grown with the substrate held at room temperature, with a layer thickness of 15 nm or 20 nm at the rate of 0.016 nm/s. The quality and crystallographic structure of the obtained Co layers were verified by taking RHEED images of the surface. The Sn layer was deposited on top by evaporating the material from an effusion cell held at 1050 °C with the sample held at room temperature. The Sn growth was monitored using RHEED, where a doubling of lattice constant was observed. The sample was covered with a Py layer using a recipe similar to the one for MgO/Co/Sn/Py/Si, and capped with a $10 - 20$ nm layer of Si.

Chapter 4

Characterisation of Magnetic Properties

Determining physical properties of magnetic thin films requires sensitive equipment tailored to the task. In this chapter, a brief description of the methods used for the characterisation of the magnetic properties of the grown samples is presented.

4.1 SQUID Vibrating Sample Magnetometry

A magnetometer is a device used to measure the magnetic field produced by a magnetised body. The sample is placed between a set of two coils and moved periodically. The voltage generated in the coils, resulting from a change in magnetic flux, is proportional to the magnetisation of the sample along the coils axis. High sensitivity of the Superconducting Quantum Interference Device (SQUID) magnetometer is achieved by cooling it down below the temperature at which the superconducting tunnel junction becomes superconducting. A superconducting loop is created between the pick-up and the input coils. Any small change in the flux results in a current that is detected by the coupled LRC circuit.

The magnetometery measurements of the samples discussed in this work were performed using a Quantum Design MPMS 3 SQUID magnetometer (located at Beamline I10, Diamond Light Source) which is capable of operating in the temperature range of $1.8 - 400\,\mathrm{K}$, achieving a magnetic field of $7\,\mathrm{T}$, and providing a sensitivity of $\leq 10^{-8}\,\mathrm{emu}$. The samples were mounted on a quartz rod using GE varnish.

The SQUID magnetometer was used to verify the magnetic properties of the grown samples, determine the coercive field and the value of the magnetisation at saturation. By cooling and heating the sample, the effect of temperature on the saturation magnetisation and the shape of the hysteresis loops was studied.

4.2 X-ray magnetic circular dichroism (XMCD)

For samples that consist of multiple magnetic layers the above method will give a collective response from all magnetic layers. In order to separately determine the properties of each of the magnetic layers in a multilayer sample an element sensitive measurement is required. This is possible with X-ray magnetic circular dichroism (XMCD) which makes use of a polarisation dependent absorption of the X-ray radiation by a magnetised sample.

The absorption of light by a material is determined by its energy, polarisation and the available energy transitions. By performing an energy sweep in the neighbourhood of the $L_{2,3}$ absorption edges, an X-ray absorption spectra (XAS) is obtained. In the $3d$ transition metals that are the central subject of this thesis, the $L_{2,3}$ edge corresponds to the transition from spin-split $2p_{\frac{1}{2},\frac{3}{2}}$ core states to the $3d$ valence states [45]. When the incident X-rays are circularly polarised, the probability of transition into the unoccupied valence band states is different for the left- and right-circularly polarised light. This results in two different XAS spectra depending on the polarity of a circularity polarised X-ray radiation. The difference between the two is known as the XMCD signal:

$$\mathrm{XMCD}(E) = \mu^{-}(E) - \mu^{+}(E) \tag{4.1}$$

where μ^{+}, μ^{-} are the absorption coefficients for the left- and right-circularly polarised light, respectively. If two magnetic layers in the sample are made of different magnetic elements, the magnetisation of the individual layers is recovered by examination of the XMCD at the X-ray energy associated with the $L_{2,3}$ absorption edges of that material.

In the presented research, XMCD was used to confirm ferromagnetic properties of the individual layers in a sample, and to obtain layer-specific magnetic hysteresis loops.

4.3 Ferromagnetic Resonance (FMR)

The phenomenon of ferromagnetic resonance, discussed in detail in chapter 2, occurs when a magnetised sample is subjected to a driving magnetic field whose frequency is of order of a few GHz. A magnetic field oscillating at such a high frequency can be obtained by placing a sample near a conductor with a high frequency current passing through, or by placing it in a microwave resonance cavity.

In a typical FMR experiment, a sample is placed in a static external magnetic field whose magnitude ranges between $0 - 2\,\mathrm{T}$. Additionally, an oscillating magnetic field is introduced, whose magnitude is small in comparison to its static part ($\sim 150\,\mu\mathrm{T}$), and whose frequency ranges between $0.1 - 20\,\mathrm{GHz}$. If the static magnetic field and the frequency of the microwave current are chosen appropriately the phenomenon of ferromagnetic resonance occurs. This leads to high amplitude oscillations of the magnetisation vector, and to high impedance of the waveguide. Generation and detection of microwave frequency currents is not as simple as it is at low frequencies [46]. The experimental equipment used to measure these quantities is discussed bellow.

4.3.1 Cavity Ferromagnetic Resonance (Cavity FMR)

Enhancement of the FMR signal can be obtained by placing a sample in a resonance cavity, whose geometry is tuned to coincide with the frequency of the driving magnetic field. Most commercial FMR spectrometers characterise the FMR by measuring the reflectance at a fixed band frequency. The microwave is generated by a klystron, which is connected to a metallic cavity via a waveguide. The signal reflected back from the cavity travels through the same waveguide to a detector build of a Schottky barrier diode [47]. The driving and the reflected microwaves are separated using a circulator, such that the reflected microwave does not travel back to the source. The FMR absorption spectrum is obtained by comparing the incident and the reflected signal. The signal quality (signal-to-noise ratio) can be enhanced by application of a lock-in amplifier.

In my work the cavity FMR system at IFPAN was used. The system was capable of achieving magnetic fields as high as $2\,\mathrm{T}$, and it had a fixed driving frequency of $9.38\,\mathrm{GHz}$. This allowed the measurement of the FMR signal of a

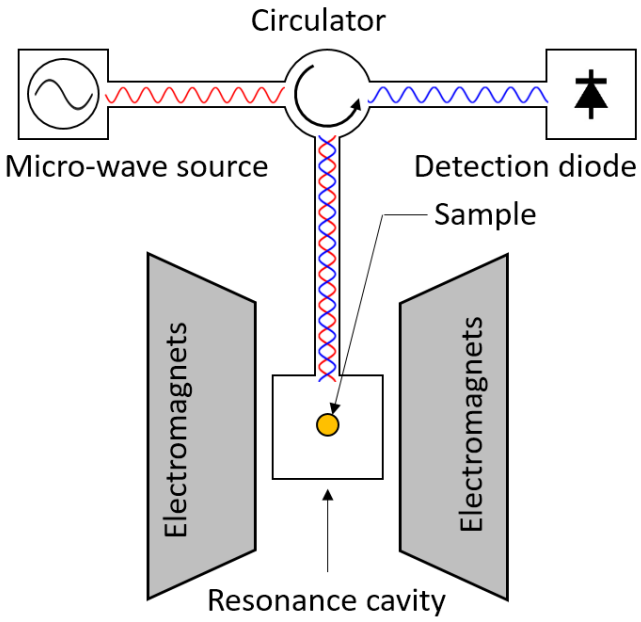

Figure 4.1: Illustration of the cavity FMR setup. A sample is placed into the microwave resonance cavity using a glass rod. Red and blue sine waves illustrate the generated microwaves and the ones reflected by the sample.

sample when an external magnetic field was oriented in either the easy- or hard-axis of magnetisation. This property was crucial for achieving a low uncertainty of the estimated anisotropy constants.

4.3.2 Vector Network Analyser Ferromagnetic Resonance (VNA-FMR)

The limiting factor of cavity FMR is the fixed value of the driving frequency. In order to perform FMR measurements for various values of the microwave frequency, a Vector Network Analyser (VNA) is used. The VNA provides a source of microwave current, and it detects the transmitted and reflected current after interaction with the device under study.

In the VNA-FMR experiment, a sample is placed on a co-planar waveguide (CPW) and inserted into a static magnetic field generated by strong electromagnets. The VNA is driving the CPW, creating an oscillating weak magnetic field in its proximity. A sweep in frequency is performed, and the impedance of the

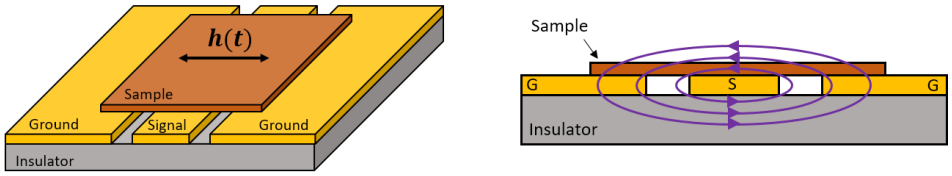

Figure 4.2: Illustration of the setup used in VNA-FMR experiments with the sample placed on the co-planar waveguide. Purple lines in the right image illustrate the magnetic field lines created by the current flowing through the signal line in the centre.

sample is measured. By placing the sample in an external magnetic field, the field-frequency absorption spectrum is obtained.

Here, the external magnetic field was provided by an octopole magnet capable of creating a magnetic field of up to 0.8 T in any direction. The sample was placed in a chamber inside the magnet that could be pumped down to ultrahigh vacuum, and cooled down with liquid nitrogen (down to 80 K) or helium (down to 20 K). The VNA allows for probing the frequency range from 0.1 to 20 GHz.

4.3.3 Time-resolved X-ray Ferromagnetic Resonance (XFMR)

A time-resolved X-ray ferromagnetic resonance (XFMR) is an element-sensitive method used to study ferromagnetic resonance in thin magnetic films. The ferromagnetic resonance is excited by placing a sample on a CPW with a microwave current passing through it. The X-ray synchrotron radiation is used to measure the amplitude of the oscillations of the magnetisation vector.

Electrons in the synchrotron storage ring are used to generate X-ray radiation by curving their trajectory using so-called insertion devices. The electrons are stored in packets which arrive at the insertion device in equal intervals at a frequency of 499.65 MHz. This results in X-rays radiation spikes: each time an electron packet travels through the insertion device, the spike lasts for up to 30 μs. Synchronising the X-ray generation with the phase of the driving magnetic field allows for stroboscopic measurements of the magnetisation vector precession in the studied sample.

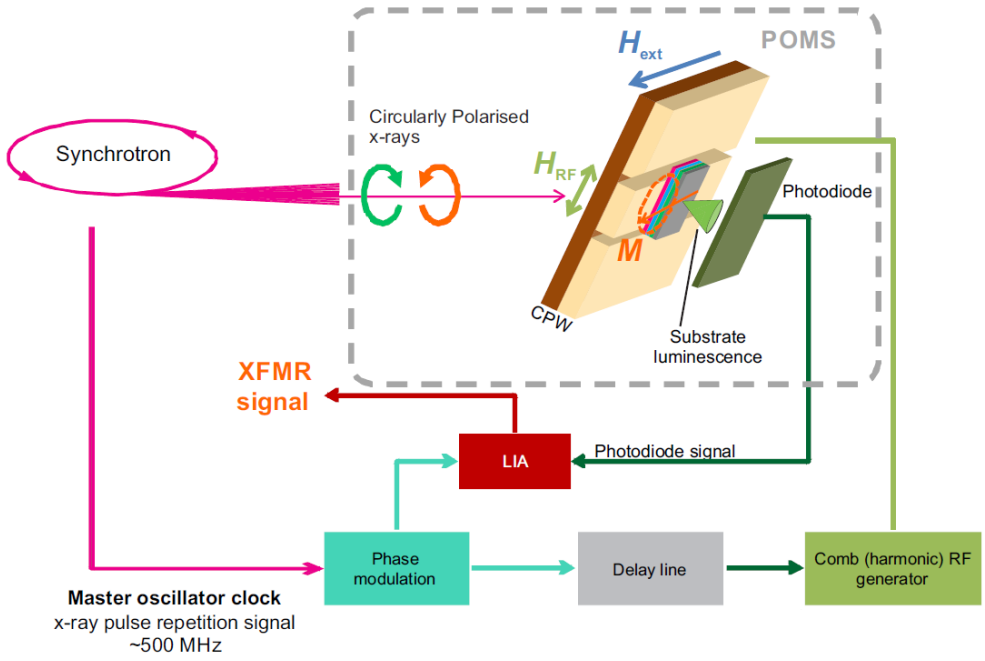

Figure 4.3: Schematic of the XFMR setup used for the layer-specific characterisation of the magnetisation dynamics of the magnetic heterostructure. Figure taken from Ref. [2].

A schematic of the XFMR setup used in the experiment is shown in Figure 4.3. The sample is placed on the CPW, and the external static magnetic field is produced by a portable octupole magnet system (POMS). The surface of the sample is illuminated with X-ray radiation trough a hole in the CPW signal line. The circularly polarised X-rays are used with their energy tuned to one of the $L_{2,3}$ absorption edges of the material under study. The exact energy value is chosen by performing the XMCD measurements and determining the energy where signal is the strongest.

The CPW signal line is powered by a micro-wave current whose frequency is a multiple of the synchrotron frequency. Higher harmonics are provided by a comb generator (Atlantic Microwave) driven by the synchrotron master oscillator. For the purpose of the conducted experiments, driving frequencies in range between $2 - 10\,\mathrm{GHz}$ were used. The phase shift between the synchrotron master clock and the micro-wave current was adjusted using a programmable delay with step resolution of $\sim 0.5\,\mathrm{ps}$. By varying the delay it was possible to take stroboscopic snapshots of the magnetic vector precession at different phases of its motion.

The absorption of the circularly polarised X-ray radiation depends on the projection of the magnetisation vector onto the beam direction, which can be decomposed into a static term and one varying with time. By taking a stroboscopic image at two time intervals, when the phase of the magnetisation vector oscillations is shifted by 180° one can dispose of the static component by taking the difference of those two measurements.

The X-ray light not absorbed by the magnetic layers is absorbed by the substrate that is chosen to have a high luminosity (such as MgO or sapphire). The intensity of the substrate lumination is registered with a diode placed behind the sample. XFMR measurements are subject to large amounts of noise. The signal is filtered using a lock-in amplifier that measures alternately the signal produced by the magnetisation vector at a studied phase of oscillation, and one shifted in phase by 180°. The switching between the two was done at the frequency of about $1\,\mathrm{kHz}$ (the frequency was optimised to minimise the signal to noise ratio).

As discussed in chapter 2, the magnetisation vector subjected to a driving magnetic field follows a trajectory that is an ellipse elongated in the direction of the driving magnetic field, which coincides with the plane of the sample and CPW.

Therefore, the highest XFMR signal is achieved when X-rays illuminate the sample at high incidence angle. Due to technical limitations, the maximal incidence angle that can be achieved with the experimental setup was 35° (all of the measurements were performed at this orientation).

A typical XFMR study consisted of multiple delay scans. Each scan was performed at fixed external conditions: excitation frequency, orientation of the external magnetic field, and its magnitude. During a single delay scan, the phase difference between the incoming X-ray pulses and the phase of the driving current was varied. By measuring the stroboscopic XMCD signal at various time delays (phase differences), the projection of the magnetisation vector onto the X-ray beam direction at different phases of its motion was registered. The delay scans were performed for different values of the external magnetic field and orientation, and for the sample held at room temperature and at 80 K.

Chapter 5

Model Fitting and Hypothesis Testing

The physical parameters of the studied heterostructures can be determined by finding a model that best describes the obtained experimental data. For example, cavity FMR measurements are used to determine the sample anisotropy constants and the electron gyromagnetic ratio, the VNA-FMR measurements are helpful in estimating the EC parameter, and the XFMR experiments give detailed information about EC and SP in the system.

Sometimes, multiple competing models can give a reasonable agreement with the measured values, and a tool to decide which of them has the best explanatory power is needed. For example, in the case of cavity FMR measurements, the models with one or two crystalline anisotropy terms can be used, and in the case of the XFMR measurements, a model with only EC or with both, EC and SP, can be used. A model with additional fitting parameters will always result in a closer fit. However, additional parameters are related to physical phenomena that may not be present in the system, and therefore it may not be justified to include them in the fitting procedure. If there is no other source of information that would indicate if a model is suitable, a statistical test can be performed to reject models, while those with high probability are not valid. In this work, the goodness of fit was measured using likelihood function and models were compared using the likelihood-ratio test (LR).

In this chapter, a brief summary of the LR test is presented, followed by the methodology used for fitting the theoretical models to the data obtained by cavity

FMR, VNA-FMR and XFMR experiments. In the case of cavity FMR, the LR test is performed to distinguish between the models with one (like for Py) and two (like for Co) anisotropy terms. In the case of XFMR, the LR test is performed to distinguish between a model that includes SP coupling, and a model that does not include SP coupling. Such a comparison allows then to determine whether the inclusion of SP is justified.

5.1 The Likelihood Ratio Test

The experimental data acquired in a measurement is subjected to noise. In an idealised situation of an unbiased measurement, a measured value can be treated as a random variable Y with probability density function $p(y)$ that has an expected value equal to the true value of an unknown parameter: $\bar{y} = \mathrm{E}[Y]$. In general, a single measurement may be described by multiple real numbers, therefore let $y \in \mathbb{R}^k$. If the probability distribution of the variable is unknown, it is customary to assume it to be a multivariate normal distribution, which has a probability density given by:

$$p(y) = \frac{1}{\sqrt{(2\pi)^k \left|\Sigma\right|}} \exp\left(-\frac{1}{2}(y-\bar{y})^T \Sigma^{-1} (y-\bar{y})\right) \quad , \tag{5.1}$$

which in case of $k = 1$ takes the form:

$$p(y) = \frac{1}{\sigma\sqrt{2\pi}} \exp\left(-\frac{(y-\bar{y})^2}{2\sigma^2}\right) \quad , \tag{5.2}$$

where Σ is the covariance matrix and σ is the standard deviation.

A measurement series y_i is a set of measurements performed for different values of the control parameters x_i (parameters that can be changed between measurements such as the magnetic field magnitude and its orientation). Here, i denotes the measurement number and $x_i \in \mathbb{R}^m$, where m is the number of control parameters. The measured values will be denoted as the vector $\boldsymbol{y}$ with components y_i, and corresponding random variables will be denoted as vector $\boldsymbol{Y}$ with components Y_i. The values of control parameters will be denoted as vector $\boldsymbol{x}$ with components x_i.

A statistical model is the mathematical model that embodies a set of statistical assumptions concerning the generation of sample data [48]. Here, obtained from the experiments. We will consider the statistical model:

$$\boldsymbol{Y} = F\left(\boldsymbol{x}, \boldsymbol{\xi}\right) \tag{5.3}$$

of the form:

$$Y_i = f\left(x_i, \boldsymbol{\xi}\right) + \epsilon_i \quad , \tag{5.4}$$

where $\boldsymbol{\xi}$ is a vector of fitting parameters, $f(x_i, \boldsymbol{\xi})$ is a real valued function representing the underlying theoretical model, and ϵ_i represent the noise terms. ϵ_i will be modelled as independent random variables with distribution $\mathcal{N}(0,\, \Sigma_i)$ and Σ_i being the covariance matrix of the i^{th} measurement. In case of $k = 1$: $\epsilon_i \sim \mathcal{N}(0,\, \sigma_i^2)$.

Having a vector of measured values $\boldsymbol{y}$ and a model (5.4) defined by parameters $\boldsymbol{\xi}$, the likelihood is computed:

$$\mathcal{L}(\boldsymbol{\xi}; \boldsymbol{y}, \boldsymbol{x}) = \prod_{i=1}^{N} p_{\boldsymbol{\xi}}(y_i; x_i) \quad , \tag{5.5}$$

where $p_{\boldsymbol{\xi}}(y_i; x_i)$ is the probability of obtaining the measurement value y_i having the best estimate of a true value given by $f\left(x_i, \boldsymbol{\xi}\right)$:

$$p_{\boldsymbol{\xi}}(y_i; x_i) = \frac{1}{\sqrt{(2\pi)^k \left|\Sigma_i\right|}} \exp\left(-\frac{1}{2}(y_i - f\left(x_i, \boldsymbol{\xi}\right))^T \Sigma_i^{-1} (y_i - f\left(x_i, \boldsymbol{\xi}\right))\right) \quad . \tag{5.6}$$

Fitting a model (5.4) to a set of measured data points is an optimisation procedure aimed at finding $\boldsymbol{\xi}$ such that the likelihood (5.5) is maximised. In the case of independent, identically distribute error terms, this is equivalent to the least square optimisation. Such a generalisation of the least square procedure is widely used [49]. Here, the optimisation was done using the conjugate gradient method [50, 51].

In this work, competing models are fitted using the method above. In the following section, a test to asses whether a more complex model is warranted is developed. Two models are considered: $\boldsymbol{Y}^0 = f^0(x, \boldsymbol{\xi}^0) + \epsilon_i^0$ (a null hypothesis) and $\boldsymbol{Y} = f(x, \boldsymbol{\xi}) + \epsilon_i$ (an alternative hypothesis), where $\boldsymbol{\xi}^0 \in \Xi^0$ and $\xi \in \Xi$, such that $\Xi^0 \subset \Xi$, i.e., model f has a broader fitting parameter space than f_0. This

is, for example, the case when two models describing the ferromagnetic resonance of coupled magnetic layers are considered: one including only a single type of magnetic layer coupling (a null hypothesis), and the other including two different types of coupling (an alternative hypothesis). The likelihood ratio test is used to compare both models:

$$\lambda_{LR} = -2 \ln \left[\frac{\sup_{\boldsymbol{\xi}^0 \in \Xi^0} \mathcal{L}(\boldsymbol{\xi}^0)}{\sup_{\boldsymbol{\xi} \in \Xi} \mathcal{L}(\boldsymbol{\xi})} \right] \tag{5.7}$$

and provide a decision criterion: if $\lambda_{LR} > C$, the null hypothesis cannot be rejected (a simpler model is preferred), while if $\lambda_{LR} < C$, the null hypothesis is rejected (a more complex model is preferred over the simple model). The threshold value C is chosen to obtain a desired significance level α:

$$P(\lambda_{LR} < C | \, \text{Null hypothesis}) = \alpha \quad . \tag{5.8}$$

P is the probability of obtaining a given value λ_{LR} smaller than C under the assumption of the null hypothesis being true.

In practice, determination of C can be easily done only for a simple model. Since the experimental values are subjected to uncertainty and can be treated as random variables, so does the resulting value of λ_{LR}. The Λ is denoting the distribution of λ_{LR}. In the present case, where $\Xi^0 \subset \Xi$, according to Wilks' theorem [52], if the number of measurements approaches infinity: $\Lambda \underset{D}{\rightarrow} \chi^2_k$. χ^2_k is the chi-squared distribution with the number of degrees of freedom k equal to the number of additional fitting parameters used for the alternative hypothesis that were not present in the null hypothesis model. Therefore, the value C can be chosen using the formula for the cumulative density function of χ^2_k to achieve a desired significance level. Alternatively, knowing the value of λ_{LR} obtained in the LR test, a corresponding significance level can be found as: $\alpha = F^k_\chi(\lambda_{LR})$ with F^k_χ being the cumulative distribution function of the χ^2_k distribution.

Pinheiro and Bates (2000) showed that the true distribution of this likelihood ratio χ^2 statistics could be substantially different from the naive χ^2 – often dramatically so [53]. We generated a sample of values from the Λ distribution, and validated that the χ^2_k distribution is a good approximation. Details of the procedure are explained in the following example 5.1.1.

It is noted that the LR test cannot validate a given alternative hypothesis. It can only reject a null hypothesis when tested against the alternative hypothesis. This is true in general: no test exist that could definitively confirm whether or not a given model is a proper description of the observed phenomena [54]. The validity of the model can be authenticated by performing several measurement series testing the dependence on all of its parameters. Additionally, a model can be tested against other sensible proposals to determine whether it provides the best description of the observed measurements.

5.1.1 Example

A simple example is presented to provide a more intuitive introduction to the concept of LR tests. Consider a statistical model describing the distribution of measurements given by:

$$y_i = 2x_i^2 + 0.25 + \epsilon_i \quad \text{where} \quad \epsilon_i \sim \mathcal{N}(0,\, \sigma^2) \quad . \tag{5.9}$$

A set of measurements y_i is obtained for the measurement points $x = \{0.1, 0.2, ..., 0.9\}$. Two cases are presented: $\sigma_L = 0.25$ and $\sigma_S = 0.025$. For the external observer, the underlying theoretical model is an unknown and two hypothesis are tested: a linear model described as $y^0(x) = ax + b$ (a null hypothesis) and an alternative model $y(x) = ax^2 + bx + c$. For the purpose of the example it is assumed that σ is known to the observer (for example the measurement uncertainty). By preforming the optimisation procedure, values of the parameters (a, b, c) maximising the likelihood for each case are determined. The results are shown in Figure 5.1. For the respective cases, the LR is evaluated to be:

$$\lambda_L = 0.42 \quad \text{and} \quad \lambda_S = 181.80 \quad . \tag{5.10}$$

Those λ values by itself do not determine if the null hypothesis can be rejected. Instead, a threshold value C or a significance level α must be estimated. According to Wilks' theorem, the distribution of λ_{RL} is given by the χ^2_1 distibution (in this case $3 - 2 = 1$). To show that this is indeed true, a hypothetical measurement

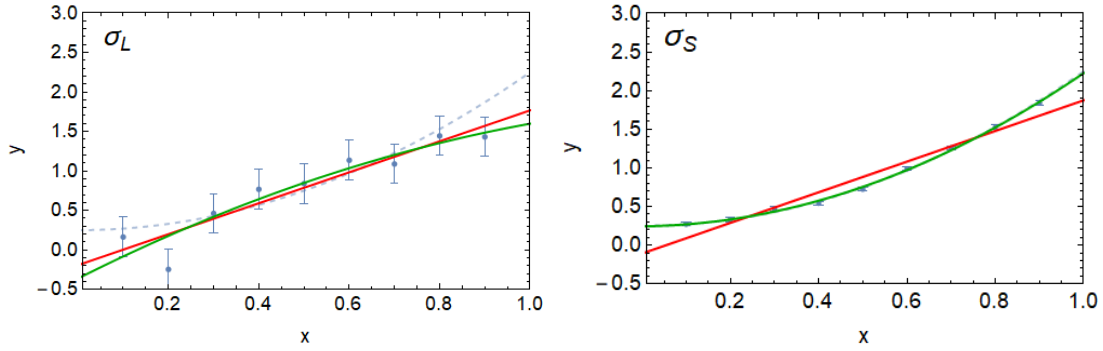

Figure 5.1: Null (red) and alternative (green) hypothesis models fitted to the observed data. The graph on the left shows the case where the error is given by the normal distribution with σ_L and on the right with σ_S. The true dependence given by $2x^2 + 0.25$ is marked with a dashed line.

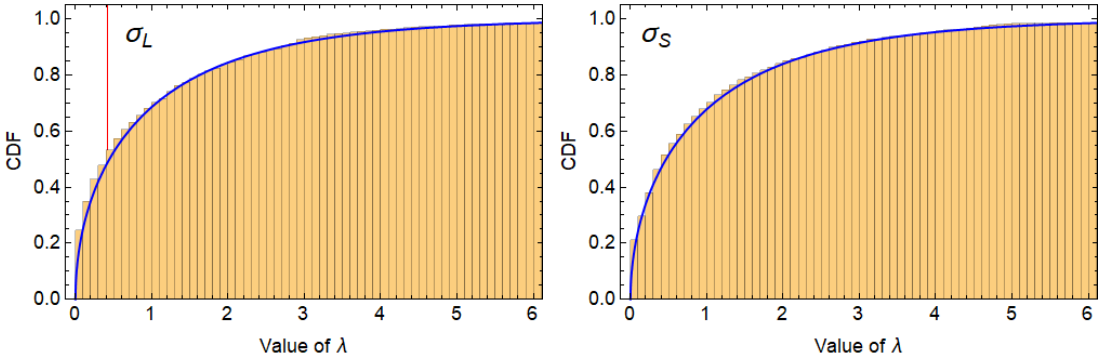

Figure 5.2: The cumulative probability distribution of the LR under the assumption that the null hypothesis is true for the data obtained from the model (5.9). The case of σ_L is shown on the left and σ_S on the right. The respective values of the LR obtained in the test are indicated by the red vertical lines. In the second case, the LR value is outside of the horizontal axis range. The fitted χ^2 distribution is represented by the blue solid line.

series y'_i is generated using the model described by the null hypothesis with fitted values of $\boldsymbol{\xi}$:

$$y'_i = y_i^0(x) + \epsilon_i \quad \text{where} \quad \epsilon_i \sim \mathcal{N}(0,\, \sigma^2) \quad . \tag{5.11}$$

For this measurement series, the above procedure is repeated and the likelihood ratio is evaluated. By performing this procedure multiple times, the probability distribution of the possible likelihood ratios is obtained. Having generated the sample, a χ^2 distribution is fitted with the number of degrees of freedom being the fitting parameter.

With this information, the chance of obtaining a value which is at most the same as the achieved likelihood ratio for the true measurement series under the assumption that the null hypothesis is true, can be determined. For the presented examples, the obtained significance levels are 49% in the case of $\sigma = 0.25$ and effectively 100% in the case of $\sigma = 0.025$. In both examples the fitted χ^2 distribution was close to χ^2_1 ($\chi_{0.99}$ and $\chi^2_{1.01}$ in the respective cases). This shows that for the measurements that had low uncertainty, the null hypothesis, stating that the data was obtained from a system described by a linear model, is invalid. Such a conclusion cannot be, however, made when analysing the data for which the measurement uncertainty is high (the null hypothesis cannot be rejected).

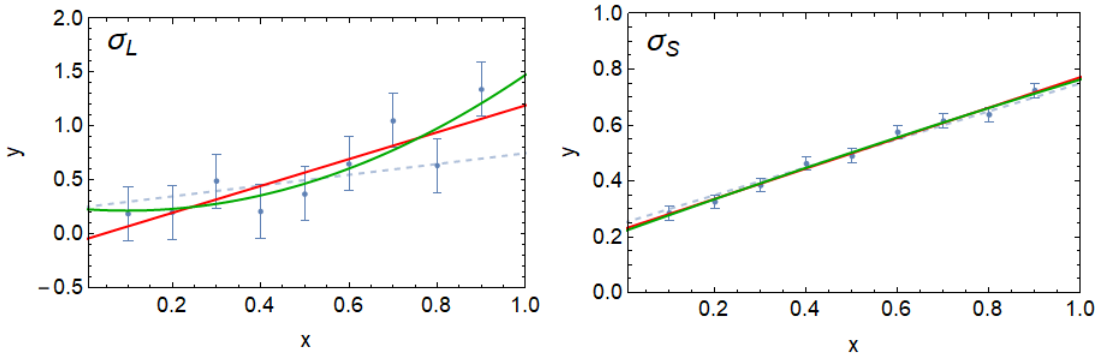

Figure 5.3: Null (red) and alternative (green) hypothesis models fitted to the observed data. The graph on the left shows the case where the error is given by the normal distribution with σ_L and on the right with σ_S. The true dependence given by $0.5x + 0.25$ is marked with a dashed line.

An alternative case is considered, where the system is described by:

$$y = 0.5x + 0.25 + \epsilon \quad \text{where} \quad \epsilon \sim \mathcal{N}(0,\, \sigma^2) \quad , \tag{5.12}$$

and the procedure described above is repeated by considering the same two hypothesis. The resulting significance levels are 71% and 24%, respectively. Both are too low to reject the null hypothesis, which in this case is the correct one. Therefore, it is not justified to include an additional x^2 term when modelling such a measurement series.

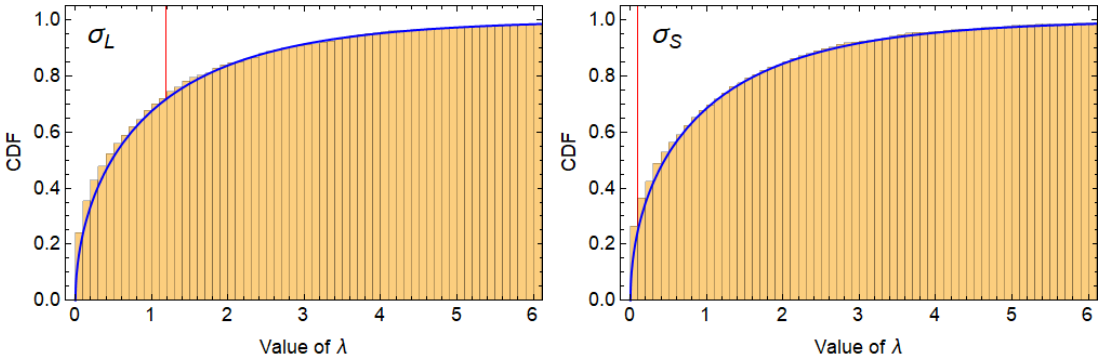

Figure 5.4: The cumulative probability distribution of the LR under the assumption that the null hypothesis is true for the data obtained from the model (5.12). The case of σ_L is shown on the left and σ_S on the right. The respective values of LR obtained in the test are indicated with the red vertical lines. The fitted χ^2 distribution is shown by a blue line.

When the LR test is applied to the real data, the terms like x^2 in the alternative hypothesis model can be related to a specific physical phenomenon. With help of the LR test, one can show that the model not including such terms is sufficient, and the validity of the alternative hypothesis can be doubted. Examples of applying the LR test to FMR experimental data are discussed below.

5.2 The Cavity FMR Model Fitting

The raw data obtained from the cavity FMR experiments include the absorption spectra of microwaves for a fixed frequency of the driving current in dependence on the magnetic filed strength at a given magnetic field orientation. The data is used to determine the magnitude of the resonance magnetic field, and to plot its dependence on the field orientation. In theory, the absorption spectra should resemble the dependence given in Equation (2.87), yet in experiments, due to the imperfections in the measurement equipment, this is rarely the case.

In order to extract the magnitude of the resonance magnetic field from the measured data, a Lorentzian function is used:

$$L(B; B_0, \Delta B) = \frac{1}{\pi} \frac{\Delta B/2}{(B - B_0)^2 + (\Delta B/2)^2} \quad , \tag{5.13}$$

as well as its counterpart in the Kramers-Kronig relations:

$$D(B; B_0, \Delta B) = \frac{1}{\pi} \frac{B - B_0}{(B - B_0)^2 + (\Delta B/2)^2} \quad . \tag{5.14}$$

The linear combination of the above, with the addition of a bias A_3, is fitted to the data:

$$I(B; B_0, \Delta B) = A_1 L(B; B_0, \Delta B) + A_2 D(B; B_0, \Delta B) + A_3 \tag{5.15}$$

with respect to A_1, A_2, A_3, B_0, and ΔB. The parameter ΔB describes the width of the resonance peak, the A_1 and A_2 factors describe the magnitude of symmetric and asymmetric components, respectively. The value of the resonance magnetic field B_0 resulting from the fitting of Equation (5.15) is expected not to deviate much from the true value, however, it can depend on the quality of the measured data. The uncertainty of the B_0 estimation is taken to be equal to the fitted value ΔB (approximately the half-with at the half-maximum).

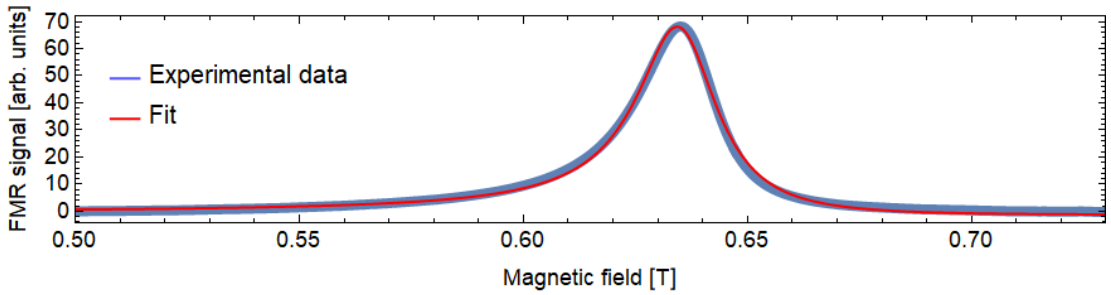

Figure 5.5: FMR absorption in dependence on the magnetic field acquired in the cavity FMR experiment at a driving frequency of 9.38 GHz and a magnetic field orientation of $\theta_H = 10°$ in blue, along with the fitted model (5.15) in red. The values of the fitted parameters: $B_0 = (635.21 \pm 0.02)$ mT, $\Delta B = (21.82 \pm 0.05)$ mT, $A_1 = 2.343 \pm 0.004$, $A_2 = -0.396 \pm 0.004$, $A_3 = -0.723 \pm 0.013$.

Knowing the value of the resonance magnetic field B_0 in dependence on the magnetic field orientation, a theoretical dependency (2.82) can be fitted to the

data with respect to the anisotropy constants D_1, D_2 and the gyromagnetic ratio γ. It is assumed that damping (α) is low and that it does not influence the value of the resonance magnetic field significantly. Depending on the sample studied, D_1 or both, D_1 and D_2, may be required to sufficiently describe the experimental data. The number of terms required for a sample is determined using the LR test.

An example are measurements done for Co at $T = 80\,\mathrm{K}$. A null hypothesis, stating that a single D_1 term is satisfactory, is tested against an alternative hypothesis, stating that both terms D_1 and D_2 are required. Figure 5.6 shows the obtained results. The values of the fitted parameters for the alternative hypothesis

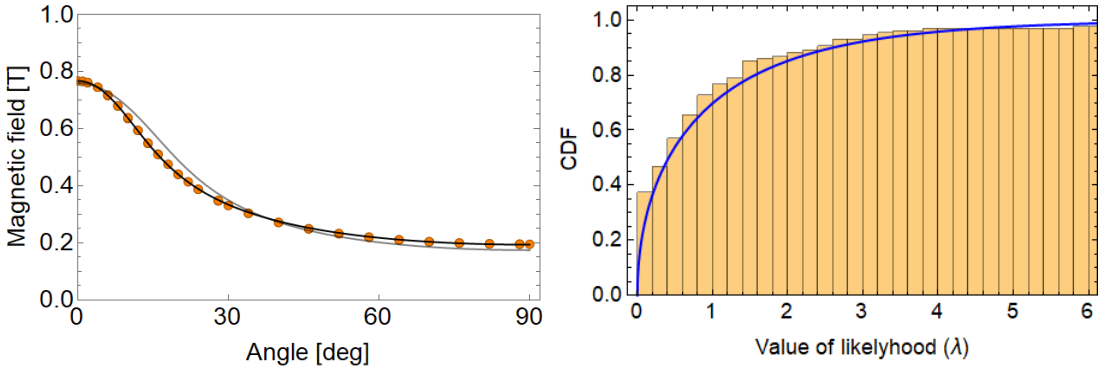

Figure 5.6: Experimental data (orange circles) for the Co sample at $T = 80\,\mathrm{K}$ together with model fits. The null hypothesis was marked by a semi-transparent black line, alternative hypothesis with black line. The cumulative probability distribution of LR under the assumption, that null hypothesis is true, is shown on the right plot. The obtained value LR (5.18) is far to the right of the plot range.

are:

$$\begin{aligned} D_1 &= (-0.3190 \pm 0.0012)\,\mathrm{T}, \\ D_2 &= (-0.1330 \pm 0.0013)\,\mathrm{T}, \\ \gamma &= (234\,900 \pm 200)\,\frac{\mathrm{rad}}{\mathrm{T}\cdot\mathrm{s}}, \end{aligned} \tag{5.16}$$

and for the null hypothesis they are:

$$D_1 = (-0.4332 \pm 0.0045)\,\mathrm{T}, \quad \gamma = (227\,300 \pm 2\,100)\,\frac{\mathrm{rad}}{\mathrm{T}\cdot\mathrm{s}} \quad . \tag{5.17}$$

The log-likelihood of the alternative hypothesis is 228.6 ± 0.4, and that of the null hypothesis: $-1\,072 \pm 55$, giving the likelihood ratio of:

$$\lambda_{LR} = 2\,602 \pm 110 \quad . \tag{5.18}$$

The uncertainty of the log-likelihoods and the likelihood ratio were calculated using error propagation, based on the mean value of the fitted parameters and their covariance matrix.

The obtained value of the LR was compared with the LR probability distribution. The LR distribution was found numerically assuming the null hypothesis, generating a hypothetical measurement result, and testing both the null and the alternative hypothesis against the artificially created experimental data. The procedure was repeated 128 times resulting in a histogram shown in the Figure 5.6. The χ^2 distribution was fitted to the data with respect to the number of degrees of freedom, resulting in a value of 0.95 (which is sufficiently close to 1, as predicted by Wilks' theorem).

It is concluded that in the present case, the null hypothesis is rejected and inclusion of the second term D_2 is required, with the obtained significance level of $1.0 - 0.6 \times 10^{-567}$ which is effectively equal to 100%. This is in an agreement with the accepted view that the description of the HCP Co anisotropy requires at least two trigonometric expansion terms.

5.3 XFMR Model Fitting

In an XFMR experiment, delay scans are performed for different external conditions: the magnetic field strength, its orientation, and the sample temperature. The change in the delay results in a change in phase between the driving magnetic field and the incoming X-ray pulses. The magnitude of the XFMR signal is a sinusoidal function of the delay, its amplitude is the strength of the XFMR signal, and its phase is the phase of the magnetic vector oscillations with respect to driving magnetic field.

Both values, amplitude and phase, can be recovered from the measured XFMR delay scans by fitting a sinusoidal function to the obtained data (Figure 5.7). Such

fitting can be done in several ways, in this work by using the function:

$$\mathrm{XFMR}(\phi) = A\sin\phi + B\cos\phi \tag{5.19}$$

is fitted with respect to the parameters A and B, which are related to the XFMR signal amplitude and phase by:

$$I_{\mathrm{XFMR}} = \sqrt{A^2 + B^2}, \quad \tan\left(\phi_{\mathrm{XFMR}}\right) = B/A \quad . \tag{5.20}$$

As the two parameters are fitted, the uncertainty of the parameter estimation of A and B is given by a covariance matrix. Here, the covariance matrix was characterised by close to zero off-diagonal terms. This shows that noise associated with the A and B variables is uncorrelated.

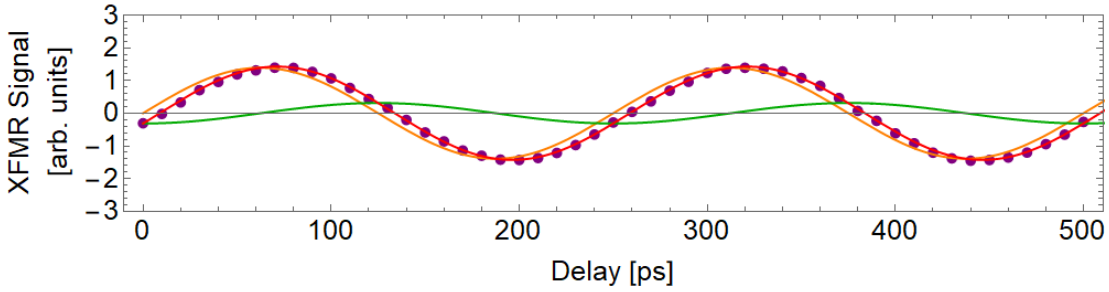

Figure 5.7: XFMR measurements for various values of delay (purple points) together with the fitted sinusoidal function (red). Green and orange graphs represent the sine and cosine components of the fitted model (5.19). The measurements were performed on a 10 nm thick Co sample at a driving frequency of 4 GHz, the magnetic field oriented in-plane ($\theta_H = \pi/2$), a magnetic field strength of $B = 13\,\mathrm{mT}$, and the sample held at a temperature of $T = 80\,\mathrm{K}$. The values of the fitted parameters are: $A = 1.391 \pm 0.007$, $B = -0.313 \pm 0.007$.

A measurement series was obtained by performing the delay scans for different values of the external magnetic field strength under a fixed magnetic field orientation. By fitting Equation (5.19) to each delay scan, the dependence of A and B on the external magnetic field was obtained. Using Equation(5.20), the amplitude and phase of the XFMR signal was recovered.

I_{XFMR} and ϕ_{XFMR} can be modelled using Equation (2.138) (or Equation (2.92) in case of single magnetic layer), however, this has several drawbacks. In particular the uncertainty of the phase estimation has a bigger impact when the value of

the amplitude is higher, and the uncertainties of found I_{XFMR} and ϕ_{XFMR} are correlated. Instead, the theoretical model was rearranged to express the values of (A, B) as a function of the fitting parameters, and such a model was optimised to fit the experimental (A, B) data (see Figure 2.19).

The fitting procedure makes use of the conjugate gradient optimisation algorithm, maximising the likelihood of the model. For the heterostructures composed of a pair of magnetic layers, two hypotheses are considered: a null hypothesis stating that the EC coupling is the only coupling present in the system, and an alternative hypothesis, stating that both, EC and SP, are relevant. The hypotheses are compared using the LR test to determine if the null hypothesis (only EC) can be rejected.

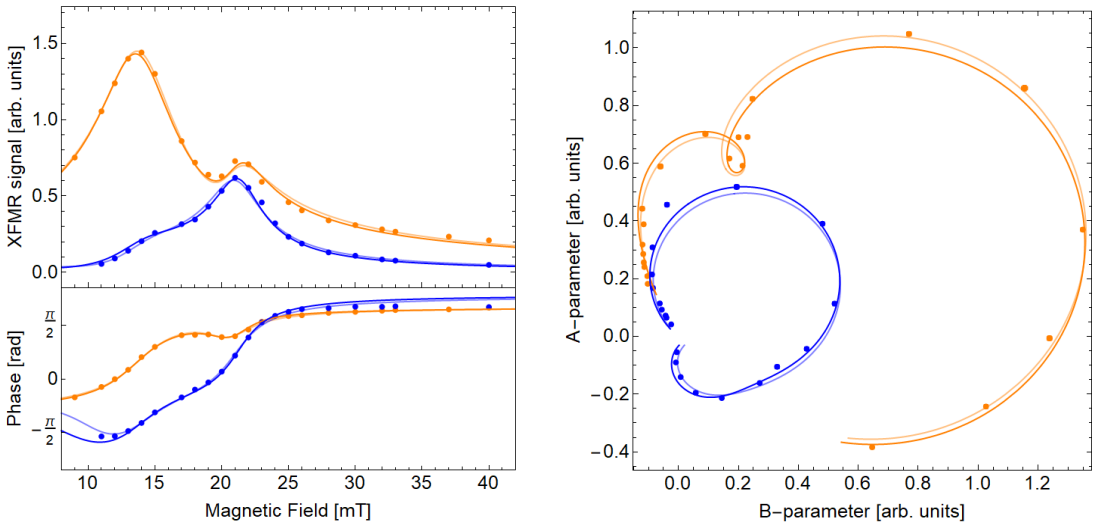

Figure 5.8: Amplitude and phase (left), and the in- and out-of-plane components of the XFMR signal (right) for Co/MgO/Py (S1655_II introduced in chapter 6) measured at room temperature, with the magnetic field oriented in-plane of the sample. The XFMR measurement data are represented by points (orange for Co, and blue for Ni). The fitted models are shown by solid lines, whereby the alternative hypothesis is represented by an opaque line, and the null hypothesis by a semi-transparent line.

Example results are shown in Figure 5.8, where both the null hypothesis model (only EC) and the alternative hypothesis model (EC and SP are both included) are presented. The difference between the quality of the fit for the two models is

visible, yet it is hard to judge if the alternative hypothesis model is sufficiently better than the null hypothesis. The LR test is used to resolve this issue. The resulting log-likelihoods are -231 for null hypothesis, and 57 for the alternative hypothesis. The LR is evaluated to be:

$$\lambda_{LR} = 577. \tag{5.21}$$

The value of the obtained LR is compared with the probability distribution of the LR values. It was verified that in this case, the distribution asymptomatically approaches the χ^2_1 distribution. The probability distribution is estimated creating a new set of data assuming the null hypothesis is true and using uncertainty covariance matrix as obtained for the values A and B. For the new data, both the null hypothesis and the alternative hypothesis models are fitted. This procedure is repeated 320 times and the likelihood ratio for each data set is evaluated. The χ^2 distribution is fitted to the sample of the likelihood ratio estimates. It was found that the value of $\lambda_{LR} = 577$ gives a significance level of effectively 100%.

Concluding, the alternative hypothesis model sufficiently improves on the null hypothesis model. This indicates that SP may be present in the system as the addition of this parameter significantly improves the fit quality, as suggested by the appropriate statistical testing.

Chapter 6

Classical Insulators

In this chapter, magnetic tunnel junctions (MTJs) consisting of two ferromagnetic layers separated by an insulating non-magnetic spacer are discussed. The role of the insulating layer is to physically separate magnetic layers that otherwise would be directly coupled by the inter-atomic exchange interaction [55]. The thickness of the spacer is kept small enough to still allow for some coupling between the magnetic layers. One way the magnetic layers can interact with each other is when current is being passed through the sample. Electrons become spin polarised when passing through the first magnetic layer, and by tunnelling through the insulating barrier, they exert a spin transfer torque on the other magnetic layer (Figure 6.1). The efficiency of the tunnelling depends on the relative orientation of the layers' magnetisation, known as a magnetoresistive effect. The resistance of the MTJ is smallest when the ferromagnetic layers are oriented in the same direction, and highest when they are opposite.

Magnetic tunnel junctions have attracted attention due to their applications in the spin-based electronics. Research was focused on fabricating devices with large tunnelling magnetoresistance ratio (TMR), which was predicted to reach over 1000% for iron based junctions [5]. The experiments resulted in lower but still impressive values: 180% was reached at room temperature for Fe/MgO/Fe MTJs [11], and 410% for Co/MgO/Co MTJs [56]. The MgO insulator was found to provide high efficiency in the conservation of the spin of tunnelling electrons. The interfacial effects at the FM/MgO interface lead to spin filtering, and allow for high TMR values even with low spin polarization in the individual magnetic

layers [55].

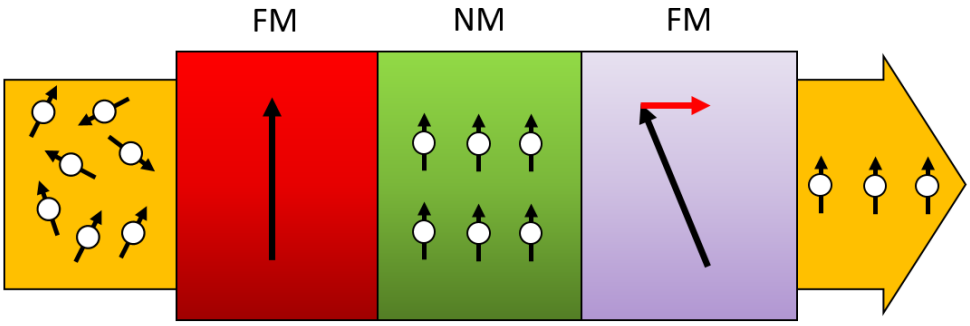

Figure 6.1: Illustration of spin dynamics in a MTJ when current flows through the junction. The electrons spins become polarised in the first magnetic layer (left), tunnel through the non-magnetic insulating barrier, and exert torque on the other magnetic layer (right).

No external current source is needed to obtain spin current coupling across the insulating barrier. When a ferromagnetic layer is at resonance, it radiates spin polarised current. This current may reach a neighboring magnetic layer and exert torque on it. This exotic type of coupling is usually weak and hard to distinguish from the Heisenberg-like exchange coupling between layers. With little research done in this area, we have designed special samples, and employed advanced theoretical and experimental techniques, to estimate the influence of spin-current coupling on the dynamics of MTJs.

The magnetic materials for the engineered samples were chosen such that each of the magnetic layers is made of elements not present in the other magnetic layer. This restriction allows for the independent measurement of the magnetisation of each layer using an element-sensitive method, such as XMCD or XFMR. Py was chosen for one of the layers as its properties do not vary with temperature. Py is also easy to grow and its deposition can be precisely controlled. Co was used as the second magnetic layer. This material exhibits strong uniaxial anisotropy with its value dependent on the sample temperature. Heating or cooling of the sample results in the change of the Co layer parameters, and in turn provides an opportunity to study heterostructures with various anisotropies of one magnetic layer, while maintaining the properties of the other magnetic layer (Py). The

magnets were separated by an insulating MgO layer whose thickness was varied between samples.

6.1 Initial studies

In order to provide evidence for magnetic layer coupling in the proposed MTJs, two extreme cases were tested first. Samples were grown with MgO layer thicknesses of 2 nm and 10 nm (refereed to, respectively, as S1644_I and S1644_II). It was expected that a 10 nm thick insulating barrier will prevents current tunneling between the magnetic layers and effectively fully decouple them. The minimal thickness of 2 nm was imposed by the MgO growth dynamics. During the initial growth of the MgO on the Co layer, the MgO does not provide a full layer coverage. If the material deposition is stopped with the expected layer thickness of 1 nm or less, one can anticipate holes in the MgO structure and direct contact between the adjacent Co and Py films. This would be a highly unfavorable situation. Therefore, a layer thickness of 2 nm was chosen to assure a continuous MgO layer separating Co from Py.

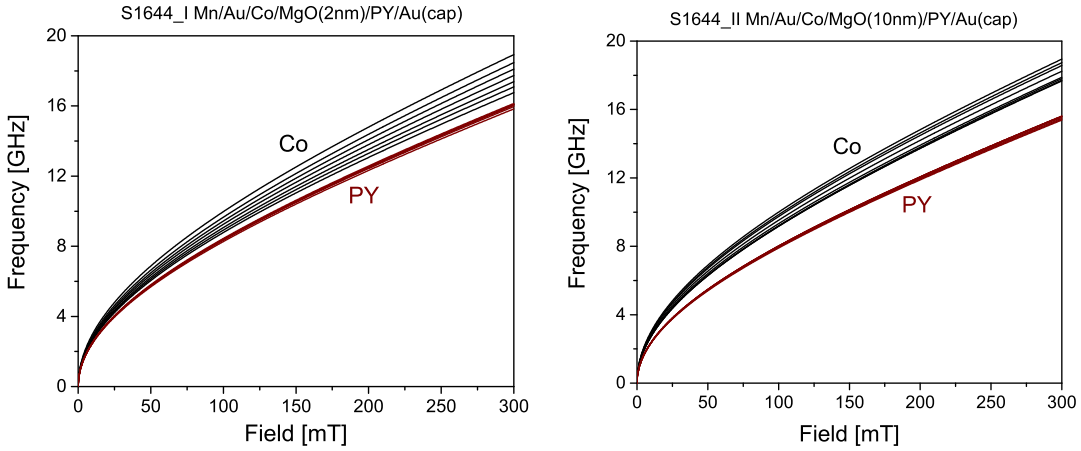

Figure 6.2: Resonance curves depending on temperature for samples with 2 nm (left) and 10 nm (right) MgO barriers. The Py characteristics do not change with temperature. For a fixed value of the magnetic field, the Co resonance frequency decreases with decreasing temperature. Measurements done at temperatures (starting from the top curve): 332 K, 284 K, 247 K, 214 K, 184 K, 148 K, 112 K.

The samples were grown using the recipe described in chapter 3.4.4, and characterised using RHEED, XRD, XRR (Figure 6.3), and TEM. Basic characterisation of the magnetic properties was done using VNA-FMR (Figure 6.2) and SQUID (Figure 6.4). The resonance curves were measured with the external magnetic field oriented in-plane of the sample for specimen temperatures in the range between 112 K and 332 K. It was observed that the change in the sample temperature mostly affects the Co layer, whose resonance frequency decreases with decreasing temperature. This effect is not equal between the samples. It seems reasonable to assume that in case of the sample with thick MgO layer the decrease in the Co resonance frequency is caused only by the change in its anisotropy. A stronger effect for the sample with thin MgO spacer would indicate the presence of an interaction between the magnetic layers. The interaction seems to be temperature dependent and strongest at low temperatures. This coincides with the spin-current transport properties as it is expected that electron tunneling will be more effective when temperatures are low.

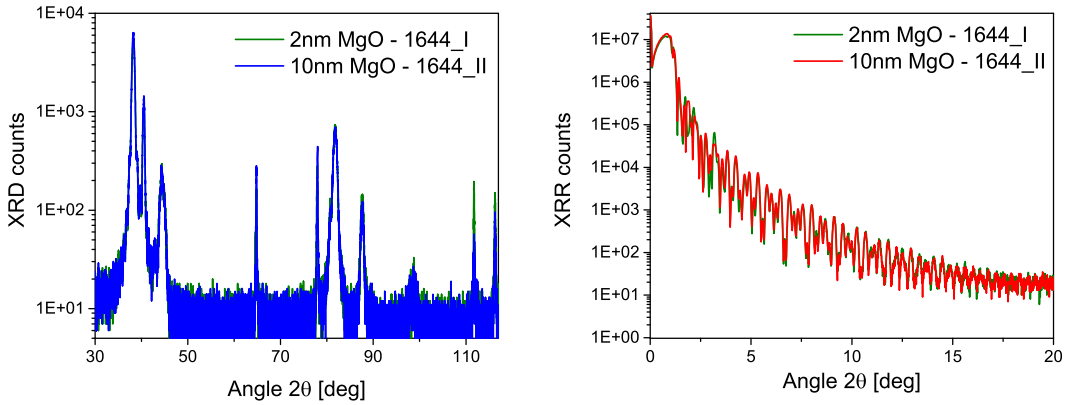

Figure 6.3: XRD (left) and XRR (right) measurements of the S1644_I and S1644_II samples.

For a heterostructure consisting of two magnetic layers, the measured hysteresis loops are a superposition of the response of the individual magnetic layers. As the coercive field is different for the Co and Py layer, the resulting hysteresis loop has multiple inflection points (Figure 6.4). The difference in the qualitative behaviour is noticed between a sample with 2 nm and 10 nm thick MgO layer. The

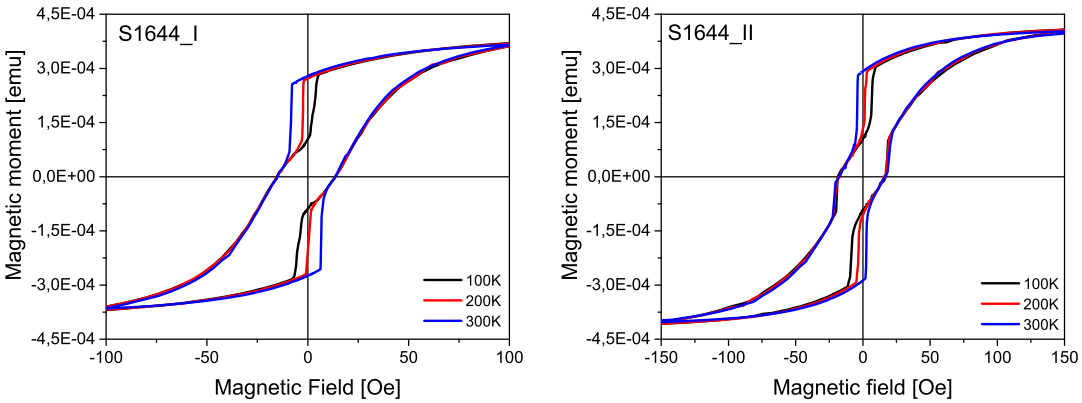

Figure 6.4: Magnetic Hysteresis curves at 100 K, 200 K, and 300 K (room temperature) for the S1644_I (left) and S1644_II (right) samples, respectively

Material	S1655_I	S1655_II	S1656_II
Co	8.6 ± 0.8 nm	9.2 ± 1.2 nm	4.2 ± 0.9 nm
MgO	1.4 ± 0.8 nm	1.4 ± 0.8 nm	2.5 ± 0.8 nm
Py	5.4 ± 0.8 nm	4.6 ± 1.0 nm	4.4 ± 1.0 nm

Table 6.1: Thickness of the individual layers estimated from the TEM images (See Figure 6.5)

.

shape of the hysteresis loops is dependent on temperature, presumably this is the consequence of the temperature dependent properties of the Co layer.

Initial research showed promising results, which motivated further and more detailed studies. The sample growth process was optimised and additional samples with a 1.5 nm MgO layer were fabricated (referred to as S1655_I, S1655_II, and S1656_II). The samples were characterised using XRR, XRD, TEM, SQUID, Cavity FMR, VNA-FMR, and XFMR. The strength and type of the interaction between the layers was determined by comparing the obtained XFMR data with the theoretical model for a system coupled by EC and SP interactions.

6.2 Cavity FMR measurements

The initial characterisation of the magnetic properties of the sample was performed using cavity FMR at a driving frequency of 9.38 GHz. The microwave absorption

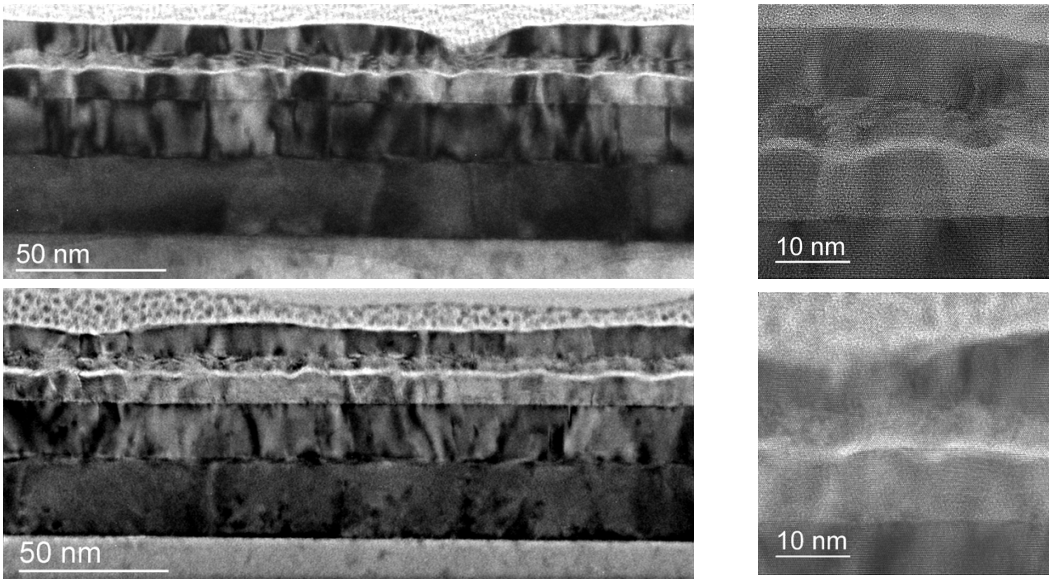

Figure 6.5: TEM images of the S1655_I (top) and S1655_II (bottom) samples.

was measured as a function of the magnetic field strength at multiple magnetic field orientations, at room temperature (∼300 K) and at 80 K. For samples that consist of two magnetic layers, the resulting absorption spectrum is composed of two overlapping resonance absorption peaks. The values of the magnetic field corresponding to each resonance were found by approximating each of the resonance peaks using a Lorentzian function:

$$f(B) = \sum_{i=1,2} A_i \frac{\Delta B_i}{\Delta B_i^2 + (B - B_i)^2} + C_i \frac{(B - B_i)}{\Delta B_i^2 + (B - B_i)^2} \tag{6.1}$$

and by fitting such a model to the data, where $A_{1/2}$ and $C_{1/2}$ are the amplitude of the symmetric and asymmetric part of the resonance peak, $\Delta B_{1/2}$ is the resonance half-width, $B_{1/2}$ is the value of the resonance magnetic field, and the subscripts label the resonance peaks. An example of the experimental data, together with the fitted Lorentzian model, is shown in Figure 6.6.

The cavity FMR measurements were repeated for the magnetic field orientation in the range between 0° (out-of-plane) and 90° (in-plane). The Lorentzian model is fitted, and the resonance magnetic fields are found for each measurement. The resulting dependence of the magnetic resonance field on the field orientation can be compared to the theoretical model. Fitting the theoretical dependence can be

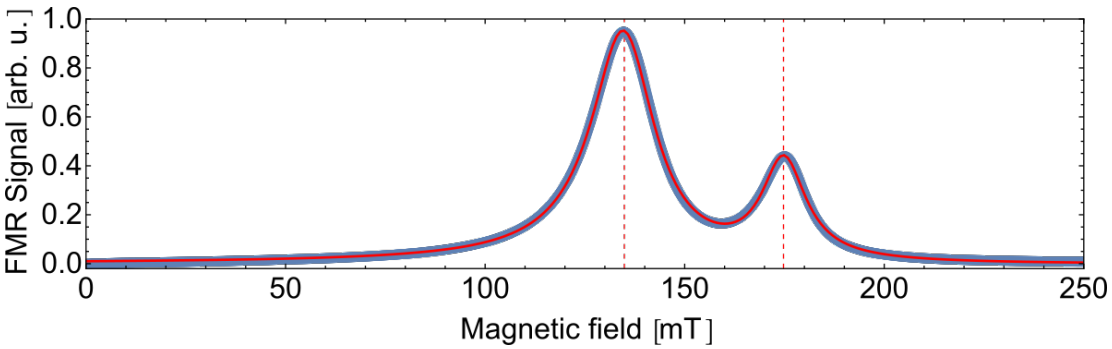

Figure 6.6: Strength of the FMR microwave absorption in dependence on the external magnetic field magnitude. Measurements are marked in blue, the fitted curve in red. Vertical dashed lines mark found resonance peaks position at: 135 mT, 175 mT.

troublesome as there are multiple parameters that are unknown: the anisotropy constants, the gyromagnetic ratios, and the strength of the coupling between the magnetic layers. Additionally, the model parameters are correlated (similar theoretical dependence can be obtained for very different parameter values; the change in the value of one parameter can be partially compensated by change in the value of the other parameters). Reference values for the parameters, such as crystalline anisotropy, can be found in the literature [57], yet it is known that in thin films, the interfacial effects can influence the effective value of those parameters [58].

More reliable values are obtained by studying additional samples with the same structure as the S1655 samples, but with only one magnetic layer (Al_2O_3/Mo/Au-/Co/MgO/Au and Al_2O_3/Mo/Au/MgO/Py/Au). The samples were studied using cavity FMR and the theoretical model for a single magnetic layer system was fitted (Figure 6.7). Good agreement between the theoretical model and the experimental data was obtained for the 5 nm sample of Co and Py. It has proven sufficient to use a single crystalline anisotropy term to describe the results for the Py layer. In the case of the 5 nm Co layer, two hypothesis were tested: one assuming a single anisotropy term, and the second, including two anisotropy terms. The validity of the two models was compared using the likelihood ratio test which showed that the model with a single anisotropy term is insufficient, and two terms should be used instead. The resulting values are shown in Table 6.2.

Sample	Temp.	γ [m/(s · A)]	D_1 [T]	D_2 [T]
Co(10 nm)	300 K	$255\,800 \pm 2\,200$	-1.134 ± 0.039	-0.298 ± 0.039
Co(10 nm)	80 K	$238\,600 \pm 1\,600$	-1.052 ± 0.030	-0.238 ± 0.032
Co(5 nm)	300 K	$240\,170 \pm 280$	-0.634 ± 0.003	-0.102 ± 0.003
Co(5 nm)	80 K	$234\,610 \pm 180$	-0.320 ± 0.002	-0.133 ± 0.002
Py(5 nm)	300 K	$232\,350 \pm 290$	-0.665 ± 0.002	—
Py(5 nm)	80 K	$231\,380 \pm 170$	-0.709 ± 0.001	—

Table 6.2: Theoretical model parameters fitted to the Cavity FMR data for the samples with a single magnetic layer.

The model fit was not optimal for the 10 nm thick Co sample, where some discrepancies between the theoretical model and the experimental data were observed. The modelled magnetic resonance field values are too high near the in-plane ($\theta_H = 90°$) and out-of-plane ($\theta_H = 0°$) magnetic field directions, with the discrepancy being larger for the sample at room temperature. Additional, the fitted value of the gyromagnetic ratio γ_{Co} is very high and seemed to be non-physical. The result suggests that at this thickness of the Co layer, its anisotropy can no longer be approximated as being uniaxial. This is possibly caused by the 10 nm Co layer being a mixture of the HCP and FCC crystalline phases. In that case, the crystalline anisotropy of the Co layer should be modelled as a mixture of uniaxial and cubic anisotropy. Inclusion of the cubic anisotropy terms leads to an energy dependence of the azimuthal orientation of the magnetisation vector that is beyond the scope of the theoretical model introduced in chapter 2. A work-around will be used in later studies where a good approximation of the sample anisotropy is required.

Having data for each of the magnetic layers, it is possible to study how the exchange coupling affects the resonance magnetic field for a sample with two magnetic layers. A hypothetical sample is considered consisting of 5 nm Co and 5 nm Py with the anisotropy parameters as in table 6.2. It is found that the introduction of EC results in a shift in value of the resonance magnetic field towards the lower values. For the magnetic field oriented out-of-plane ($\theta_H = 0°$), the difference resonance field for both layers decreases with increase in the value of j. For the magnetic field oriented in-plane ($\theta_H = 90°$), the difference in resonance field increases with increasing j value.

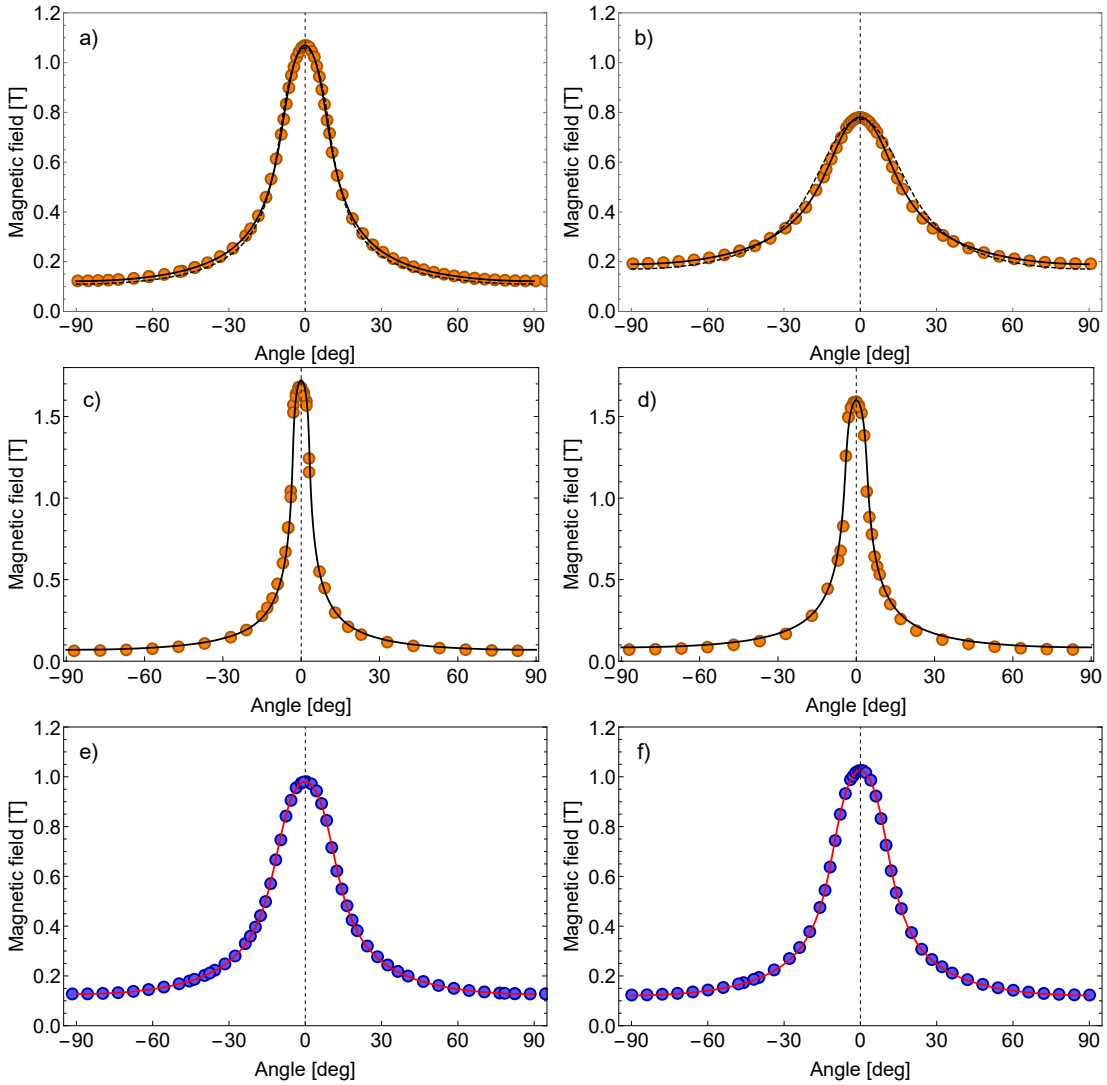

Figure 6.7: Magnetic resonance field as a function of the magnetic field direction (θ_H) for: 5 nm Co sample at (a) 300 K and (b) 80 K, 10 nm Co sample at (c) 300 K and (d) 80 K, and 5 nm Py sample at (e) 300 K and (f) 80 K, 10 nm. The fitted theoretical dependence is represented by solid black lines. In case of the 5 nm Co sample, additionally, a fitted model with a single anisotropy term is shown by a dashed line.

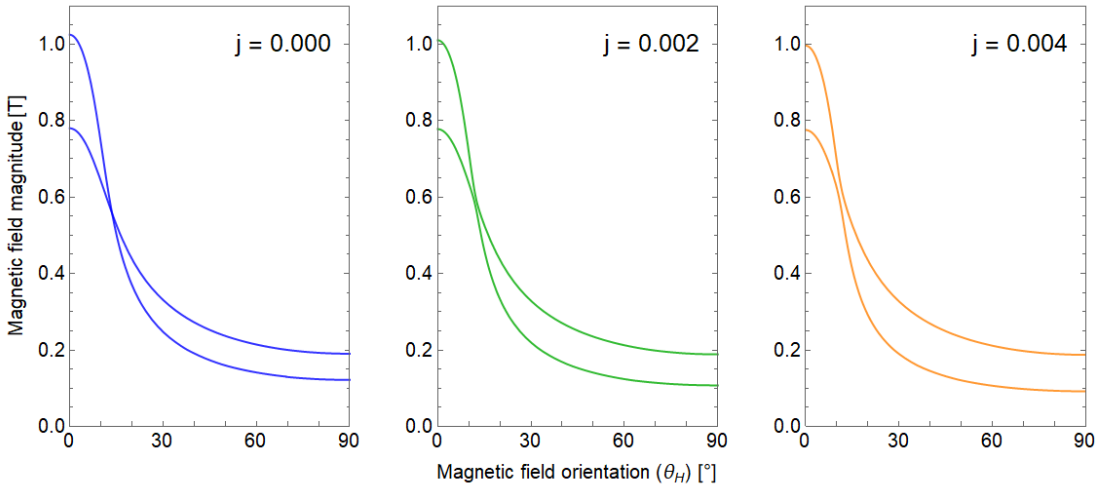

Figure 6.8: Theoretical predictions for the magnetic resonance field for the sample with two magnetic layers. The Co and Py parameters were taken from Table 6.2 for the materials at 80 K. Three graphs show the results for different values of the EC parameter j.

The obtained anisotropy constants for the samples with a single magnetic layer were used as starting values for the fitting procedure for the two magnetic layer model to the cavity FMR data gathered for the samples with two magnetic layers (S1655_I and S1655_II). As the SP coupling has a negligible effect onto the position of the resonance peaks here only the EC was assumed.

Even though samples were produced using MBE with great care, it was very difficult to obtain the exactly identical layer thickness in separate grows (this was especially troublesome in case of the Co layer). Thickness is an important parameter that affects the anisotropy of a layer. As a result, the values of the anisotropy constants for Co obtained from the experiments with one and two magnetic layers can differ. For the purpose of the fitting procedure, the values for the Py layer were considered fixed, and equal to the once obtained for the single layer sample, while the values for the Co layer were fitted.

The cavity FMR data is insufficient to provide the estimate for the ζ coefficient. Its value was set to 0.13, which has been estimated based on the magnetic layer thickness and magnetisation at saturation (assumed to be $M_s^{Co} = 1.4 \times 10^6$ A/m

and $M_s^{Py} = 0.4 \times 10^6$ A/m).

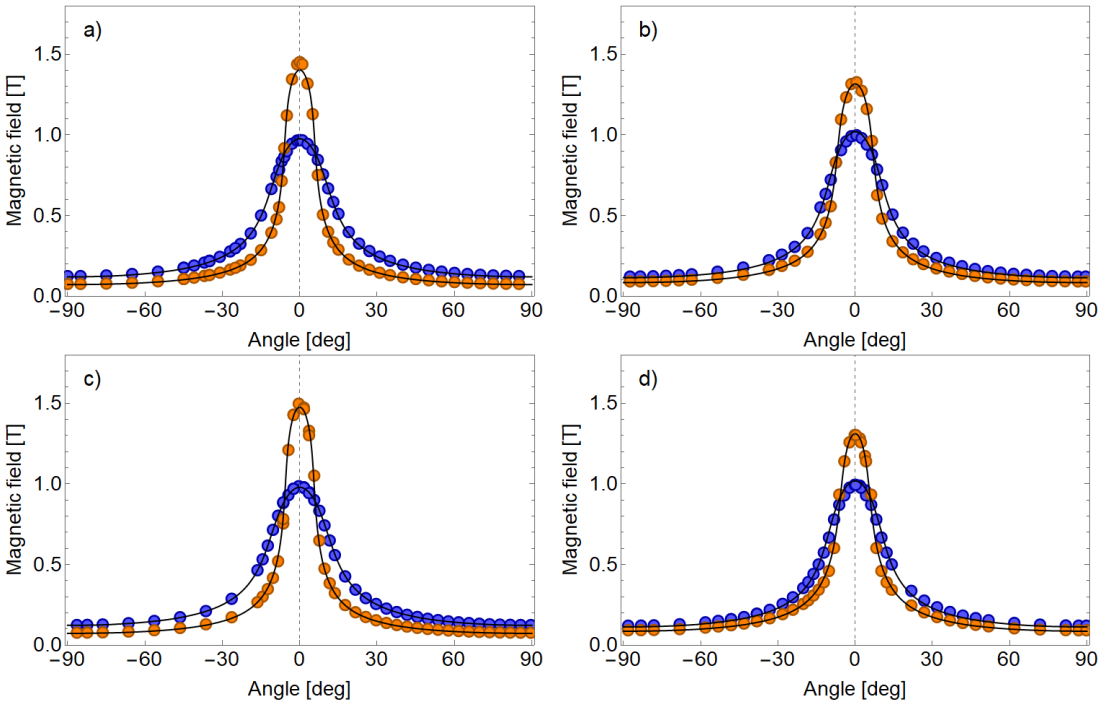

Figure 6.9: Ferromagnetic resonance field in dependence on magnetic field direction (θ_H) for S1655_I at (a) 300 K and (b) 80 K, and S1655_II at (c) 300 K and (d) 80 K. Measurement points for Co are marked with orange dots, Py with blue. Fitted theoretical curves are shown in black.

The resulting fits are shown in Figure 6.9, and the values of the optimised coefficients are shown in Table 6.3. It can be noticed that the fitted model is not accurate, which can have several causes. As it was already discussed, the uniaxial anisotropy model does not give a perfect match for the Co results even in case of single magnetic layer samples. Additionally, parameters such as Py anisotropy and ζ are fixed and their values are assumed arbitrary. Fitting those parameters together with the model leads to a better fit, yet resulting values are non-physical.

With the research performed, it is concluded that the cavity FMR data is not sufficient to allow for the precise estimation of the values of the j and $a^{\uparrow\downarrow}$ coupling parameters. Other measurement techniques were used to gather additional data that could potentially improve the quality of the estimations.

Sample	Temp.	$\gamma_{\mathrm{Co}}\,[\mathrm{m}/(\mathrm{s}\cdot\mathrm{A})]$	$D_1^{\mathrm{Co}}\,[T]$	$D_2^{\mathrm{Co}}\,[T]$	$j\,[10^{-3}]$
S1655_I	300 K	$246\,300 \pm 800$	-1.151 ± 0.037	0.048 ± 0.029	1.03 ± 0.06
S1655_I	80 K	$238\,400 \pm 500$	-1.040 ± 0.038	0.034 ± 0.036	0.99 ± 0.06
S1655_II	300 K	$240\,500 \pm 900$	-1.200 ± 0.038	0.032 ± 0.038	0.60 ± 0.05
S1655_II	80 K	$251\,300 \pm 1200$	-0.889 ± 0.040	-0.129 ± 0.045	1.20 ± 0.06

Table 6.3: Parameters of the fitted two magnetic layer model to the Cavity FMR data for the studied samples. The table does not include parameters that were fixed: $D_1^{\mathrm{Py}}(80\,\mathrm{K}) = -0.709\,\mathrm{T}$, $D_1^{\mathrm{Py}}(300\,\mathrm{K}) = -0.665\,\mathrm{T}$, $\gamma_{\mathrm{Py}}(80\,\mathrm{K}) = 232\,350\,\mathrm{m}/(\mathrm{s}\cdot\mathrm{A})$, $\gamma_{\mathrm{Py}}(300\,\mathrm{K}) = 231\,380\,\mathrm{m}/(\mathrm{s}\cdot\mathrm{A})$, and $\zeta = 0.13$.

6.3 VNA-FMR measurements

VNA-FMR experiments allow for the study of the FMR signal as a function of the excitation frequency, which results in valuable information about the investigated magnetic samples. This study was performed using the VNA-FMR setup with the excitation frequency range of 0–20 GHz, field strength range of $0 - 300$mT, and field orientation between in-plane ($\theta = 0°$) and out-of-plane ($\theta = 90°$) every 5 degrees.

The results of the VNA-FMR measurements are presented using a two-dimensional plot that captures the dependence of the resonance frequency on the external magnetic field direction and its magnitude. Such data can be compared with the theoretical model to determine values of the sample parameters. The VNA-FMR method can be particularly useful when trying to estimate the value of the EC parameter j. Figure 6.10 shows how the resonance curves are affected by the change in the value of j. The effect is most evident in the region where two resonance frequencies are similar in value. In the presented case, the effect is strongest for low values of the magnetic field, the top resonance branch is lifted (for $j > 0$) resulting in a non-zero resonance frequency even with no external magnetic field.

The measurements were performed for the S1655_I and S1655_II samples at room temperature and at 80 K (Figure 6.11). Two resonance curves were observed. The EC interaction between the magnetic layers is evident as a non-zero resonance frequency value, which is observed even if the magnetic field is zero. The effect is best visible for the samples at room temperature with $\theta_H = 10°$. The VNA-FMR spectra were compared with the theoretical predictions using anisotropy

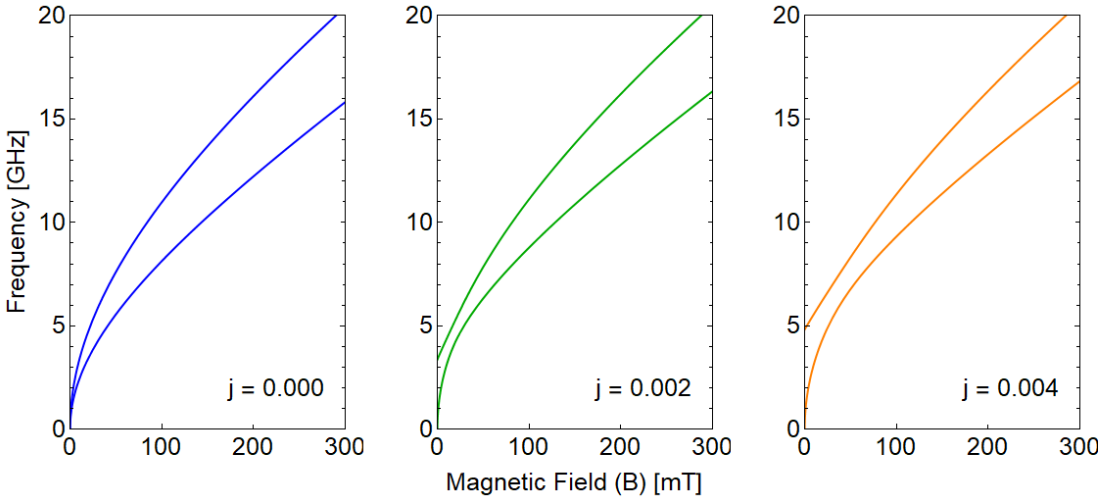

Figure 6.10: Calculations of the resonance frequency dependence on the magnitude of the external magnetic field at $\theta_H = 90°$ for the sample consisting of 10 nm Co layer and 5 nm Py layer held at room temperature. It is assumed that the magnetic layers interact only via EC. The anisotropy constants determined for the sample S1655_II (Table 6.3) are used. The value $\zeta = 0.13$ is assumed. The three graphs show plots for different values of the EC parameter j.

parameters determined by cavity FMR measurements, and by adjusting the j parameters, giving a typical value of $j = 1.4 \times 10^{-3}$. The j parameter was adjusted manually, therefore it is subject to a high uncertainty.

It was found that in many cases, the theoretical model predicts the resonance frequency well. Discrepancies were found for low values of θ_H. Certain features, such as a cusp of the resonance curve at around 40 mT for S1655_II measured at 80 K and $\theta = 10°$, cannot be explained if an uniaxial anisotropy of the Co layer is assumed. This indicates that the Co layer could be composed of a mixture of the HCP and FCC phases.

Proper modelling of the sample anisotropy is crucial as the chosen values and the type of anisotropy will affect the values of the other estimated parameters such as the EC coupling parameter j. It is concluded that VNA-FMR can give great insight into the sample characteristics, yet in real world cases, the available magnetic field range was insufficient to give a satisfying estimate for the magnetic layer interactions.

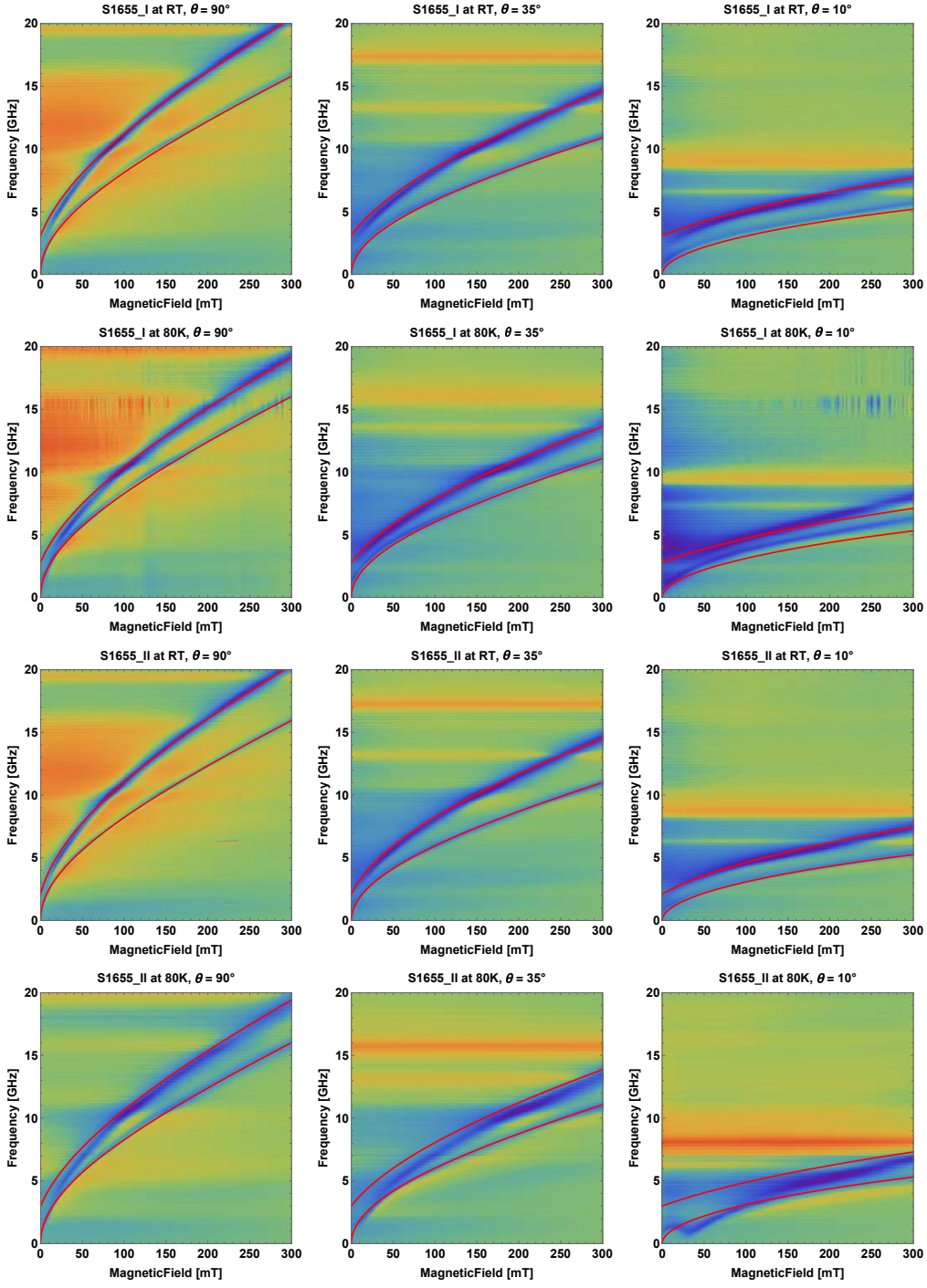

Figure 6.11: VNA-FMR measurements with superimposed theoretical curves (in red), calculated using parameters determined by cavity FMR measurements. From top to bottom: S1655_I at RT, S1655_I at 80 K, S1655_II at RT, S1655_II at 80 K. From left to right: field in-plane, 35°, and 10° away from the surface normal.

6.4 XFMR measurements

The research conducted using cavity FMR and VNA-FMR suggests that the magnetic layers in the studied samples interact, and that their dynamics are interdependent. The data available so far, was however not sufficient to determine whether this is caused by exchange coupling (EC), SP coupling, or both. It was also not possible to estimate the values of the respective parameters with sufficient precision, namely the j and $a^{\uparrow\downarrow}$ coupling parameters. Determining the type of coupling between the magnetic layers in the heterostructure is a difficult problem that has been approached by some researchers [59].

In the present work, a state-of-the-art experimental technique (XFMR) was employed. The experimental results were compared with the theoretical model based on micromagnetic theory, and a criterion was established to determine the presence of spin-current coupling in the studied MTJ systems. This is the first time that such a detailed and extensive comparison between theory and experimental XFMR data has been performed. Details of the experimental method were discussed in chapter 4.3.3 and the theoretical model was introduced in chapter 2.

The XFMR measurements were performed on S1655_I, S1655_II, and S1656_II at a driving frequency of 4 GHz, for multiple orientations of the external magnetic field ($\theta_H \in [15°, 90°]$), at room temperature (300 K) and at 80 K. The magnetic field magnitude was varied in the range chosen based on the previous VNA-FMR results in such a way that the full resonance peaks for the Co and Py layers were recovered. As the Py is composed of Ni and Fe, it is possible to measure the XFMR at any of the respective absorption edges. Here, the Ni edge was used.

For all of the studied samples, evidence of a strong interaction between the magnetic layers was found (Figures 6.12, 6.13, and 6.14). Each of the magnetic layers is shown to have two resonance peaks, which is an indication that the layers are coupled, and each of the resonances are distributed across both of them. Such effects can only be seen if a layer-sensitive method is used. In case of cavity FMR and VNA-FMR methods, the absorption signal is a sum of the absorption on each layer, and the contribution by the individual layers cannot be distinguished. Two types of interaction between the magnetic layers are considered for the investigated heterostructure. The first one is the static exchange interaction, and the second

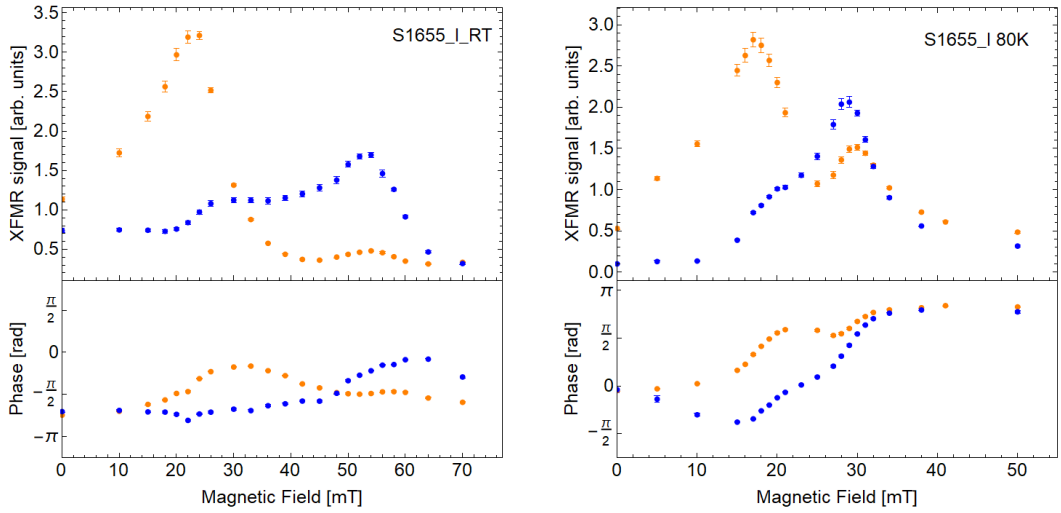

Figure 6.12: Amplitude and phase of the XFMR signal measured for the S1655_I sample at room temperature and at 80 K for the magnetic field orientation $\theta_H = 35°$.

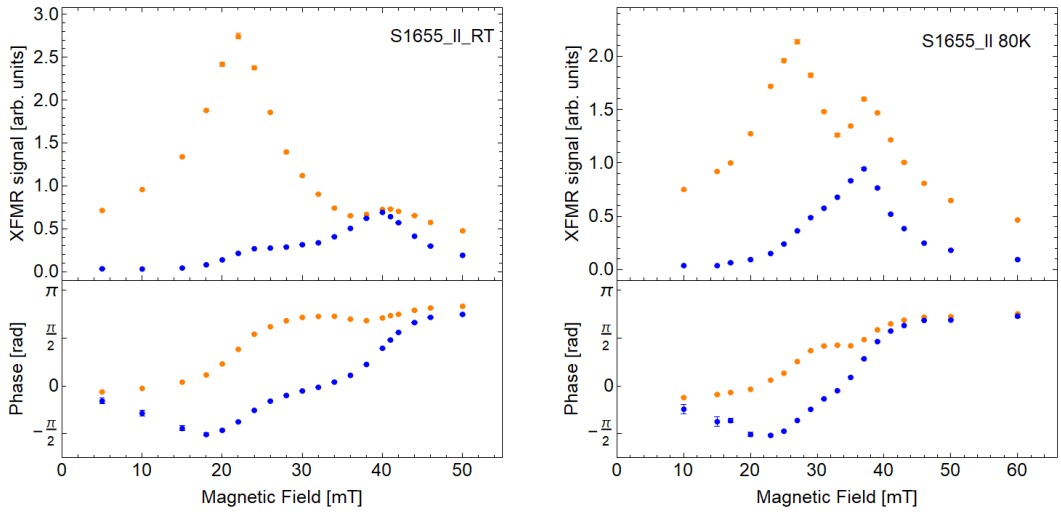

Figure 6.13: Amplitude and phase of the XFMR signal measured for the S1655_II sample at room temperature and at 80 K for the magnetic field orientation $\theta_H = 45°$.

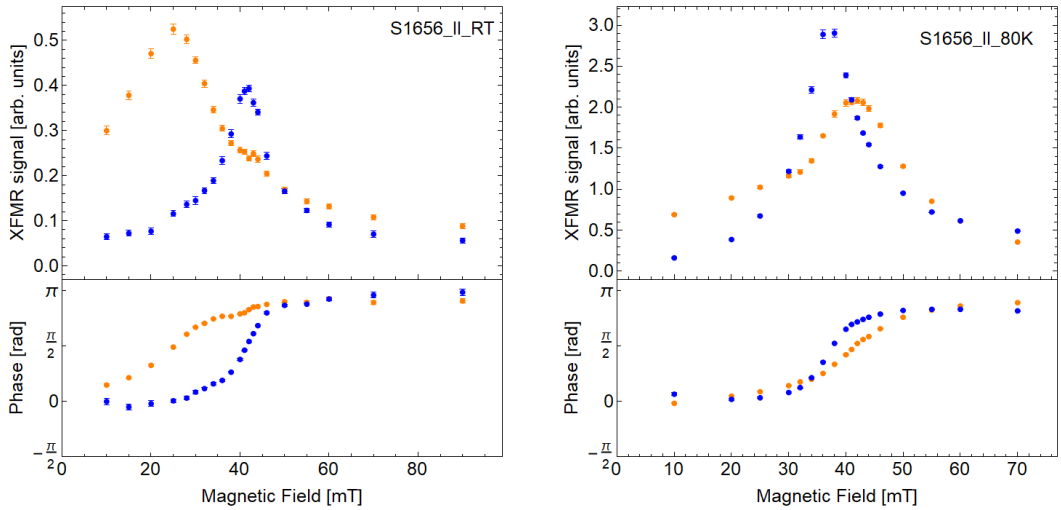

Figure 6.14: Amplitude and phase of the XFMR signal measured for the S1656_II sample at room temperature and at 80 K for the magnetic field orientation $\theta_H = 35°$.

due to the spin current exchange between magnetic layers. By comparing the XFMR results with the theoretical model for the magnetisation dynamics in the coupled magnetic layer, the contribution of two effects can be quantified.

The theoretical model (introduced in chapter 2):

$$\begin{aligned} \bar{P}^{\mathrm{Co}}_{\mathrm{XFMR}}(\theta_H, B) &= \bar{r}^{\mathrm{Co}}_{\theta_H} + \bar{A}^{\mathrm{Co}}_{\theta_H} \left(\bar{y}_{\mathrm{Co}} \cos\beta + \bar{p}_{\mathrm{Co}} \sin\theta_{\mathrm{Co}} \sin\beta\right) \\ \bar{P}^{\mathrm{Py}}_{\mathrm{XFMR}}(\theta_H, B) &= \bar{r}^{\mathrm{Py}}_{\theta_H} + \bar{A}^{\mathrm{Py}}_{\theta_H} \left(\bar{y}_{\mathrm{Py}} \cos\beta + \bar{p}_{\mathrm{Py}} \sin\theta_{\mathrm{Py}} \sin\beta\right) \end{aligned} \tag{6.2}$$

was fitted to the obtained XFMR data. The values decorated with a bar are complex values. The amplitude of the XFMR signal and its phase is recovered by taking the norm and the argument, respectively. The $\bar{r}_{\theta_H}$ parameters are introduced to account for the background noise, and $\bar{A}_{\theta_H}$ is used to normalise the signal amplitude and adjust its phase. The $\bar{y}_{\mathrm{Co/Py}}$ and $\bar{p}_{\mathrm{Co/Py}}$ values are solutions to Equations (2.127), and $\theta_{\mathrm{Co/Py}}$ are the orientations of the magnetisation vector of the respective magnetic layers, which are found as a solution to Equation (2.116). The values $\bar{y}_{\mathrm{Co/Py}}$, $\bar{p}_{\mathrm{Co/Py}}$, and $\theta_{\mathrm{Co/Py}}$ are dependent on the system parameters: B, θ_H, $\alpha_{\mathrm{Co/Py}}$, $\gamma_{\mathrm{Co/Py}}$, j, $a^{\uparrow\downarrow}$, ζ, and the anisotropy constants of the layer. The β parameter is the inclination angle of the sample plane with respect to the X-ray beam direction (set in all experiments to $\beta = 35°$). The magnitude of the driving

magnetic field was assumed equal for both magnetic layers, and a sensible value was chosen: $b_{\mathrm{Co/Py}} = 1 \times 10^{-4}\,\mathrm{T}$ [60].

When optimising the parameters of the model (6.2), it is common for the optimisation algorithm to get stuck at a local maximum (of the likelihood) instead of finding the global maximum. This issue is overcome if the starting values of the fitting parameters are chosen close to the optimal ones. The initial guess can be made based on the results obtained in the independent experiments. The thickness of the magnetic layers is best estimated using the TEM images, and the value of the magnetisation at saturation of Co and Py is assumed based on the values found in the bulk of 1.422×10^6 A/m and 0.4×10^6 A/m, respectively. The layer thickness and the magnetisation at saturation gives an estimate for the ζ parameter to be approximately 0.15. The initial value of the dimensionless Gilbert damping for both layers was chosen to be a typical value of $\alpha_{\mathrm{Co/Py}} = 0.02$. The gyromagnetic ratios $\gamma_{\mathrm{Co/Py}}$ were fixed and equal to $\gamma_{\mathrm{Co}} = 240\,000\,\frac{\mathrm{rad}}{\mathrm{T{\cdot}s}}$, $\gamma_{\mathrm{Py}} = 232\,350\,\frac{\mathrm{rad}}{\mathrm{T{\cdot}s}}$ at 300 K and $\gamma_{\mathrm{Co}} = 235\,572\,\frac{\mathrm{rad}}{\mathrm{T{\cdot}s}}$, $\gamma_{\mathrm{Py}} = 233\,093\,\frac{\mathrm{rad}}{\mathrm{T{\cdot}s}}$ at 80 K (values chosen based on cavity FMR measurements).

As already mentioned when discussing the results of the cavity FMR study, the uniaxial anisotropy model is insufficient to adequately describe the anisotropy of the Co layer in the produced samples. On the other hand, this parameter defines the position of the ferromagnetic resonance peaks, and a deviation from the real value will have a major effect on the other fitting parameters such as the EC parameter j and the SP parameter $a^{\uparrow\downarrow}$. The estimation of those two parameters (j and $a^{\uparrow\downarrow}$) is crucial for this study. Therefore, the energy of the crystalline anisotropy was modelled as:

$$\begin{aligned} e_{\mathrm{Co}}(\theta_{\mathrm{Co}}) &= -K_{\theta_H}^{\mathrm{Co}} \cos^2(\theta_{\mathrm{Co}}) \\ e_{\mathrm{Py}}(\theta_{\mathrm{Py}}) &= -K_{\theta_H}^{\mathrm{Py}} \cos^2(\theta_{\mathrm{Py}}) \end{aligned} \tag{6.3}$$

where $K_{\theta_H}^{\mathrm{Co/Py}}$ was fitted independently for measurement performed at different orientations of the magnetic field (θ_H). The initial values of $K_{\theta_H}^{\mathrm{Co/Py}}$ were chosen to be the same for all θ_H, and equal to the values obtained in cavity FMR measurements. In the model (6.2), the fitting parameters ζ, j, $a^{\uparrow\downarrow}$, α_{Co}, and α_{Py} were shared between fits for measurements at different magnetic field orientations (θ_H).

When fitting a theory to the experimental data, the results can often be misleading. A good quality fit does not categorically prove the validity of the model itself. However, if the model is unable to reproduce the experimental data. it is a definite indication that it is not valid. With this in mind, it was considered crucial to provide an objective criterion for determining if SP is present in the system. Two hypothesis were tested: the first one assumed that both types of coupling are present (an alternative hypothesis), and the second assumed that the EC alone is sufficient to describe the system dynamics (a null hypothesis). The theoretical models related to both approaches were optimised to best match the measured data. The goodness of the fitted models was compared using the likelihood ratio test.

Up to this point, the uncertainty of the XFMR values was considered to be equal to the uncertainty of the parameter estimation resulting from the delay scan measurements. This, however, does not include any uncertainties that are related to the experimental procedure. Due to multiple possible sources of such measurement uncertainties, they were assumed to be identical for all measurement points associated with a given magnetic layer. The uncertainty values were optimised together with the optimisation of the model.

The best results were obtained for S1655_II (due to the high background signal, the results for S1655_I and S1656_II were inconclusive). The model recovered the values found in the experiment well (Figure 6.15, 6.16, and Appendix C). The model including SP gives better results, with the effect being clearly visible when the sample is held at 80 K. The value of the estimated variance was low in all presented cases, giving an estimate for the measurement uncertainty equal to about 0.049 in case of the Co layer and about 0.019 in case of the Co layer. The values have the same units as the units of the XFMR signal amplitude. Based on the discussion presented in chapter 5.3, the likelihood ratio test was performed to quantify the difference in the fit quality for both models. For the sample at 80 K the LR test gave a value of $\lambda_{LR}^{80\mathrm{K}} = 318$ and at room temperature the value of $\lambda_{LR}^{300\mathrm{K}} = 42$. The values of the fitted parameters is shown in Table 6.4, and the value of the resulting $K_{\theta_H}^{\mathrm{Co/Py}}$ constants is plotted in Figure 6.17.

Comparing the obtained LR test values with the χ^2 distribution, it can be concluded with great certainty that the null hypothesis (no SP) can be rejected

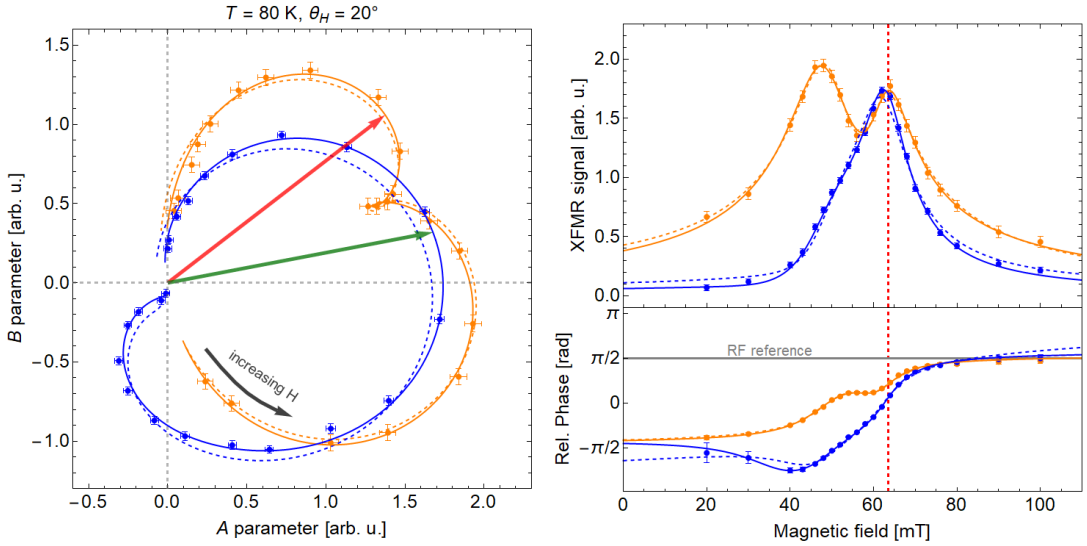

Figure 6.15: XFMR results for sample S1655_II at 80 K, and the external field direction $\theta_H = 20°$. Orange and blue points represent the data for Co and Py, respectively. The solid lines represent the theoretical model with SP and EC, while the dashed lines represent the EC only model. The plot on the left shows the data in (A, B) coordinates, while the plots on the right show the results in on the amplitude and phase graphs as a function of external magnetic field. Green and red arrows, and a dashed vertical line were used to mark points for the same value of the external magnetic field (63.6 mT).

Temp	α_{Co} $[10^{-3}]$	α_{Py} $[10^{-3}]$	ζ	j $[10^{-3}]$	$a^{\uparrow\downarrow}$ $[10^{-3}]$
80 K	14.6 ± 0.2	20.3 ± 0.2	0.294 ± 0.019	0.871 ± 0.017	—
80 K	8.1 ± 0.5	17.9 ± 0.2	0.157 ± 0.010	0.713 ± 0.019	1.078 ± 0.050
300 K	16.1 ± 0.2	16.5 ± 0.1	0.160 ± 0.013	0.667 ± 0.020	—
300 K	12.5 ± 0.7	15.5 ± 0.2	0.141 ± 0.011	0.638 ± 0.020	0.473 ± 0.075

Table 6.4: Values of the fitted parameters that are shared across all measurements for all θ_H for S1655_II held at 80 K and at 300 K. The rows with no value for $a^{\uparrow\downarrow}$ indicate the fitted parameters for the model with no SP.

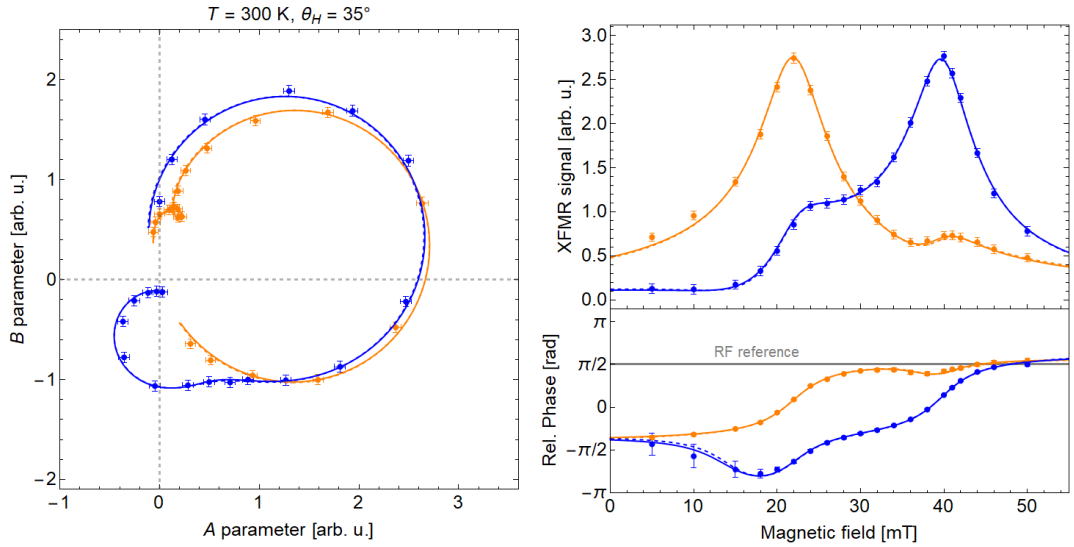

Figure 6.16: XFMR results for sample S1655_II at 300 K, and the external field direction $\theta_H = 35°$. Orange and blue points represent the data for Co and Py, respectively. The solid lines represent the theoretical model with SP and EC, while the dashed lines represent the EC only model. The plot on the left shows the data in (A, B) coordinates, while the plots on the right show the results in on the amplitude and phase graphs as a function of external magnetic field.

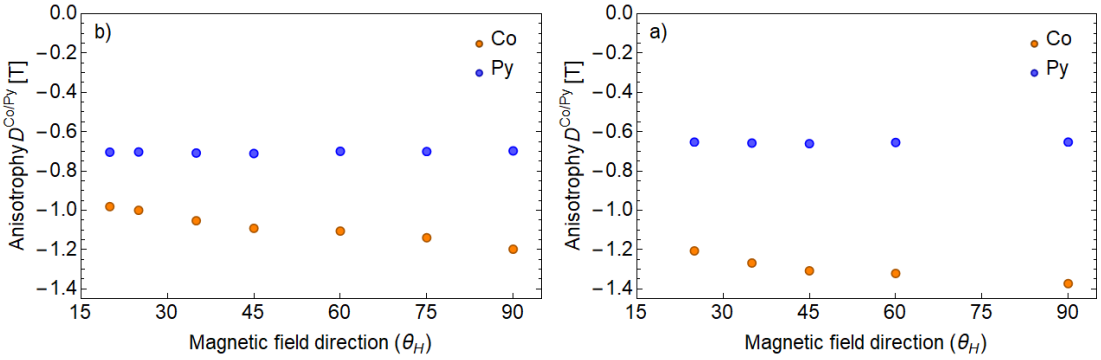

Figure 6.17: Values of the fitted anisotropy constants $D_{\theta_H}^{\mathrm{Co/Py}} = 2K_{\theta_H}^{\mathrm{Co/Py}}/M_{\mathrm{s}}^{\mathrm{Co/Py}}$ for S1655_II at (a) 300 K and (b) 80 K. Similar results were obtained for both cases, i.e., with and without SP. For clarity, the results for the fit of the model with SP is shown.

(Wilk's theorem). This is especially clear in case of $T = 80\,\mathrm{K}$ where the value of the likelihood ratio test is very high. An improvement is also observed in case of the sample at $T = 300\,\mathrm{K}$.

The heuristic approach of fitting the anisotropy constants independently for measurements at different θ_H has given good results. The value of anisotropy for Py, K^{Py} (or D^{Py}), is very similar for all magnetic field orientations (Figure 6.17). This is consistent with the fact that the anisotropy of Py is uniaxial. It was observed that the fitted values differed by $\pm 0.5\%$ between measurements for different θ_H values. This small adjustment was important and allowed for better model agreement, which shows great sensitivity of the model on the value of anisotropy parameters. The value of the Co anisotropy K^{Co} (or D^{Co}) differs between measurements performed at different θ_H, with the value being smaller for the magnetic field orientation close to the $\theta_H = 0$ orientation. This is partially due to the fact that it is expected that the Co layer anisotropy requires a second anisotropy term K_2. Yet, the inclusion of such a term did not resolve the issue, which is possibly caused by the mixed HCP and FCC phases of the Co layer.

The values of the fitted dimensionless Gilbert damping are lower in case of the model with SP interaction. This is mostly due to the fact that the addition of SP causes an increase in the resonance peak width, as it was shown in chapter 2.5.3. If no SP is assumed, this effect is partially compensated in the fitting procedure by an increase in the value of the Gilbert damping. The effect is not proportional for both layers. The proportionality is defined by the ζ parameter:

$$\alpha_{\mathrm{Co}}^{\mathrm{EC}} \approx \alpha_{\mathrm{Co}}^{\mathrm{SP}} + a^{\uparrow\downarrow} \csc \zeta^{\mathrm{SP}}\,, \quad \alpha_{\mathrm{Py}}^{\mathrm{EC}} \approx \alpha_{\mathrm{Py}}^{\mathrm{SP}} + a^{\uparrow\downarrow} \sec \zeta^{\mathrm{SP}} \tag{6.4}$$

where the values obtained in the model with SP are labelled with "SP", and the ones for the model without SP with "EC". For example, for values obtained for S1655_II at 80 K this gives an estimate of $\alpha_{\mathrm{Co}}^{\mathrm{EC}} \approx 15.0$ and $\alpha_{\mathrm{Py}}^{\mathrm{EC}} \approx 19.9$, which are very close to the ones for the model without SP.

It is expected that spin pumping is more efficient at lower temperatures. This is confirmed by the values of the fitted parameters. The intensity of spin-pumping is about twice as high in case of the sample at80 K than at room temperature.

By comparing the theoretical results with the experimental data, and given the value of the resulting fitting parameters and their estimation uncertainty, and

the rejection of the null hypothesis (stating that no spin-pumping occurs in the system) by the likelihood ratio test, it can be concluded that the spin-pumping occurs in the studied samples.

Chapter 7

Topological Insulators

Topological insulators (TI) are exotic materials that, although they are insulating in the bulk, exhibit metallic surface states [61]. Such materials have been predicted [62–65] and their existence has been experimentally verified [66–68]. For a TI to form, strong spin-orbit coupling is required that modifies the electronic structure of the material significantly [61]. The electrons confined to a quasi-two dimensional surface of the TI act like Dirac fermions and are protected by the band gap in the bulk states, with backward scattering forbidden by time reversal symmetry [69].

The topologically protected surface state can exert a torque on the spins in the neighbouring ferromagnet (FM) through exchange coupling [69]. This can have a great effect on the dynamic properties of the magnetic layers in a FM/TI/FM heterostructure, possibly increasing the strength of the interaction between the magnetic layers, allowing for quicker response times of magnetisation switching, suitable for electronic device applications.

In this chapter, the possibility of fabricating a spin-valve device with a α-Sn topological insulator acting as a spacer between the ferromagnetic thin films is explored. The topological properties of the α-Sn thin film grown on a InSb(100) substrate have been confirmed by angle-resolved photo-emission spectroscopy (ARPES) [70]. Sn is particularly attractive as it exhibits a phase transition between the α-Sn and β-Sn phases at temperatures that are accessible ($\sim$13.2° C for the bulk crystal). This property may allow the synthesis of a sample where properties of the spacer layer change between TI (α-Sn) and normal conductor (β-Sn) — depending on temperature — thereby allowing for an in depth study of the TI itself. α-Sn

is the only known monoatomic 3D TI, a fact which can potentially simplify the fabrication of the TI devices.

7.1 α-Sn TI overview

Growth of α-Sn has been performed successfully only on a few substrates. A few monolayers thick α-Sn films have been successfully deposited on silicon [71–75] and germanium [76–79], yet the best results were obtained when depositing Sn on InSb(100) [80–82]. Strain induced by the lattice mismatch at the interface between InSb and α-Sn favours the α phase (at room temperature).

In search for a suitable magnetic material that would allow for the successful α-Sn growth, the surface of the HCP Co(0001) was chosen. Comparing the (0001) crystallographic plane of the HCP Co crystal with the (111) crystallographic plane of the α-Sn crystal, it can be argued that an energetically favourable configuration of atoms at the interface between those materials is possible. The Co atoms on a (0001) crystallographic plane are arranged in a triangular lattice with the distance between atomic sites equal to $a = 2.519\,\text{Å}$ [3] (Figure 7.1a). Similarly, atoms of α-Sn on the (111) crystallographic plane of the diamond cubic crystal form a triangular lattice with the distance between atomic sites equal to $b_{\text{Sn}} = 4.572\,\text{Å}$ [4] (Figure 7.1b). Sn atoms can be arranged over the Co lattice as shown in Figure 7.1c which results in a distance between atomic sites of Sn equal to $b_{\text{Co}} = 4.364\,\text{Å}$, resulting in a lattice mismatch of only $\frac{b_{\text{Sn}} - b_{\text{Co}}}{b_{\text{Sn}}} \approx 5\%$. This observation motivated our experimental research and development of a growth recipe.

7.2 Device fabrication

Multiple configurations and growth conditions were tested in search for the best recipe for Sn growth on the HCP Co surface. The most successful samples have been grown on a Al_2O_3/Mo/Au heterostructure, which has been manufactured at the Institute of Physics Polish Academy of Sciences, and transported to the Diamonds Light Source for further material deposition. At arrival, the quality of the substrates was verified using AFM, and the composition of the surface was studied using X-ray photoelectron spectroscopy (XPS). Results have shown that

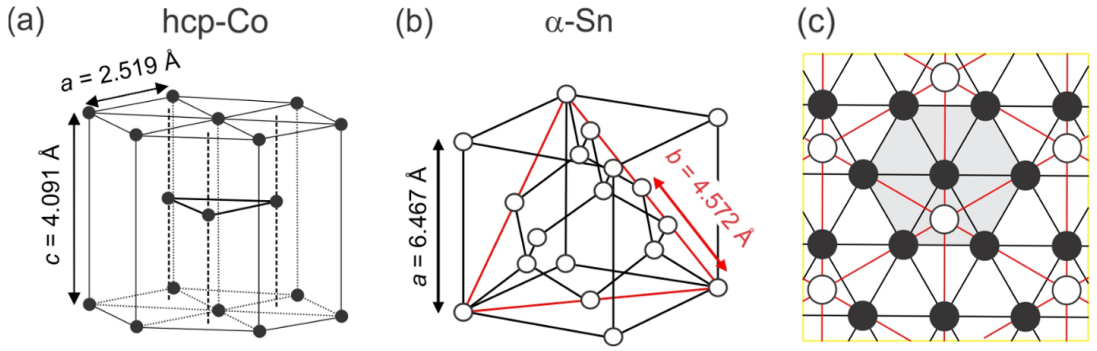

Figure 7.1: Crystallographic structure of (a) the HCP Co and b) the diamond cubic α-Sn. The Co(0001) direction corresponds to the hexagonal plane of the HCP crystal. (111) plane of the diamond cubic crystallographic structure of the α-Sn was marked with red triangle in panel (b). The value of $b = 4.572\,\text{Å}$ is the distance between atomic sites in this cross-section. Panel (c) illustrates a possible configuration of the α-Sn crystal atoms (white circles connected with red lines) on the Co surface (black disks connected with black lines) corresponding to the distance between the Sn atoms equal to 4.363 Å. This results in a $\sim 5\%$ mismatch with the α-Sn lattice. The values for the lattice constant of Co and Sn were taken from Refs. [3] and [4], respectively.

the surface is flat and no major defects were acquired during the transport. XPS has shown a carbon contamination that is possibly resulting from the organic residue collected during the transport. The samples were placed in vacuum and the surface quality was recovered by heating up the sample to 500 K.

Deposition of the Co layer was performed on the sample held at room temperature. Depending on the sample, a 15 nm - 20 nm thick layer of Co was deposited onto the Al_2O_3/Mo/Au heterostructure. The quality of the Co layer was monitored during growth using RHEED. By taking RHEED images of the complete Co layer with the sample oriented in different directions, a 6-fold symmetry of the Co surface (Figure 7.2a and 7.2b) was observed, confirming the good quality of this layer. For further verification, the Co layer was capped with a Si layer and the magnetic properties of the Co layer were confirmed by performing VNA-FMR measurements.

The Al_2O_3/Mo/Au/Co heterostructures were used as a base substrate for the Sn growth with the sample held at 20° C, which was the lowest possible temperature in our setup. Sn was evaporated out of a crucible heated to about 1050 K, which

allowed for a very slow deposition. The deposition was monitored by taking a RHEED image every 30 s with the sample orientated along two of its distinct symmetry axes. It was found that the deposition of Sn initially resulted in a clear RHEED image with streaks corresponding to the doubling of the lattice constant of the Co layer (Figure 7.2c and 7.2d). With thicker Sn layers, the image became blurry and dots appeared, suggesting that the Sn layer is not flat. The Sn growth was terminated at various deposition times, and the topography of the surface of the sample was studied using AFM. Results have shown that the Sn layer is initially flat, yet after some critical thickness, pillars form on the surface that can grow as high as a couple of hundreds nm.

A spin-valve was prepared by terminating the Sn growth before the vertical Sn pillar formation would begin, thereby achieving a flat Sn layer. A 5 nm Py magnetic layer was deposited onto the Sn layer, and the sample was capped with Si to prevent oxidation. Two samples were successfully fabricated using this recipe: Al_2O_3/Mo/Au/Co(15 nm)/Sn(2 nm)/Py(5 nm)/Si (LG002) and Al_2O_3/Mo/Au-/Co(20 nm)/Sn(4 nm)/Py(5 nm)/Si (LG003). The structural properties of these samples were determined using XRR, XRD, AFM, and TEM.

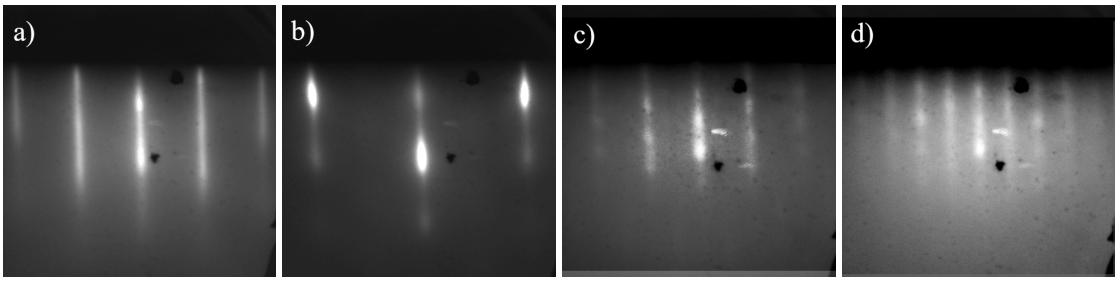

Figure 7.2: RHEED images of the Co(111) layer for the sample oriented along two distinct symmetry axes rotated by 30° with respect to each other [(a) and (b)]. The corresponding RHEED images of the Sn layer along the same two symmetry axes [(c) and (d)].

7.3 Characterisation of structural properties

In the bulk under normal conditions, the phase change between α- and β-Sn occurs at 285 K [83]. This temperature can, however, vary for strained samples and thin

films. In order to determine if the phase transition occurs in our samples, X-ray reflectivity (XRR) and X-ray diffraction (XRD) measurements were performed at temperatures ranging between 80 K and 300 K. The results are shown in Figures 7.3 and 7.4. It can be noticed that with a change in temperature, a shift in the measured Bragg peaks is observed. This is a consequence of the change in lattice constant of the layers due their thermal expansion. No qualitative change is observed that would indicate the occurrence of a phase change.

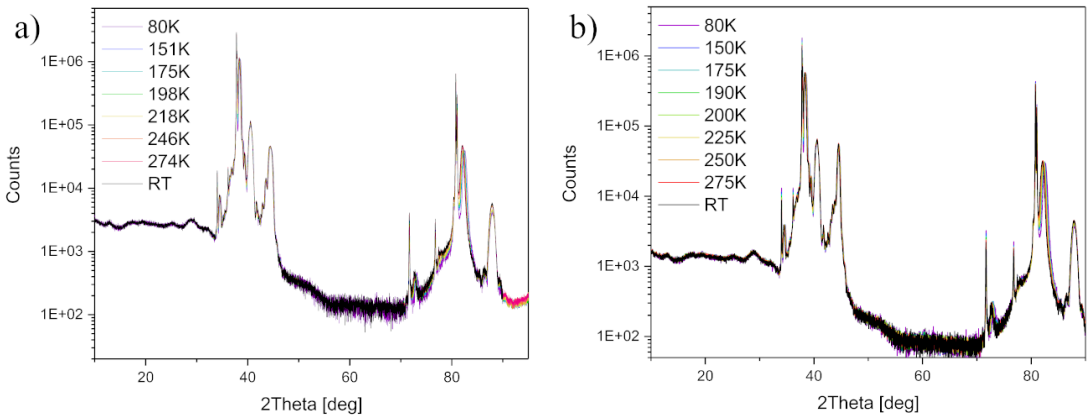

Figure 7.3: X-ray diffraction (XRD) measurements of the (a) LG002, (b) LG003 samples performed in a temperature range between 80 K and 300 K (RT).

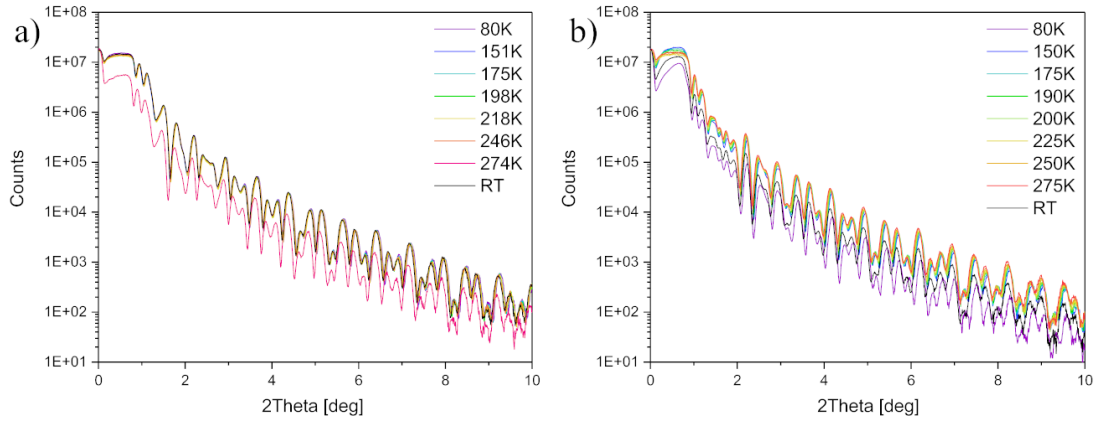

Figure 7.4: X-ray reflectivity (XRR) measurements of (a) LG002 and (b) LG003 samples performed in the temperature range between 80 K and 300 K (RT). Some of the measurements (at 274 K for LG002 and 80 K and 150 K for LG003) have a lower signal count, which is probably caused by misalignment of the sample.

Due to the complex layer structure of our samples, it was difficult to judge the quality of the Sn layer based on the XRR data. A detailed view of the Sn layer was obtained by performing cross-sectional TEM on the sample (Figure 7.5), with the composition of the individual layers determined using Energy-dispersive X-ray spectroscopy (EDX).

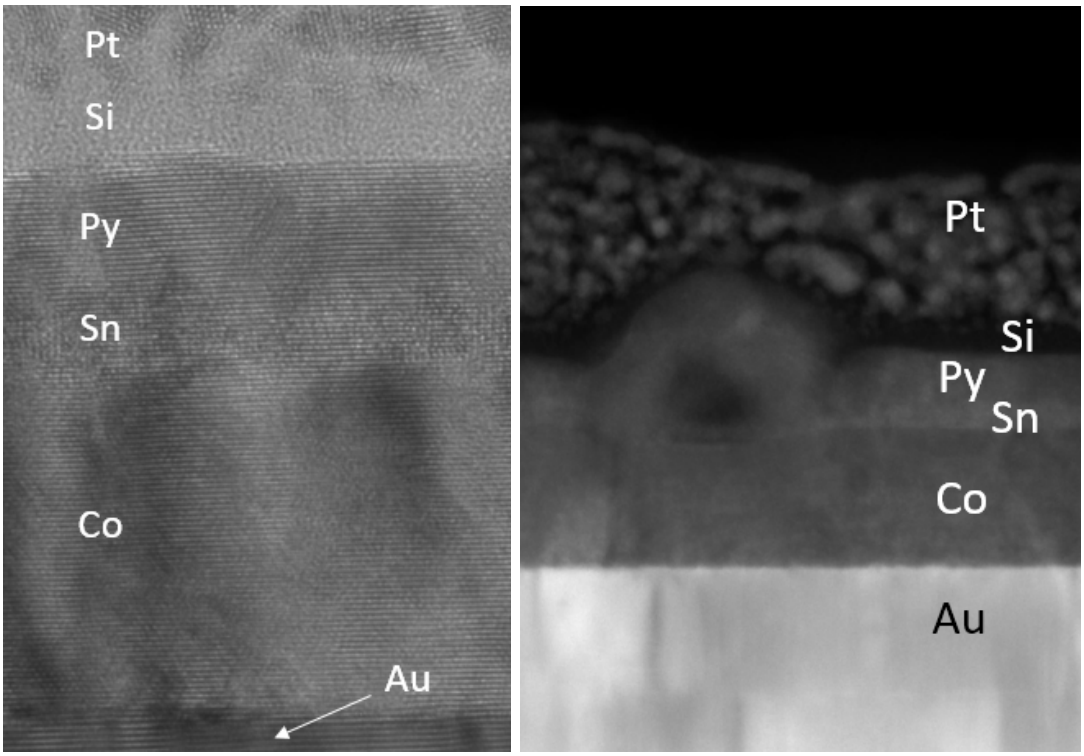

Figure 7.5: Cross-sectional transmission electron microscopy (TEM) images of LG002 (left) and LG003 (right). The composition of individual layers was determined using EDX. A Pt capping layer was added for the purpose of TEM sample preparation. Images were taken by Prof. Piotr Dłużewski at the Institute of Physics, Polish Academy of Sciences.

The TEM results show that Co, Sn, and Py form individual layers. In the case of LG002, the interface is not ideally flat, with variations in height of the Co layer at the Co/Sn interface. For LG003, the Sn layer is flat over a large area with noticeable irregularities that indicate that the growth was terminated at an early stage of pillar growth of Sn. Although the Sn layer quality is not perfect, in both cases it appears that the Py and Co layers are fully separated by the Sn

Sample	Co	Sn	Py
LG002	$14.1 \pm 1.2\,\mathrm{nm}$	$2.6 \pm 0.8\,\mathrm{nm}$	$4.9 \pm 0.5\,\mathrm{nm}$
LG003	$21.3 \pm 2.1\,\mathrm{nm}$	$4.1 \pm 0.9\,\mathrm{nm}$	$5.1 \pm 0.5\,\mathrm{nm}$

Table 7.1: Thickness of the individual layers of the LG002 and LG003 samples estimated using the TEM images. The thickness of the Sn layer in case of the LG003 sample was measured in the regions where it formed a flat layer over the Co surface.

layer, which made those samples suitable for further studies. The thicknesses of the individual layers were measured using the TEM images, and the results are shown in Table 7.1.

7.4 Characterisation of magnetic properties

The magnetic properties of the samples were studied by investigating the ferromagnetic resonance of the magnetic Co and Py layers by performing cavity FMR, VNA-FMR, and XFMR measurements. The cavity FMR measurements were performed at a frequency of 9.38 GHz in the same way as in case of the MgO samples. The results for the LG003 sample at room temperature (300 K) are shown in Figure 7.6. The theoretical model was fitted to the data, and the values for the anisotropy constants and the gyromagnetic ratio were extracted.

The VNA-FMR measurements were performed to gain a more detailed view of the magnetic properties of the sample. The measurements were performed at frequencies in the range $0.5\,\mathrm{GHz} - 20\,\mathrm{GHz}$, for magnetic in-plane fields of $0\,\mathrm{mT} - 300\,\mathrm{mT}$, and in the temperature range between $80\,\mathrm{K} - 347\,\mathrm{K}$. The results are shown in Figure 7.7 and Figure 7.8. It is concluded that a change in temperature mostly affects the anisotropy of the Co layer with the ferromagnetic resonance frequency of the Co layer being higher at higher temperatures. For both the LG002 and LG003 samples, the resonance of the Co and Py layers can be distinguished more easily at higher temperatures.

The experiments mentioned above allow the for the estimation of the anisotropy constants, and provide a qualitative understanding of the system. Results obtained so far are, however, not sufficient to provide information about the coupling be-

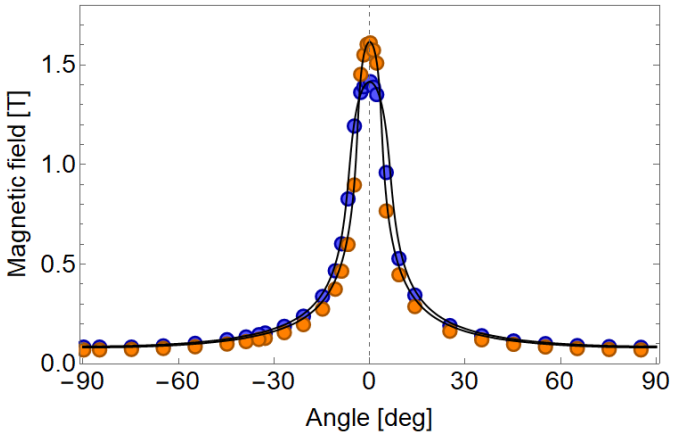

Figure 7.6: The cavity FMR measurements for the LG003 sample performed at driving a frequency of $f = 9.38\,\mathrm{GHz}$. Two resonance peaks were identified and are marked with orange (Co) and blue circles (Py). The theoretical model for a system with two magnetic layers was fitted to the data resulting in the following values for the magnetic parameters: $\gamma_{\mathrm{Py}} = 224\,771\,\mathrm{m/(s \cdot A)}$, $\gamma_{\mathrm{Co}} = 245\,429\,\mathrm{m/(s \cdot A)}$, $D_{\mathrm{Py}} = -1.09\,\mathrm{T}$, $D^{1}_{\mathrm{Co}} = -1.01\,\mathrm{T}$, $D^{2}_{\mathrm{Co}} = -0.31\,\mathrm{T}$, and $j = 0.6 \times 10^{-3}$. The value of $\zeta = 0.068$ was estimated based on the layer thickness found in the TEM measurements, and assuming the layer magnetisation at saturation equal to $M_{\mathrm{s}}^{\mathrm{Co}} = 1.4 \times 10^{6}\,\mathrm{A/m}$ and $M_{\mathrm{s}}^{\mathrm{Py}} = 0.4 \times 10^{6}\,\mathrm{A/m}$.

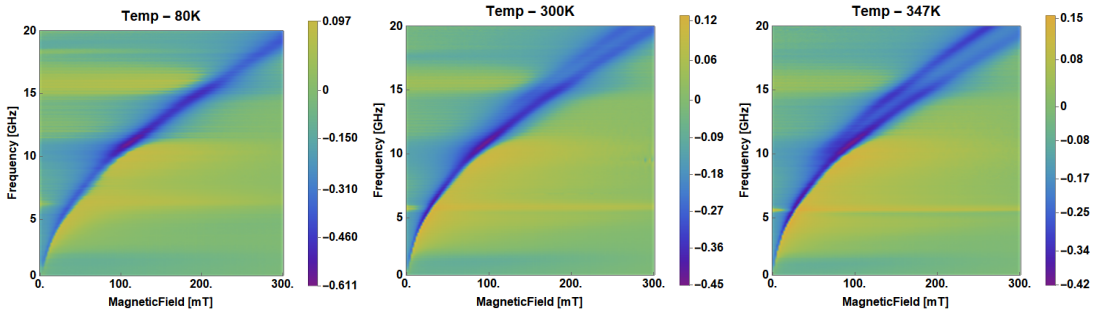

Figure 7.7: VNA-FMR measurements on LG002 at 80 K, 300 K, and 347 K; with the magnetic field oriented in-plane.

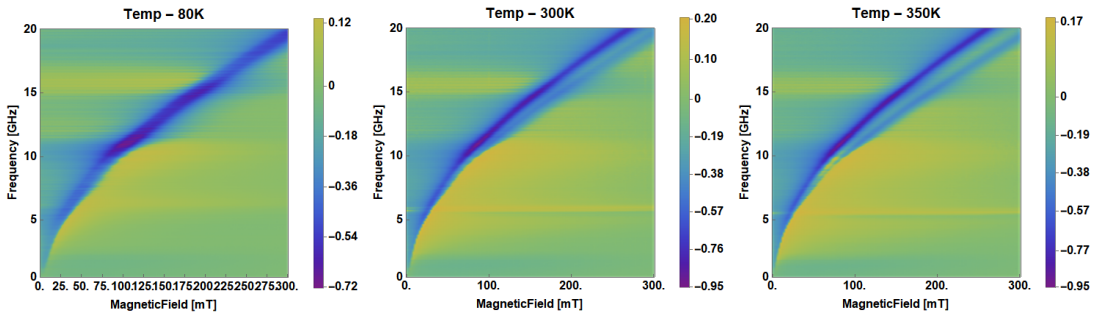

Figure 7.8: VNA-FMR measurements on LG003 at: 80 K, 300 K, and 350 K; with the magnetic field oriented in-plane.

tween the layers. The study of the layer interaction was performed using the XFMR in a similar fashion as it was done for the MgO MTJs.

All XFMR experiments were performed with the magnetic field oriented in-plane of the sample. The excitation frequency was fixed at 10 GHz, which was the highest possible frequency in our experimental setup, and it provided the best results. The XFMR delay scans were performed at the Co and Fe L_2 absorption edges for various magnetic fields covering the ferromagnetic resonance of both magnetic layers (this range was determined based on the data acquired in the VNA-FMR measurements). The measurements were performed for samples at temperatures in the range between 80 K − 328 K. Example results are shown in Figures 7.9, 7.10, 7.11, and 7.12 (all results are presented in Appendix D and E).

The acquired XFMR data show a double resonance peak for the Co layer, and an asymmetric peak for the Py layer (which is a superposition of the two resonance peaks). This suggests a strong interaction between the magnetic layers. Two theoretical hypotheses were tested, in the same fashion as it was done for the MgOs, to determine the type of coupling between the magnetic layers. The null hypothesis states that EC is the only coupling in the system, and an alternative hypothesis states that both EC and SP occur. Those two hypotheses were tested using the likelihood-ratio test. The results are shown in Table 7.2. It is observed that the likelihood-ratio test returns low values that, once compared with the χ^2_1 distribution, do not justify the rejection of the null hypothesis. It seems that the model including only EC is good enough to describe the obtained results, therefore it can not be concluded that spin-current is exchanged between the magnetic layers.

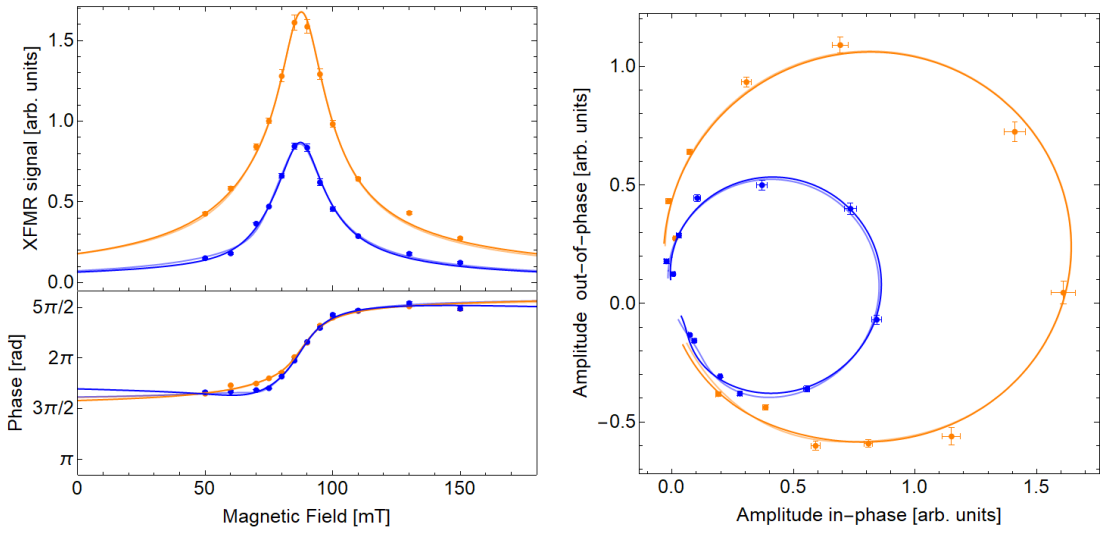

Figure 7.9: XFMR results for the LG002 sample at 152 K, and the external field direction $\theta_H = 90°$. Orange and blue points represent the data for the Co and Py layers, respectively.

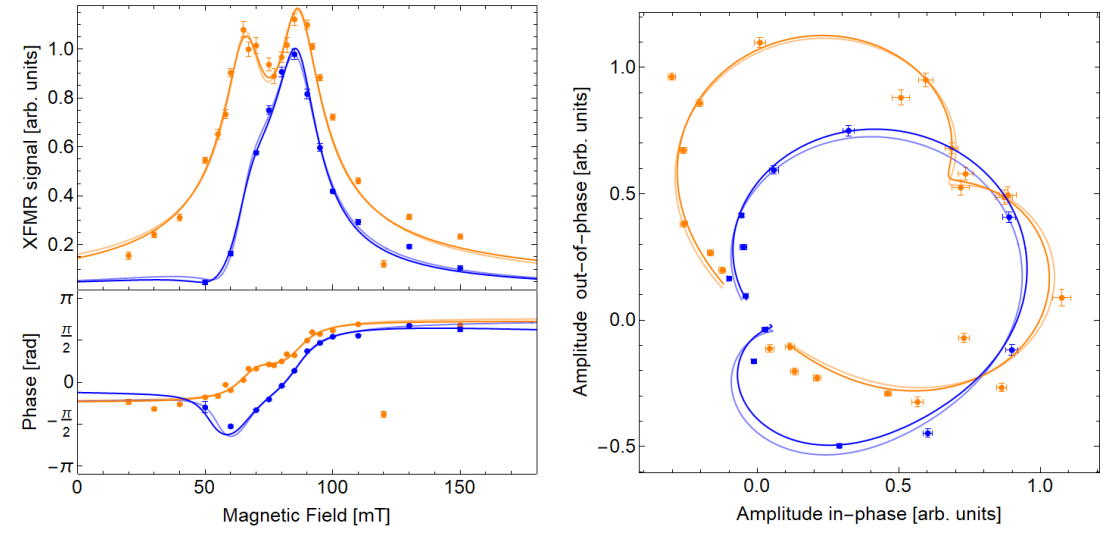

Figure 7.10: XFMR results for the LG002 sample at 328 K, and the external field direction $\theta_H = 90°$. Orange and blue points represent the data for the Co and Py layers, respectively.

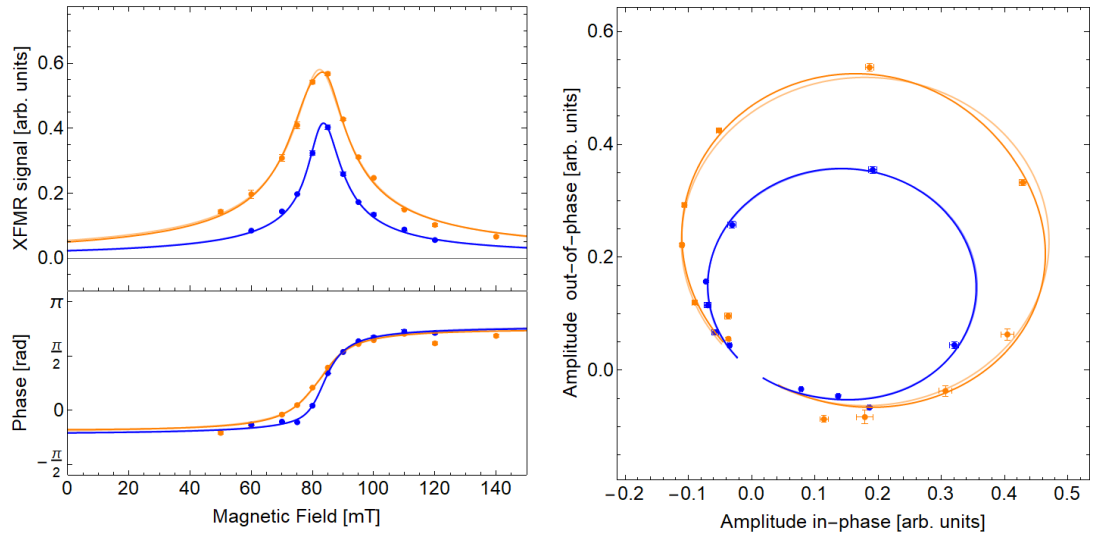

Figure 7.11: XFMR results for the LG003 sample at 201 K, and the external field direction $\theta_H = 90°$. Orange and blue points represent the data for the Co and Py layers, respectively.

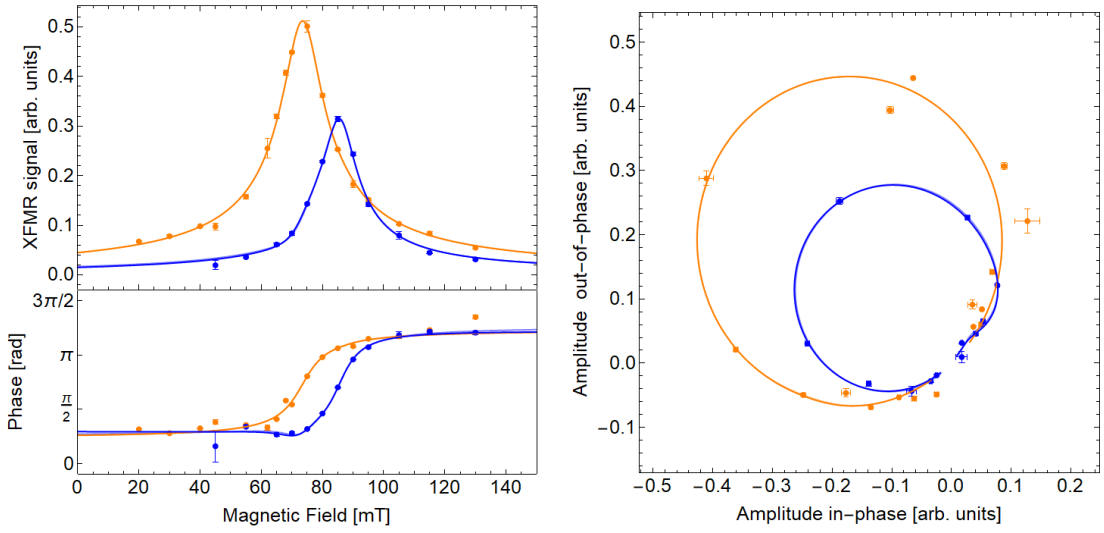

Figure 7.12: XFMR results for the LG003 sample at 300 K, and the external field direction $\theta_H = 90°$. Orange and blue points represent the data for the Co and Py layers, respectively.

Sample	Temp	$j[10^{-3}]$	λ_{LR}	P_{χ^2}
LG002	300 K	4.67 ± 0.87	0.23	0.36
	274 K	4.12 ± 1.42	0.05	0.17
	246 K	4.03 ± 1.60	0.42	0.48
	218 K	7.29 ± 1.40	4.50	0.96
	199 K	6.29 ± 1.00	0.41	0.48
	152 K	2.69 ± 1.84	2.26	0.87
	80 K	7.70 ± 10.28	3.26	0.92
LG003	300 K	0.14 ± 0.50	0.11	0.25
	275 K	0.29 ± 0.35	4.73	0.97
	256 K	0.56 ± 0.23	7.59	0.99
	201 K	0.00 ± 0.00	5.12	0.98
	173 K	1.42 ± 2.05	2.30	0.87
	163 K	0.70 ± 2.00	0.66	0.58
	80 K	1.21 ± 0.88	0.30	0.42

Table 7.2: The values of the fitted exchange coupling constants form the XFMR data for the LG002 and LG003 samples using the model only including the EC term j. The values of the likelihood-ratio test λ_{LR} are obtained by comparing the null hypothesis (only EC) with the alternative hypothesis (EC and SP). The values of the cumulative distribution function of the χ^2_1 distribution corresponding to the values of λ_{LR} are shown in the P_{χ^2} column.

The resulting exchange coupling was much higher in case of the sample with a 2 nm Sn layer and a 15 nm Co layer (LG002). This could have been caused by multiple factors. First, judging from the TEM images, the quality of the Sn layer was better in case of the LG002 sample than in case of the LG003, where bumps in thickness of the Sn layer were observed. The thickness of the Sn layer in case of the LG002 sample was lower, therefore a stronger interaction between the Co and Py layers is expected. In both cases, the resonance peaks of the Co and Py layers are observed at similar magnetic fields, often causing an overlap of the two vibrational modes. In this case, the fitted model is not able to properly estimate the EC and SP coupling constants (j and $a^{\uparrow\downarrow}$).

7.5 Summary of the results for the α-Sn spin-valves

A recipe for the α-Sn growth on the surface of a magnetic material has been developed. It was found that it is possible to grow thin layers of α-Sn on the (0001) crystallographic surface of HCP Co. Good quality layers were obtained with thicknesses of up to 2 nm (LG002 sample).

The XFMR measurements showed that two modes of vibrations can be distinguished for LG002, whereby both of them were distributed across the Co and Py layers. Theoretical model optimisation allowed for the determination of the value of the EC parameter j to be 4.03×10^{-3} - 7.70×10^{-3}. By comparing this value with the MgO MTJ samples of similar thickness ($\sim 1.0 \times 10^{-3}$), it can be concluded that the samples with the Sn layer exhibit much stronger EC coupling between magnetic layers. The likelihood-ratio test of a model with and without SP coupling returns the λ_{LR} values that do not suggest the presence of the SP coupling in the system.

Chapter 8

Summary and conclusions

This thesis deals with the study of the dynamics of magnetisation in thin film of a single magnetic material and heterostructures consisting of two magnetic layers. A theoretical model was introduced, which allowed for a qualitative understanding of the data, and provided predictions of the effect of coupling between magnetic layers determining the static and dynamic behaviour of a system. Two types of coupling were discussed: the Heisenberg type exchange coupling and the coupling resulting from the flow of spin-currents between the magnetic layers. It was shown that both types of coupling result in different qualitative behaviour. The EC affects the static orientation of the magnetisation vectors and the conditions for ferromagnetic resonance. The SP mostly affects the peak width, illustrating the fact that the energy transferred from one layer to the other has a similar effect as the damping forces in this layer. Independent of what type of coupling is introduced, both result in normal modes of oscillation being localised on both magnetic layers, meaning that both layers vibrate at each of the vibrational modes. The main qualitative difference between the two types of coupling is predicted to be a phase shift that happens near the resonance. In case of the EC coupling, the phase shift in the second layer resembles a bell curve, while in case of SP coupling the phase shift is similar to a bipolar sigmoid function.

The experimental techniques used in this work allowed for the characterisation of the sample structure and its magnetic properties. The dynamics of the magnetisation were studied using cavity FMR, VNA-FMR, and XFMR, where each technique has its specific advantages. The employed cavity FMR system is ca-

pable of reaching high magnetic fields, enabling the estimation of the anisotropy constants and the gyromagnetic ratio of the studied magnetic material. VNA-FMR gave a detailed picture of the ferromagnetic resonance in dependence on both the magnetic field and frequency of excitation. As it was shown, due to the properties of the EC coupling, its value can be estimated by studying the ferromagnetic resonance near zero magnetic field, allowing for the estimation of the j coupling parameter using the VNA-FMR results. The XFMR experiment provided the most detailed picture of the system dynamics, including the phase and amplitude of oscillations of the individual magnetic layers. The detailed insight obtained using XFMR was used to give a precise estimation for both the j and $a^{\uparrow\downarrow}$ values in the studied samples, a procedure which is not possible using other methods.

The comparison between the experimental data and the theoretical model was done by adjusting the model parameters to obtain the best match between the two. The goodness of the model was measured using likelihood function, which was optimised using the conjugate-gradient algorithm. For each of the experimental techniques, the cavity FMR, VNA-FMR, and XFMR, a custom computer code was implemented. In case of the XFMR measurements, two hypothesis were investigated: one stating that EC is the only coupling in the system (null hypothesis) and second stating that both EC and SP occur in the system (alternative hypothesis). The comparison between the two hypotheses was performed using the likelihood-ratio test, which is the most powerful test among all possible statistical tests. The approach resulted in a powerful tool that is capable of determining whether SP is present in the studied system.

8.1 Summary of the results for the MgO samples

The applicability of the presented model, and the suitability of the experimental scheme, were verified studying the magnetisation dynamics in MgO-based magnetic tunnel junctions. The samples contained two magnetic layers: Py and Co(HCP), separated by an insulating MgO layer. Its thickness was varied, and chosen to be small enough to allow for the magnetic layers to interact, but thick enough to prevent direct electrical contact between them. It was found that a

thickness of 1.5 nm was optimal. The study of the layers' magnetic anisotropies showed that the uni-axial model is adequate for 5 nm thick Py and Co layers. For samples with thicker Co layers, it was found that the uni-axial model does not reproduce the experimental results. It was concluded that for Co layer thicknesses greater than 5 nm, the Co film shows a mixture of HCP and FCC crystalline phases. The XFMR measurements showed a strong coupling between the magnetic layers. Two normal modes of vibration were found, where each of the oscillation modes showed signals at both the Co and Ni absorption edges. The experimental results were compared with the theoretical models, and the likelihood-ratio test was performed to test the existence of SP in the system. It was proven that both, EC and SP coupling exist in the studied samples. The values for j and $a^{\uparrow\downarrow}$ were found for the sample at room temperature (300 K) and at 80 K. It was found that $a^{\uparrow\downarrow}$ is about twice as high at 80 K than it is at room temperature.

8.2 Summary of the results for the tin samples

The possibility of using α-Sn as a spacer between the magnetic layers in a spin-valve structure was explored. The deposition of tin onto the HCP Co(0001) surface resulted in the growth dominated by α-Sn. The RHEED images show that in the initial phases of the Sn growth, its lattice constant is double of that of Co, and that it has a 6-fold symmetry. Deposition of more than a few molecular layers of Sn resulted in pillar growth. The research was focused on optimising the growth conditions to obtain Sn layers with low roughness. It was found that the best results are obtained for the substrate held at a low temperatures. Co/Sn/Py heterostructures were fabricated, and the structural properties of the sample were investigated at temperatures in the range between $80\,\mathrm{K} - 328\,\mathrm{K}$ using XRD and XRR techniques. No phase transition of the Sn layer was observed. The dynamics of the magnetisation of the Co and Py layers were studied using XFMR at temperatures in the range of $80\,\mathrm{K} - 328\,\mathrm{K}$. A strong coupling between the Co and Py layers was observed. A comparison between the theoretical model and the experimental results showed a strong EC, and did not provide evidence for SP in the studied samples. The negative result is most probably caused by the poor quality of the fabricated samples, as it was evident in the TEM images.

8.3 Perspective for further research

The conducted research gave an insight into the fundamental aspects of the heterostructures, incorporating layers of magnetic materials, and it displayed clear avenues for further investigations. The theoretical modelling and the likelihood-ratio testing provide useful tools for studying the XFMR results, and for reliably determining the existence of SP in the system. Such investigations can be used to study how the system parameters, such as layer thickness, magnetic anisotropy, and interface between magnetic material and the insulating layers, affect the value of the SP coupling parameter. It has been shown that incorporating Sn into the system is a troubling task, and several research paths have been explored and rejected. Those negative results will be helpful for other researchers trying to evaluate Sn spacer layer further. In my opinion, the most promising approach would be to perform the Sn growth with the substrate temperature decreased to about 100 K.

This work resulted in two peer-reviewed publications that summarise our work on MgO-based magnetic tunnel junctions [84] and α-Sn spin valve systems [85]. It is the first time such a detailed comparison between XFMR data and micromagnetic theory has been done successfully. We believe that the results are of importance for the magnetism community.

Appendix A

Extrema of the energy potential

In chapter 2, possible orientations of the magnetisation vector were discussed for an energy functional given by:

$$E' = \frac{E}{|D|M_s} = \begin{cases} -\frac{1}{2}\cos^2\theta - b\left[\cos\theta\cos\theta_H + \cos\left(\phi-\phi_H\right)\sin\theta\sin\theta_H\right] & D>0 \\ -\frac{1}{2}\cos^2\theta + b\left[\cos\theta\cos\theta_H + \cos\left(\phi-\phi_H\right)\sin\theta\sin\theta_H\right] & D<0 \end{cases} . \tag{A.1}$$

For a given orientation of the magnetisation to be valid at a given external magnetic field (θ, ϕ), it must minimise the potential energy of the system. For a system parametrised with two variables, this is achieved when the first derivatives of the potential energy are zero:

$$\frac{\partial E}{\partial \theta} = 0 \quad \text{and} \quad \frac{\partial E}{\partial \phi} = 0 \quad , \tag{A.2}$$

and the second derivatives satisfy (as long as $0 < \theta < \pi$ and $0 < \theta_H < \pi$):

$$\frac{\partial^2 E}{\partial \theta^2} + \frac{\partial^2 E}{\partial \phi^2} > 0, \quad \text{and} \quad \frac{\partial^2 E}{\partial \phi^2}\frac{\partial^2 E}{\partial \theta^2} - \left(\frac{\partial^2 E}{\partial \phi \partial \theta}\right)^2 > 0 \quad . \tag{A.3}$$

Applying the second condition (A.2) to the studied functional results in:

$$b\sin\theta\sin\theta_H\sin\left(\phi-\phi_H\right) = 0 \quad , \tag{A.4}$$

which is satisfied only for $\phi = \phi_H$ or $\phi = \pi + \phi_H$. Using this result, the first condition in (A.2) can be expressed as:

$$\begin{cases} 2b\sin(\theta-\theta_H) + \sin 2\theta = 0 & \text{for } D>0 \text{ and } \phi = \phi_H \\ 2b\sin(\theta+\theta_H) + \sin 2\theta = 0 & \text{for } D>0 \text{ and } \phi = \phi_H + \pi \\ 2b\sin(\theta-\theta_H) - \sin 2\theta = 0 & \text{for } D<0 \text{ and } \phi = \phi_H \\ 2b\sin(\theta+\theta_H) - \sin 2\theta = 0 & \text{for } D<0 \text{ and } \phi = \phi_H + \pi \end{cases} . \tag{A.5}$$

This gives all possible extremum points. The type of the extremum can be checked using (A.3) assuming that $\theta \in (0, \pi)$, $\theta_H \in (0, \pi)$ and $b > 0$.

A.0.1 $D > 0$, $\phi = \phi_H$

In the first case of $D > 0$, a solution with $\phi = \phi_H$ is a stable equilibrium iff[1]

$$\begin{array}{c} \cos 2\theta + b \cos\theta \cos\theta_H + 2b \sin\theta \sin\theta_H > 0 \\ \cos 2\theta + b \cos\theta \cos\theta_H + b \sin\theta \sin\theta_H > 0 \end{array} , \tag{A.6}$$

where the first and second equation are the explicit form of the (A.3) conditions. It is noted that the first condition is always met when the second one is fulfilled. This results in a single condition for a stable equilibrium that can be summarised as:

$$\cos 2\theta + b \cos(\theta - \theta_H) > 0 \quad . \tag{A.7}$$

A.0.2 $D > 0$, $\phi = \phi_H + \pi$

In the second case of $D > 0$, a solution with $\phi = \phi_H + \pi$ is a stable equilibrium iff:

$$\begin{array}{c} \cos 2\theta + b \cos\theta \cos\theta_H - 2b \sin\theta \sin\theta_H > 0 \\ \cos 2\theta + b \cos\theta \cos\theta_H - b \sin\theta \sin\theta_H < 0 \end{array} , \tag{A.8}$$

where the first and second equation are the explicit form of the (A.3) conditions. The first and second conditions are contradictory (i.e., cannot be meet at any point). Therefore, no stable equilibrium position exists in this case.

A.0.3 $D < 0$, $\phi = \phi_H$

In the first case of $D < 0$, a solution with $\phi = \phi_H$ is a stable equilibrium iff:

$$\begin{array}{c} \cos 2\theta - b \cos\theta \cos\theta_H - 2b \sin\theta \sin\theta_H < 0 \\ \cos 2\theta - b \cos\theta \cos\theta_H - b \sin\theta \sin\theta_H < 0 \end{array} , \tag{A.9}$$

where the first and second equation are the explicit form of the (A.3) conditions. It is noted that the first condition is always met when the second one is fulfilled. This results in a single condition for a stable equilibrium that can be summarised as:

$$\cos 2\theta - b \cos(\theta - \theta_H) < 0 \quad . \tag{A.10}$$

[1] if and only if

A.0.4 $D < 0$, $\phi = \phi_H + \pi$

In the second case of $D > 0$, a solution with $\phi = \phi_H + \pi$ is a stable equilibrium iff:

$$\begin{array}{c} \cos 2\theta - b\cos\theta\cos\theta_H + 2b\sin\theta\sin\theta_H < 0 \\ \cos 2\theta - b\cos\theta\cos\theta_H + b\sin\theta\sin\theta_H > 0 \end{array} \quad , \tag{A.11}$$

where the first and second equation are the explicit form of the (A.3) conditions. The first and second condition are contradictory (i.e., cannot be meet at any point). Therefore, no stable equilibrium position exists in this case.

A.1 Edge cases

The edge cases of $\theta = 0$ and $\theta = \pi$ need to be treated separately. The first point to check is if the energy function is a smooth function around the poles: $\theta = 0$ and $\theta = \pi$. This is done by expanding the potential energy around these points up to the first term in the Taylor series (here, the case of $D > 0$ and $\theta = 0$ is presented):

$$E(\theta, \phi) \approx \left(-\frac{1}{2} - b\cos\theta_H\right) - \left[b\cos(\phi - \phi_H)\sin\theta_H\right]\theta + O(\theta^2) \quad . \tag{A.12}$$

As this function is of the form:

$$E(\theta, \phi) = A + B\sin(\phi + \phi_0)\,\theta + O(\theta^2) \quad , \tag{A.13}$$

it is concluded that the energy function is smooth around the poles of the spherical coordinate system. The same procedure can be repeated for other cases giving the same result. One can then check if $\theta = 0$ and $\theta = \pi$ are a stable equilibria by checking the conditions:

$$\frac{\partial E}{\partial \theta} = 0 \quad \text{and} \quad \frac{\partial^2 E}{\partial \theta^2} > 0 \quad . \tag{A.14}$$

The first condition gives (independent on sign of D):

$$b\cos(\phi - \phi_H)\sin\theta_H = 0 \quad , \tag{A.15}$$

which means that these point can only be extrema of the energy function if $\theta_H = 0$ or $\theta_H = \pi$. The second condition demands for a point to be a minimum:

$$\begin{cases} 1 + b\cos\theta_H > 0 & \text{for } D > 0 \text{ and } \theta = 0 \\ 1 - b\cos\theta_H > 0 & \text{for } D > 0 \text{ and } \theta = \pi \\ -1 + b\cos\theta_H > 0 & \text{for } D < 0 \text{ and } \theta = 0 \\ -1 - b\cos\theta_H > 0 & \text{for } D < 0 \text{ and } \theta = \pi \end{cases} , \tag{A.16}$$

which concludes the characterisation of the extreme points at $\theta = 0$ and $\theta = \pi$.

Appendix B

Static solutions for an uni-axial anisotropy with two terms

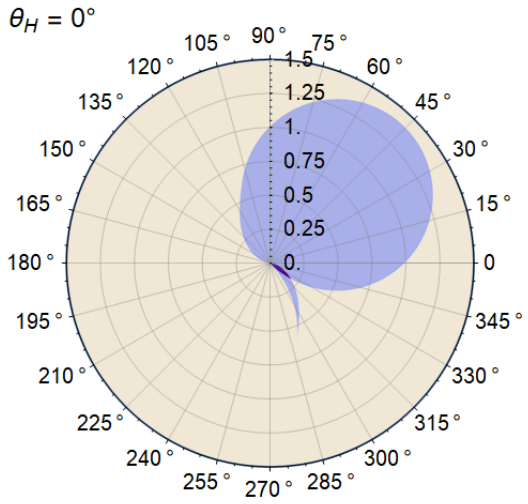
θ_H = 0°
90 °
75 °
60 °
45 °
30 °
15 °
0
345 °
330 °
315 °
300 °
285 °
270 °
255 °
240 °
225 °
210 °
195 °
180 °
165 °
150 °
135 °
120 °
105 °
1.5
1.25
1.
0.75
0.5
0.25
0.

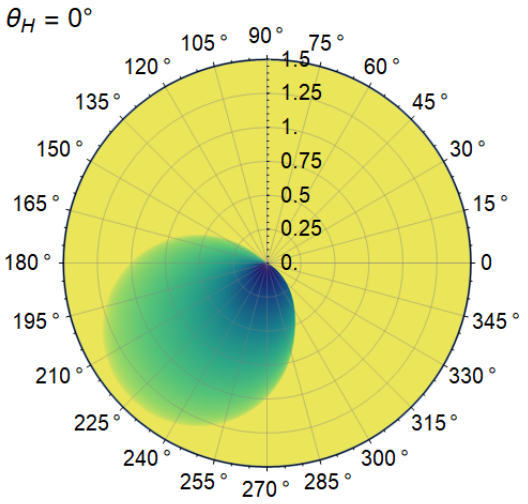
θ_H = 0°
90 °
75 °
60 °
45 °
30 °
15 °
0
345 °
330 °
315 °
300 °
285 °
270 °
255 °
240 °
225 °
210 °
195 °
180 °
165 °
150 °
135 °
120 °
105 °
1.5
1.25
1.
0.75
0.5
0.25
0.

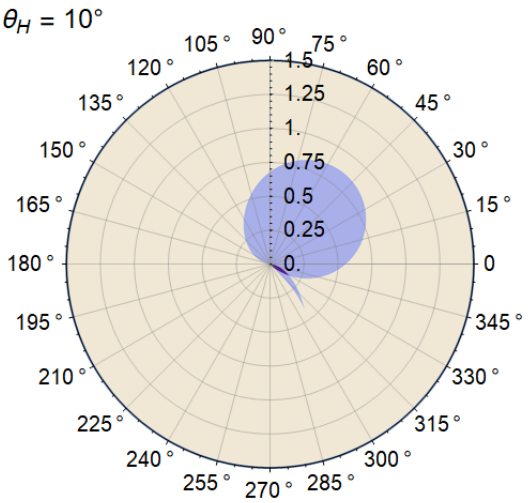
θ_H = 10°
90 °
75 °
60 °
45 °
30 °
15 °
0
345 °
330 °
315 °
300 °
285 °
270 °
255 °
240 °
225 °
210 °
195 °
180 °
165 °
150 °
135 °
120 °
105 °
1.5
1.25
1.
0.75
0.5
0.25
0.

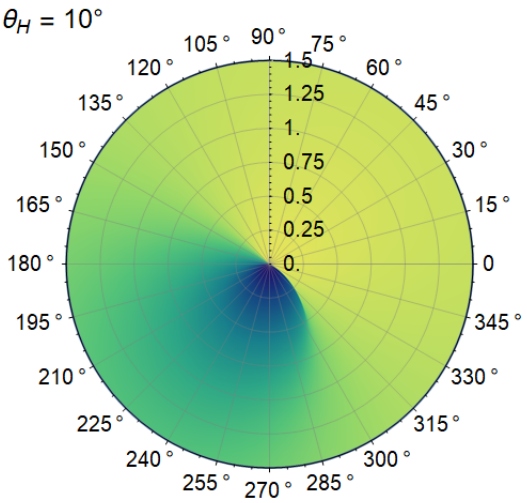
θ_H = 10°
90 °
75 °
60 °
45 °
30 °
15 °
0
345 °
330 °
315 °
300 °
285 °
270 °
255 °
240 °
225 °
210 °
195 °
180 °
165 °
150 °
135 °
120 °
105 °
1.5
1.25
1.
0.75
0.5
0.25
0.

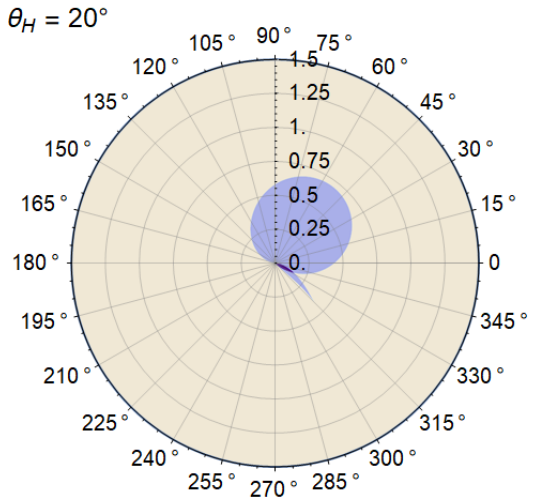
θ_H = 20°
90° 75° 60° 45° 30° 15° 0° 345° 330° 315° 300° 285° 270° 255° 240° 225° 210° 195° 180° 165° 150° 135° 120° 105°
1.5 1.25 1. 0.75 0.5 0.25 0.

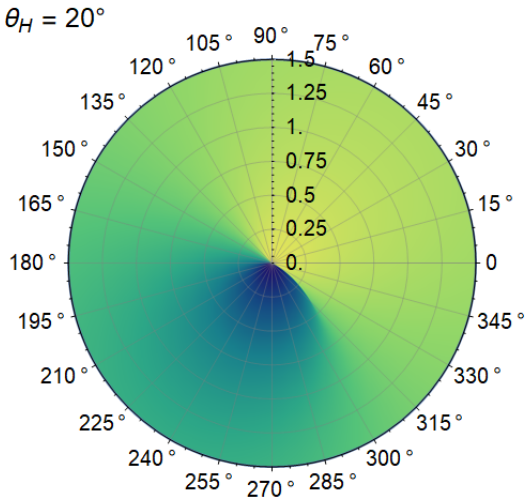
θ_H = 20°
90° 75° 60° 45° 30° 15° 0° 345° 330° 315° 300° 285° 270° 255° 240° 225° 210° 195° 180° 165° 150° 135° 120° 105°
1.5 1.25 1. 0.75 0.5 0.25 0.

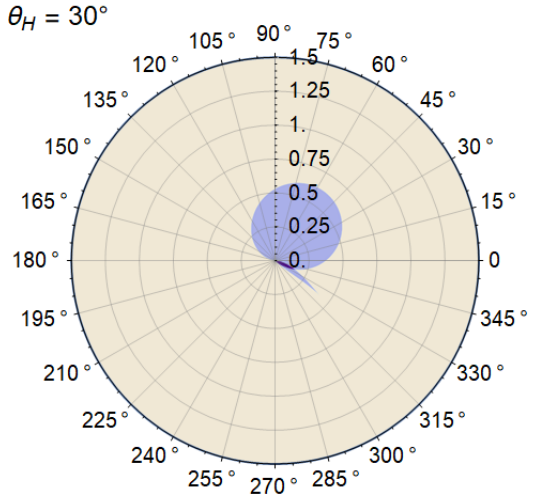
θ_H = 30°
90° 75° 60° 45° 30° 15° 0° 345° 330° 315° 300° 285° 270° 255° 240° 225° 210° 195° 180° 165° 150° 135° 120° 105°
1.5 1.25 1. 0.75 0.5 0.25 0.

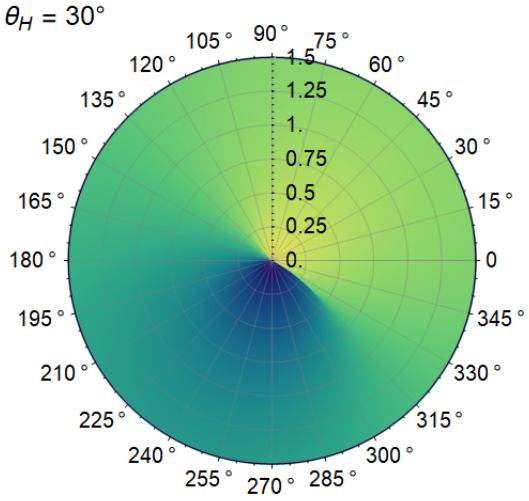
θ_H = 30°
90° 75° 60° 45° 30° 15° 0° 345° 330° 315° 300° 285° 270° 255° 240° 225° 210° 195° 180° 165° 150° 135° 120° 105°
1.5 1.25 1. 0.75 0.5 0.25 0.

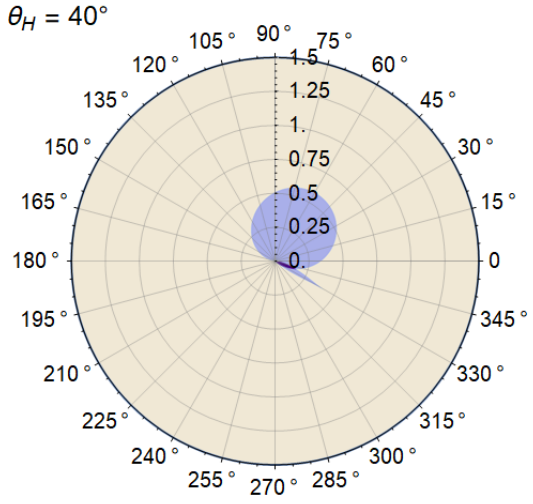
θ_H = 40°
90° 75° 60° 45° 30° 15° 0° 345° 330° 315° 300° 285° 270° 255° 240° 225° 210° 195° 180° 165° 150° 135° 120° 105°
1.5 1.25 1. 0.75 0.5 0.25 0.

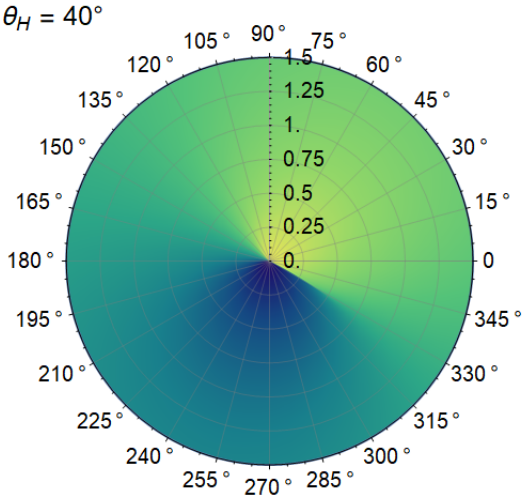
θ_H = 40°
90° 75° 60° 45° 30° 15° 0° 345° 330° 315° 300° 285° 270° 255° 240° 225° 210° 195° 180° 165° 150° 135° 120° 105°
1.5 1.25 1. 0.75 0.5 0.25 0.

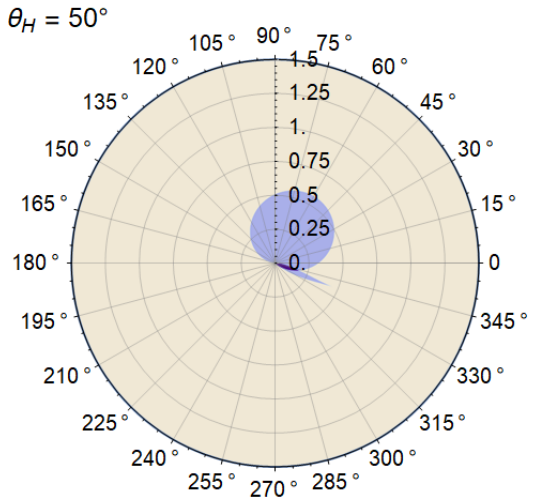
θ_H = 50°
90°
75°
60°
45°
30°
15°
0
345°
330°
315°
300°
285°
270°
255°
240°
225°
210°
195°
180°
165°
150°
135°
120°
105°
1.5
1.25
1.
0.75
0.5
0.25
0.

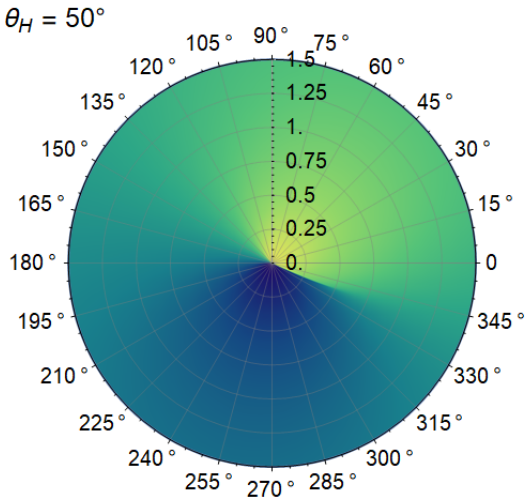
θ_H = 50°
90°
75°
60°
45°
30°
15°
0
345°
330°
315°
300°
285°
270°
255°
240°
225°
210°
195°
180°
165°
150°
135°
120°
105°
1.5
1.25
1.
0.75
0.5
0.25
0.

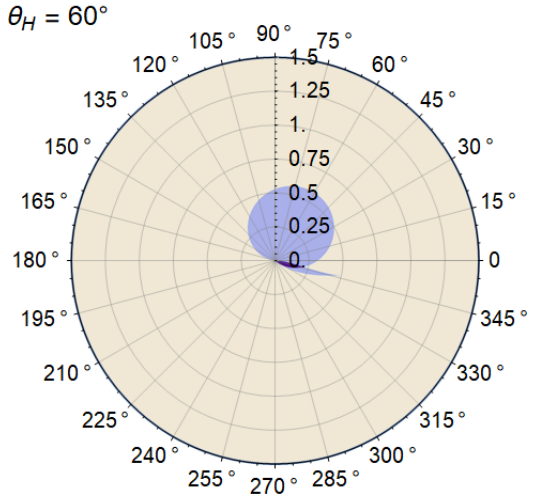
θ_H = 60°
90°
75°
60°
45°
30°
15°
0
345°
330°
315°
300°
285°
270°
255°
240°
225°
210°
195°
180°
165°
150°
135°
120°
105°
1.5
1.25
1.
0.75
0.5
0.25
0.

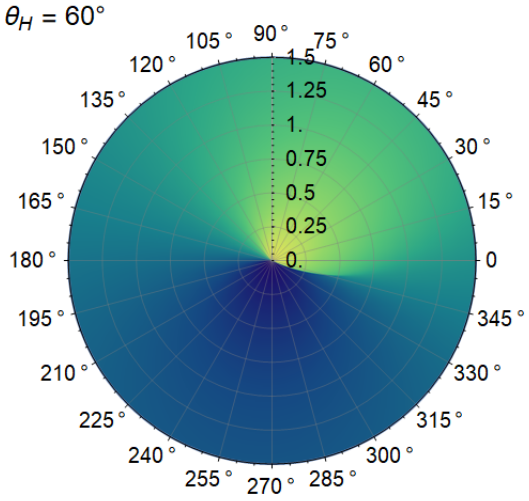
θ_H = 60°
90°
75°
60°
45°
30°
15°
0
345°
330°
315°
300°
285°
270°
255°
240°
225°
210°
195°
180°
165°
150°
135°
120°
105°
1.5
1.25
1.
0.75
0.5
0.25
0.

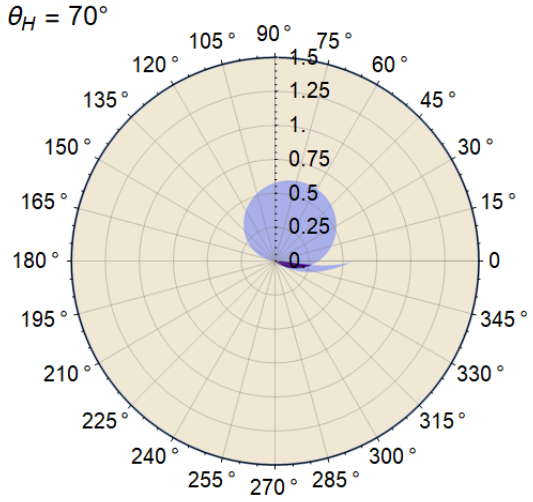
θ_H = 70°
90°
75°
60°
45°
30°
15°
0
345°
330°
315°
300°
285°
270°
255°
240°
225°
210°
195°
180°
165°
150°
135°
120°
105°
1.5
1.25
1.
0.75
0.5
0.25
0.

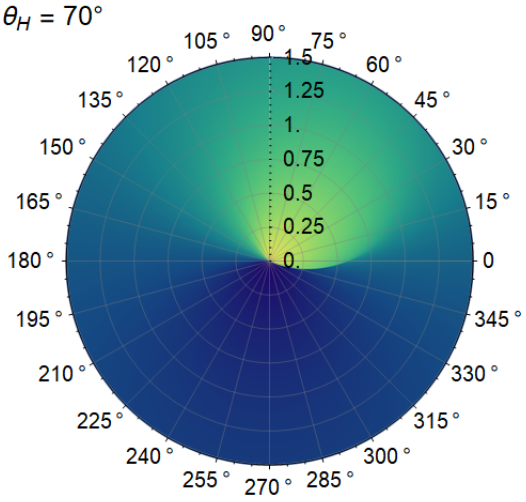
θ_H = 70°
90°
75°
60°
45°
30°
15°
0
345°
330°
315°
300°
285°
270°
255°
240°
225°
210°
195°
180°
165°
150°
135°
120°
105°
1.5
1.25
1.
0.75
0.5
0.25
0.

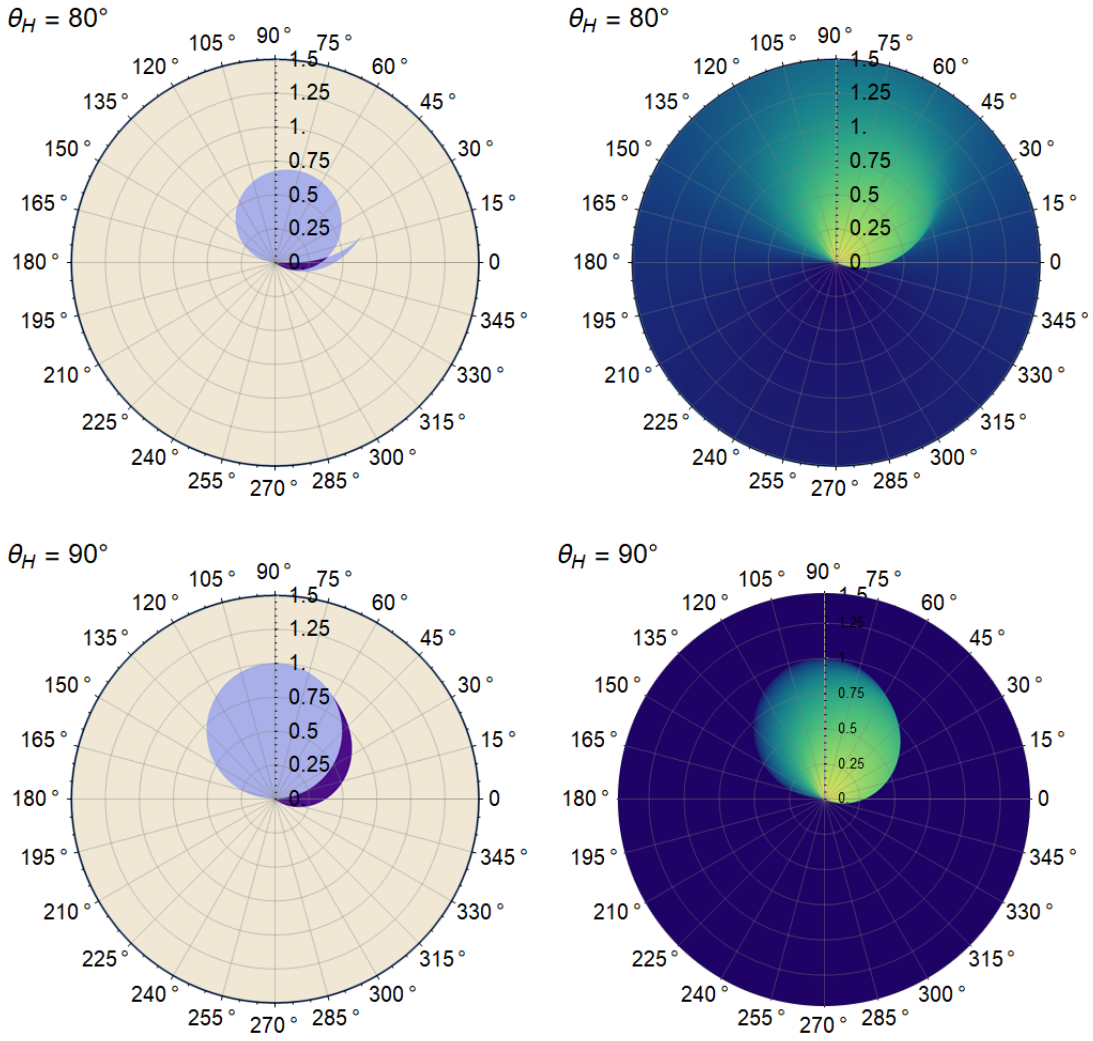

Figure B.1: Number of solutions (left) and orientation of the magnetisation θ at the global energy minimum (right) in dependence on the anisotropy (the azimuthal angle ψ), and the field strength (b is distance from the centre), at different orientations of the external magnetic field (θ_H) as indicated.

Appendix C

XFMR measurements for the S1655_II sample

Results of the XFMR measurements and theoretical model fits for the sample S1655_II at room temperature and at 80 K are shown on the figures below. Orange and blue points were used to mark the experimental data for Co and Py, respectively. Solid lines represent the theoretical model fit. The dashed lines refer to the EC-only model and the continuous lines to the EC&SP model.

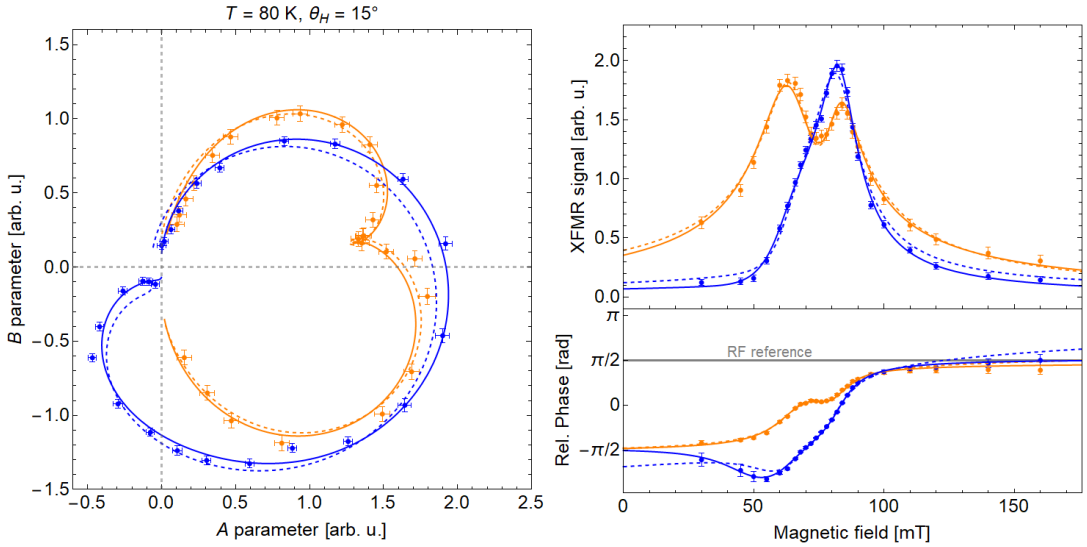

Figure C.1: XFMR results for S1655_II at 80 K, and the external field direction $\theta_H = 15°$. Orange and blue point represent the data for Co and Py, respectively.

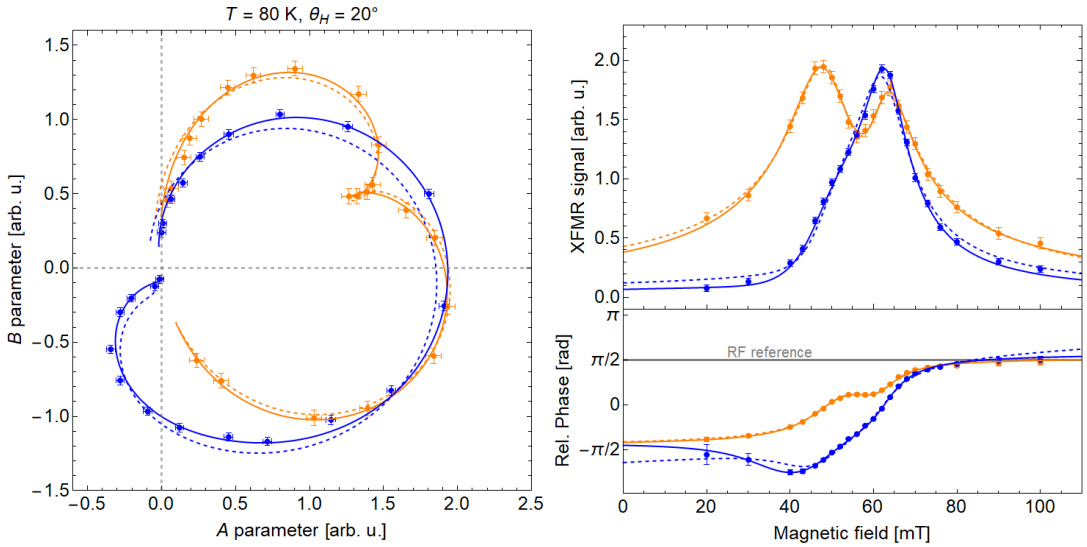

Figure C.2: XFMR results for S1655_II at 80 K, and the external field direction $\theta_H = 20°$. Orange and blue point represent the data for Co and Py, respectively.

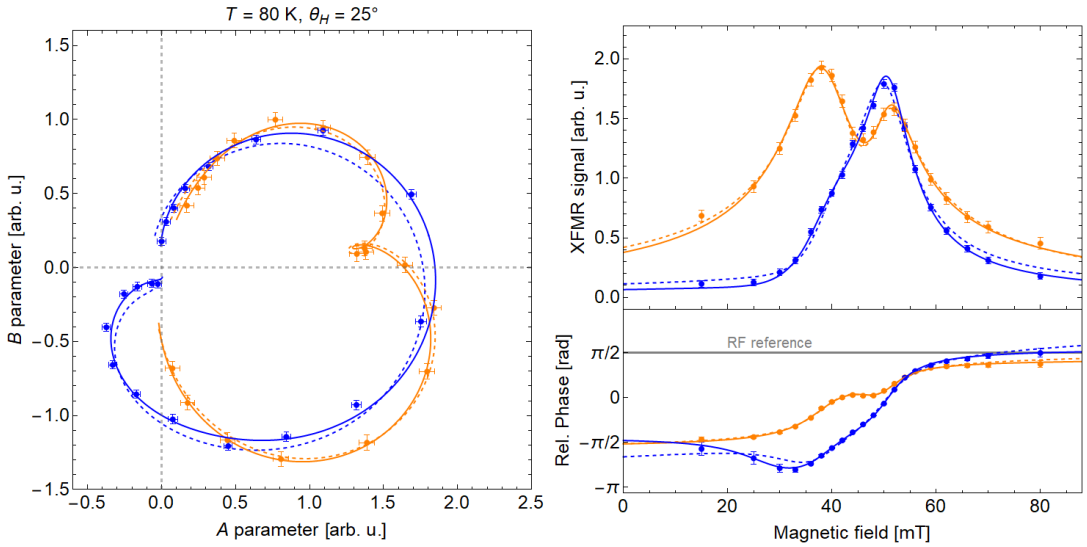

Figure C.3: XFMR results for S1655_II at 80 K, and the external field direction $\theta_H = 25°$. Orange and blue point represent the data for Co and Py, respectively.

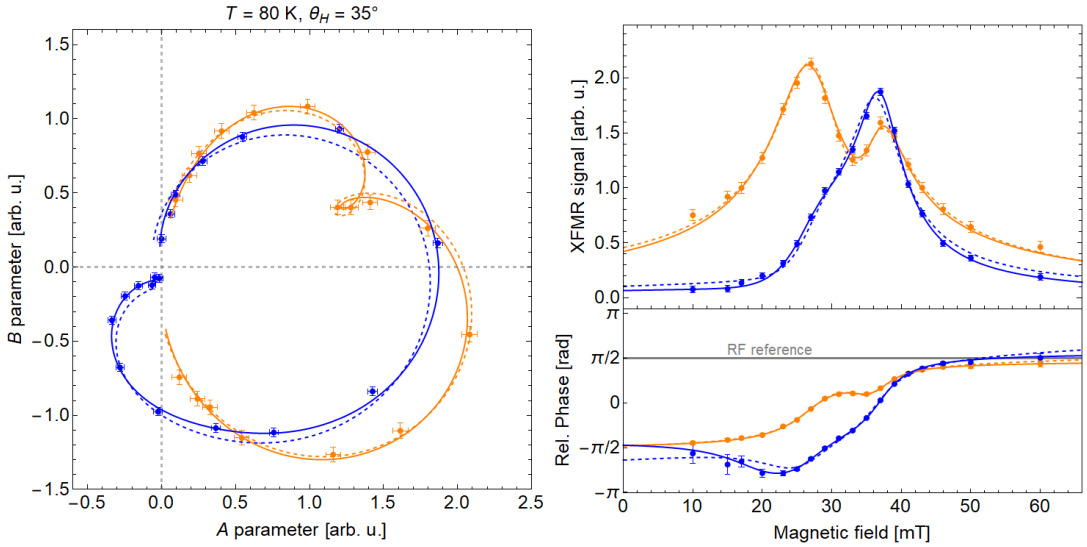

Figure C.4: XFMR results for S1655_II at 80 K, and the external field direction $\theta_H = 35°$. Orange and blue point represent the data for Co and Py, respectively.

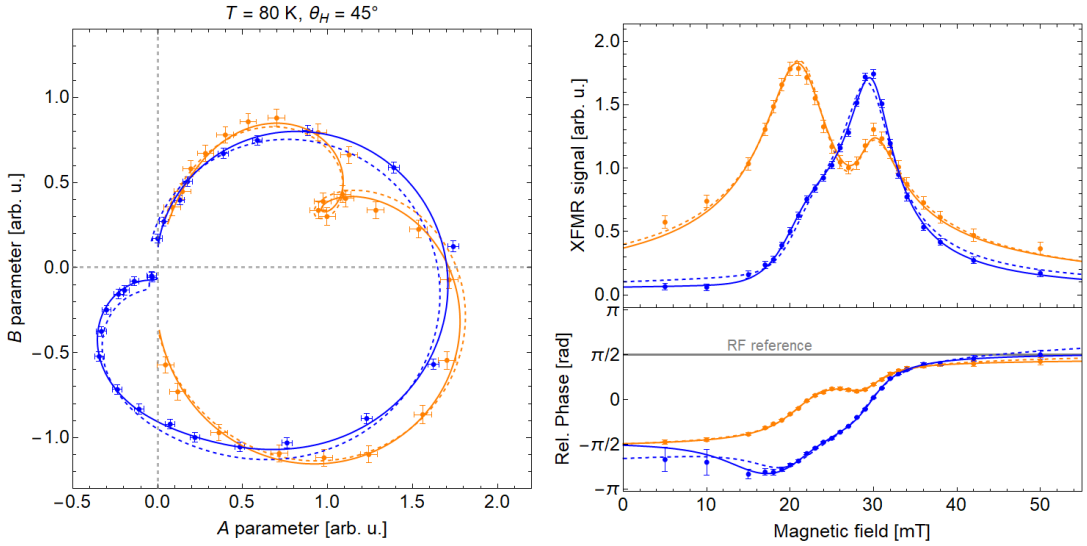

Figure C.5: XFMR results for S1655_II at 80 K, and the external field direction $\theta_H = 45°$. Orange and blue point represent the data for Co and Py, respectively.

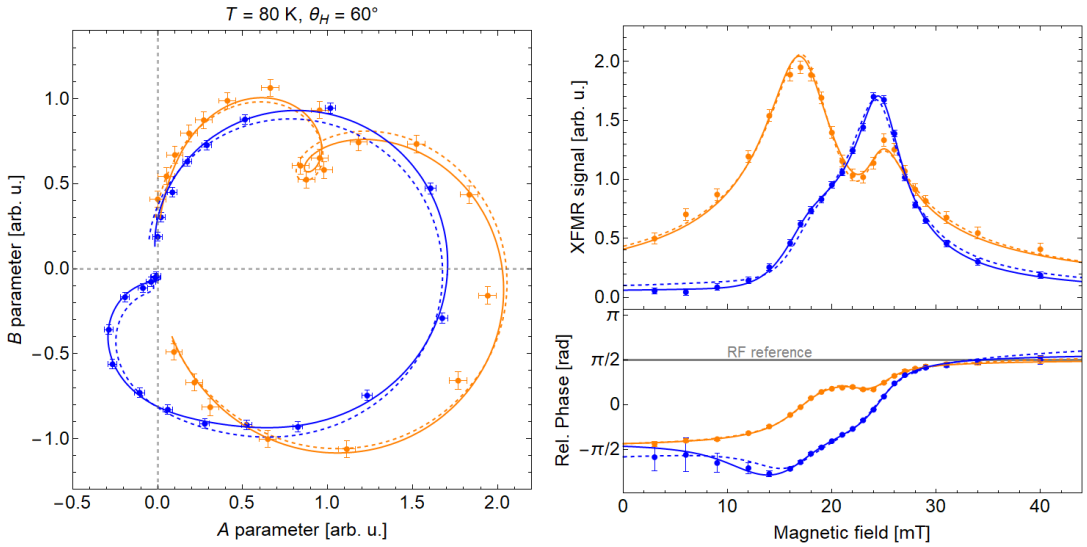

Figure C.6: XFMR results for S1655_II at 80 K, and the external field direction $\theta_H = 60°$. Orange and blue point represent the data for Co and Py, respectively.

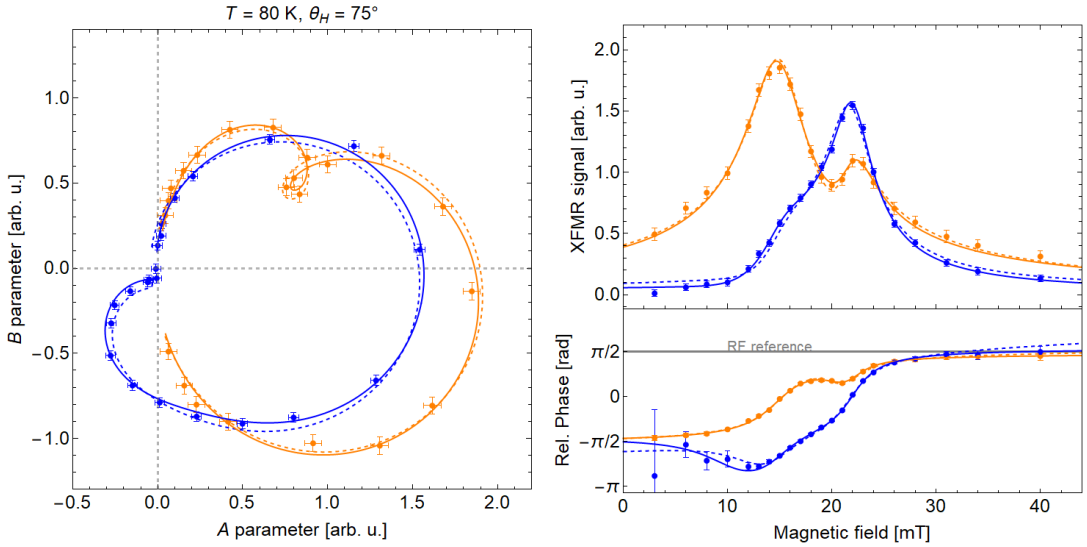

Figure C.7: XFMR results for S1655_II at 80 K, and the external field direction $\theta_H = 75°$. Orange and blue point represent the data for Co and Py, respectively.

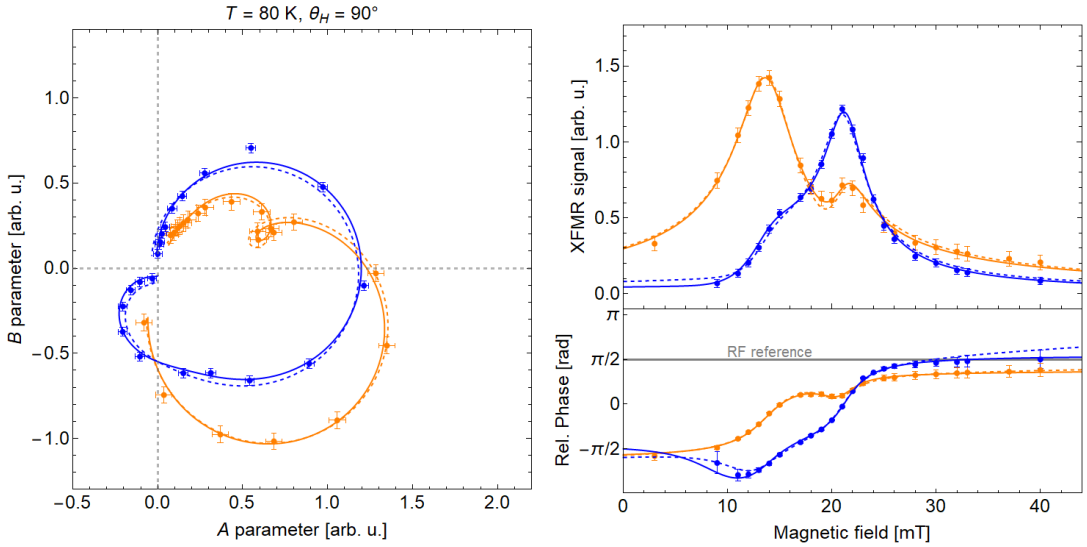

Figure C.8: XFMR results for S1655_II at 80 K, and the external field direction $\theta_H = 90°$. Orange and blue point represent the data for Co and Py, respectively.

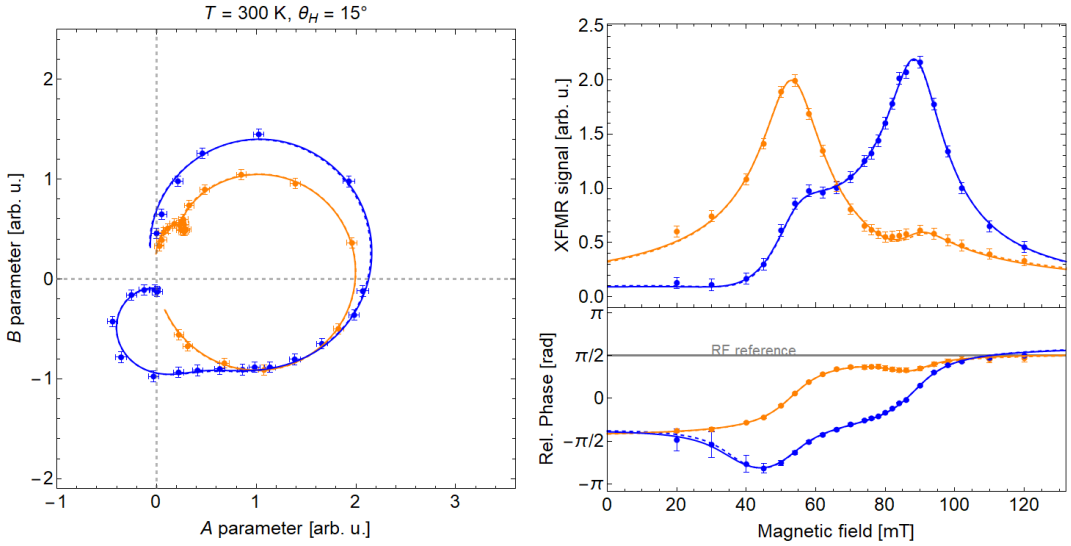

Figure C.9: XFMR results for S1655_II at 300 K, and the external field direction $\theta_H = 15°$. Orange and blue point represent the data for Co and Py, respectively.

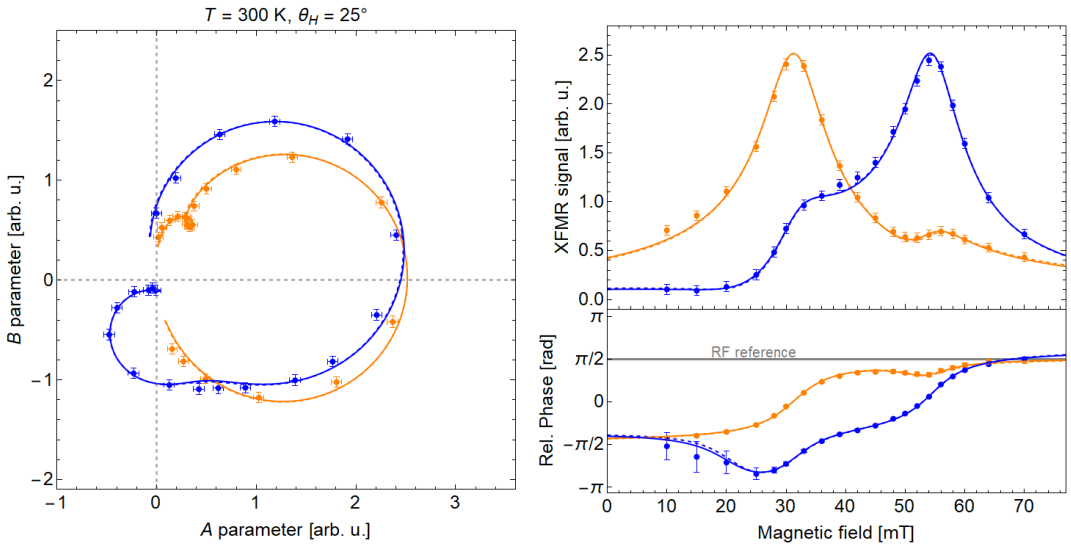

Figure C.10: XFMR results for S1655_II at 300 K, and the external field direction $\theta_H = 25°$. Orange and blue point represent the data for Co and Py, respectively.

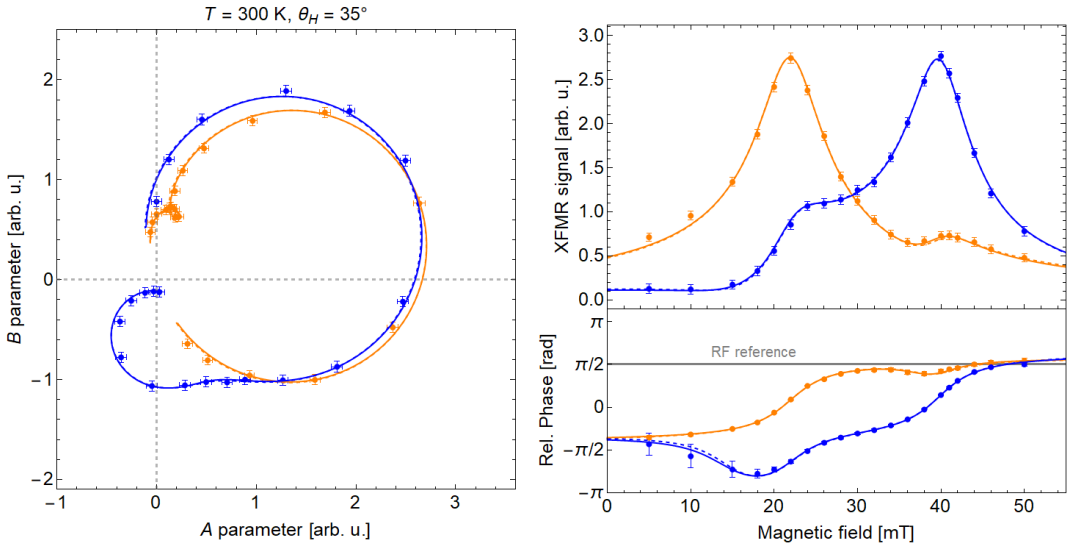

Figure C.11: XFMR results for S1655_II at 300 K, and the external field direction $\theta_H = 35°$. Orange and blue point represent the data for Co and Py, respectively.

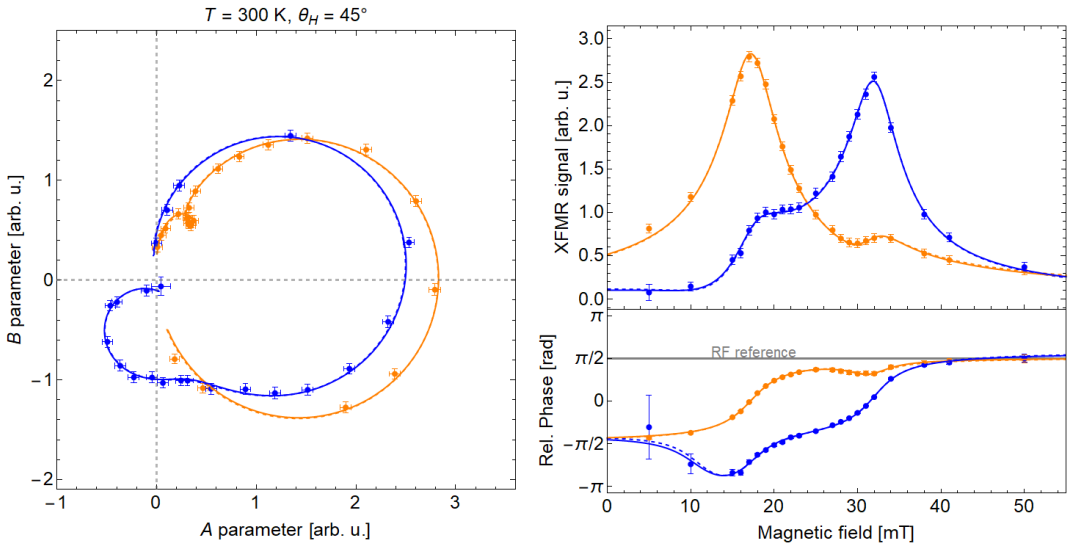

Figure C.12: XFMR results for S1655_II at 300 K, and the external field direction $\theta_H = 45°$. Orange and blue point represent the data for Co and Py, respectively.

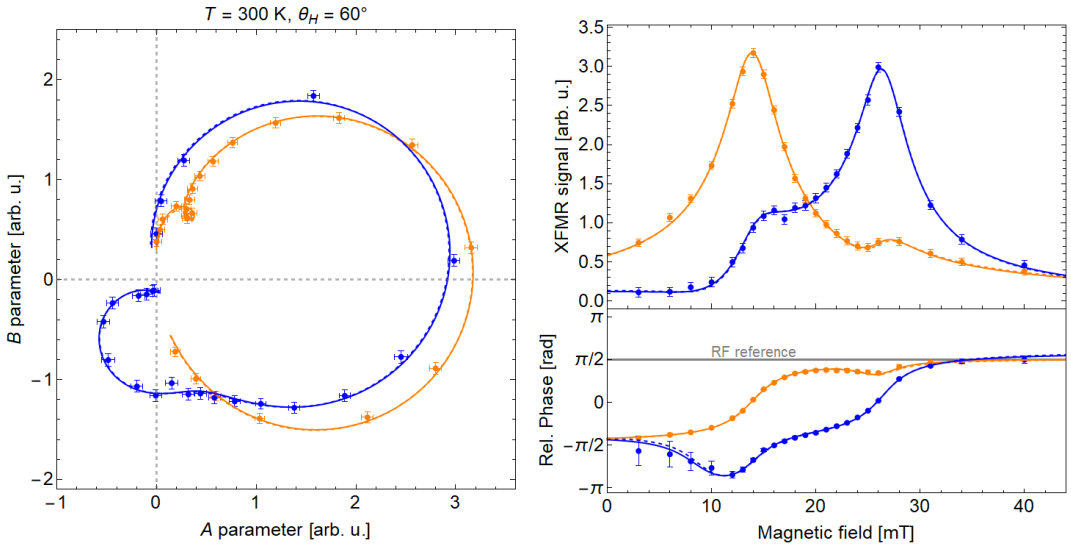

Figure C.13: XFMR results for S1655_II at 300 K, and the external field direction $\theta_H = 60°$. Orange and blue point represent the data for Co and Py, respectively.

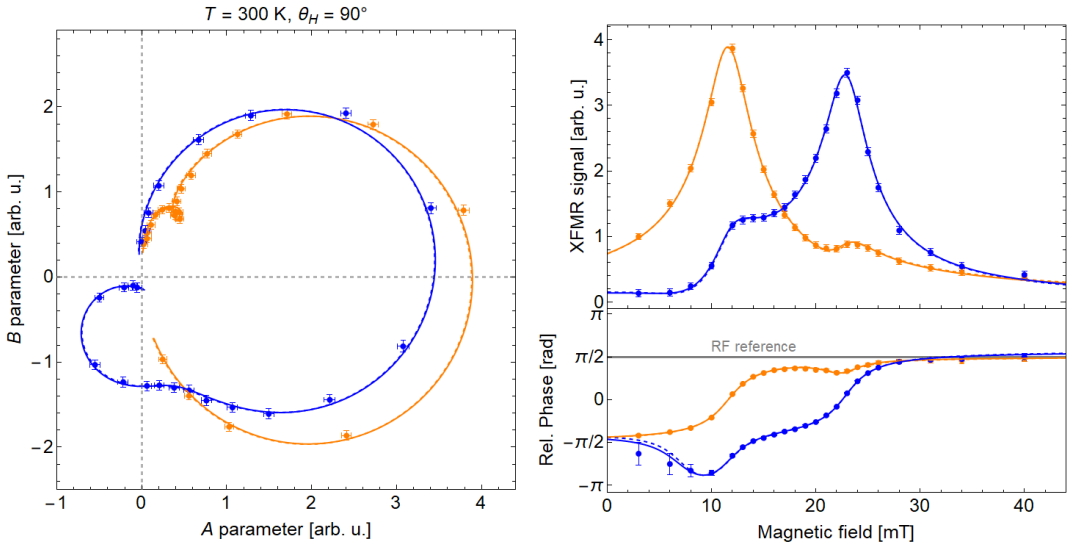

Figure C.14: XFMR results for S1655_II at 300 K, and the external field direction $\theta_H = 90°$. Orange and blue point represent the data for Co and Py, respectively.

Appendix D

XFMR measurements for the LG002 sample

Results of the XFMR measurements and theoretical model fits for the sample LG002 measured with the magnetic field directed in-plane of the sample ($\theta_H = 90°$) at temperatures in range between 80K and 328K. Orange and blue points were used to mark the experimental data for Co and Py respectively. Solid lines represent the theoretical model fit. The semitransparent lines refer to the model with EC only and the opaque lines to the model with EC and SP.

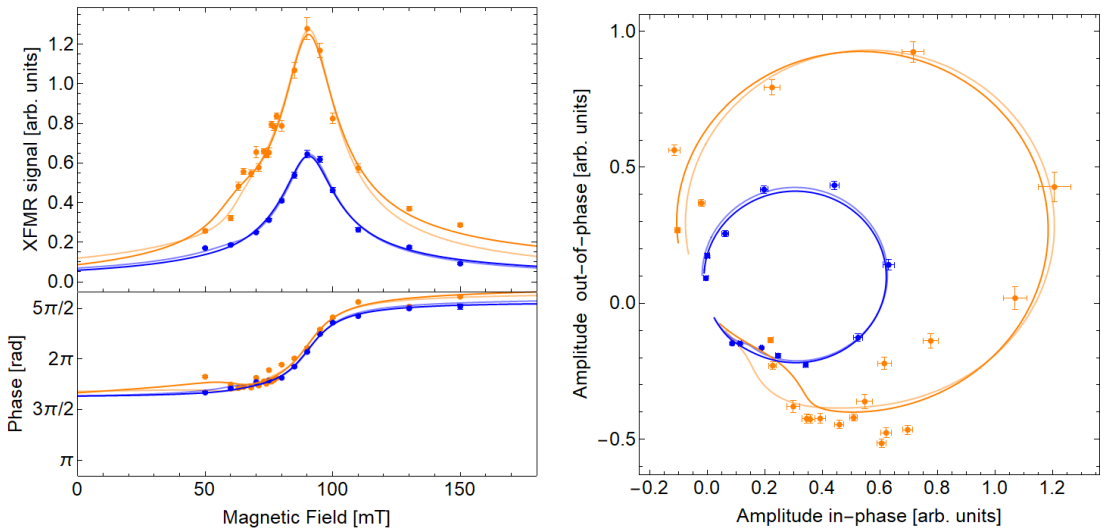

Figure D.1: XFMR results for the LG002 sample at 80 K, and the external field direction $\theta_H = 90°$. Orange and blue point represent the data for Co and Py respectively.

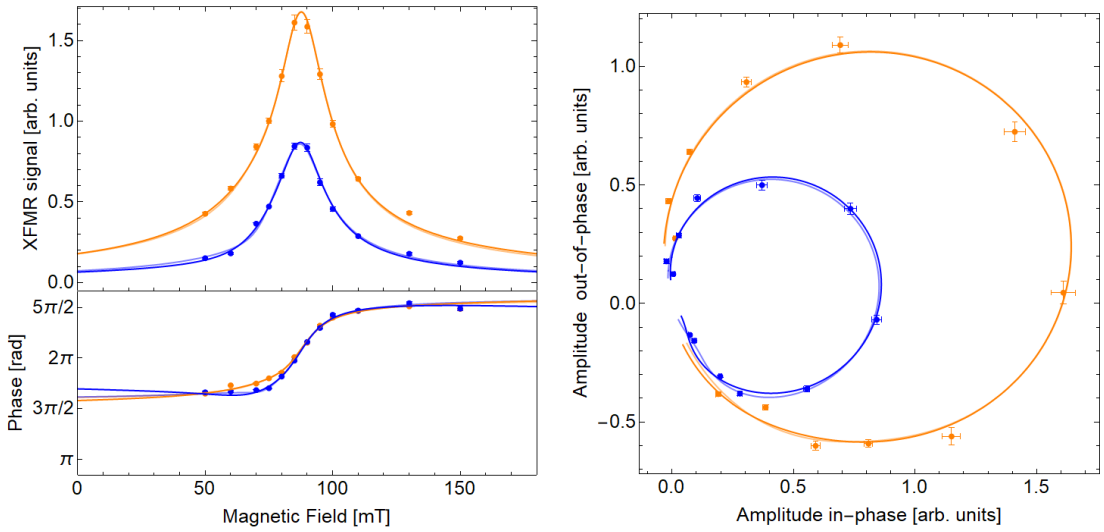

Figure D.2: XFMR results for the LG002 sample at 152 K, and the external field direction $\theta_H = 90°$. Orange and blue point represent the data for Co and Py respectively.

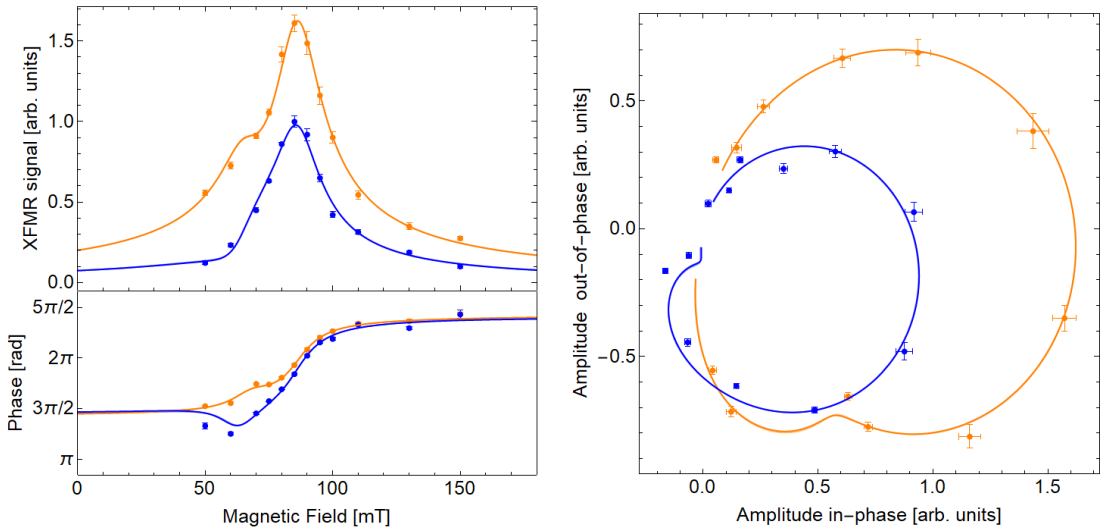

Figure D.3: XFMR results for the LG002 sample at 199 K, and the external field direction $\theta_H = 90°$. Orange and blue point represent the data for Co and Py respectively.

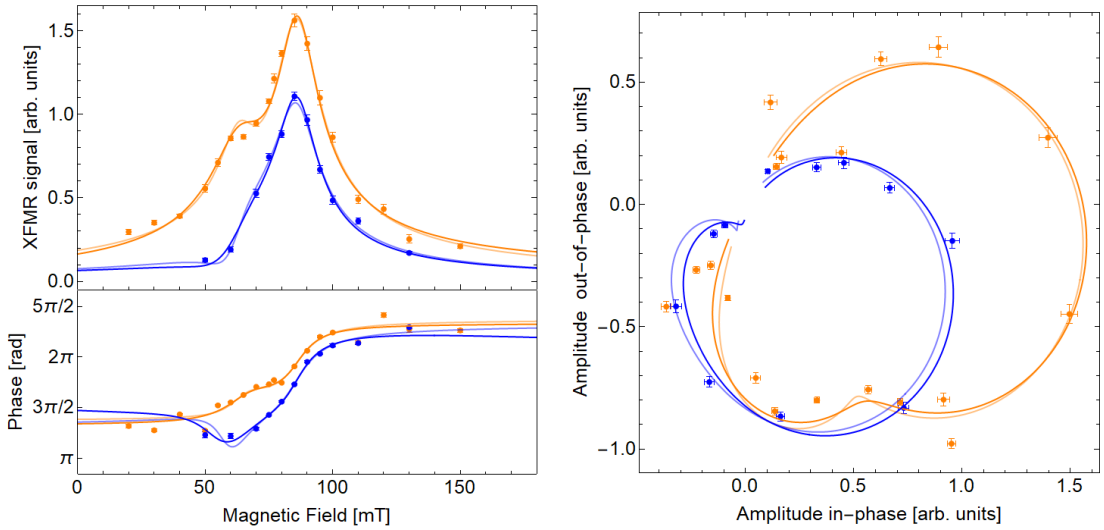

Figure D.4: XFMR results for the LG002 sample at 218 K, and the external field direction $\theta_H = 90°$. Orange and blue point represent the data for Co and Py respectively.

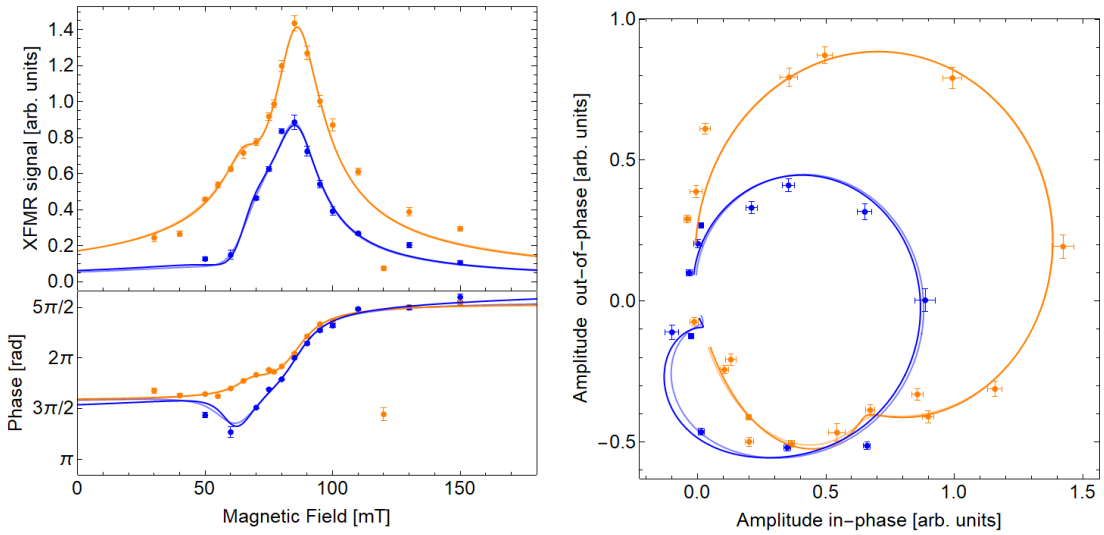

Figure D.5: XFMR results for the LG002 sample at 246 K, and the external field direction $\theta_H = 90°$. Orange and blue point represent the data for Co and Py respectively.

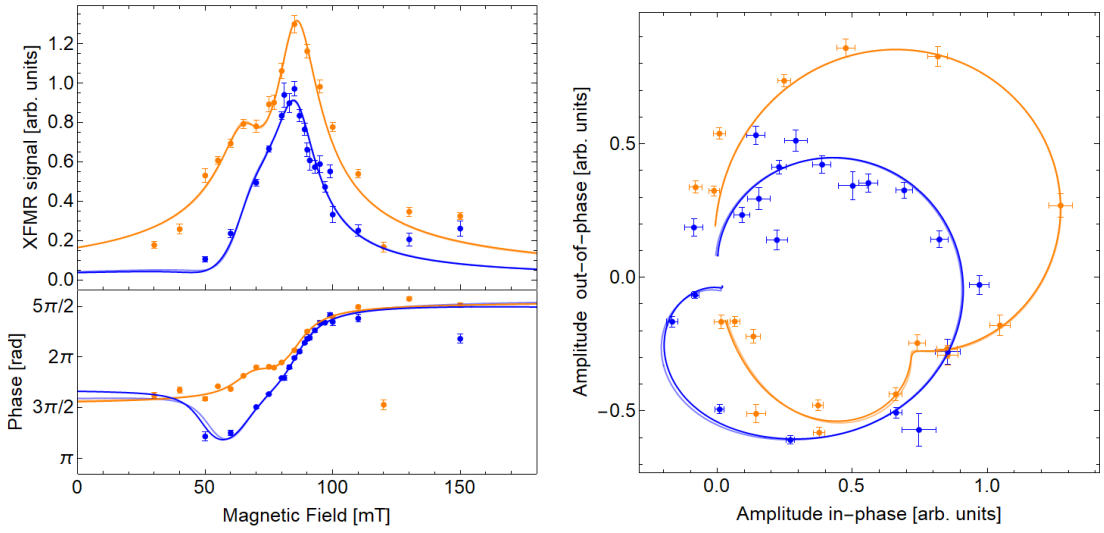

Figure D.6: XFMR results for the LG002 sample at 274 K, and the external field direction $\theta_H = 90°$. Orange and blue point represent the data for Co and Py respectively.

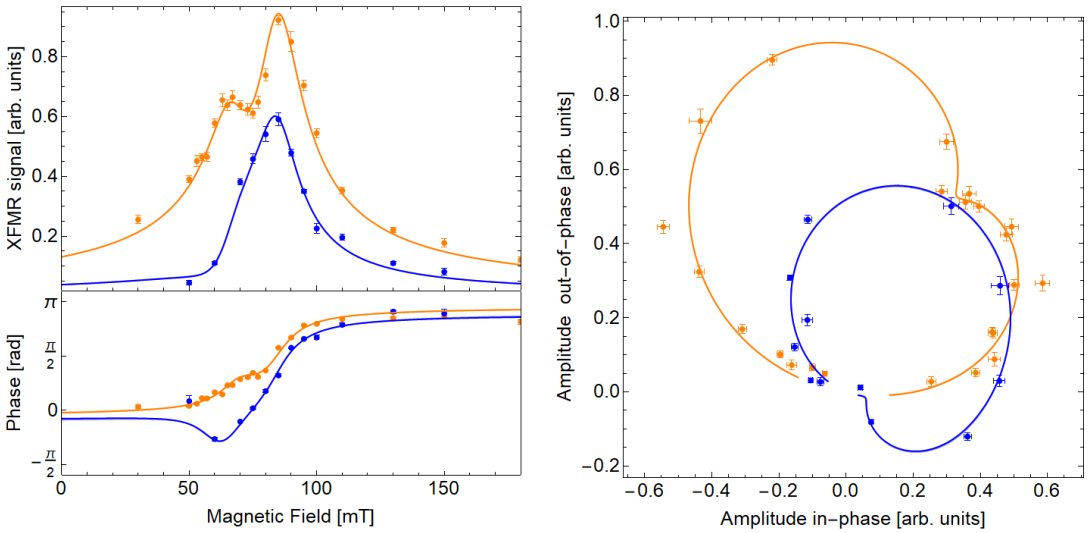

Figure D.7: XFMR results for the LG002 sample at 300 K, and the external field direction $\theta_H = 90°$. Orange and blue point represent the data for Co and Py respectively.

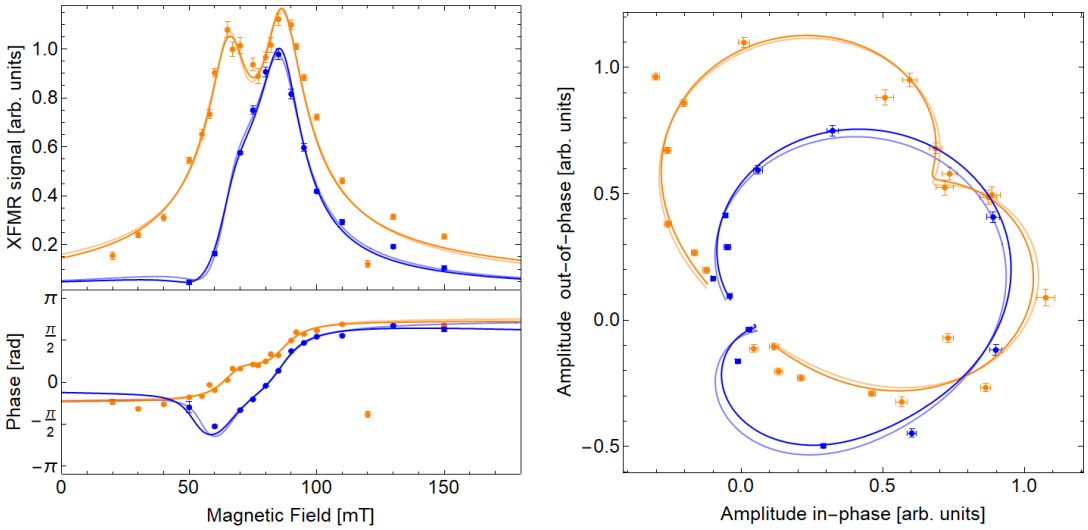

Figure D.8: XFMR results for the LG002 sample at 328 K, and the external field direction $\theta_H = 90°$. Orange and blue point represent the data for Co and Py respectively.

Appendix E

XFMR measurements for the LG003 sample

Results of the XFMR measurements and theoretical model fits for the sample LG003 measured with the magnetic field directed in-plane of the sample ($\theta_H = 90°$) at temperatures in range between 80K and 300K. Orange and blue points were used to mark the experimental data for Co and Py respectively. Solid lines represent the theoretical model fit. The semitransparent lines refer to the model with EC only and the opaque lines to the model with EC and SP.

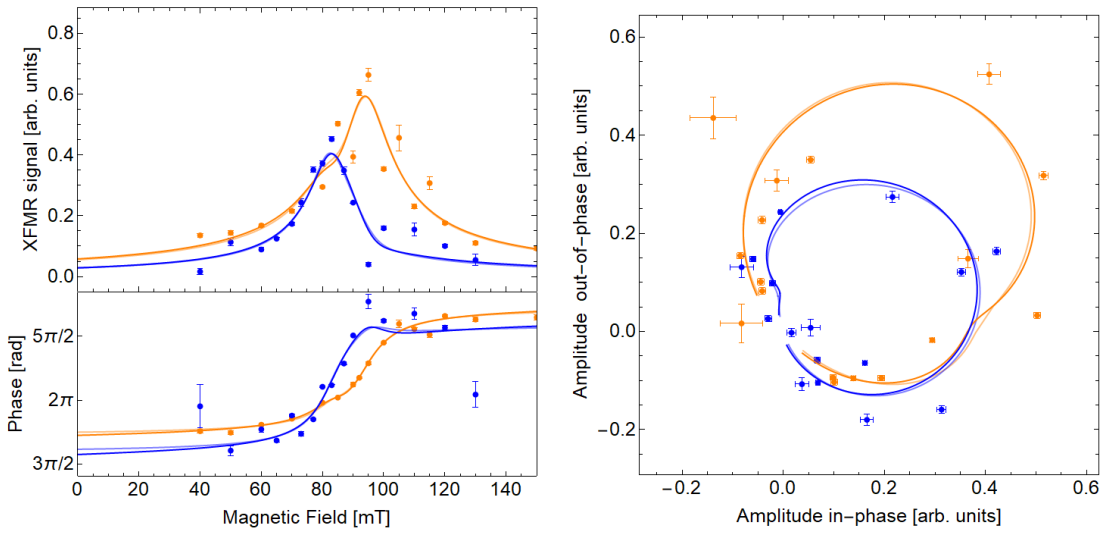

Figure E.1: XFMR results for the LG003 sample at 80 K, and the external field direction $\theta_H = 90°$. Orange and blue point represent the data for Co and Py respectively.

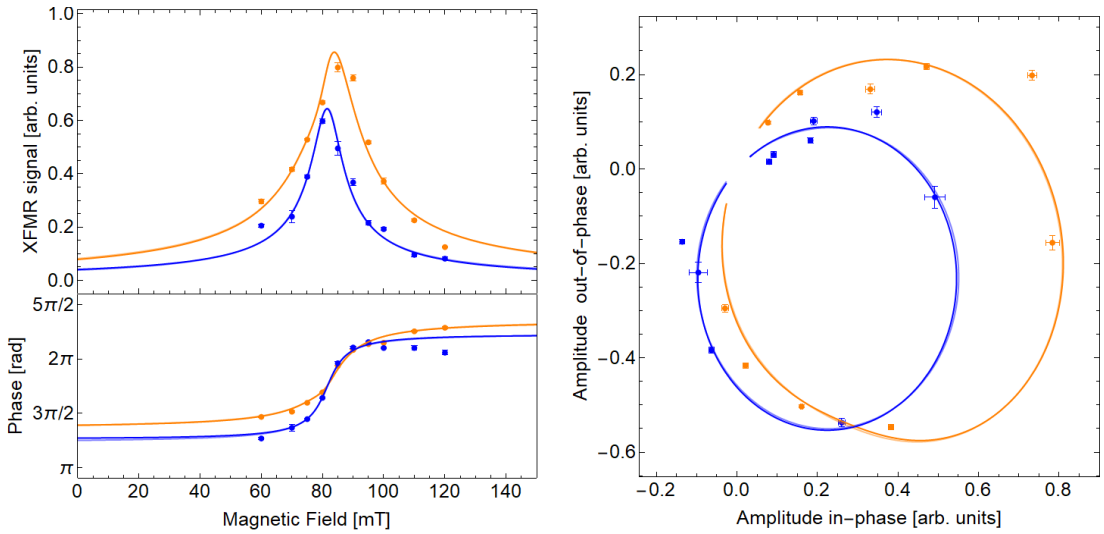

Figure E.2: XFMR results for the LG003 sample at 163 K, and the external field direction $\theta_H = 90°$. Orange and blue point represent the data for Co and Py respectively.

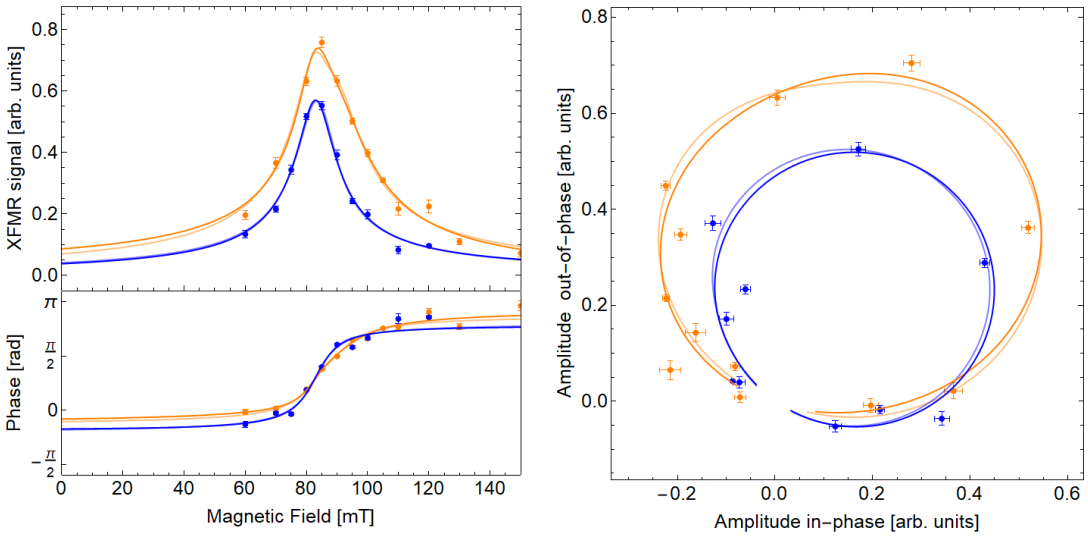

Figure E.3: XFMR results for the LG003 sample at 173 K, and the external field direction $\theta_H = 90°$. Orange and blue point represent the data for Co and Py respectively.

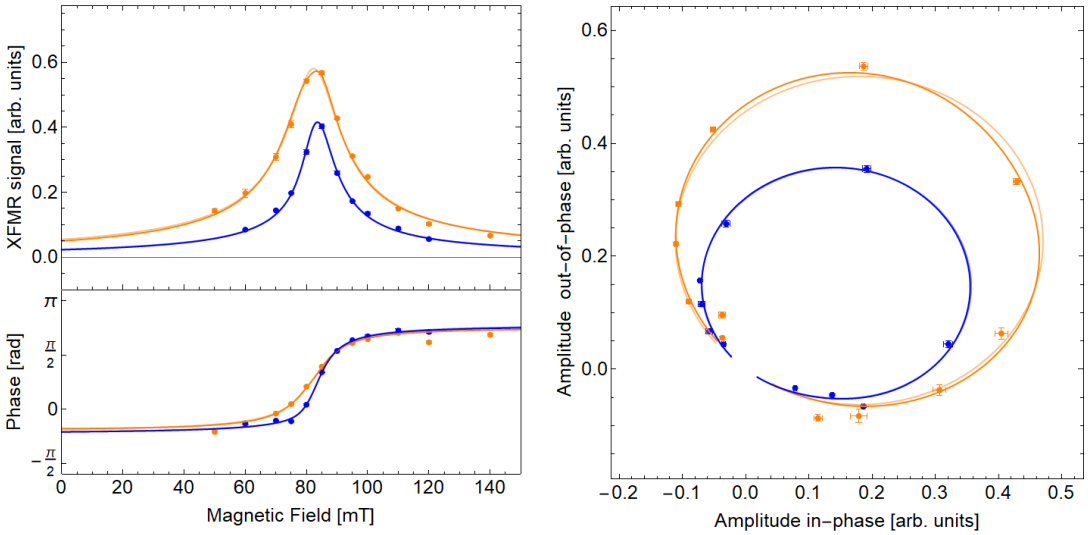

Figure E.4: XFMR results for the LG003 sample at 201 K, and the external field direction $\theta_H = 90°$. Orange and blue point represent the data for Co and Py respectively.

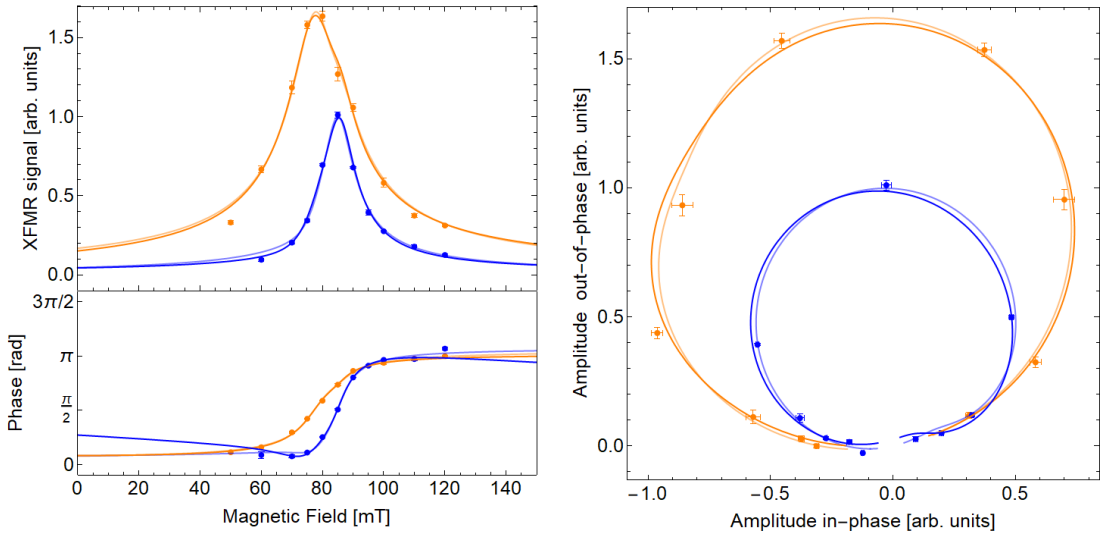

Figure E.5: XFMR results for the LG003 sample at 256 K, and the external field direction $\theta_H = 90°$. Orange and blue point represent the data for Co and Py respectively.

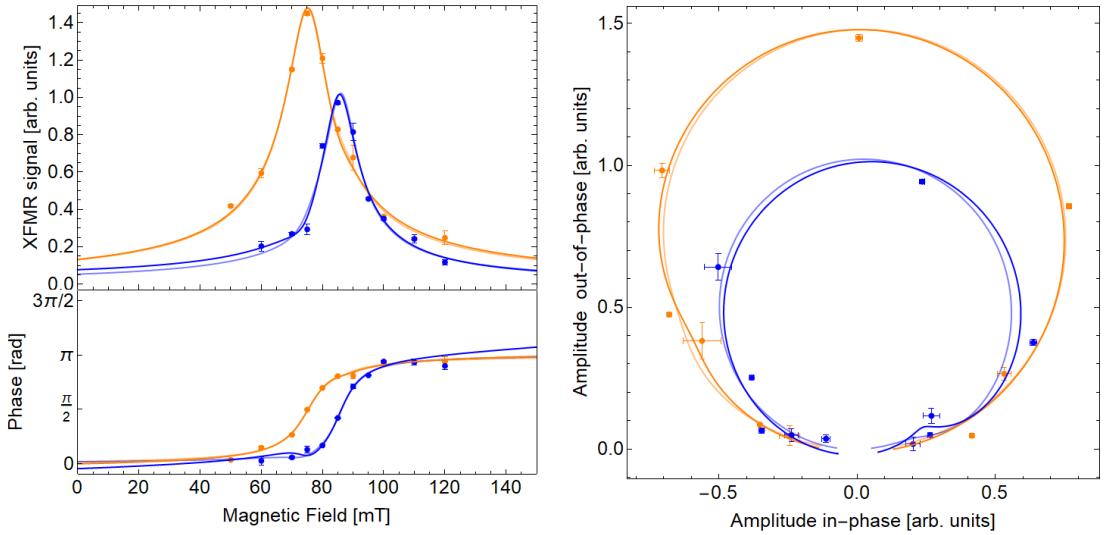

Figure E.6: XFMR results for the LG003 sample at 275 K, and the external field direction $\theta_H = 90°$. Orange and blue point represent the data for Co and Py respectively.

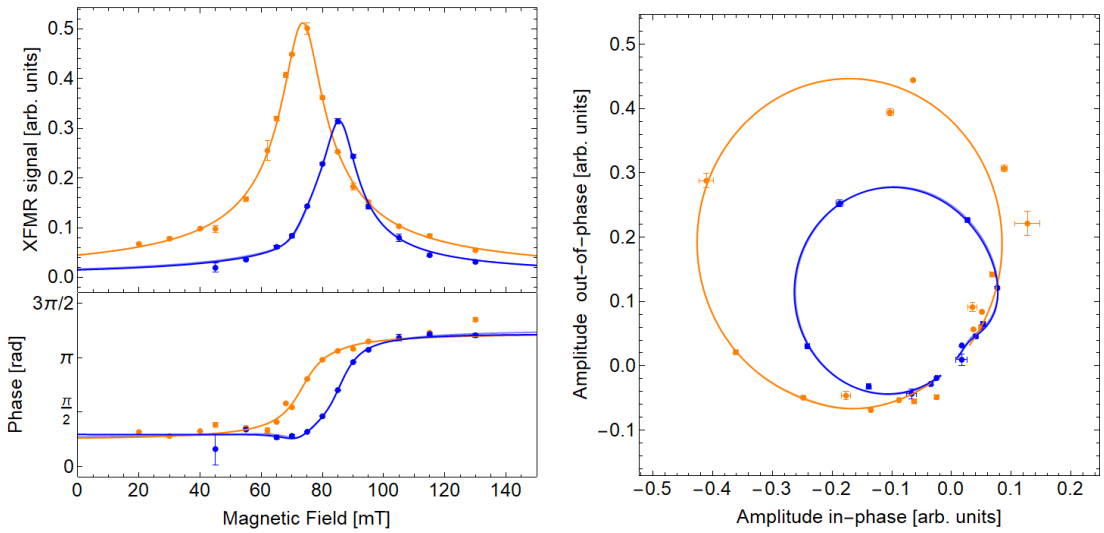

Figure E.7: XFMR results for the LG003 sample at 300 K, and the external field direction $\theta_H = 90°$. Orange and blue point represent the data for Co and Py respectively.

Bibliography

[1] J. D. Levine, S. H. McFarlane, and P. Mark. Si (111) 7 ×7 surface structure: Calculations of LEED intensity and comparison with experiment. *Physical Review B*, 16(12):5415–5425, 1977.

[2] A. I. Figueroa, A. A. Baker, L. J. Collins-McIntyre, T. Hesjedal, and G. van der Laan. Spin pumping through a topological insulator probed by x-ray detected ferromagnetic resonance. *Journal of Magnetism and Magnetic Materials*, 400:178–183, 2016.

[3] L. Marick. Variation of Resistance and Structure of Cobalt with Temperature and a Discussion of Its Photoelectric Emission. *Physical Review*, 49(11):831–837, 1936.

[4] N. Oehl, G. Schmuelling, M. Knipper, R. Kloepsch, T. Placke, J. Kolny-Olesiak, T. Plaggenborg, M. Winter, and J. Parisi. In situ X-ray diffraction study on the formation of α-Sn in nanocrystalline Sn-based electrodes for lithium-ion batteries. *CrystEngComm*, 17(44):8500–8504, 2015.

[5] W. H. Butler, X.-G. Zhang, T. C. Schulthess, and J. M. MacLaren. Spin-dependent tunneling conductance of Fe/MgO/Fe sandwiches. *Physical Review B*, 63:054416, 2001.

[6] E. Y. Tsymbal, O. N. Mryasov, and P. R. LeClair. Spin-dependent tunnelling in magnetic tunnel junctions. *Journal of Physics: Condensed Matter*, 15(4):R109–R142, 2003.

[7] J. Mathon and A. Umerski. Theory of tunneling magnetoresistance of an epitaxial Fe/MgO/Fe(001) junction. *Physical Review B*, 63:220403, 2001.

[8] J. S. Moodera, L. R. Kinder, T. M. Wong, and R. Meservey. Large Magnetoresistance at Room Temperature in Ferromagnetic Thin Film Tunnel Junctions. *Physical Review Letters*, 74:3273–3276, 1995.

[9] T. Miyazaki and N. Tezuka. Giant magnetic tunneling effect in Fe/Al_2O_3/Fe junction. *Journal of Magnetism and Magnetic Materials*, 139(3):L231–L234, jan 1995.

[10] S. S. P. Parkin, C. Kaiser, A. Panchula, P. M. Rice, B. Hughes, M. Samant, and S.-H. Yang. Giant tunnelling magnetoresistance at room temperature with MgO (100) tunnel barriers. *Nature Materials*, 3:862–867, 2004.

[11] S. Yuasa, T. Nagahama, A. Fukushima, Y. Suzuki, and K. Ando. Giant room-temperature magnetoresistance in single-crystal Fe/MgO/Fe magnetic tunnel junctions. *Nature Materials*, 3:868–871, 2004.

[12] H. Sato, M. Yamanouchi, S. Ikeda, S. Fukami, F. Matsukura, and H. Ohno. Perpendicular-anisotropy CoFeB-MgO magnetic tunnel junctions with a MgO/CoFeB/Ta/CoFeB/MgO recording structure. *Applied Physics Letters*, 101(2):022414, 2012.

[13] V. B. Naik, H. Meng, R. S. Liu, P. Luo, S. Yap, and G. C. Han. Electric-field tunable magnetic-field-sensor based on CoFeB/MgO magnetic tunnel junction. *Applied Physics Letters*, 104(23):232401, 2014.

[14] W. J. Gallagher and S. S. P. Parkin. Development of the magnetic tunnel junction MRAM at IBM: From first junctions to a 16-Mb MRAM demonstrator chip. *IBM Journal of Research and Development*, 50:5–23, 2006.

[15] I. L. Prejbeanu, S. Bandiera, J. Alvarez-Hérault, R. C. Sousa, B. Dieny, and J.-P. Nozières. Thermally assisted MRAMs: ultimate scalability and logic functionalities. *Journal of Physics D: Applied Physics*, 46:074002, 2013.

[16] M. D. Stiles. Interlayer exchange coupling. *Journal of Magnetism and Magnetic Materials*, 200(1):322–337, 1999.

[17] P. Poulopoulos and K. Baberschke. Magnetism in thin films. *Journal of Physics: Condensed Matter*, 11(48):9495–9515, 1999.

[18] J. C. Slonczewski. Current-driven excitation of magnetic multilayers. *Journal of Magnetism and Magnetic Materials*, 159(1):L1–L7, 1996.

[19] L. Berger. Emission of spin waves by a magnetic multilayer traversed by a current. *Physical Review B*, 54(13):9353–9358, 1996.

[20] M. Tsoi, A. G. M. Jansen, J. Bass, W.-C. Chiang, M. Seck, V. Tsoi, and P. Wyder. Excitation of a Magnetic Multilayer by an Electric Current. *Physical Review Letters*, 80:4281–4284, 1998.

[21] A. Kalitsov, M. Chshiev, I. Theodonis, N. Kioussis, and W. H. Butler. Spin-transfer torque in magnetic tunnel junctions. *Physical Review B*, 79:174416, 2009.

[22] D. C. Ralph and M. D. Stiles. Spin transfer torques. *Journal of Magnetism and Magnetic Materials*, 320(7):1190–1216, 2008.

[23] S. Lepadatu, M. C. Hickey, A. Potenza, H. Marchetto, T. R. Charlton, S. Langridge, S. S. Dhesi, and C. H. Marrows. Experimental determination of spin-transfer torque nonadiabaticity parameter and spin polarization in permalloy. *Physical Review B*, 79:094402, 2009.

[24] M. K. Marcham, L. R. Shelford, S. A. Cavill, P. S. Keatley, W. Yu, P. Shafer, A. Neudert, J. R. Childress, J. A. Katine, E. Arenholz, N. D. Telling, G. van der Laan, and R. J. Hicken. Phase-resolved x-ray ferromagnetic resonance measurements of spin pumping in spin valve structures. *Physical Review B*, 87:180403, 2013.

[25] A. A. Baker, A. I. Figueroa, D. Pingstone, V. K. Lazarov, G. van der Laan, and T. Hesjedal. Spin pumping in magnetic trilayer structures with an MgO barrier. *Scientific Reports*, 6(1):35582, 2016.

[26] A. A. Baker, A. I. Figueroa, T. Hesjedal, and G. van der Laan. Antidamping torques from simultaneous resonances in ferromagnet-topological insulator-ferromagnet heterostructures. *Journal of Magnetism and Magnetic Materials*, 473:470–476, 2019.

[27] M. R. Scholz, V. A. Rogalev, L. Dudy, F. Reis, F. Adler, J. Aulbach, L. J. Collins-McIntyre, L. B. Duffy, H. F. Yang, Y. L. Chen, T. Hesjedal, Z. K. Liu, M. Hoesch, S. Muff, J. H. Dil, J. Schäfer, and R. Claessen. Topological surface state of α-Sn on InSb(001) as studied by photoemission. *Physical Review B*, 97(7):075101, 2018.

[28] A. H. Morrish. *The Physical Principles of Magnetism*. John Wiley & Sons, Ltd, 2013.

[29] C. A. Gonano, R. E. Zich, and M. Mussetta. Definition for Polarization P and Magnetization M Fully Consistent with Maxwell's Equations. *Progress In Electromagnetics Research B*, 64:83–101, 2015.

[30] Alessio Caciagli, Roel J. Baars, Albert P. Philipse, and Bonny W. M. Kuipers. Exact expression for the magnetic field of a finite cylinder with arbitrary uniform magnetization. *Journal of Magnetism and Magnetic Materials*, 456:423–432, 2018.

[31] A. N. Bogdanov and I. E. Dragunov. Metastable states, spin–reorientation transitions, and domain structures in planar hexagonal antiferromagnets. *Low Temperature Physics*, 24(12):852–857, 1998.

[32] E. T. Ferguson. Uniaxial magnetic anisotropy induced in Fe–Ni alloys by magnetic anneal. *Journal of Applied Physics*, 29(3):252–253, 1958.

[33] W. F. Brown. Magnetostatic principles in ferromagnetism. *Journal of the Franklin Institute*, 275(2):150, 1963.

[34] W. F. Brown. *Magnetostatic principles in ferromagnetism*, volume 1. North-Holland Publishing Company, 1962.

[35] L. Landau and E. Lifshitz. On the theory of the dispersion of magnetic permeability in ferromagnetic bodies. *The Collected Papers of E. M. Lifshitz*, pages 51–65, 1992.

[36] M. C. Hickey and J. S. Moodera. Origin of Intrinsic Gilbert Damping. *Physical Review Letters*, 102(13):137601, 2009.

[37] Y. Zhang, X. S. Wang, H. Y. Yuan, S. S. Kang, H. W. Zhang, and X. R. Wang. Dynamic magnetic susceptibility and electrical detection of ferromagnetic resonance. *Journal of Physics: Condensed Matter*, 29(9):095806, 2017.

[38] Yaroslav Tserkovnyak, Arne Brataas, Gerrit E. W. Bauer, and Bertrand I. Halperin. Nonlocal magnetization dynamics in ferromagnetic heterostructures. *Reviews of Modern Physics*, 77(4):1375–1421, 2005.

[39] C. B. Duke. Semiconductor Surface Reconstruction: The Structural Chemistry of Two-Dimensional Surface Compounds. *Chemical Reviews*, 96(4):1237–1260, 1996.

[40] W. Mönch. *Semiconductor Surfaces and Interfaces*. Springer Berlin Heidelberg, Berlin, Heidelberg, 2001.

[41] W. Haynes. *CRC handbook of chemistry and physics : a ready-reference book of chemical and physical data*. CRC Press, Boca Raton, FL, 2011.

[42] R. E. Honig and D. A. Kramer. *Vapor Pressure Data for the Solid and Liquid Elements*. RCA Laboratories, David Sarnoff Research Center, 1969.

[43] C. Julian Chen. Introduction to Scanning Tunneling Microscopy, 2007.

[44] L. Gladczuk, P. Aleshkevych, K. Lasek, and P. Przyslupski. Magnetic anisotropy of Au/Co/Au/MgO heterostructure: Role of the gold at the Co/MgO interface. *Journal of Applied Physics*, 116(23):233909, 2014.

[45] A. Baker. *Tailoring of magnetic anisotropy and interfacial spin dynamics.* PhD thesis, University of Oxford., 2016.

[46] L. F. Chen. *Microwave electronics: measurement and materials characterization*. Wiley, Chichester Hoboken, NJ, 2004.

[47] C.-K. Lo. Instrumentation for Ferromagnetic Resonance Spectrometer. In *Ferromagnetic Resonance - Theory and Applications*. InTech, July 2013.

[48] H. J. Adèr. *Advising on research methods: a consultant's companion*, chapter Modelling, pages 271–304. Johannes van Kessel Pub, 2008.

[49] T. Hastie, R. Tibshirani, and J. Friedman. *The Elements of Statistical Learning*. Springer New York, 2009.

[50] M. R. Hestenes and E. Stiefel. Methods of conjugate gradients for solving linear systems. *Journal of Research of the National Bureau of Standards*, 49(6):409, 1952.

[51] T. A. Straeter. On the Extension of the Davidon-Broyden Class of Rank One, Quasi-Newton Minimization Methods to an Infinite Dimensional Hilbert Space with Applications to Optimal Control Problems. Technical report, 1971.

[52] S. S. Wilks. The Large-Sample Distribution of the Likelihood Ratio for Testing Composite Hypotheses. *The Annals of Mathematical Statistics*, 9(1):60–62, 1938.

[53] D. M. Bates J. C. Pinheiro. *Mixed-Effects Models in S and S-Plus*. Springer-Verlag GmbH, January 2000.

[54] K. Popper. *The Logic of Scientific Discovery*. Routledge, 2005.

[55] Y. Xu, D. Awschalom, and J. Nitta. *Handbook of Spintronics*. Springer, 2016.

[56] S. Yuasa, A. Fukushima, H. Kubota, Y. Suzuki, and K. Ando. Giant tunneling magnetoresistance up to 410% at room temperature in fully epitaxial Co/MgO/Co magnetic tunnel junctions with bcc Co(001) electrodes. 89:042505, 2006.

[57] S. J. Barnett and G. S. Kenny. Gyromagnetic Ratios of Iron, Cobalt, and Many Binary Alloys of Iron, Cobalt, and Nickel. *Physical Review*, 87(5):723–734, sep 1952.

[58] K. Sasage, K. Harii, K. Ando, K. Uchida, D. Kikuchi, and E. Saitoh. Modulation of gyromagnetic ratio in thin film due to spin pumping. 322:1425–1427, 2010.

[59] Y. Pogoryelov, M. Pereiro, S. Jana, A. Kumar, S. Akansel, M. Ranjbar, D.Thonig, D. Primetzhofer, P. Svedlindh, J. Åkerman, O. Eriksson, O. Karis, and D. A. Arena. Nonreciprocal spin pumping damping in asymmetric magnetic trilayers. *Physical Review B*, 101(5), 2020.

[60] G. B. G. Stenning, L. R. Shelford, S. A. Cavill, F. Hoffmann, M. Haertinger, T. Hesjedal, G. Woltersdorf, G. J. Bowden, S. A. Gregory, C. H. Back, P. A. J. de Groot, and G. van der Laan. Magnetization dynamics in an exchange-coupled NiFe/CoFe bilayer studied by x-ray detected ferromagnetic resonance. *New Journal of Physics*, 17(1):013019, 2015.

[61] J. E. Moore. The birth of topological insulators. *Nature*, 464(7286):194–198, 2010.

[62] C. L. Kane and E. J. Mele. Z_2 Topological Order and the Quantum Spin Hall Effect. *Physical Review Letters*, 95(14), 2005.

[63] Liang Fu, C. L. Kane, and E. J. Mele. Topological Insulators in Three Dimensions. *Physical Review Letters*, 98(10), 2007.

[64] J. E. Moore and L. Balents. Topological invariants of time-reversal-invariant band structures. *Physical Review B*, 75(12), 2007.

[65] R. Roy. Topological phases and the quantum spin Hall effect in three dimensions. *Physical Review B*, 79(19), 2009.

[66] B. A. Bernevig, T. L. Hughes, and S.-C. Zhang. Quantum Spin Hall Effect and Topological Phase Transition in HgTe Quantum Wells. *Science*, 314(5806):1757–1761, 2006.

[67] Y. L. Chen, J. G. Analytis, J.-H. Chu, Z. K. Liu, S.-K. Mo, X. L. Qi, H. J. Zhang, D. H. Lu, X. Dai, Z. Fang, S. C. Zhang, I. R. Fisher, Z. Hussain, and Z.-X. Shen. Experimental Realization of a Three-Dimensional Topological Insulator, Bi_2Te_3. *Science*, 325(5937):178–181, 2009.

[68] Y. L. Chen, J. H. Chu, J. G. Analytis, Z. K. Liu, K. Igarashi, H. H. Kuo, X. L. Qi, S. K. Mo, R. G. Moore, D. H. Lu, M. Hashimoto, T. Sasagawa, S. C. Zhang, I. R. Fisher, Z. Hussain, and Z. X. Shen. Massive Dirac Fermion on the Surface of a Magnetically Doped Topological Insulator. *Science*, 329(5992):659–662, 2010.

[69] T. Yokoyama, J. Zang, and N. Nagaosa. Theoretical study of the dynamics of magnetization on the topological surface. *Physical Review B*, 81(24):241410(R), 2010.

[70] V. A. Rogalev, F. Reis, F. Adler, M. Bauernfeind, J. Erhardt, A. Kowalewski, M. R. Scholz, L. Dudy, L. B. Duffy, T. Hesjedal, M. Hoesch, G. Bihlmayer, J. Schäfer, and R. Claessen. Tailoring the topological surface state in ultrathin α -Sn(111) films. *Physical Review B*, 100(24):245144, 2019.

[71] D. T. Wang, N. Esser, M. Cardona, and J. Zegenhagen. Epitaxy of Sn on Si(111). *Surface Science*, 343(1-2):31–36, 1995.

[72] J. T. Ryu, M. Katayama, and K. Oura. Sn thin film growth on Si(111) surface studied by CAICISS. *Surface Science*, 515(1):199–204, 2002.

[73] B. R. Cuenya, M. Doi, and W. Keune. Epitaxial growth and interfacial structure of Sn on Si(111)-(7×7). *Surface Science*, 506(1-2):33–46, 2002.

[74] W. Tu. Structure Analysis of Sn Bilayer Films on Si (111) . Master's thesis, University of Tennessee, August 2014.

[75] M. Jäger, C. Brand, A. P. Weber, M. Fanciulli, J. H. Dil, H. Pfnür, and C. Tegenkamp. α -Sn phase on Si(111): Spin texture of a two-dimensional Mott state. *Physical Review B*, 98(16):165422, 2018.

[76] T. Ichikawa. Structural study of ultrathin Sn layers deposited onto Ge(111) and Si(111) surfaces by RHEED. *Surface Science*, 140(1):37–63, 1984.

[77] F. Ronci, S. Colonna, A. Cricenti, and G. L. Lay. Detecting and localizing surface dynamics with STM: a study of the Sn/Ge(111) and Sn/Si(111) α-phase surfaces. *Journal of Physics: Condensed Matter*, 22(26):264003, 2010.

[78] R. Cortés, A. Tejeda, J. Lobo-Checa, C. Didiot, B. Kierren, D. Malterre, J. Merino, F. Flores, E. G. Michel, and A. Mascaraque. Competing charge ordering and Mott phases in a correlated Sn/Ge(111) two-dimensional triangular lattice. *Physical Review B*, 88(12):125113, 2013.

[79] W. Srour, A. Tejeda, M. Stoffel, M. Abuín, Y. Fagot-Revurat, P. Le Fèvre, A. Taleb-Ibrahimi, and D. Malterre. Atomic and electronic structure of the(23×23)R30° strained Sn reconstruction on Ge/Si(1 1 1). *Journal of Electron Spectroscopy and Related Phenomena*, 195:174–178, 2014.

[80] B. F. Mason and B. R. Williams. Growth and annealing behaviour of α-Sn on InSb(001) measured by LEED and He atom scattering. *Surface Science*, 262(1-2):169–179, 1992.

[81] T. Osaka, H. Omi, K. Yamamoto, and A. Ohtake. Surface phase transition and interface interaction in the α-Sn/InSb{111} system. *Physical Review B*, 50(11):7567–7572, 1994.

[82] C.-Z. Xu, Y.-H. Chan, Y. Chen, P. Chen, X. Wang, C. Dejoie, M.-H. Wong, J. A. Hlevyack, H. Ryu, H.-Y. Kee, N. Tamura, M.-Y. Chou, Z. Hussain, S.-K. Mo, and T.-C. Chiang. Elemental Topological Dirac Semimetal: α -Sn on InSb(111). *Physical Review Letters*, 118(14):146402, 2017.

[83] K. Houben, J. K. Jochum, D. P. Lozano, M. Bisht, E. Menéndez, D. G. Merkel, Rudolf Rüffer, Aleksandr I. Chumakov, Sam Roelants, Bart Partoens, Milorad V. Milošević, François M. Peeters, Sebastien Couet, André Vantomme, Kristiaan Temst, and Margriet J. Van Bael. In situ study of the α-Sn to β-Sn phase transition in low-dimensional systems: Phonon behavior and thermodynamic properties. *Physical Review B*, 100(7):075408, 2019.

[84] Ł. Gladczuk, L. Gladczuk, P. Dluzewski, K. Lasek, P. Aleshkevych, D. M. Burn, G. van der Laan, and T. Hesjedal. Spin-current mediated exchange coupling in MgO-based magnetic tunnel junctions. *Physical Review B*, 103(6):064416, 2021.

[85] Ł. Gladczuk, L. Gladczuk, P. Dluzewski, G. van der Laan, and T. Hesjedal. Study of Spin Pumping through α-Sn Thin Films. *physica status solidi – Rapid Research Letters*, page 2100137, 2021.